UNIVERSIDAD DE CHILE
FACULTAD DE CIENCIAS FÍSICAS Y MATEMÁTICAS
DEPARTAMENTO DE GEOLOGÍA

THE ROLE OF THE SUBCONTINENTAL LITHOSPHERIC MANTLE IN METALLOGENESIS

TESIS PARA OPTAR AL GRADO DE DOCTOR EN CIENCIAS, MENCIÓN GEOLOGÍA

CARLOS SANTIAGO TASSARA

PROFESOR GUÍA:
DIEGO MORATA CÉSPEDES

PROFESOR CO-GUÍA:
MARTIN REICH MORALES

MIEMBROS DE LA COMISIÓN:
FERNANDO BARRA PANTOJA
CLAUDIA CANNATELLI
MANUEL E. SCHILLING

Este trabajo ha sido financiado por el Núcleo Milenio Trazadores de Metales en Zonas de Subducción, el Centro de Excelencia en Geotermia de los Andes, CEGA (FONDAP-CONICYT #15090013), y la beca doctoral CONICYT #21170857.

SANTIAGO DE CHILE
2019

RESUMEN DE LA TESIS PARA OPTAR AL GRADO DE: Doctor en Ciencias, mención Geología.
POR: Carlos Santiago Tassara
FECHA: abril 2019
PROFESOR GUÍA: Diego Morata Céspedes

THE ROLE OF THE SUBCONTINENTAL LITHOSPHERIC MANTLE IN METALLOGENESIS

The synergistic alignment of geological processes leading to the efficient accumulation of metals to form magmatic ore deposits starts with magma genesis in the deep interior of the Earth's mantle. Upon ascent, magmas must break their way through the thick, ancient, and stagnant subcontinental lithospheric mantle (SCLM). However, the degree to which this interaction diversifies the geochemical nature of ascending magmas and governs their metallogenic fertility remains largely unknown. Considering its long-term stability and complex history of chemical depletion and subsequent refertilization, the SCLM may act as a key layer of the Earth in the genesis and regional scale distribution of ore deposits within the crust.

In Chapter 2, I provide the first direct evidence linking a gold-rich reservoir in the SCLM to the formation of an auriferous province in the overlying crust. I propose that the combination of an initial stage of mantle-plume activity that produced gold refertilization with the later emplacement of a subduction zone, resulted in favorable conditions for the early magmatic stages that ultimately resulted in the formation of the world-class El Deseado Massif gold province.

In Chapter 3, I combine whole-rock and in-situ geochemical data to explore the effects of partial melting and metasomatism on the highly-siderophile element (HSE) budget of the peridotite xenoliths that sample the SCLM beneath El Deseado Massif. I show that several generations of base metal sulfides resulted from different metasomatic styles, providing valuable constraints to understand the mechanisms leading to HSE refertilization in the SCLM.

Chapter 4 explores the role of the redox conditions of the SCLM on gold and sulfur solubility of ascending magmas. I present a novel approach of interrogating the speciation of sulfur in mantle-derived apatite using in-situ synchrotron-based techniques. I show that substantial and heretofore unrecognized redox gradients may exist between primitive magmas ascending from the subduction zone and the more oxidized SCLM. By constraining the gradients in the valence state of sulfur recorded in apatite, I propose that redox reactions between ascending melt and the SCLM can have a profound effect on the ore-fertility of magmas.

Chapter 5 aims to deepen our understanding of redox processes in the Earth's mantle by focusing on olivine-hosted melt inclusions from highly primitive basalts from the southern Andes. Synchrotron-based techniques are combined with major and trace element data to assess the oxidation state of primitive arc melts. Despite their primitive nature, the studied melts appear to have undergone significant changes in their oxidation state during ascent and evolution, opening new questions regarding their reliability as redox tracers of their mantle source.

In summary, this study shows that the spatial and temporal overlapping of petrogenetic processes in the SCLM can significantly increase the metallogenic fertility of overlying crustal blocks. Time-integrated fluid fluxes result in complex metasomatic signals that reflect the mechanisms of HSE enrichment and formation of an enriched SCLM reservoir. These metallogenically fertile reservoirs can be tapped by ascending melts as a result of redox gradients that boost the sulfur and metals solubility. These results provide a new framework to explain why certain crustal blocks are significantly endowed with gold and other metals, highlighting the importance of understanding the time-integrated history of SCLM domains as a tool for regional exploration targeting.

RESUMEN DE LA TESIS PARA OPTAR AL GRADO DE: Doctor en Ciencias, mención Geología.
POR: Carlos Santiago Tassara
FECHA: abril 2019
PROFESOR GUÍA: Diego Morata Céspedes

THE ROLE OF THE SUBCONTINENTAL LITHOSPHERIC MANTLE IN METALLOGENESIS

El alineamiento óptimo de procesos geológicos que resultan en la acumulación eficiente de metales y formación de depósitos minerales de origen magmático comienza con la fusión parcial en el manto terrestre. Durante el ascenso, los magmas deben atravesar el manto litosférico subcontinental (MLSC). Sin embargo, el efecto de esta interacción en la geoquímica de los magmas y su fertilidad metalogénica permanece enigmática. Considerando su estabilidad a largo plazo y su compleja historia de empobrecimiento químico y posterior refertilización, el MLSC podría actuar como una capa clave de la tierra en la génesis y distribución regional de depósitos minerales en la corteza.

En el Capítulo 2 revelo la primera evidencia directa que conecta a un reservorio rico en oro del MLSC con la formación de una provincia aurífera en la corteza suprayacente. Propongo que la combinación la actividad de una pluma mantélica que produjo enriquecimiento en oro de la litosfera, con el posterior emplazamiento de una zona de subducción, resulto en condiciones favorables para las etapas magmáticas iniciales de un sistema que resulto en la formación del Macizo del Deseado, una provincia aurífera de clase mundial.

En el Capítulo 3 combino datos geoquímicos de roca total e in-situ para explorar los efectos de la fusión parcial y metasomatismo en la distribución y sistemática de los elementos altamente siderófilos en xenolitos peridotíticos que representan el MLSC bajo el Macizo del Deseado. Demuestro que distintas generaciones de sulfuros se originan como respuesta a distintos estilos metasomáticos, proporcionando información clave para comprender los mecanismos de enriquecimiento en metales del MLSC y la formación de reservorios fértiles.

En el Capítulo 4 exploro el efecto de las condiciones redox del MLSC en la solubilidad de oro y azufre de los magmas en ascenso. Mediante el uso de técnicas basadas en radiación sincrotrón, evaluamos la especiación del azufre incorporado en apatitos mantélicos. Propongo que la existencia de gradientes redox entre magmas en ascenso y el MLSC tiene un efecto fundamental en la fertilidad metalogénica de los magmas.

El Capítulo 5 se enfoca en el estudio de inclusiones vítreas en cristales de olivino de basaltos altamente primitivos de Los Andes Sur, para explorar la evolución redox de los magmas en la litosfera profunda. Se combinan técnicas de radiación sincrotrón con la composición de elementos mayores y trazas para evaluar el estado de oxidación de magmas primitivos de arco. A pesar de su naturaleza primitiva, los magmas estudiados parecen haber sufrido cambios substanciales en su estado de oxidación durante su ascenso, abriendo nuevas preguntas respecto de su evolución redox temprana y su relación con el estado de oxidación de su fuente mantélica.

Este estudio destaca que la sobreimposición espacial y temporal de procesos petrogenéticos en el MLSC puede incrementar significativamente la fertilidad metalogénica de su corteza suprayacente. La percolación de numerosos fluidos resultan en señales metasomáticas complejas que reflejan los mecanismos de enriquecimiento en metales y formación de dominios fértiles del MLSC. Estos metales pueden ser extraídos de manera eficiente por los magmas en ascenso como resultado de la formación de gradientes redox. Estos resultados presentan un nuevo marco para explicar la distribución heterogénea de bloques corticales enriquecidos en metales, remarcando la importancia de comprender la historia integrada del MLSC como una herramienta clave para la exploración mineral regional.

“A mis padres”

ACKNOWLEDGMENTS

Firstly, I would like to acknowledge my advisor Prof. Diego Morata for believing in me and giving me this incredible opportunity. I would also like to especially express my sincere gratitude to my mentor Prof. Martin Reich for his immense patience, motivation, support, and knowledge. His guidance was of significant help for the research and writing of this thesis. I could not have imagined having a better advisor and mentor for my Ph.D. study.

In addition, I would like to thank Profs. Fernando Barra, Claudia Cannatelli, and Manuel E. Schilling for their insightful comments, additional guidance, and encouragement. My sincere thanks also go to Dr. José M. González-Jiménez, who initially guided me and enlightened me the first glance of research. I would also like to express my gratitude to Prof. Michel Grégoire, Prof. Joaquín Proenza, and Prof. Adam Simon, who provided me the opportunity to join their teams as an intern and gave me access to their laboratories and research facilities.

I am also thankful to Brian Konecke and Adrian Fiege for their thoughtful discussions and for providing me with beamtime at the GeoSoilEnviroCars (Sector 13), Advance Photon Source (APS), Argonne National Laboratory. Tony Lanzirotti and Mat Newville are also acknowledged for their assistance with the μ-XANES analyses at the APS. I also express thanks Mathieu Leisen and Rurik Romero for their assistance with LA-ICP-MS analyses, and Owen Neill for his assistance with the microprobe analyses at UMich.

I thank my fellow officemates of the "Millennium Crew" for their stimulating discussions, for their help with samples preparation and troubleshooting the long-list of SEM mishaps, and for all the fun we had in the last four years. Also, I thank my friends at the University of Michigan, who made me feel like home during the internships and provided immense help during the sleepless nights working together in the microprobe, and for all the good moments we shared in the states.

I am also grateful to many University faculty members and staff who helped me throughout the Ph.D. I spatially thank Karin Rojas, Bernardette Vasquez, Blanca Baccola y Maritza Acuña, who gave me support and guidance throughout administrative issues. This Ph.D. has been funded by a scholarship from CONICYT (#21170857). I acknowledge the financial support from Centro de Excelencia en Geotermia de Los Andes, CEGA, Proyecto FONDAP-CONICYT #15090013; and Núcleo Milenio Trazadores de Metales.

Last but not least, I would like to thank my parents and my brother for their enormous spiritual and emotional support during the development of this Ph.D. I also extend my spatial thanks to Silvina, my life partner, who stood by me during this complex process.

CONTENTS

TABLES INDEX

FIGURES INDEX

CHAPTER 1. INTRODUCTION

1.1. GENERAL OVERVIEW AND MOTIVATION

Ore deposits are anomalous concentrations of metals of economic interest (*hereafter* "ore metals"). The genesis of magmatic-hydrothermal ore deposits, as well as their distribution in space and time, is a vastly complex natural phenomenon resulting from an optimal alignment of elements involving the different spheres of the Earth. These factors range from the composition of the mantle and degree of partial melting in the source of magmas (*asthenosphere*) to the composition of the fluids entrained into subduction zones assisting magma generation (*hydrosphere*), the differentiation of magmas during ascent across the lithosphere and exsolution of hydrothermal fluids (*lithosphere*), and even the climatic conditions leading, in some cases, to supergene enrichment of ore deposit at the Earth's surface (*atmosphere*).

The arrangement of processes leading to ore genesis is hardly unique and changes between different tectonic settings, mineralizing styles, and even among different individual deposits of the same type (*i.e.*, epithermal Au or porphyry Cu deposits). However, there are certain factors in the chain of processes leading to ore genesis that, regardless of the nature of each deposit style, will optimize the potential of magmas to accumulate economic concentrations of selected metals in certain regions of the crust, at a certain time (*e.g.*, Richards, 2015). Identifying and understanding how these "*metallogenic boosters*" operate is of significant value for scientific studies and has also practical applications for targeting concealed ore deposits during exploration (Hronsky et al., 2012).

The classical model holds that the formation of ore deposits is controlled by the combination of the nature of the parental magmas (*e.g.*, water content, oxygen fugacity), the relative timing of sulfide and volatile saturation in magmas, and efficient magmatic-hydrothermal enrichment processes. Alternatively, several lines of evidence indicate that the existence of a fertile reservoir from which ore-metals could be extracted and transferred to magmas is a key factor in the production and localization of regions of the crust endowed with ore deposits. The existence of a source region rich in ore metals is a matter of debate in modern economic geology (*e.g.*, Griffin et al., 2013; Arndt, 2013). Such a fertile reservoir has been proposed to occur in the mantle wedge (McInnes et al., 1999), the subcontinental lithospheric mantle (SCLM), lower crust (Sillitoe, 2008; Richards, 2009; Hronsky et al., 2012; Griffin, 2013; Chiaradia, 2014; Hou et al., 2015; Zheng et al., 2019), and even in the subducting oceanic slab (Mungall, 2002).

The SCLM is particularly attractive to the notion of a fertile reservoir because it is the most stable and long-lived portion of the Earth's mantle-crust system (Griffin et al., 2009; Herzberg and Rudnick, 2012), being likely to survive through tectonic cycles (Wilson, 1968). Therefore, the SCLM has a complex, time-integrated history that has shaped its composition leading to heterogeneously distributed domains of variable geochemical compositions. For instance, certain portions of the SCLM that remained stagnant over dehydrating slabs or mantle plumes might have been refertilized with ore metals such as gold (Rielli et al., 2017; Webber et al., 2012), thus becoming fertile reservoirs. Still, (*i*) the processes leading to metal enrichment in the SCLM are not fully understood, (*ii*) the effective mechanisms by which magmas source the metals from the SCLM the crust are unclear (*iii*) the spatial and temporal links between enriched domains of the SCLM and the formation of ore deposits in the overlying crust are diverse and in many cases incidental. All these issues have fostered the debate on the role of the SCLM in metallogenesis and motivated the development of this Ph.D. thesis.

1.2. THEORETICAL FRAMEWORK

1.2.1. The subcontinental lithospheric mantle

The subcontinental lithospheric mantle (SCLM) is the uppermost non-convective portion of the Earth's mantle located beneath the continents. It also represents a chemical, thermal, and mechanical boundary layer insulating the continental crust from the hotter and more dynamic Earth's asthenosphere (Griffin et al., 1999). The SCLM formation started in the mid to late Archean eon (Griffin et al., 2009; Herzberg and Rudnick, 2012) and since then has changed the fate of our planet by favoring the stabilization and preservation of the continental crust.

The origins of the SCLM remain controversial. However, two main hypotheses dominate the debate. The traditional notion holds that the continued accretion of subducted oceanic slabs, depleted in incompatible elements because of shallow partial melting in mid-ocean ridges, resulted in the formation of isolated fragments of SCLM (Griffin et al., 2007). The second and more recent perspective suggests that high degrees of partial melting resulted in the formation of large volume residues, constituting the SCLM (*e.g.*, Griffin et al., 2009). In the latter case, this could only have occurred through high-temperature melting of the ambient upper mantle, likely where mantle plumes rise from the deep Earth's interior and result in a regional temperature increase (Wyman and Kerrich, 2002).

Regardless of the mechanisms forming the SCLM, there is a consensus that it was originally highly depleted in incompatible elements (*e.g.*, Fe, Al, Ca, Na, K, LREE: Light rare earth elements) due to partial melting. Given that Fe is an incompatible element in mantle rocks, the depleted SCLM will be characterized by a low Fe/Mg ratio. This geochemical feature is largely responsible for the overall positive buoyancy of the SCLM, in turn providing the key to stabilize continents for billions of years. Therefore, since its formation, the SCLM has been infiltrated by fluids and melts coming from the deeper mantle, or from the oceanic slab in subduction zones, resulting in the enrichment of the SCLM in incompatible elements (*i.e.*, mantle metasomatism or refertilization).

1.2.2. Mantle metasomatism

Mantle metasomatism is a relatively modern term used to describe the change in the chemical composition of SCLM rocks due to interaction and reaction with fluids or melts from a deeper origin (Lloyd and Bailey, 1973; Harte, 1983; Dawson, 1984; O'Reilly and Griffin, 2012).

Mantle metasomatism, as called refertilization, is sometimes evident as for the presence of minerals that could have not been present after the SCLM formation by partial melting. This is referred to as "modal metasomatism" and includes the presence of hydrous and/or volatile-rich minerals (*e.g.*, amphibole, phlogopite, apatite, carbonates) (Harte, 1983). However, mantle metasomatism not always result in the formation of new phases but only in changes in the major and/or trace element geochemistry of the primary mineral assemblage of peridotites. This is referred to as "cryptic/stealth metasomatism" and includes, for example, high concentrations of LREE in clinopyroxene (Dawson, 1984; Griffin et al., 2009). Thus, the compositional nature of the fluids/melts that metasomatized a certain portion of the SCLM (*hereafter*: metasomatic agents) can be traced back from the imprint they left on the mantle rocks. There are many different types of metasomatic agents that have altered the composition of the SCLM since its origin. They range from hydrous and anhydrous alkaline to sub-alkaline silicate melts of mafic to ultramafic compositions, to carbonate melts, sulfide melts, C-O-H fluids ranging from water to methane and

CO_2, and even hydrocarbon-bearing fluids (O'Reilly and Griffin, 2012; and references therein). Furthermore, each type of metasomatic agent can affect a different volume of the SCLM at variable melt/rock ratios. As they percolate and react with the mantle wall-rock, they continue to evolve in their geochemical composition, a process known as the chromatographic effect (Navon and Stolper, 1987), multiplying the compositional effects of the possible metasomatic styles.

If we add to the above-mentioned factors the fact that the SCLM has long-lived history, we find that a single portion of the SCLM could have been affected by several metasomatic agents of different nature. For example, SCLM domains below cratonic regions may record the imprint of metasomatism by slab-derived fluids (e.g., Zheng et al., 2005). These events have repeatedly overprinted and modified in variable degrees the original mantle wall-rocks. This has produced a complex, essentially ubiquitously metasomatized lithospheric mantle, which is heterogeneous on scales of microns to the terrane-scale, and in cases leaving little to no primary mantle wall-rock (O'Reilly and Griffin, 2012).

1.2.3. The formation of SCLM fertile domains

Ore metals are concentrated in trace levels in upper mantle rocks, i.e., in less than tens of ppb for the noble metals (include platinum group elements: Os, Ir, Ru, Rh, Pt, Pd; plus Re and Au) and hundreds of ppm for Cu (e.g., Lorand and Luguet, 2016; Saunders et al., 2018). However, due to their highly siderophile and chalcophile behavior, their distribution is primarily controlled by base metal sulfide hosts (BMS; e.g., pyrrhotite, chalcopyrite, pentlandite, millerite). In turn, these BMS are accessory phases with noble metals concentrations of tens to hundreds of ppm and wt% levels of Cu and Ni. Therefore, although BMS are minor phases, they exert a fundamental control on the behavior and distribution of ore metals in mantle rocks.

The BMS, like silicate minerals, are sensible to episodes of mantle partial melting and metasomatism (e.g., Alard et al., 2000; Griffin et al., 2004). There is consensus that as a result of partial melting of the mantle, the most compatible of the ore metals (Os, Ir, Ru) are retained in residual BMS in the peridotite, and in cases in platinum group minerals (e.g., Lorand et al., 2010; Luguet et al., 2003; 2007). In contrast, mantle metasomatism can lead to the addition of newly formed sulfides rich in the more incompatible noble metals, i.e., Pt, Pd, Au, and Re (Lorand et al., 2013; Luguet et al., 2013; Saunders et al., 2015).

Despite this significant knowledge, the exact nature of the metasomatic agents responsible for the formation of ore metal-rich sulfides in the SCLM remains poorly constrained. This has nurtured the notion that SCLM metasomatism can result in a resupply of ore metals to the SCLM leading to the formation of metalogenically fertile domains (Griffin et al., 2013).

1.2.4. The lithospheric mantle connections of ore deposits

The connections between SCLM fertility and the formation and localization of ore deposits in the overlying crust are built on geochemical and geophysical evidence collected from a variety of deposit styles in different tectonic scenarios. This relation was first introduced to explain the formation and distribution of anorogenic ore deposits (Begg et a., 2010). More recently, it was adopted to explain certain features of orogenic ore deposits as briefly summarized below.

1.2.4.1. The SCLM and anorogenic ore deposits

The first connections between upper mantle metasomatism and the formation of ore deposits originated to explain the formation of kimberlite and lamproite diamond pipes in South Africa. Diamond deposits occur when kimberlites and/or lamproites formed by low degrees of partial melting entrain diamonds from the deeper roots of the SCLM during their eruption (Helmstaedt and Gurney, 1995). Since carbon behaves as an incompatible element during partial melting of the mantle, the presence of diamonds in the depleted SCLM requires the metasomatic addition of carbon. Furthermore, diamond-bearing kimberlites distribute near the edges of SCLM blocks mapped in magnetotelluric surveys (Griffin et al., 2013), also indicating a structural control on their localization. Thus, this type of ore deposit provides a clear example of how the metasomatic refertilization of the mantle is linked to economic mineralization in the crust.

The origin of magmatic Ni-Cu-PGE deposits is also related to the composition and architecture of the SCLM. This relationship is manifested at crustal levels by the proximity of these deposits to the craton margins as a result of the SCLM control on the pathways of magma ascent (Begg et al., 2010). In this case, the role of the SCLM as the source of metals is vigorously debated (Arndt, 2013). Simple partial melting of a primitive upper mantle (PUM)-like peridotite cannot explain the high PGE contents in some magmas nor their provinciality (Maier and Groves, 2011). This has led to models that invoke additional sources of metals for the formation of Ni-Cu-PGE deposits, for example, the SCLM given its strong architectural control on Ni-Cu-PGE mineralization. Interestingly, Zhang et al. (2008) found geochemical and isotopic differences between fertile and barren large igneous provinces, suggesting that the first ones have interacted with volumes of ancient metasomatized SCLM. Furthermore, Richardson and Shirey (2008) found similar Re-Os isotopic signatures between the Bushveld complex ore minerals and SCLM sulfide inclusions trapped within diamonds, indicating that the SCLM could have contributed substantially to the metal endowment of the Bushveld magmas.

Another notable example of the mantle control on the formation of giant ore deposits is the Witwatersrand basin in South Africa. This is the largest known gold province in the world and has nurtured much controversy about the ore-forming processes (i.e., hydrothermal vs. placer model, Phillips and Law, 2000; Frimmel and Minter, 2002). Kirk et al. (2002) performed Re-Os isotopic analyses of native gold and pyrite and obtained isochrones ages yielding 3.03 ± 0.2 Ga. These data also placed constraints on the source of Au, with initial $^{187}Os/^{188}Os$ ratios of 0.109-0.108 that are indicative of a mantle-derived mafic/ultramafic rock source. This provided strong evidence for a mantle-crust link during the genesis of these deposits.

1.2.4.2. The SCLM and orogenic ore deposits

The distribution of ore deposits in Phanerozoic orogens shows a marked provincialism (Sillitoe, 2008). Gold deposits of various types, for example, are concentrated in highly endowed regions of the crust forming districts, belts, or metallogenic provinces that were typically formed during short time spans (less than 20 m.y.) (e.g., Singer, 1995; Henry et al., 1996; Harris et al., 2008; Sillitoe, 2008). In addition, the distribution of some of these mineralized regions is commonly associated to major trans-lithospheric structures (Hildenbrand et al., 2000; Grauch et al., 2003; Heinson et al., 2018). The spatial and temporal control on the distribution of ore deposits around the world remains enigmatic because similar magmatic-hydrothermal processes elsewhere resulted in smaller or no mineralization (Sillitoe, 2008). Therefore, ore deposit formation may be linked to some fundamental predisposition of particular crustal segments to mineralization. The idea that the localization of highly endowed regions of the Earth's crust is related to anomalously metal-rich lower crust or mantle blocks offers an attractive solution to an otherwise fortuitous

distribution (e.g., McInnes et al., 1999; Core et al., 2006; Sillitoe, 2008; Richards, 2009; Hronsky et al., 2012).

This mantle-crust link has also been supported by geochemical evidence. In orogenic settings, primitive magmas associated with mineralization show distinctive patterns relative to "average" arc basalts (Hronsky et al., 2012). They have higher Nb, Th, and other incompatible lithophile elements as well as higher Nb/Y, Th/Yb, and Ba/Zr ratios. Loucks and Ballard (2003) concluded that the parental magmas in arcs derive from unusually low degrees of partial melting in the asthenospheric mantle wedge or the melting of refertilized lithospheric mantle regions (Hronsky et al., 2012). These observations are also accompanied by the close association between alkali-rich magmas (commonly ascribed to the melting of K-refertilized SCLM) and gold mineralization (Rock et al. 1987; Muller and Groves 1995; Sillitoe 1997; Jensen and Barton 2000; Muller 2002).

Perhaps, a more robust indicator of the mantle-crust connection in orogenic regions comes from the study of the isotopic signature of the ore minerals. The Re-Os isotopic system is a robust geochemical tool for tracing the source of metals in various environments, particularly in the mantle (Luck and Allegre, 1980; Becker et al., 2016; Harvey et al., 2016). Because Re is highly incompatible during mantle partial melting, the Re/Os ratio of the crust is significantly higher than that of the mantle. Given that the SCLM has formed as a result of multiple cycles of partial melting over the Earth's history, its $^{187}Os/^{188}Os$ ratio has evolved to significantly lower values (0.127) than that of the crust (e.g., >2) (Morgan et al., 1995; Shen et al., 1996). Mathur et al. (2000) presented Re-Os data of ore minerals from porphyry Cu-Mo deposits in Chile. The analyses showed an anti-correlation between Cu tonnage and $^{187}Os/^{188}Os$ ratios. In some of the largest deposits such as El Teniente, the sulfide mineralization has $^{187}Os/^{188}Os$ ratios that are comparable to those of the mantle, pointing to a deep source for metals. Similar initial $^{187}Os/^{188}Os$ have been observed in several deposit styles, including Cu and Au porphyry and IOCG deposits (e.g., McInnes et al, 1999; Barra et al., 2017). Furthermore, Zheng et al. (2018) has recently linked the Cu isotopic composition of metasomatized portions of the SCLM to that of porphyry copper deposits in the southern Tibet, suggesting Cu enrichment of the mantle source.

In summary, several lines of evidence point to a link between a mantle source of ore metals, and the development of ore deposits. However, no direct evidence exists that unequivocally links a particular domain of the SCLM to the formation of a single ore deposit (or group of deposits) in the overlying crust.

1.2.5. Sourcing metals from a fertile SCLM reservoir

The ore metal budget of a particular SCLM domain will be primarily controlled by BMS. BMS have low melting temperatures compared to the primary silicate assemblage of upper mantle rocks. Experimental studies have suggested the presence of both crystalline sulfide phases and sulfide liquids at upper mantle temperature and pressure (Bockrath et al., 2004). As long as BMS or sulfide liquids exist in the SCLM, they will retain ore metals because of their highly siderophile and chalcophile behavior. Sulfides are exhausted from the peridotite residue only after 15 to 20% of partial melting (Lorand and Grégoire, 2006), depending on sulfur abundance, pressure, and oxygen fugacity (Jugo et al., 2010; Mavrogenes and O'Neill, 1999). Therefore, sourcing the metals from the SCLM after partial melting will only occur after relatively high degrees of partial melting. However, extracting such a large volume of magmas from the SCLM is unlikely because of its overall refractory nature (Arndt and Christensen, 1992). In addition, a large degree of partial

melting would not result in the highly alkaline and incompatible element rich nature of magmas commonly associated with gold mineralization (Hronsky et al., 2012). Therefore, and even though a metalogenically fertile domain of the SCLM can be formed by metasomatism, partial melting processes cannot be accounted exclusively for the extraction of ore metals from the mantle.

The oxygen fugacity of the solid mantle and its melts is a key variable controlling the behavior of sulfur and chalcophile and siderophile elements (Jugo, 2009; Lorand and Luguet, 2016). This parameter reflects the oxidation state of the system and is commonly expressed as log units relative to the fayalite-magnetite-quartz mineral buffer (ΔFMQ). Experimental studies have shown that sulfide (S^{2-}) is the dominant oxidation state of sulfur in silicate melts under reducing conditions (ΔFMQ <0). In contrast, at ΔFMQ >2 the melt is dominated by sulfate (S^{6+}) whereas a sharp transition from sulfide towards the more soluble oxidized sulfate is observed around ΔFMQ +1 (Jugo et al., 2010). Hence, partial melting under oxidizing conditions will effectively promote the break-down of sulfide hosts and release its contained metals, ultimately increasing the ore metal endowment of magmas (Sillitoe, 2008; Richards, 2015). However, the origin of the oxidized nature of magmas in arc settings remains controversial (e.g., Lee et al., 2010; Tang et al., 2018; Evans et al., 2012; Kelley and Cottrel, 2009), puzzling the mechanisms of metal extraction from the mantle source.

The evidence summarized above indicates that the processes and conditions by which magmas extract ore metals from a fertile reservoir in the SCLM remain unclear.

1.3. CASES OF STUDY

This thesis focuses on two different and unique cases of study in Argentina and Chile. The first case study corresponds to the Deseado Massif gold province in southern Patagonia, where the systematics, budget, and mobility of the ore metals in the SCLM are explored from a peridotite xenolith perspective. The Deseado Massif is a world-class auriferous province located in the southernmost Argentinian Patagonia, South America (Shalamuk et al., 1997). It comprises several Au-Ag epithermal deposits of Jurassic age genetically linked to the late magmatic stages of the Chon Aike large igneous province (Echavarría et al., 2005). The unique setting of this auriferous province is that extensive Neogene magmatism brought to the surface deep-seated mantle xenoliths from beneath the crust hosting the Au mineralization (e.g., Rivalenti et al., 2004). Thus, it provides a unique opportunity to explore the inners working of the Earth's upper mantle during the formation of a metallogenic province. Further details on the geological background of the Deseado Massif and its mantle xenoliths is provided in Chapters 2 and 3.

The second case study focuses on primitive basalts from the transitional southern volcanic zone in the Andes of southern Chile. The Los Hornitos monogenetic cones comprise two small vents located ~9 km south of the Cerro Azul/Quizapu stratovolcano, in the Descabezado Grande Volcanic Field (DGVF), within the Chilean Transitional southern Volcanic Zone (TSVZ). The volcanic products include basalts and tephra that are among of the most primitive compositions reported in the Southern Volcanic Zone (SVZ) (Salas et al., 2017), thus representing a direct window into the deep lithospheric processes in the southern Andean arc. Further details on the geological background of the TSVZ and the Los Hornitos primitive basalts is provided in Chapter 5.

1.4. OBJECTIVE OF THE THESIS

The main goal of this thesis is to assess the impact of the subcontinental lithospheric mantle in processes metallogenesis. The aim is to identify key petrological and geochemical characteristics of the SCLM that may have an influence on the formation and localization of giant ore deposits and metallogenic provinces in the overlying continental crust.

1.4.1. Specific goals

I. Define the petrogenesis of the various mineral, glass and melt inclusion assemblages of the studied peridotite xenoliths and primitive basalts, with a special focus on metasomatic styles that affected the studied blocks of the SCLM.
II. Identify the distribution and systematics of the BMS controlling the budget of ore metals in the SCLM.
III. Constrain the links between the different metasomatic styles and the formation of the different BMS generations, and its impact on whole-rock geochemistry.
IV. Explore the possible existence of an enriched SCLM source beneath the Deseado Massif auriferous province, and its potential connection to the formation of Au-Ag epithermal deposits in the crust.
V. Understand the redox processes during melt-SCLM interaction and their effect on sulfur and metal solubility and transport to the overlying crust.
VI. Assess the potential of olivine-hosted melt inclusions as tracers of the oxidation state of primitive melts in the southern Andes and understand their early redox evolution and potential impact on petrological and metallogenetic studies.

1.5. HYPOTHESES

I. Mantle metasomatism results in ore metal enrichment of the SCLM beneath restricted blocks of crust, acting as a source of metals for the genesis of world-class deposits and metallogenic provinces.
II. Redox gradients between ascending magmas and the SCLM trigger redox processes that enhance their potential to efficiently scavenge magmas from enriched mantle domains, boosting their metallogenic fertility.

1.6. THESIS STRUCTURE

The thesis is focused on the study of peridotite xenoliths and primitive basalts to understand the connection between the mantle metasomatism, the generation of fertile reservoirs in the SCLM, the oxidation state of arc magmas, and the formation of ore deposits.

Chapter II offers the first direct connection between the existence of a fertile reservoir in the SCLM and the formation of a gold-rich province in the crust. This chapter was published in the journal *Nature Communications*.

Chapter III uses a wide range of analytical techniques to understand the effect of the different styles of metasomatism on the distribution of HSE in the upper mantle. This chapter was published in the journal *Lithos*.

Chapter IV uses synchrotron-based techniques to explore the valence state of sulfur in upper mantle apatite. These data are used to understand the mechanisms leading to oxidation and fertility of ore-forming magmas. This chapter has been submitted for publication and it is currently *under review.*

Chapter V explores the origin of the oxidized nature of arc magmas from the perspective of olivine-hosted melt inclusions in primitive basalts from the southern Andes. This chapter will be submitted for review in April-May 2019.

Chapter VI summarizes the main conclusions of this thesis.

1.7. PUBLICATIONS AND CONFERENCES

1.7.1. Publications

1. 2017 **Tassara, S.**, González-Jiménez J.M., Reich, M., Schilling, M.E., Morata, M., Begg, G., Saunders, E., Griffin, W.L., O´Reilly, S.Y., Grégoire, M., Barra, F. and Corgne, A. Plume-subduction interaction forms large auriferous provinces. Nature Communications 8, 843. doi: https://doi.org/10.1038/s41467-017-00821-z.

2. 2018 **Tassara, S.**, González-Jiménez J.M., Reich, M., Saunders, E., Luguet, A., Morata, D., Grégoire, M., Van Acken, D., Schilling, M.E., Barra, F., Nowell, G., Corgne, A. Highly siderophile elements mobility in the subcontinental lithospheric mantle beneath southern Patagonia. Lithos 314-315, 579- 596. doi: https://doi.org/10.1016/j.lithos.2018.06.022.

3. 2019 **Tassara, S.**, Reich, M., Konecke, B.A., González-Jiménez, J.M., Simon, A.C., Morata, D., Barra, F., Fiege, A., M.E. Schilling, A. Corgne. The role of the lithospheric mantle in the oxidation state and ore fertility of arc magmas. *Under review.*

4. 2019 **Tassara, S**., Reich, M., Cannatelli, C., Konecke, B.A., Kausel, D., Morata, D., Barra, F., Simon, A.C., Fiege, A., Morgado, E**.** A complex redox record in primitive melts from the southern Andes. *To be submitted.*

1.7.2. Conference abstracts as leading author

1. 2016 **Tassara, S.**, Garrido, L., Romero, R., González-Jiménez, J.M., Reich, M., Barra, F., Morata, D., Schilling, M. and Plissart, G. Noble Metals in Sulfides and Arsenides from Ultramafic rocks within the Andean Subduction Factory. *2nd European Mineralogical Conference (Rimini, Italy), n. 42, page 710.* ***Obtained the "Best Poster Award" of the conference.***

2. 2016 **Tassara, S.,** González-Jiménez J.M., Reich M., Barra, F. and Morata, D. Unraveling the role of the Subcontinental Lithospheric Mantle in the genesis of metal-rich melts beneath the Andes. Poster presented at the *Gordon Research Conference: Geochemistry of Mineral Deposits (Les Diablerets, Switzerland June 19-24)*

3. 2017 **Tassara, S**., González-Jiménez, J.M., Reich, M., Morata, D., Schilling, M., Barra, F. Gold particles in upper mantle xenoliths. Poster presented at the *Goldschmidt Conference (Paris, France, August 13-18).*

4. 2017 **Tassara, S**., González-Jiménez, J.M., Reich, M., Morata, D., Barra, F., Grégoire, M., Saunders, E., Cannatelli, C. Refertilization of the Subcontinental Lithospheric Mantle and its link to the formation of Metallogenic Provinces. Oral presentation given at the *American Geophysical Union Fall Meeting (New Orleans, USA, December 11-15).*

5. 2018 **Tassara, S.**, Reich, M., González-Jiménez, J.M., Morata, D., Schilling, M., Barra, F., Corgne, A. Lithospheric mantle control on the formation of auriferous provinces: Insights from southern Patagonian peridotite xenoliths. Oral presentation given at the *Chilean Geological Conference (Concepción, Chile, November 18-23).*

6. 2018 **Tassara, S**., Reich, M., Konecke, B., González-Jiménez, J.M., Fiege, A., Simon, A., Morata, D., Barra, F. Sulfur XANES investigation of upper mantle metasomatic apatite. Poster presented *Goldschmidt Conference (Boston, MA, USA, August 12-17).*

7. 2018 **Tassara, S**., Reich, M., Morata, D., Barra, F., González-Jiménez, J.M. The role of the subcontinental lithospheric mantle in metallogenesis. Invited talk presented at the *Gordon Research Seminar: Geochemistry of Mineral Deposits (Waterville Valley, NH, USA, August 5-10).*

1.7.3. Conference abstracts as co-author

1. 2016 Colás, V., **Tassara, S**., Padrón-Navarta, J.A., J.M., González-Jiménez, J.M., Griffin, W.L., Fanlo, I., O´Reilly, S.Y., Gervilla, F., Proenza, J.A., Pearson, N., Camprubí, A., and Escayola, M. The effect of Composition on minor and trace elements in spinels: Insights from exsolved chromite. *2nd European Mineralogical Conference (Rimini, Italy), n. 42, pages 394-395.*

2. 2017 González-Jiménez, J.M., Roque, J., **Tassara, S.**, Baurier, S., Aiglsperger, T., Proenza, J.A. and Gervilla, F. Nanopartículas de metales nobles en sistemas magmáticos ultramáficos. *Meeting of the Spanish Mineralogical Association (Oviedo, Spain)*

3. 2018 Corgne, A., Schilling, M.E., Grégoire, M., Langlade, J., **Tassara, S**., González-Jiménez, J.M. Experimental constraints on metasomatism of mantle wedge peridotites by carbonatitic melts. *Chilean Geological Conference (Concepción, Chile, November 18-23).*

1.8. BIBLIOGRAPHY

Alard, O., Griffin, W.L., Lorand, J.-P., Jackson, S.E. and O'Reilly, S.Y. (2000) Non-chondritic distribution of the highly siderophile elements in mantle sulfides. Nature **407**, 891-894.

Arndt, N. and Christensen, U. (1992) Role of lithospheric mantle in continental volcanism: Thermal and geochemical constraints. Journal of Geophysical Research **97**, 199-215.

Arndt, N. (2013) The lithospheric mantle plays no active role in the formation of orthomagmatic ore deposits. Economic Geology **108**, 1953-1970.

Barra, F., Reich, M., Selby, D., Rojas, P., Simon, A., Salazar, E. and Palma, G. (2017) Unraveling the origin of the Andean IOCG clan: A Re-Os isotope approach. Ore Geology Reviews **81**, 62-78.

Becker, H. and Dale, C.W. (2016) Re-Pt-Os Isotopic and Highly Siderophile Element behavior in oceanic and continental mantle tectonites. Reviews in Mineralogy and Geochemistry **81**, 369-440.

Begg, G. C., Hronsky, J.A.M., Arndt, N., Griffin, W.L., O'Reilly, S.Y. and Hayward, N. (2010) Lithospheric, cratonic and geodynamic setting of Ni-Cu-PGE sulfide deposits. Economic Geology **105**, 1057–1070.

Bockrath, C., Ballhaus, C. and Holzheid, A. (2004) Fractionation of the platinum-group elements during mantle melting. Science **305**, 1951–1953.

Chiaradia, M. (2014) Copper enrichment in arc magmas controlled by overriding plate thickness. Nature Geoscience **7**, 43–46.

Core, D.P., Kesler, S.E. and Essene, E.J. (2006) Unusually Cu-rich magmas associated with giant porphyry copper deposits: evidence from Bingham, Utah. Geology **34**, 41-44.

Dawson, J.B. (1984) Contrasting types of upper mantle metasomatism. In: Kornprobst J (ed) Kimberlites II: the mantle and crust-mantle relationships. Elsevier, Amsterdam.

Evans, K.A. (2012) The redox budget of subduction zones. Earth-Science Reviews **113**, 11-32.

Frimmel, H.E. and Minter, W.E.L. (2002) Recent developments concerning the geological history and genesis of the Witwatersrand gold deposits, South Africa. Society of Economic Geologists Special Publication **9**, 17-45.

Grauch, V.J.S., Rodriguez, B.D. and Wooden, J.L. (2003) Geophysical and isotopic constraints on crustal structure related to mineral trends in northcentral Nevada and implications for tectonic history. Economic Geology **98**, 269-286.

Griffin, W. L. and O'Reilly, S. Y. (2007) Cratonic lithospheric mantle: Is anything subducted? Episodes **30**, 43–53.

Griffin, W. L., O'Reilly, S. Y. and Ryan, C. G. (1999). The composition and origin of subcontinental lithospheric mantle. In: Fei, Y., Bertka, C. M. and Mysen, B. O. (eds) Mantle petrology: field observations and high-pressure experimentation: a tribute to Francis F. (Joe) Boyd. The Geochemical Society, 13-45.

Griffin, W. L., O'Reilly, S. Y., Afonso, J. C. and Begg, G. C. (2009) The composition and evolution of lithospheric mantle: A re-evaluation and its tectonic implications. J. Petrology **50**, 1185–1204.

Griffin, W.L., Begg, G.C. and O´Reilly, S.Y. (2013) Continental-root control on the genesis of magmatic ore deposits: Nature Geoscience **6**, 905-910.

Griffin, W.L., Graham, S., O'Reilly, S.Y. and Pearson, N.J. (2004) Lithospheric evolution beneath the Kaapvaal Craton: Re-Os systematics of sulfides in mantle-derived peridotites. Chemical Geology **208**, 89-118.

Harris, A.C., Dunlap, W.J., Reiners, P.W., Allen, C.M., Cooke, D.R., White, N.C., Campbell, I.H. and Golding, S.D. (2008) Multimillion year thermal history of a porphyry copper deposit: Application of U-Pb, 40Ar/39Ar and (U-Th)/He chronometers, Bajo de la Alumbrera copper-gold deposit, Argentina. Mineralium Deposita **43**, 295–314.

Harvey, J., Warren, J. and Shirey, S.B. (2016) Mantle Sulfides and their role in Re-Os and Pb isotope geochronology. Reviews in Mineralogy and Geochemistry **81**, 579-651.

Harte, B. (1983) Mantle peridotites and processes: the kimberlite sample. In: Hawkesworth CJ, Norry MJ (eds) Continental basalts and their xenoliths. Shiva, Nantwich.

Heinson, G., Didana, Y., Soeffky, P., Thiel, S. and Wise, T. (2018) The crustal geophysical signature of a world-class magmatic mineral system. Scientific Reports **8**, 10608.

Helmstaedt, H. H. and Gurney, J. J. (1995) Geotectonic controls of primary diamond deposits: implications for area selection. J. Geochem. Explor. **53**, 125–144.

Henry, C.D., Castor, S.B. and Elson, H.B. (1996) Geology and 40Ar/39Ar geochronology of volcanism and mineralization at Round Mountain, Nevada: Geology and Ore Deposits of the American Cordillera, Geological Society of Nevada Symposium, Reno/Sparks, 1995, Proceedings **1**, 283–307.

Herzberg, C. and Rudnick, R. (2012) Formation of cratonic lithosphere: an integrated thermal and petrological model. Lithos **149**, 4–15.

Hildenbrand, T.G., Berger, B., Jachens, R.C. and Ludington, S. (2000) Regional crustal structures and their relationship to the distribution of ore deposits in the western United States, based on magnetic and gravity data. Economic Geology **95**, 1583-1603.

Hou, Z.Q., Yang, Z.M., Lu, Y.J., Kemp, A., Zheng, Y.C., Li, Q., Tang, J., Yang, Z. and Duan, L. (2015) A genetic linkage between subduction- and collision-related porphyry Cu deposits in continental collision zones: Geology **43**, 247–250

Hronsky, J.M.A., Groves, D.I., Loucks, R.R. and Begg, G.C. (2012) A unified model for Au mineralization in accretionary orogens and implications for regional-scale exploration targeting methods. Mineralium Deposita. **47**, 339-358.

Jensen, E.P. and Barton, M.D. (2000) Gold deposits related to alkaline magmatism. Reviews in Economic Geology **13**, 279–314.

Jugo, P.J., Wilke, M. and Botcharnikov, R.E. (2010) Sulphur K-edge XANES analysis of natural and synthetic basaltic glasses: implications for S speciation and S content as a function of oxygen fugacity. Geochimica et Cosmochimica Acta **74**, 5926-5938.

Kelley, K. and Cottrell, E. (2009) Water and the oxidation state of subduction zone magmas. Science **325**, 605-607.

Kirk, J., Ruiz, J., Chesley, J., Walshe, J. and England, G. (2002) A major Archean, gold and crust forming event in the Kaapvaal craton, South Africa. Science **297**, 1856-1858.

Lee, C-T.A., Luffi, P., Le Roux, V., Dasgupta, R., Albarède, F. and Leeman, W.P. (2010) The redox state of arc mantle using Zn/Fe systematics. Nature **468**, 681-685.

Lloyd, F.E. and Bailey, D.K. (1973) Light element metasomatism of the continental mantle: the evidence and the consequences. Physics and Chemistry of the Earth **9**, 389–416.

Lorand, J.-P., Alard, O. and Luguet, A. (2010) Platinum-group element micronuggets and refertilization process in the Lherz peridotite. Earth and Planetary Science Letters **289**, 298–310.

Lorand, J.-P. and Grégoire, M. (2006) Petrogenesis of base metal sulfide assemblages of some peridotites from the Kaapvaal craton (South Africa). Contributions to Mineralogy and Petrology **151**, 521-538.

Lorand, J.-P., Luguet, A. and Alard, O. (2013) Platinum-group element systematics and petrogenetic processing of the continental upper mantle: A review. Lithos **164-167**, 2-21.

Lorand, J-P. and Luguet, A. (2016) Chalcophile and Siderophile Elements in Mantle Rocks: Trace Elements Controlled By Trace Minerals. Reviews in Mineralogy and Geochemistry **81**, 441-488.

Loucks, R.R. and Ballard, J.R. (2003) Report 2C: Petrochemical characteristics, petrogenesis and tectonic habits of gold-ore-forming arc magmas. Unpublished report for industry-sponsored research project: Predictive Guides to Copper and Gold Mineralization at Circum-Pacific Convergent Plate Margins. 69p

Luck, J. and Allegre, C. (1980) Osmium isotopes as petrogenetic and geologic tracers: Earth and Planetary Science Letters **48**, 148–154.

Luguet, A., Lorand, J.-P. and Seyler, M. (2003) Sulfide petrology and highly siderophile element geochemistry of abyssal peridotites: a coupled study in samples from the Kane Fracture Zone (45°W 23°20 N, MARK Area, Atlantic Ocean). Geochimica et Cosmochimica Acta **67**, 1553–1570.

Luguet, A., Shirey, S.B., Lorand, J.-P., Horan, M.F. and Carlson, R.W. (2007) Residual platinum-group minerals from highly depleted harzburgites of the Lherz massif (France) and their role in HSE fractionation of the mantle. Geochimica et Cosmochimica Acta **71**, 3082-3097.

Maier, W. D. and Groves, D. I. (2011) Temporal and spatial controls on the formation of magmatic PGE and Ni-Cu deposits. Mineralium Deposita **46**, 841–857 (2011).

Mavrogenes, J.A. and O'Neill, C. (1999) The relative effects of pressure, temperature and oxygen fugacity on the solubility of sulfide in mafic magmas. Geochimica et Cosmochimica Acta **63**, 1173-1180.

McInnes, B.I.A., McBridge, J.S., Evans, N.J., Lambert, D.D. and Andre, A.S. (1999) Osmium isotope constraints on ore metal recycling in subduction zones. Science **286**, 512-516.

Morgan, J.W., Horan, M.F., Walker, R.J., and Grossman, J.N. (1995) Rhenium-osmium concentration and isotope systematics in group IIAB iron meteorites. Geochimica et Cosmochimica Acta **59**, 2331–2334.

Muller, D. (2002) Gold-copper mineralization in alkaline rocks. Mineralium Deposita **37**, 1–3

Muller, D., and Groves, D.I. (1995) Potassic igneous rocks and associated gold-copper mineralization. Lecture notes in Earth Sciences **56**. Springer, Berlin

Mungall, J.E. (2002) Roasting the mantle: Slab melting and the genesis of major Au and Au-rich Cu deposits. Geology **30**, 915–918.

Navon, O., and Stolper, E. (1987) Geochemical consequences of melt percolation: the upper mantle as a chromatographic column. J. Geol. **95**, 285–307.

O'Reilly, S.Y. and Griffin, W.L. (2012) Mantle metasomatism. In: Harlov, D. and Austrheim H. (eds) Metasomatism and the chemical transformation of rock. Spinger.

Phillips, N.G. and Law, J.D.M. (1995) Witwatersrand gold fields: geology, genesis, and exploration. Reviews in Economic Geology **13**, 439-500.

Richards, J. P. (2009) Post-subduction porphyry Cu-Au and epithermal Au deposits: Products of remelting of subduction-modified lithosphere. Geology **37**, 247–250.

Richards, J.P. (2015) The oxidation state, and sulphur and Cu contents of arc magmas: implications for metallogeny. Lithos **233**, 27-45.

Richards, J.P. (2011) High Sr/Y arc magmas and porphyry Cu ± Mo ± Au deposits: Just add water. Economic Geology **106**, 1075–1081.

Richardson, S. H. and Shirey, S. B. (2008) Continental mantle signature of Bushveld magmas and coeval diamonds. Nature **453**, 910–913.

Rielli, A., Romkins, A., Nebel, O., Brugger, J., Etschmann, B., Zhong, R., Yaxley, G.M. and Paterson, D. (2017) Evidence of sub-arc mantle oxidation by sulphur and carbon. Geochemical perspectives **3**, 124-132.

Rock, N.M.S., Duller, P., Haszeldine, R.S. and Groves, D.I. (1987) Lamprophyres as potential gold exploration targets: Some preliminary observations and speculations. In SE Ho, DI Groves

(eds) Recent Advances in Understanding Precambrian Gold Deposits, Geology Dept. and University Extension, Univ WA Publ **11**, 271–286.

Saunders, J.E., Pearson, N.J., O'Reilly, S.Y. and Griffin, W.L. (2018) Gold in the mantle: A global assessment of abundance and redistribution processes. Lithos **322**, 376-391.

Saunders, J.E., Pearson, N.J., O'Reilly, S.Y. and Griffin, W.L. (2015) Sulfide metasomatism and the mobility of gold in the lithospheric mantle. Chemical Geology **410**, 149-161.

Shen, J.J., Papanastassiou, D. and Wasserberg, G.J. (1996) Precise Re-Os determinations and systematics of iron meteorites. Geochimica et Cosmochimica Acta **60**, 2887–2900.

Salas, P.A., Rabbia, O.M., Hernández, L.B. and Ruprecht, P. (2017) Mafic monogenetic vents at the Descabezado Grande volcanic field ((35.5°S–70.8°W): the northernmost evidence of regional primitive volcanism in the Southern Volcanic Zone of Chile. International Journal of Earth Sciences **106**, 1107-1121.

Sillitoe, R.H. (1997) Characteristics and controls of the largest porphyry copper-gold and epithermal gold deposits in the circum-Pacific region. Australian Journal of Earth Sciences **4**, 373–388.

Sillitoe, R.H. (2008) Major gold deposits and belts of the North and South American Cordillera: distribution, tectonomagmatic settings, and metallogenic considerations. Economic Geology **103**, 663-687.

Singer, D.A. (1995) World class base and precious metal deposits—a quantitative analysis. Economic Geology **90**, 88-104.

Tang, M., Erdman, M., Eldridge, G. and Lee, C-T.A. (2018) The redox "filter" beneath magmatic orogens and the formation of continental crust. Science Advances **4**, 5, eaar4444.

Webber, A.P., Roberts, S., Taylor, R.N. and Pitcairn, I.K. (2012) Golden plumes: substantial Au enrichment of oceanic crust during ridge-plume interaction. Geology **41**, 87-90.

Wyman, D. A. and Kerrich, R. (2002) Formation of Archaean continental lithospheric roots: The role of mantle plumes. Geology **30**, 543–546.

Zhang, M., O'Reilly, S. Y., Wang, K-L., Hronsky, J. and Griffin, W. L. (2008) Flood basalts and metallogeny: the lithospheric mantle connection. Earth Science Reviews **86**, 145–174.

Zheng, J., Sun, M., Zhou, M.-F. and Robinson, P. (2005) Trace elemental and PGE geochemical constraints of Mesozoic and Cenozoic peridotitic xenoliths on lithospheric evolution of the North China Craton. Geochimica et Cosmochimica Acta **69**, 3401–3408.

Zheng, Y-C., Liu, S-A., Wi, C-D., Griffin, W.L., Li, Z-Q., Xu, B., Yang, Z-M., H., Z-Q. and O'Reilly, S.Y. (2018). Cu isotopes reveal initial Cu enrichment in sources of giant porphyry deposits in a collisional setting. Geology **47**, 135-138.

CHAPTER 2. PLUME-SUBDUCTION INTERACTION FORMS LARGE AURIFEROUS PROVINCES

Santiago Tassara[1*], José M. González-Jiménez[1,2], Martin Reich[1], Manuel E. Schilling[3], Diego Morata[1], Graham Begg[4], Edward Saunders[5,6], William L. Griffin[6], Suzanne Y. O´Reilly[6], Michel Grégoire[7], Fernando Barra[1], Alexandre Corgne[3]

[1]*Department of Geology and Andean Geothermal Center of Excellence (CEGA), FCFM, Universidad de Chile, Plaza Ercilla 803, Santiago, Chile.*
[2]*Departamento de Mineralogía y Petrología, Facultad de Ciencias, Universidad de Granada, Fuentenueva s/n 180002, Granada, Spain.*
[3]*Instituto de Ciencias de la Tierra, Facultad de Ciencias, Universidad Austral de Chile, Valdivia, 5090000, Región de Los Ríos, Chile.*
[4]*Minerals Targeting International PL, 17 Prowse St, West Perth, Western Australia 6005, Australia.*
[5]*Division of Earth Sciences, School of Environmental and Rural Science, University of New England, Armidale, NSW 2351, Australia.*
[6]*ARC Centre of Excellence for Core to Crust Fluid Systems/GEMOC, Macquarie University, NSW 2109, Australia.*
[7]*GET, CNRS-CNES-IRD-UPS, Toulouse University, 14 av. Edouard Belin, 31200 Toulouse, France.*

(*) Corresponding author: tassara.carlos.sant@ug.uchile.cl
Keywords: Au, mantle plume, subduction, metallogenic province, xenolith, Deseado Massif.

2.1. ABSTRACT

Gold enrichment at the crustal or mantle source has been proposed as a key ingredient in the production of giant gold deposits and districts. However, the lithospheric scale processes controlling gold endowment in a given metallogenic province remain unclear. Here we provide the first direct evidence of native gold in the mantle beneath the Deseado Massif in Patagonia that links an enriched mantle source to the occurrence of a large auriferous province in the overlying crust. A precursor stage of mantle refertilisation by plume-derived melts generated a gold-rich mantle source during the Early Jurassic. The interplay of this enriched mantle domain and subduction-related fluids released during the Middle-Late Jurassic resulted in optimal conditions to produce the ore-forming magmas that generated the gold deposits. Our study highlights that refertilisation of the subcontinental lithospheric mantle is a key factor in forming large metallogenic provinces in the Earth's crust, thus providing an alternative view to current crust-related enrichment models.

2.2. INTRODUCTION

The traditional notion of Au endowment in a given metallogenic province is that Au accumulates by highly efficient magmatic-hydrothermal enrichment processes operating in a chemically "average" crust. However, more recent views point to anomalously enriched source regions and/or melts that are critical for the formation of Au provinces at a lithospheric scale[1-4]. Within this perspective, Au-rich melts/fluids might originate from a mid or lower crust reservoir

and later migrate through favorable structural zones to shallower crustal levels where the Au deposits form[5]. Alternatively, the subcontinental lithospheric mantle (SCLM) may also play a role as a source of metal-rich magmas[2,3,6,7]. This model involves deep-seated Au-rich magmas that may infiltrate the edges of buoyant and rigid domains in the SCLM producing transient Au storage zones. Upon melting, the ascending magma scavenges the Au as it migrates towards the uppermost overlying crust[6,8]. Discontinuities between buoyant and rigid domains in the SCLM provide the channelways for the uprising of Au-rich fluids or melts from the convecting underlying mantle, and when connected to the overlying crust by trans-lithospheric faults a large Au deposit or well-endowed auriferous province can be formed[7]. Thus, the generation of Au deposits in the crust may result from the conjunction in time and space of three essential factors: an upper mantle or lower crustal source region particularly enriched in Au, a transient remobilization event and favorable lithospheric-scale plumbing structures. The giant Ladolam Au deposit in Papua New Guinea gives a good single-deposit case example of this mechanism since deep translithospheric faults connect the crustal Au deposit directly with the mantle source, and similar Os isotopic compositions are exhibited by Au ores and metal-enriched peridotite of the underlying mantle[1]. Despite these evidences, the genetic relation between a pre-enriched mantle source and the occurrence of gold provinces in the upper crust remains controversial since limited evidence is available at a broader regional scale.

In this paper we provide the first empirical evidence connecting the genesis of a large Au province (Deseado Massif, Argentina ~15 Moz Au, ~400 Moz Ag[2,9,10] see additional references in supplementary information) to the occurrence of "visible" Au in the underlying SCLM. Our observations of ultramafic xenoliths sampled from monogenetic volcanoes from the Deseado Massif, southern Patagonia, provide unprecedented evidence that an enriched SCLM might be the primary source for the generation of this auriferous province.

2.3. GEOLOGICAL SETTING AND XENOLITH PETROLOGY

The Deseado Massif is an underexplored auriferous province of ~ 60,000 km^2 located in the southernmost part of Argentina in South America[9]. It hosts several Au-Ag epithermal deposits including low sulphidation, intermediate sulphidation and polymetallic epithermal deposits associated with calc-alkaline rhyolites, basaltic andesites and basalts from the late magmatic stages of the Chon Aike Silicic Large Igneous Province (CA-SLIP)[11,12] (Fig. 1). The CA-SLIP is represented by the extensive volcanism that was active from 187 to 144 Ma contemporaneously with the initial break-up of Gondwana[13], and includes two main stages of petrogenesis. The Early Jurassic magmatic pulses of the CA-SLIP are ascribed to crustal melting caused by spreading of the Karoo plume head (~180 Ma), whereas the geochemical signature of Middle to Late Jurassic events show the influence of an active subduction margin in a back-arc position (~155 Ma). The latter is coincident to the migration of magmatism away from the Karoo mantle plume towards the proto-Pacific margin of Gondwana during rifting and break-up[14,15]. An extensive Neogene back-arc plateau magmatism composed of alkaline basalts (~3.5 Ma) has brought to the surface deep-seated mantle xenoliths from beneath the crust that host the Au mineralization[16-22]. Dominantly spinel lherzolites of the Cr-diopside suite[23], these xenoliths record Meso to Paleoproterozoic partial melting[20-22] and subsequent multistage modification of the mantle, including carbonatitic, silica-undersaturated alkaline, and subduction-related metasomatism[17-19].

The Au-bearing ultramafic xenolith studied here was collected from the Cerro Redondo cinder cone, located at the south-western edge of the Deseado Massif (49°7'15.41"S;

70°8'28.56"W), and was chosen as a case study since it samples the mantle directly beneath the Au-Ag deposits of "Manantial Espejo", and "La Rosita" and "La Sarita" Au-Ag prospects (Fig. 1). The targeted xenolith is a protogranular anhydrous mantle lherzolite that equilibrated in the spinel facies (up to 1.76 GPa, ca. ~ 53 km depth) at temperatures of 1,020-1,150°C (Supplementary Table S1). The lherzolite xenolith records at least three stages of chemical depletion and enrichment: *Stage I* comprises the formation of a chemically depleted residue after the removal of ~5 to 10% partial melt, which is recorded in primary olivine with very low Al_2O_3 and CaO and Mg# = 90.1-91.1 (Supplementary Table S2) and slightly depleted LREE/HREE ratios in clinopyroxene. *Stage II* involved melt infiltration and precipitation of metasomatic pyroxene with high Al_2O_3 and TiO_2 contents and LREE enrichment from silicate alkaline to sub-alkaline melts (Supplementary Table S3 and Supplementary Figure S1). A third event (*Stage III*) is evidenced by the infiltration of metasomatic melts just before the xenolith was entrained into the Neogene basalt, which resulted in the formation of interstitial silicate glass containing native Au particles. This interstitial glass is unrelated to the host basalt and is partially altered to secondary clays that overprint the entire sample. The unaltered mineral assemblage in this glass consists of incompletely reacted olivine and pyroxenes together with armalcolite [$(Mg,Fe^{2+})Ti_2O_5$], ilmenite, feldspar and apatite (Supplementary Table S2). Composite aggregates (10-120 μm) of chalcopyrite, pentlandite, and millerite are common within the glass, and to a lesser extent within the primary silicates (Fig. 2A, B) (Supplementary Table S4).

2.4. GOLD ENTRAINED BY INFILTRATING MELTS

Gold particles (< 2 μm) were found enclosed within primary olivine and pyroxene (Fig. 2D, E) and embedded in the glass matrix (Fig. 2F) or sulfides (Fig. 2B, C, G, H) in the interstitial glass. Energy dispersive X-ray spectra (EDS) obtained using a high-resolution, field-emission scanning electron microscope (FE-SEM) and filtered for host matrix composition (Supplementary Figure S3-S8) indicate that all these grains are almost pure Au. Gold grains found in primary silicates and in the groundmass of the interstitial glass are small (< 750 nm across), irregular and commonly aligned forming planar arrays within the silicate host (Fig. 2D). In contrast, Au particles located inside larger sulfide grains, mainly chalcopyrite, embedded in the interstitial glass are relatively larger (~ 1.5 μm) and display well-developed polygonal faces of the cubic crystallographic system. Detailed inspection of the chalcopyrite hosts reveals abundant native Au nanoparticles (Fig. 2G, H), which are consistent with the high Au (up to 6 ppm) obtained by LA-ICP-MS analysis of these sulfides. It is relevant to note that these sulfides contain significant amounts of Ag (up to 163 ppm, Supplementary Table S5). The Au/Ag ratios of the mantle sulfides are similar to the Au/Ag ratios of the bulk ores, and may exert and important control on the economic metal ratios of epithermal Au-Ag deposits of the Deseado Massif (Au/Ag~0.01-1, see Supplementary Figure S2).

The occurrence of native Au particles forming planar arrays within olivine or pyroxene suggests a physical entrapment mechanism, most likely facilitated by structural discontinuities (*e.g.*, cleavage planes or zones for local accumulation of dislocations) during magmatic silicate growth. These native Au particles are free of any secondary hydrothermal markers such as Pb, Ag, Te, Bi, Cu, Sb[24,25] ruling out the possibility that these Au particles were included within olivine during secondary subsolidus growth as observed in peridotites of the Lherz massif (France)[26]. Furthermore, the estimated temperatures for the equilibration of primary silicates in the studied xenolith exceeded >1,000ºC, which precludes an origin related to secondary silicate growth.

The fact that Au is included in pyroxene and olivine that crystallized at different stages of the depletion-refertilisation history of the SCLM and at a different time-scale also excludes the possibility that Au found in these silicates crystallized contemporaneously from the same parental melt. Instead, the fact that Au particles in primary silicates are only found in those grains that are in close proximity (<500 μm) to the interstitial glass also containing Au particles more likely indicates that Au was introduced later by an infiltrating melt now quenched as a glassy vein. Deposition of Au by the infiltrating melt could have occurred through discontinuities or micro-sized crack-seals, which would be later sealed during silicate annealing. Crack propagation is a well-known mechanism for the almost instantaneous movement of fluids in the mantle[27], and it can occur due to fluid overpressure or where crystallization in pore space in subsolidus matrices is more rapid than the viscous relaxation of the rock.

2.5. THE ROLE OF ALKALI MELTS ON GOLD MOBILITY IN THE SCLM

Experimental studies have reported the formation of metallic Au-rich alloys at magmatic temperatures (>1,200 ºC) from S-undersaturated and Fe-containing silicate melts, under either reducing conditions buffered by iron-wustite (IW)[28] or at fO_2 near the Fayalite-Magnetite-Quartz (FMQ) buffer[29]. The results of these experiments demonstrate that native Au can crystallize over a wide range of fO_2 conditions depending on the sulphur content in the basaltic melt. In fact, native Au micronuggets have been documented in the glassy groundmass of mantle-derived rocks such as lamproite dykes segregated at fO_2 near the IW buffer[30] and basanite lavas from Hawaii formed at $\Delta FMQ \approx +0.4$[31]. The former author linked the direct crystallization of native Au from the lamproite magma to strongly reducing conditions whereas the latter argued for the solidification of droplets of immiscible Au liquids. In the latter, an increase in alkali contents upon fractionation of the melt increased the solubility of sulphur, which promoted the resorption of sulfides entrained in the melt and the segregation of immiscible Au liquid droplets.

The Au-bearing interstitial glass from the Cerro Redondo mantle xenolith contains a mineral assemblage that includes armalcolite, ilmenite, feldspar, apatite, and Au-bearing sulfides, reflecting the crystallization of alkalic melts unusually enriched in incompatible elements[32,33] and slightly more reduced ($\Delta FMQ \approx -2.35$ at 1,150-1,200°C and 1.3 GPa[33]) than estimated for the primary silicates ($\Delta FMQ \approx +0.12$ - +1.06; Supplementary Table S6). These fO_2 values reflect the infiltration of the alkalic melt into a slightly more oxidized mantle peridotite. The idea that Au could be transported by sulfide melts entrained in the silicate melt[34] is supported by the fact that clusters of native Au nanoparticles and euhedral Au inclusions are found hosted in Cu-rich sulfides (Fig. 2). Upon ascent, the infiltrating melt should undergo decompression, as well as fractionation and oxidation by reaction with the country rocks. The combination of these processes may have shifted the balance between the stability of sulfide towards the more soluble sulfate field[35-37], promoting sulfide resorption as evidenced by the presence of oxide rims in some of the studied grains (Supplementary Figure S8). This would result in the liberation of Au as discrete grains from the sulfides with relatively high contents of Au (Fig. 2, Supplementary Table S5). Subsequent quenching of the melt into a glass would prevent complete dissolution of Au particles, whereas injection of some of them in primary silicates would prevent further reaction with the infiltrating silicate melt(s). These Au-bearing sulfides would undergo further closed-system subsolidus modification during transport or after solidification of the host silicate melt, promoting decomposition of the original monosulfide solid solution into Ni-rich and Cu-rich sulfides.

2.6. THE GOLD-BEARING GLASSY VEIN AS A FINGERPRINT OF A FORMER "GOLDEN PLUME"

As noted above, a late infiltrating melt, *i.e.*, the glassy vein, introduced Au into the Cerro Redondo mantle peridotite. This Au-bearing glass vein could represent: (1) host basalt that penetrated the xenolith, (2) melt(s) produced by decompression melting of the mantle peridotite during its ascent to the surface, (3) small volume melt(s) that infiltrated the mantle before the entrapment of the xenoliths by the host basalt. If the glass resulted from the injection of the enclosing basalt or from peridotite-host basalt interaction, the interstitial vein and enclosing basalt should have similar composition and mineral assemblages. Instead, the interstitial glass contains a very rare mineral assemblage made up of armalcolite, ilmenite, feldspar and apatite. This type of mineral assemblage has been related to the crystallization of highly alkaline melts, anomalously enriched in incompatible elements[33], with a significant chemical mismatch with the host basalt or eventual products of the reaction between the host basalt and the mantle xenolith. This exotic mineral assemblage could not have been formed by simple decompression melting owing the nature of the primary minerals forming the xenolith. Therefore, the Au-bearing interstitial glass observed in the studied xenolith most likely represents the quenched product of a distinctive melt that predates the eruption of the alkali basalts that brought the xenoliths to the surface ~3.5 Ma ago.

A similar metasomatic assemblage including armalcolite, ilmenite, feldspar, and apatite was documented in peridotite xenoliths that have sampled the mantle underlying the plume-related hotspot of the Kerguelen Islands[32,33]. Moreover, terrestrial occurrences of armalcolite, although not very rare, are mostly restricted to certain picritic lavas from the Karoo igneous province[38], high TiO_2 basalts from the Kilauea volcano, Hawaii[39], and ultrapotassic lavas from southeastern Spain[40]. The first two are related to plume activity and the latter to a highly enriched lithospheric mantle. Furthermore, native Au particles have been reported in the Kilauea and southeastern Spain lavas[30,31]. Therefore, we interpret that the Au-bearing highly alkaline melt might also represent the melting product of a mantle domain previously affected by infiltration of plume-related melts.

Interestingly, mantle plume activity has been suggested to produce large enrichments of Au (and noble metals) in the lithospheric mantle and related crust overlying the Iceland plume[4]. Further evidence for such type of enrichment includes a 30 μm bleb of pure Au enclosed in a fresh olivine phenocryst in a picritic lava from the Emeishan Large Igneous Province in southwestern China. This Au bleb was interpreted as a xenocryst of the deep mantle transported to shallow depths by a rising plume and then captured by picritic melts[41]. Rising plumes originating in the Core-Mantle boundary may potentially add Au into the SCLM during their final ascent[42].

2.7. AN OPTIMAL ALIGNMENT OF EVENTS PRODUCED THE DESEADO MASSIF AURIFEROUS PROVINCE

During the Jurassic, active volcanism took place in Patagonia in a geodynamical environment characterized by: (i) an extensional regime related to the initial stages of break-up of Gondwana, and the emplacement of the Karoo superplume to the east; (ii) episodic subduction from southern America to Antarctica to the west[13,43]. Interestingly, the epithermal Au-Ag deposits of the Deseado Massif auriferous province are related to the calc-alkaline stages of the CA-SLIP. Contrary to models of purely crustal origin, some authors have suggested that the bimodal CA-SLIP was produced from melts derived from a portion of SCLM that was metasomatized and later thermally eroded by the effects of the Karoo mantle plume[44-47].

Considering this scenario, infiltration of melts derived from the Karoo superplume could have added Au to the SCLM beneath the Patagonian auriferous province (Fig. 3A). It is likely that this mantle domain was affected by partial melting and already transferring metals to the overlying continental crust since at least the Proterozoic[21,22]. The fact that the Au-bearing glassy vein in the studied xenolith was formed just before its exhumation in the Neogene, suggests that not all of the enriched SCLM was affected by the processes involved in the generation of the gold deposits of the Deseado Massif province during the late Jurassic. This provides evidence that enriched domains of the SCLM might be relatively durable and store Au (and Ag) over large periods of time until a later melting event triggers the release of the stored metals[7]. As noted above, the Au-bearing metasomatic vein in the Cerro Redondo peridotite xenolith represents the re-melting of these mantle domains, highly enriched in both lithophile and siderophile incompatible elements.

Consequently, the Patagonian CA-SLIP and concomitant auriferous province is the result of mantle plume activity generated during extension in a back-arc setting while subduction of oceanic lithosphere occurred at the western margin of Gondwana[13,14] (Fig. 3B). Subduction was a necessary component to trigger mantle melting, as it lowered the peridotite solidus and contributed oxidized fluids capable of scavenging Au (*i.e.*, ~FMQ>1). This is in good agreement with the fact that the Deseado Massif mineralization is hosted by the calc-alkaline stages of the CA-SLIP.

The Deseado Massif auriferous province was the result of an optimal amalgamation of three main factors: (i) the influence of a mantle plume, which enriched a SCLM domain in incompatible elements (including Au) and provided the necessary heat to produce large volumes of magma over almost ~40 Ma during the Jurassic (Fig. 3A); (ii) the influence of the subduction zone setting at the western (Pacific) margin of Gondwana, which may have oxidized portions of the enriched mantle domain, enhancing the potential of magmas to transport Au as dissolved species (Fig. 3B); and (iii) an extensional geodynamic setting that facilitated these enriched magmas to ascend to crustal levels and form the epithermal Au-Ag deposits (Fig. 3B).

We argue for a genetic model involving processes operating at a lithospheric scale as the first order factor controlling the early stages of the formation of an auriferous province. These processes may be overlapped in space but separated by large periods of time. Thus, understanding global tectonics and evolution of the SCLM through Earth´s history is of fundamental importance to understand the factors that control metal transfer from deep mantle sources to the uppermost crust, and is a critical step in the development of new strategies for successful gold exploration worldwide.

2.8. BIBLIOGRAPHY

1. McInnes, B.I.A., McBridge, J.S., Evans, N.J., Lambert, D.D. and Andre, A.S. Osmium isotope constraints on ore metal recycling in subduction zones. *Science* 286, 512-516 (1999).
2. Sillitoe, R.H. Major gold deposits and belts of the North and South American Cordillera: distribution, tectonomagmatic settings, and metallogenic considerations. *Economic Geology* 103, 663-687 (2008).
3. Begg, G.C. et al. Lithospheric, cratonic and geodynamic setting of Ni-Cu-PGE sulfide deposits. *Economic Geology* 105, 1057-1070 (2010).
4. Webber, A.P., Roberts, S., Taylor, R.N. and Pitcairn, I.K., 2012, Golden plumes: substantial Au enrichment of oceanic crust during ridge-plume interaction. *Geology* 41, 87-90 (2012).
5. Core, D.P., Kesler, S.E. and Essene, E.J. Unusually Cu-rich magmas associated with giant porphyry copper deposits: evidence from Bingham, Utah. *Geology* 34, 41-44 (2006).

6. Hronsky, J.M.A., Groves, D.I., Loucks, R.R. and Begg, G.C. A unified model for Au mineralization in accretionary orogens and implications for regional-scale exploration targeting methods. *Mineralium Deposita.* 47, 339-358 (2012).
7. Griffin, W.L., Begg, G.C. and O´Reilly, S.Y. Continental-root control on the genesis of magmatic ore deposits: *Nature Geoscience* 6, 905-910 (2013).
8. Muntean, J.L., Cline, J.S., Simon, A.C. and Longo, A.A. Magmatic-hydrothermal origin of Nevada´s Carlin-type gold deposits. Nature Geoscience 4, 122-127 (2011).
9. Schalamuk, I.B., Zubia, M., Genini, A. and Fernandez, R.R. Jurassic epithermal Au-Ag deposits of Patagonia, Argentina. *Ore Geology Reviews* 12, 173-176 (1997).
10. Permuy Vidal, C., Guido, D.M., Moreira, P., Ríos, F.J. and Melgarejo, J.C. Características metalogenéticas de Eureka West, principal clavo mineralizado de la Veta Eureka, Distrito Cerro Negro, Macizo del Deseado. *Revista de la Asociación Geológica Argentina* 73, 64-77 (2016).
11. Guido, D. and Schalamuk, I.B. Genesis and exploration potential of epithermal deposits from the Deseado Massif, Argentinean Patagonia. *Mineral Exploration and Sustainable Development* 1, 493-496 (2003).
12. Echavarría, L.E., Schalamuk, I.B. and Etcheverry, R.O. Geologic and tectonic setting of Deseado Massif epithermal deposits, Argentina, based on El Dorado-Monserrat. *Journal of South American Earth Sciences* 19, 415-432 (2005).
13. Féraud, G., Alric, V., Fornari, M., Bertrand, H. and Haller, M. $^{40}Ar/^{39}Ar$ dating of the Jurassic volcanic province of Patagonia: migrating magmatism related to Gondwana break-up and subduction. *Earth and Planetary Science Letters* 172, 83-96 (1999).
14. Pankhurst, R.J., Riley, T.R., Fanning, C.M. and Kelley, S.P. Episodic silicic volcanism in Patagonia and the Antarctic Peninsula: chronology of magmatism associated with the break-up of Gondwana. *Journal of Petrology* 41, 605-625 (2000).
15. Riley, T.R., Leat, P.T., Pankhurst, R.J. and Harris, C. Origin of large volume rhyolitic volcanism in the Antarctic peninsula and Patagonia by crustal melting. *Journal of Petrology* 42, 1043-1065 (2001).
16. Gorring, M.L. et al. Neogene Patagonian plateau lavas: continental magmas associated with ridge collision at the Chile triple junction. *Tectonics* 16, 1-17 (1997).
17. Gorring, M.L. and Kay, S.M. Carbonatite metasomatised peridotite xenoliths from southern Patagonia: implications for lithospheric processes and Neogene plateau magmatism. *Contributions to Mineralogy and Petrology.* 140, 55-72 (2000).
18. Laurora, A. et al. Metasomatism and melting in carbonated peridotite xenoliths from the mantle wedge: the Gobernador Gregores case (southern Patagonia). *Journal of Petrology* 42, 69-87 (2001).
19. Rivalenti, G. et al. The backarc mantle lithosphere in Patagonia, South America. *Journal of South American Earth Sciences* 17, 121-152 (2004).
20. Schilling, M.E. et al. Spinel-facies mantle xenoliths from Cerro Redondo, Argentine Patagonia: petrographic, geochemical, and isotopic evidence of interaction between xenoliths and host basalt. *Lithos* 82, 485-502 (2005).
21. Schilling, M.E. et al. Re-Os constraints on subcontinental lithospheric mantle evolution of southern South America. *Earth and Planetary Science Letters* 268, 89-101 (2008).
22. Mundl, A. et al. Mesoproterozoic and Paleoproterozoic subcontinental lithospheric mantle domains beneath southern Patagonia: isotopic evidence for its connection to Africa and Antarctica. *Geology* 43, 39-42 (2015).

23. Wilshire, H.G. and Shervais, J.W. Al-augite and Cr-diopside ultramafic xenoliths in basaltic rocks from the western United States. *Physics and Chemistry of the Earth* 9, 257-272 (1975).
24. Chisholm, J.M. Composition of native gold. Geology Department and Extension Service, University of Western Australia, Crawley. *Gold Mineralization* 3, 65-75 (1979).
25. Fulginati, P. and Sbrana, A. Presence of native Au and tellurium in the active high-sulfidation hydrothermal system of the La Fossa volcano (Vulcano, Italy). *Journal of Volcanology and Geothermal Research* 86, 187-198 (1998).
26. Ferraris, C. and Lorand, J-P. Novodneprite ($AuPb_3$), anyuiite [$Au(Pb, Sb)_2$] and Au micro- and nano-inclusions within plastically deformed mantle-derived olivine from the Lherz peridotite (Pyrenees, France): a HRTEM–AEM–EELS study. *Physics and Chemistry of Minerals* 42, 143–50 (2014).
27. O´Reilly, S.Y. and Griffin, W.L. *Metasomatism and the chemical transformation of rock Ch. 12* (Springer, Verlag Berlin Heidelberg, 2013).
28. Borisov, A. and Palme, H. Experimental determination of the solubility of Au in silicate melts. *Mineralogy and Petrology* 56, 297-312 (1996).
29. Borisov, A. and Palme, H. Solubilities of noble metals in Fe-containing silicate melts as derived from experiments in Fe-free systems. *American Mineralogist* 85, 1665-1673 (2000).
30. Toscani, L. Magmatic Au grains in the El Tale lamproite, Fortuna, SE Spain. *Mineralogical Magazine* 63, 595-605 (1999).
31. Sisson, T.W. Native Au in hawaiian alkalic magma. *Economic Geology* 98, 643-648 (2003).
32. Ionov, D.A., Grégoire, M. and Prikhod´ko, V.S. Feldespar-Ti-oxide metasomatism in off-cratonic continental and oceanic upper mantle. *Earth and Planetary Science Letters* 165, 37-44 (1999).
33. Grégoire, M., Lorand, J-P., O´Reilly, S.Y. and Cottin, J.Y. Armalcolite-bearing, Ti-rich metasomatic assemblages in harzburgitic xenoliths from the Kerguelen Islands: Implications for the oceanic mantle budget of high-field strength elements. *Geochimica et Cosmochimica Acta* 64, 673-694 (2000).
34. Holzeid, A. Separation of sulfide melt droplets in sulfur saturated silicate liquids. *Chemical Geology* 274, 127-135 (2010).
35. Jugo, P.J., Wilke, M. and Botcharnikov, R.E. Sulfur K-edge XANES analysis of natural and synthetic basaltic glasses: implications for S speciation and S content as a function of oxygen fugacity. *Geochimica et Cosmochimica Acta* 74, 5926-5938 (2010).
36. Jégo, S., Pichavant, M. and Mavrogenes, J.A. Controls on gold solubility in arc magmas: An experimental study at 1000°C and 4 kbar. Geochim. *Geochimica et Cosmochimica Acta* 74, 2165-2189 (2010).
37. Botcharnikov, R.E. et al. High gold concentrations in sulfide-bearing magma under oxidizing conditions. *Nature Geosci*ence 4, 112-115 (2011).
38. Cawthorn, R.G. and Biggar, G.M. Crystallization of titaniferous chromite, magnesian ilmenite and armalcolite in tholeiitic suites in the Karoo igneous province. *Contributions to Mineralogy and Petrology* 114, 221-235 (1993).
39. Evans, B.W. and Wright, T.L. Composition of liquid chromite from the 1959 (Kilauea IKI) and 1965 (Makaopuki) eruptions of Kilauea volcano, Hawaii. *American Mineralogist* 57, 217-230 (1972).
40. Contini, S., Venturelli, G. and Toscani, L. Cr-Zr-armalcolite-bearing lamproites of Cancarix, SE Spain. *Mineralogical Magazine* 57, 203-216 (1993).

41. Zhang, Z., Mao, J., Wang, F. and Pirajno, F. Native Au and native copper grains enclosed by olivine phenocrysts in a picrite lava of the Emeishan large province, SW China. *American Mineralogist* 91, 1178-1183 (2006).
42. Hayden, L.A. and Watson, E. A diffusion mechanism for core-mantle interaction. *Nature* 450, 709-711 (2007).
43. Storey, B.C., Leat, P.T. and Ferris, J.K. The location of mantle-plume centers during the initial stages of Gondwana breakup: *Geological Society of America special paper* 352, 71-80 (2001).
44. Storey, B.C. and Alabaster, T. Tectonomagmatic controls on gondwana break-up models: evidence from the proto-Pacific margin of Antarctica. *Tectonics* 10, 1274-1288 (1991).
45. Yale, L.B. and Carpenter, S.J. Large igneous provinces and giant dike swarms: proxies for supercontinent cyclicity and mantle convection. *Earth and Planetary Science Letters* 163, 109-122 (1998).
46. Hawkesworth, C., Kelley, S., Turner, S., le Roex, A. and Storey, B.C. Mantle processes during Gondwana break-up and dispersal. *Journal of African Earth Sciences* 28, 223-253 (1999).
47. Rapela, C.W., Pankhurst, R.J., Fanning, C.M., and Hervé, F. Pacific subduction coeval with the Karoo mantle plume: the early Jurassic subcordilleran belt of northwestern Patagonia. *The Geological Society of London, Special publications* 246, 217-239 (2005).

2.9. FIGURES

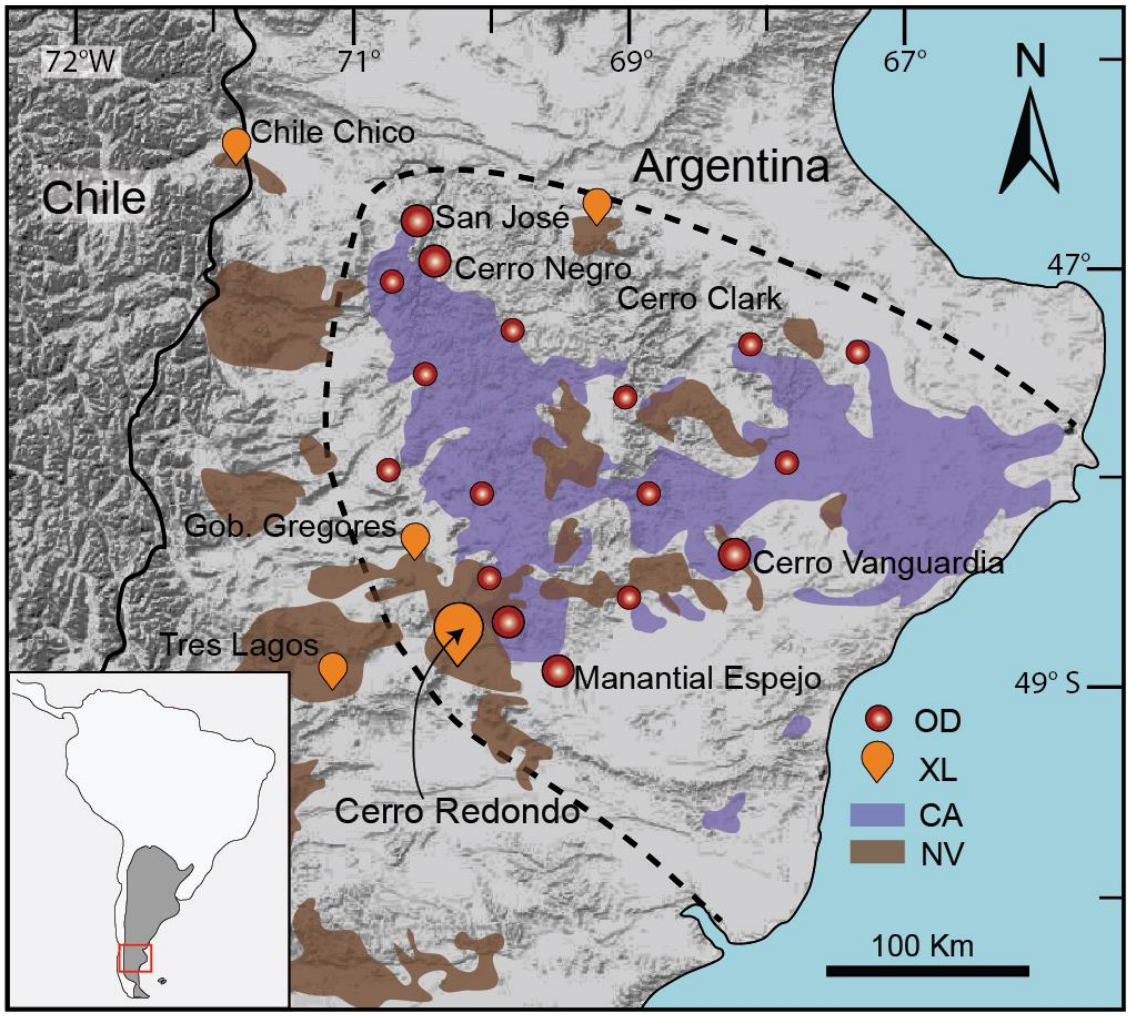

Fig. 1. Simplified geological map of southern Patagonia, Argentina. The dashed line delimits the Deseado Massif auriferous province. OD: most relevant ore deposits and prospects. XL: location of different xenolith sites in the Deseado Massif and surroundings. CA: Chon Aike volcanic sequences. NV: Neogene volcanism.

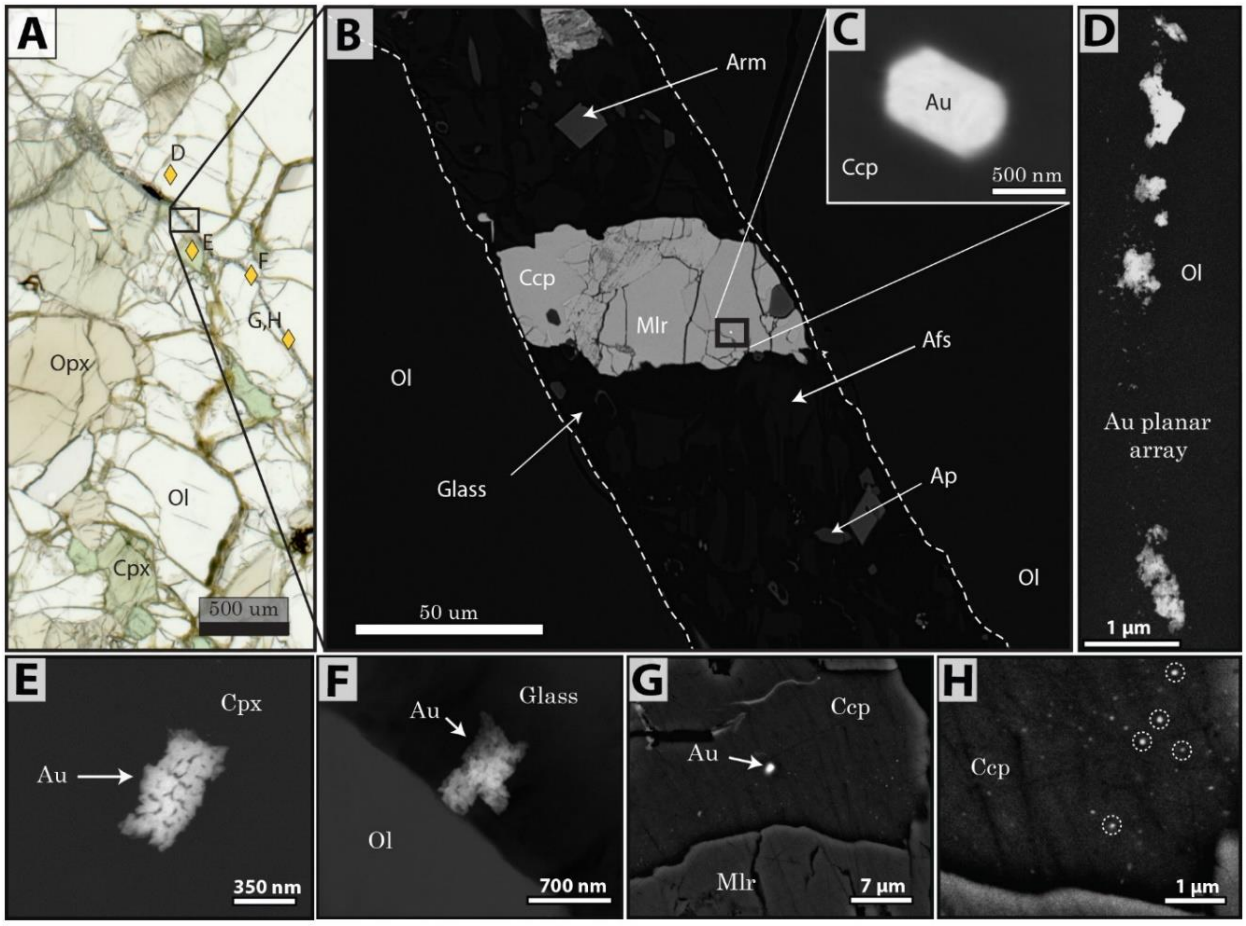

Fig. 2. Photomicrograph and BSE images of Au particles in the Cerro Redondo mantle xenolith. (A) Plane polarised light image of the lherzolite sample showing the late metasomatic glass vein and the location of Au particles (golden diamonds. Letters refers to BSE images). (B-H) Backscattered electron FE-SEM images of Au particles and their microstructural setting. (B) Detail of the glass vein showing its metasomatic assemblage and a composite sulfide grain containing a Au particle. (C) Magnification of the euhedral Au particle within chalcopyrite from the composite sulfide grain in "(B)". (D) Planar array of Au particles within olivine. (E) Au particle enclosed within clinopyroxene. (F) Au particle within the glass of the metasomatic vein in contact with olivine. (G) Au particle within chalcopyrite and arrangement of Au nanoparticles enlarged in "(H)". Opx: orthopyroxene; Ol: olivine; Cpx: clinopyroxene; Arm: armalcolite; Ccp: chalcopyrite; Mlr: millerite; Afs: alkali feldspar; Ap: apatite.

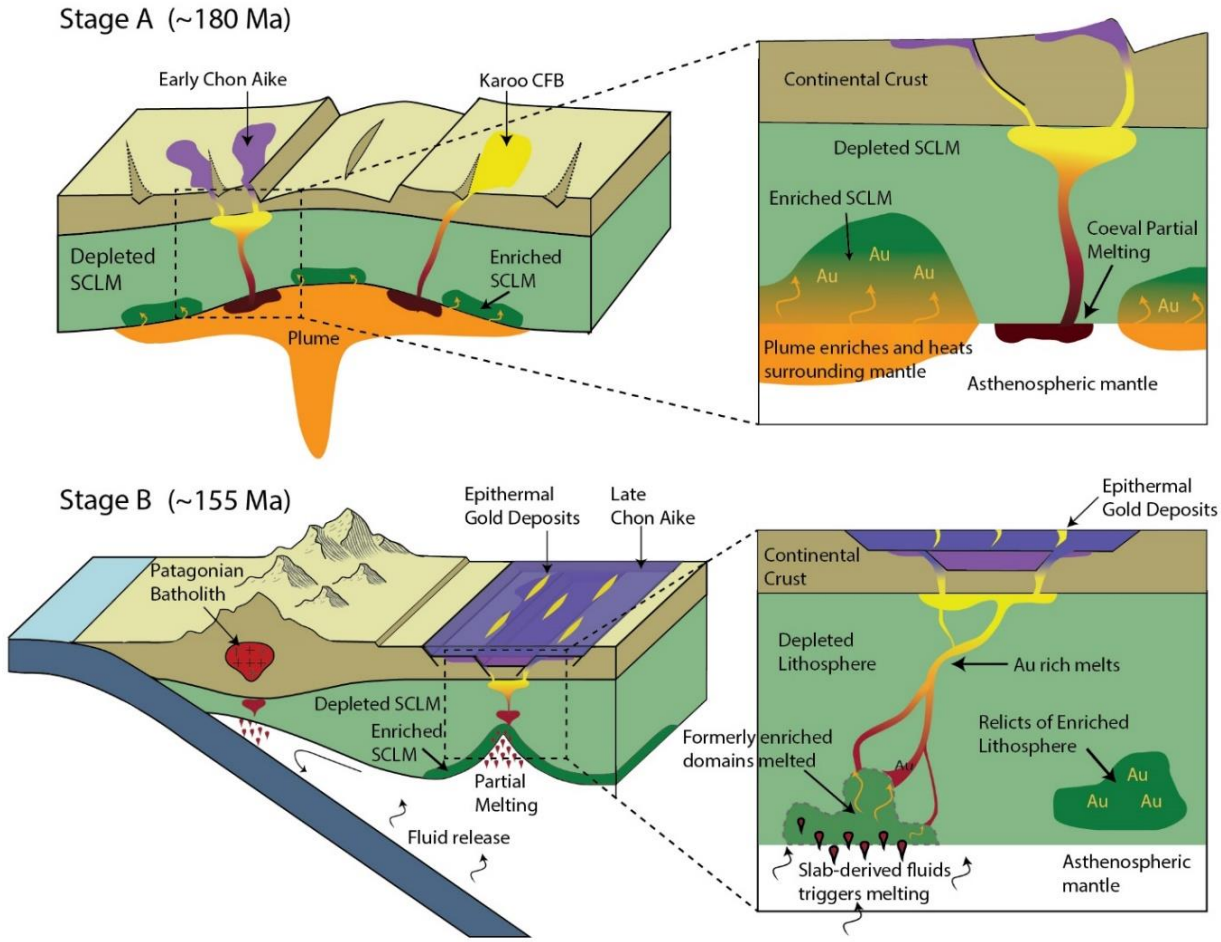

Fig. 3. Lithospheric-scale processes involved in the precursor stage of formation of the Deseado Massif auriferous province. Stage A: Plume activity during Early Jurassic related to the initial stages of Gondwana break-up induces metasomatic Au enrichment in the overlying SCLM and coeval partial melting. The inset shows the transfer of Au to the enriched domains and partial melting processes responsible for the early magmatic stages of the CA-SLIP. Stage B: Onset of the subduction zone at the western margin of Gondwana provides fluids capable of scavenging Au from formerly enriched domains and generates calc-alkaline magmatism represented by the middle-late magmatic stages of the CA-SLIP that hosts the Au deposits. The inset shows the process of partial melting of enriched domains and Au transport to crustal levels; some portions of enriched lithosphere remain unmodified.

2.10. ACKNOWLEDGEMENTS

We thank associate editor Melissa Plail for handling the manuscript. Richard Sillitoe and an anonymous reviewer are acknowledged for their constructive and helpful comments. Funding for this study has been provided by Millennium Science Initiative (MSI) through Millennium Nucleus for Metal Tracing along Subduction Grant NC130065. Additional support was provided by FONDAP project 15090013 "Centro de Excelencia en Geotermia de Los Andes, CEGA" and FONDECYT projects #11140005 and #1140780. Additional funding for LA-ICP-MS analyses of sulfides at Macquarie University was provided by RYC-2015-17596. Santiago Tassara thanks CONICYT for providing support through a Ph.D. scholarship.

2.11. AUTHOR CONTRIBUTIONS

All the authors contributed substantially to the paper as a team including the provision of samples, analytical data, contributions to the interpretation and models, and writing of the manuscript. Specifically, José M. González-Jiménez, Martin Reich, Diego Morata and Fernando Barra conceived and designed the study, which was carried out largely by Santiago Tassara. Manuel Schilling and Alexandre Corgne provided samples. Analytical work at the University of Chile was carried out by Santiago Tassara under supervision and guidance of Martin Reich, Diego Morata and Fernando Barra. Edward Saunders performed in situ analysis of sulfides at Macquarie University, under the supervision of W.L. Griffin and S.Y. O´Reilly. Santiago Tassara performed analyses at the University of Barcelona in Spain, and at the Toulouse University, France, under the guidance of Michel Grégoire. All the authors analysed and discussed the data, and revised the manuscript, which was written by Santiago Tassara, José M. González-Jiménez and Martin Reich.

CHAPTER 3. HIGHLY SIDEROPHILE ELEMENTS MOBILITY IN THE SUBCONTINENTAL LITHOSPHERIC MANTLE BENEATH SOUTHERN PATAGONIA

Santiago Tassara[1]*, José M. González-Jiménez[2], Martin Reich[1], Edward Saunders[3,4], Ambre Luguet[5], Diego Morata[1], Michel Grégoire[6], David van Acken[5], Manuel E. Schilling[7], Fernando Barra[1], Geoff Nowell[8], Alexandre Corgne[7]

[1]*Department of Geology and Andean Geothermal Center of Excellence (CEGA), FCFM, Universidad de Chile, Plaza Ercilla 803, Santiago, Chile.*
[2]*Departamento de Mineralogía y Petrología, Universidad de Granada, Facultad de Ciencias, Fuentenueva s/n 180002, Granada, Spain.*
[3]*Division of Earth Sciences, School of Environmental and Rural Science, University of New England, Armidale, NSW 2351, Australia.*
[4]*ARC Centre of Excellence for Core to Crust Fluid Systems/GEMOC, Macquarie University, NSW 2109, Australia.*
[5]*University College Dublin, School of Earth Sciences, Science Centre West, Belfield, Dublin 4, Ireland.*
[6]*GET, CNRS-CNES-IRD-UPS, OMP, Toulouse University, 14 av. Edoudard Belin, 31400 Toulouse, France.*
[7]*Instituto de Ciencias de la Tierra, Facultad de Ciencias, Universidad Austral de Chile, Valdivia, 5090000, Región de Los Ríos, Chile.*
[8]*Durham University, Department of Earth Sciences, Science Labs, Durham DH1 3LE, United Kingdom.*

(*) Corresponding author**:** Santiago Tassara

Keywords: Subcontinental lithospheric mantle; metasomatism; mobility; highly siderophile elements; base-metal sulfides.

3.1. ABSTRACT

Peridotite xenoliths collected from alkali basalts in the Argentinian Patagonia reveal the existence of an ancient depleted Paleoproterozoic mantle that records a subsequent multistage metasomatic history. Metasomatism is associated with carbonatite-like melts that evolved, after variable melt/rock ratio interaction, towards CO_2-rich and Na-bearing Mg-rich (mafic) silicate, and volatile-rich alkali silicate melts. High degrees of partial melting produced strongly depleted mantle domains devoid of base-metal sulfides (BMS). Moderate degrees of partial melting and later unrelated metasomatism produced a range of slightly depleted, slightly enriched, and strongly enriched mantle domains that preserve different types of BMS. Thus, six different BMS populations were identified including typical residual Type 1A BMS enriched in Os, Ir, and Ru relative to Pt, Pd, and Au located within primary olivine and clinopyroxene, and metasomatic Type 2A BMS that are relatively enriched in Pt, Pd, Au occurring as interstitial grains. Reworking of these two types of BMS by later metasomatism resulted in the formation of a new generation of BMS (Type 1B and Type 2B) that are intimately associated with carbonate/apatite blebs and/or empty vesicles, as well as with cryptically metasomatised or metasomatic clinopyroxene. These newly formed BMS were re-enriched in Os, Pd, Au, Re and in semi-metal elements (As, Se, Sb, Bi, Te) compared to their

Type 1A and Type 2A precursors. A third generation of BMS corresponds to Ni-Cu immiscible sulfide mattes entrained within Na-bearing silica under-saturated alkali melt. They occur systematically related to intergranular glass veins and exhibit distinctively near flat CI-chondrite normalised highly siderophile element patterns with either positive Pd (Type 3A) or negative Pt (Type 3B) anomalies. Our findings indicate that Os, Pd, Re and Au can be selectively transported by volatile-rich alkali silicate melts in the subcontinental lithospheric mantle. Moreover, the transport of sulfide mattes entrained in silicate melts is also an effective mechanism to produce HSE endowment in the SCLM and play an important role as precursors of fertile, metal-rich magmas that form ore deposits in the overlying crust.

3.2. INTRODUCTION

The six Platinum Group Elements (PGE: Os, Ir, Ru, Rh, Pt, Pd) plus gold (Au), and rhenium (Re) comprise the highly siderophile elements (HSE). Given their strong chalcophile and siderophile affinity, these elements tend to partition into sulfides or alloy phases (Luguet and Reisberg, 2016). Thus, they are increasingly used as tracers of the geochemical evolution of different layers of the solid Earth, and particularly along frontiers between the subcontinental lithospheric mantle (SCLM) and its underlying asthenosphere and overlying crust (Harvey et al., 2015; 2016).

There is agreement that during partial melting of the mantle, the most compatible HSE (IPGE: Os, Ir, Ru) are retained in the peridotitic residue within the structure of residual BMS or by forming platinum-group minerals (PGM) (Luguet et al., 2003; 2007; Lorand et al., 2008; 2010; González-Jiménez et al., 2014; O'Driscoll and González-Jiménez, 2016). These residual BMS, are typically monosulfide solid solution (mss) hosted in primary olivine or residual pyroxene, rich in IPGE, yielding relatively unradiogenic $^{187}Os/^{188}O$ ratios (Alard et al., 2002). In contrast, metasomatism can lead either to the removal or to the addition of HSE depending on the melt-fluid/rock ratio and the compositional nature of the metasomatic agents. Thus, a wide range of metasomatic agents have been proposed to explain the very different HSE systematics in SCLM peridotites (*e.g.*, Lorand et al., 2013; Luguet et al., 2015). These include S-undersaturated OIB-like melts (Lorand et al., 2004, Saunders et al., 2016), volatile-rich silicate melts exsolved after percolation and reaction with the peridotite wall-rock or S-saturated melts (*e.g.*, Grégoire et al., 1997; Moine et al., 2004); CO_2-rich (*i.e.*, carbonatite-like) melts (Saunders et al., 2015; Akizawa et al., 2017), and fluids derived from subduction zones (McInnes et al., 1999; Widom et al., 2003). Percolation of S-undersaturated melts usually removes BMS from the mantle and dilutes the whole-rock HSE concentrations in the peridotite whereas infiltration of S-saturated melts has the opposite effect producing the precipitation of Cu-Ni-rich sulfides (see Fig. 18 in Luguet and Reisberg, 2016). These Cu-Ni-rich BMS usually crystallize along grain boundaries or triple junctions of peridotite-forming silicates and oxides; they are typically rich in Pt, Pd, Re (and sometimes Au) and semi-metals with more radiogenic $^{187}Os/^{188}Os$ ratios (Alard et al., 2002; Harvey et al., 2010; 2015; 2016). However, BMS with HSE signatures similar to those that are typically originated by partial melting are being increasingly observed in metasomatic melt-pockets occurring within mantle peridotite xenoliths elsewhere, questioning our understanding of HSE mobility in the SCLM (González-Jiménez et al., 2014; Hughes et al., 2017). Contrary to what is commonly thought, these observations claim against a direct relation between the microstructural position of the BMS and their trace element composition.

In the above scenario, a better understanding of the impact of the different metasomatic styles in the formation or modification of the HSE carriers is of critical importance to understanding

how HSE are mobilized through the SCLM. This has important implications on how metals are sourced from the mantle to form ore deposits in the overlying crust (Begg et al., 2010; Hronsky et al., 2012; Griffin et al., 2013; Tassara et al., 2017). To date, few studies have addressed the relationship between HSE distribution in BMS and their petrography (*e.g.*, Alard et al., 2000; 2005; 2011; Luguet et al., 2001; 2004; 2007; Lorand and Alard, 2001; Delpech et al., 2012; González-Jiménez et al., 2014; Saunders et al., 2015, 2016; Van Acken et al., 2017) in order to define the fingerprints left at the grain-scale by each different metasomatic agent that percolated the SCLM. Despite these advances, there are significant gaps in knowledge that limit our understanding of the impact of metasomatism on HSE mobility. Particularly it is still debatable the effects that CO_2-rich melts have in mobilizing HSE in the SCLM (Saunders et al., 2015; Akizawa et al., 2017; Hughes et al., 2017).

This study aims at defining the mechanisms of mobility of HSE in the mantle by identifying fingerprints left by the different metasomatic agents that infiltrated and modified the composition of the southern Patagonian SCLM. To achieve this goal, we selected a suite of 23 peridotite xenoliths from three key localities from southern Patagonia representative of volumes of mantle having experienced significant melt extraction and subsequent metasomatism. We performed (i) major and trace elements analyses including HSE and $^{187}Os/^{188}Os$ compositions of the whole-rock, and (ii) major and trace elements analyses in silicates and non-silicates phases and HSE and semi-metals analyses in BMS. We refine previous knowledge about HSE fingerprints left by melt depletion and the multistage metasomatism in these peridotites, providing valuable insights into the mechanisms of HSE mobility in the SCLM beneath southern Patagonia. The new information provided here is of particular relevance to understanding the mechanisms of HSE enrichment in the SCLM, the formation of HSE-rich magmas, and the link between the SCLM and the formation of ore deposits in the overlying crust.

3.3. GEOLOGICAL BACKGROUND

The Patagonia region in southern South America comprises the Andean and extra-Andean (back-arc) territory of southern Chile and Argentina (Fig. 1), and its geological evolution is closely related to the subduction of the Nazca and Antarctic plates since the Jurassic (Ramos and Aleman, 2000). In the Andean Patagonia, the Southern Volcanic Zone (SVZ) and Austral Volcanic Zone (AVZ), related to the subduction of the Nazca and Antarctic plates respectively, are separated by a volcanic gap caused by the subduction of the Chile-Ridge (Forsythe et al., 1986). The back-arc region in Argentina, on the other hand, is characterised by Middle to Late Jurassic volcanism that gave rise to the Chon Aike Large Igneous Province (CA-LIP). The CA-LIP represents a period of extensive volcanism developed during the initial stages of the break-up of Gondwana (187 – 144 Ma) and comprises an early (~ 188 Ma) tholeiitic stage caused by the thermal impact of the Karoo mantle plume, followed by a late (~ 155 Ma) calc-alkaline stage formed after the influence of a subduction zone at the western margin of Gondwana (Pankhurst et al., 2000). The late stage of the CA-LIP is genetically linked to the formation of the Deseado Massif auriferous province in southern Patagonia, the world's southernmost metallogenic region. The Deseado Massif auriferous province was developed as a result of the combination of the thermal impact caused by the impingement of the Karoo plume followed by the influence of a subduction zone (Tassara et al., 2017).

During the Miocene, the subduction of the Chile-Ridge promoted the opening of a slab window that allowed the upwelling of asthenospheric melts that gave rise to an extensive Neogene

volcanism (Gorring et al., 1997), characterized by an eastward decreasing of the slab component (Stern et al., 1990; Gorring and Kay, 2001). The latter includes Miocene (~ 14 to 5 Ma) plateau basalts of tholeiitic to alkaline composition and Pliocene (~ 6 to 2 Ma) post-plateau alkaline, OIB-like basalts occurring in volcanic centres. The origin of the plateau basalts was ascribed to asthenospheric sources enriched by a weak plume that was related to the opening of the slab window (D'Orazio et al., 2001) whereas the post-plateau alkaline basalts are related to thermal perturbations induced by the subducted slab in asthenospheric levels of the mantle wedge (Stern et al., 1990). In the southernmost part of Argentina, the Pliocene post-plateau basalts sampled peridotite xenoliths from the SCLM beneath the Deseado Massif auriferous province. Numerous scoria cones, lava flows and pyroclastic deposits form nine different xenolith-sampling localities in southernmost Patagonia (Fig. 1).

Recent studies focused on the Os isotopic composition of peridotite xenoliths from southern Patagonia and determined the existence of a Mesoproterozoic-to-Paleoproterozoic depleted SCLM (1.3 – 1.9 Ga for Tres Lagos and 2.5 Ga for Pali Aike; Fig. 1) which was variably modified by the infiltration of metasomatic melts or fluids, although the timing of metasomatism remains unclear (Ntaflos et al., 2007; Schilling et al., 2008; Mundl et al., 2015; Schilling et al., 2017). The metasomatic agents identified in the SCLM beneath southern Patagonia include: (1) carbonatite-like melts and nepheline-normative alkali basalt mainly in Gobernador Gregores locality (Gorring and Kay, 2000; Laurora et al., 2001; Rivalenti et al., 2004; Aliani et al., 2009; Scamberulli et al., 2009), (2) silicate melts in the Tres Lagos locality, although not clearly determined (Ntaflos et al., 2007), and (3) slab-derived fluids in the Coyaique locality (Jalowitzki et al., 2017; Fig. 1). Additional studies have recognized the percolation of slab-derived reduced (ΔFMQ -0.2 to -0.4) fluids in peridotites from Cerro del Fraile and asthenosphere-derived melts in Pali-Aike (Wang et al., 2007, 2008).

3.4. RESULTS

3.4.1. Sample description

We studied 23 peridotite xenoliths from the Tres Lagos, Cerro Redondo, and Gobernador Gregores localities (Fig. 1). The peridotite dataset investigated here include 18 lherzolites, 2 harzburgites, 1 dunite, and 2 wehrlites (Fig. 2) representative of the variable petrological history previously described in southern Patagonia. We performed whole rock major and trace elements analysis by X-ray fluorescence and ICP-MS, as well as HSE and $^{187}Os/^{188}Os$ determinations by SF-ICP-MS and N-TIMS respectively. In addition, we determined the major and trace elements composition of silicates and sulfide phases by electron microprobe and LA-ICP-MS. The analytical procedures are described in detail in Appendix 1 and the results, along with a complete list of the samples used in this study is provided in Appendices 2 to 5.

The studied peridotite xenoliths vary in size from 6 to 30 cm and exhibit granular and porphyroblastic (Tres Lagos and Cerro Redondo; Fig. 2), or microgranular textures with strain-free silicates (Gobernador Gregores; Fig. 2). All peridotites were equilibrated in the spinel stability field and belong to the Cr-diopside series of Wilshire and Servais (1975). In addition to the typical peridotitic silicates and spinel, their mineral assemblage contains accessory metasomatic minerals such as amphibole, phlogopite, carbonates and apatite (Fig. 3). Amphibole and phlogopite form aggregates of up to 2 mm located between olivine and pyroxene as well as veins or layers of up to 8 mm (Gobernador Gregores, Fig. 3A, B). Carbonates are found as isolated crystals of up to 700 µm commonly located at the triple junction among primary silicates sometimes associated with

BMS (*i.e.*, Tres Lagos and Gobernador Gregores; Fig. 3C, D). Apatite fills interstices between main silicates (Tres Lagos; Fig. 3E) or is included within clinopyroxene or in contact with empty vesicles next to metasomatic amphibole (lherzolites and wehrlites from Gobernador Gregores; Fig. 3F, G). Other metasomatic minerals are secondary generations of clinopyroxene and olivine identified by their chemistry and cross-cutting relationships in the peridotites from Gobernador Gregores (Fig. 3H, I).

Glass occurs either as (1) a discontinuous system of melt pockets surrounding hydrous minerals such as amphibole (Gobernador Gregores), or (2) an interconnected network of veins cross-cutting the peridotite with sharp contacts against the silicate matrix (Cerro Redondo, Fig. 2C). The interstitial glass was never observed in connection with the enclosing host basalt. Overall, it constitutes less than 3 modal % of the studied peridotites, except for some lherzolites from Cerro Redondo where it reaches up to 7 modal %. The interstitial silicate glass from Cerro Redondo samples is commonly altered to zeolites, although it still preserves an unaltered mineral assemblage of incompletely reacted olivine and pyroxenes together with armalcolite [$(Mg,Fe^{2+})Ti_2O_5$], ilmenite, Na-K-feldspar, and apatite that is contained within the glass and likely formed after cooling in the lithospheric mantle (Tassara et al., 2017).

3.4.2. Whole-rock chemistry: major and trace elements

The 23 spinel peridotites investigated range from strongly depleted harzburgites and dunites to fertile lherzolites, and strongly enriched lherzolites and wehrlites (Fig. 2 – 4; Appendix 2). This broad compositional variation is reflected in the MgO vs. Al_2O_3 plot (Fig. 4A) and in the progressive increase in Ca from dunites and harzburgites (0.1 – 1 wt.%) to lherzolites (0.9 – 3.5 wt.%) and the wehrlites (up to 8.1 wt.%) (Fig. 4B), which is accompanied by a decrease in the MgO content (Appendix 2). The higher CaO content in the most fertile wehrlites and lherzolites is related to the higher abundance of clinopyroxene, amphibole, carbonates and apatite in those samples (Fig. 3). The CI chondrite-normalised trace element patterns of the studied peridotite xenoliths define four distinct groups presented below:

- *Group 1 (strongly depleted peridotites)*. These peridotites are characterized by a low trace element content (*i.e.*, 0.2 Gd - 1.7 La x CI chondrite) and a U-shaped CI chondrite-normalised REE pattern (Fig. 5A). They display a $(La/Yb)_n$ (subscript "n" = normalised to CI chondrite after McDonough and Sun (1995)) ratio between 1.65 and 4.76, a strong middle REE (MREE) depletion and a slightly positive Ti anomaly (*i.e.*, $(Ti/Eu)_n > 1 < (Ti/Gd)_n$; in this case ~1.7 for both) (Fig. 5B). This group comprises two clinopyroxene-free harzburgites (CR-01 and TL-2-1) and one clinopyroxene free-dunite (TL-05) from Cerro Redondo and Tres Lagos respectively (Appendix 2).

- *Group 2 (slightly depleted peridotites)*. These peridotites have a low trace element contents (0.3 La –1.4 Lu xCI chondrite) and a slightly positive ($(La/Yb)_n$ = 0.36 – 0.4) to flat ($(La/Yb)_n$ = 0.8 – 1.1) REE pattern (Fig. 5C). In addition, these samples show a slight decrease in high field strength element concentrations (HFSE: Nb, Ta, Zr, Hf), a slight negative Ti anomaly ($(Ti/Eu)_n$ and $(Ti/Gd)_n$ ~0.8) and a relative positive U anomaly ($(U/Th)_n$ = 0.8 – 8.6). They also display lower than the primitive mantle (McDonough and Sun, 1995) concentrations of large ion lithophile elements (LILE: *e.g.*, Rb, Ba, Sr) (Fig. 5D; Appendix 2). This group includes five lherzolites from Cerro Redondo (samples CR-02, CR-03, CR-07, CR-08, and CR-09) and one lherzolite from Tres Lagos (sample TL-2-3); all of them with less than 14 % modal clinopyroxene and no metasomatic accessory minerals (Appendix 2).

- *Group 3 (slightly enriched peridotites)*. These peridotites have trace element contents up to 5 times the CI chondrite (*e.g.*, La) values and show a nearly flat to depleted heavy REE (HREE) to MREE pattern (Fig. 5E). They are characterised by a suprachondritic $(La/Ce)_n$ (1.22 – 1.94) ratio and a noticeable LREE enrichment ($(La/Yb)_{n=}$ 0.8 - 5.44) in some of the samples (Fig. 5E). The LREE enrichment is accompanied by a slight increase in Ba and Sr compared to the *Group 2* peridotites, which is decoupled from the HFSE as evidenced in the slight negative Hf, Zr, Nb, and Ta anomalies (Fig. 5F). This group consists of 4 lherzolites from Tres Lagos (TL-01, TL-03, TL-06, and TL-08) and 3 lherzolites from Gobernador Gregores (GG-05, GG-10, and GG-13; Appendix 2).

- *Group 4 (strongly enriched peridotites)*. The peridotites from this group exhibit the highest concentrations of trace elements with values of trace elements (up to 30 times the CI chondritic values for LREE and 100 times for Nb and Ta) and are characterised by convex upward REE distribution with extreme LREE enrichment ($(La/Yb)_n$ = 4.63 - 10.22) (Fig. 5G; Appendix 2). In this group, the three samples having the highest LREE/HREE fractionation display strong positive anomalies of Ta and Nb, whereas the least enriched of the group display variable Nb/Ta ratios (Fig. 5H). All samples display slight to strong Hf, Zr, and Ti negative anomalies (Fig. 5H). Interestingly, these peridotites contain the larger modal abundance of metasomatic minerals including amphibole, phlogopite, carbonates and apatite. This group of samples include five lherzolites (GG-01-A, GG-02, GG-03, GG-07, and GG-14) and 2 wehrlites (GG-17; GG-01B) from Gobernador Gregores.

3.4.3. Whole-rock HSE and Re-Os isotopic signatures

Whole-rock HSE concentrations and Re-Os isotopic ratios were determined for 21 samples and are reported in Appendix 3. The peridotite xenoliths show HSE systematics that broadly corresponds with the lithological groups defined above and are described below (Fig. 6).

The *Group 1* peridotites have bulk-rock HSE contents between 13.3 and 28.3 $ng.g^{-1}$, defining a HSE pattern depleted in all elements relative to the CI chondrite, except for a slight Ru positive anomaly in sample CR-01 (Fig. 6A; Appendix 3). The *Group 2* peridotites have the highest total HSE abundances (18.84 – 36.80 $ng.g^{-1}$) of all groups and display flat CI chondrite-normalised HSE patterns, where the Os-Pt segments remain near the PUM values and the Pt-Re segments diverge from the PUM (Fig. 6B; Appendix 3). Noticeably, sample CR-09 has the highest Re content (1.77 x PUM) (Fig. 6B). The *Group 3* peridotites have low total HSE abundances (10.05 – 8.91 $ng.g^{-1}$) and display convex upwards shaped CI chondrite-normalised HSE patterns (Fig. 6C). This group shows systematic enrichment in Pd relative to Pt, but below the PUM, excepting sample GG-13 (Fig. 6C; Appendix 3). The *Group 4* peridotites show the lowest total HSE concentrations of all groups (4.4 and 20.9 $ng.g^{-1}$). Their CI chondrite-normalised HSE patterns are characterized by a convex upward (samples GG-02, GG-07, and GG-14) or flat to positive-sloped shapes (peridotites GG-01-A, GG-01-B, GG-03, and GG-17; Fig. 6D; Appendix 3).

The $^{187}Os/^{188}Os$ ratios of the studied peridotites are unradiogenic (0.116330 - 0.127191) with respect to the PUM ($^{187}Os/^{188}Os$ = 0.1296 +/- 0.0008; Meisel et al., 2001), except for sample GG-01-B (*Group 4*) which has a highly radiogenic $^{187}Os/^{188}Os$ composition (0.215985). In the Al_2O_3 vs. $^{187}Os/^{188}Os$ plots, the samples define a broad/loose positive trend (Fig. 7A; Appendix 3). Overall, the peridotites show no systematic correlation between the $^{187}Os/^{188}Os$ and the $^{187}Re/^{188}Os$ ratio, and most samples plot below the Enstatitic Chondritic Reservoir (ECR; $^{187}Os/^{188}Os$ = 0.1281, $^{187}Re/^{188}Os$ = 0.421; Walker et al., 2002) values in $^{187}Os/^{188}Os$ vs. $^{187}Re/^{188}Os$ graphs (Fig. 7B).

Only two samples are out of this general rule with coupled radiogenic $^{187}Os/^{188}Os$ and $^{187}Re/^{188}Os$ (wehrlite GG-01-B of *Group 4*) and uncoupled suprachondritic $^{187}Re/^{188}Os$ and subchondritic $^{187}Os/^{188}Os$ (CR-09 of *Group 2*). The $^{187}Os/^{188}Os$ ratios are uncorrelated with the whole-rock Os content (Fig. 7C).

Rhenium-depletion (T_{RD}) model ages and T_{RD} model ages vary from 1.66 to 0.13 Ga, except one wehrlite for which no meaningful model age can be derived (GG-01B: $^{187}Os/^{188}Os \sim 0.215985$; Fig. 7D; Appendix 3). The *Group 1* peridotites yielded a Mesoproterozoic T_{RD} model age (1.45 Ga) for the Cerro Redondo sample and an early Palaeozoic (0.34 Ga) for the Tres Lagos peridotite. The *Group 2* samples yielded middle Mesoproterozoic to late Paleoproterozoic T_{RD} ages (1.23 to 1.13 Ga) except for sample TL-2-3 that yielded a younger age (0.51 Ga). The *Group 3* samples have Mesoproterozoic to Neoproterozoic ages (0.9 to 0.13 Ga) T_{RD} model ages and the *Group 4* samples have Paleoproterozoic to Neoproterozoic (1.66 to 0.62) T_{RD} model ages (Fig. 7D; Appendix 3).

The *Group 1* peridotites and the *Group 4* (except samples GG-02, GG-17, and GG-01-B) exhibit T_{RD} ages $\approx$ T_{MA} ages with an offset lesser than 0.18 Ga and 0.23 Ga respectively. In contrast, a significant discrepancy exists between the T_{RD} and T_{MA} ages in the *Group 2* (offset = 0.1–1.19 Ga) and the *Group 3* peridotites (offset = 0.11–0.89 Ga). Unrealistic T_{MA} ages are also identified in the most metasomatised wehrlite (GG-01-B) and lherzolite (GG-17) whereas sample GG-02 shows a much older T_{MA} age (2.46 Ga) (Appendix 3).

3.4.4. Mineral chemistry: olivine and pyroxenes

3.4.4.1. Strongly depleted peridotites (Group 1).

Orthopyroxene and olivine from this group show the most refractory composition of all samples, consistent with their clinopyroxene-free nature. Orthopyroxene shows a Mg# ([MgO/(FeO+MgO)*100] in molar proportions) ranging from 91.8 to 92.4, and a Na_2O content below the detection limit (0.02 wt.%). Consistently, Al_2O_3 and TiO_2 contents of orthopyroxene are also low being at most 3.21 and 0.07 wt.% respectively (Appendix 4). Olivine has a Mg# ranging from 91 to 91.5, NiO contents between 0.36 and 0.43 wt.%, and variable CaO contents (up to 0.07 wt.%) (Appendix 4).

3.4.4.2. Slightly depleted peridotites (Group 2)

Clinopyroxene from this group is characterized by a Mg# between 90.3 and 93.6 and its major element composition are summarised in Table 1. This clinopyroxene (hereafter Cpx1) shows depletion in the most incompatible LREE and overall low contents of LILE and HFSE (Fig. 8A, B; Table 1). Orthopyroxene has a refractory composition characterised by a Mg# from 91 to 91.7 and a Na_2O content <0.07 wt.%. Consistently, Al_2O_3 and TiO_2 content of *Group 2* orthopyroxene is also (*i.e.*, less than 3.84 and 0.13, respectively) (Appendix 4). Olivine has Mg# values that range from 90.5 to 91.5, NiO contents between 0.3 and 0.5 wt.% and CaO contents ranging from below detection limit (0.01 wt.%) to 0.13 wt.% (Appendix 4).

3.4.4.3. Slightly enriched peridotites (Group 3)

Clinopyroxene 1 in this group is characterised by Mg# between 93 and 94 and low concentrations of Al_2O_3, Cr_2O_3, Na_2O, and TiO_2 (Table 1). Similarly to Cpx1 described in *Group 2*, this clinopyroxene shows depletion in most incompatible LREE and low HFSE and LILE contents (Fig. 8C, D; Appendix 4). A second type of clinopyroxene (Cpx2) has slightly lower Mg#

and overall higher Al_2O_3, Cr_2O_3, Na_2O and TiO_2 (Table 1). Cpx2 is also distinguished by an enrichment in the most incompatible LREE, evidenced by a higher $(La/Yb)_n$ ratio and strong negative Nb and Ti anomalies (Fig. 8C, D; Table 1). A third type of clinopyroxene (Cpx3) displays even lower Mg# and Cr_2O_3 contents but higher Al_2O_3, Na_2O, and TiO_2 (Table 1). Cpx3 shows a slight enrichment in La and Ce and convex upward LREE distribution and no marked anomalies of HFSE and Ti (Fig. 8C, D; Table 1). Orthopyroxene in this group of samples has a Mg# ranging between 90.2 and 91.8. The major element composition of the *Group 3* orthopyroxene is Al_2O_3 = 3.1 – 4.3 wt.%, Na_2O = 0.09 – 0.14 wt.%, and TiO_2 = 0.07 – 0.13 wt.% (Appendix 4). Olivine from this group has lower Mg# values compared to those obtained for *Group 2* olivine, ranging from 89.7 to 91.3, while CaO contents are between 0.01 – 0.09 wt.% and NiO between 0.3 – 0.5 wt.% (Appendix 4).

3.4.4.4. Strongly enriched peridotites (Group 4)

Three types of clinopyroxene are identified in this group based on their major and trace element composition, namely clinopyroxene 4 (Cpx4), clinopyroxene 5 (Cpx5) and Clinopyroxene 6 (Cpx6). Overall, they are characterised by a progressively lower Mg# and Cr_2O_3 and increasing Al_2O_3, TiO_2 and NaO (Table 1). Cpx4 and Cpx5 have a similar trace element composition (Appendix 4) and are characterized by a concave shaped REE pattern with $(La/Yb)_n$ ratio up to 5.5 and strong negative Zr, Hf and Ti anomalies (Fig. 8D, E; Appendix 4). Clinopyroxene 6 (Cpx6) is the most abundant type in this group of peridotites and its CI chondrite-normalised REE pattern shows an overall negative slope with high LREE/HREE ratios and slightly softer negative anomalies of Zr and Hf compared to Cpx4 and Cpx5, and no Ti negative anomalies (Fig. 8D, E; Appendix 4). Orthopyroxene from *Group 4* has the lowest Mg# of all analysed samples between 88.9 and 89.5. The decrease in the Mg# is accompanied by a decrease in Al_2O_3 (2.9 – 4.9 wt.%), and an increase in Na_2O (0.13 – 0.22 wt.%) and TiO_2 (0.12 – 0.2 wt.%) (Table 1; Appendix 4). Olivine from *Group 4* was distinguished into two different types based on the Mg# and CaO content. Olivine 1 (Ol1) has the lowest Mg of all samples varying between 88.1 to 89.6 and a CaO content between 0.03 and 0.11 wt.% whereas olivine 2 (Ol2) has higher Mg# (90.8 – 92.1), which is accompanied by an increase in the CaO content of up to 0.2 wt.% (Appendix 4).

3.4.5. Mineral chemistry: metasomatic minerals

Pargasitic amphibole is abundant in the *Group 4* samples and is characterised by a low TiO_2 (~1.28 wt.%), and high chlorine (~0.38 wt.%) and fluorine (~0.17 wt.%) content. Laurora et al. (2001) distinguished the pargasite from Gobernador Gregores samples into two groups based on their TiO_2 concentration. The pargasite identified in this study falls between these two groups with respect to the TiO_2 concentration although the pargasite from this study display higher content of Ba, Th, Nb, Ta, and Zr (Appendix 4). The major element composition of pargasite from *Group 4* is reported in Appendix 4. Its trace element composition is characterised by LREE enrichment with respect to the HREE ($(La/Yb)_n$ = 3.8 – 4.1), Ba is enriched with respect to Th and U ($(Ba/Th)_n$ = 5.3), Zr and Hf are slightly depleted compared to the REE ($(Zr/Hf)_n$ = 1.64 $(Hf/Sm)_n$ = 0.74) whereas Nb and Ta show strong positive anomalies (~500 times the CI chondrite contents) compared to the rest of the trace elements (Appendix 4).

Phlogopite identified in the *Group 4* samples has a Mg# ≈ 92.56 ± 0.04, and TiO_2 lower than 2 wt.%. Its REE content is lower than the pargasite by a factor of 2 orders of magnitude, sometimes close to or below the detection limit (10 – 60 $ng.g^{-1}$, except for La, Ce and Eu. It is characterised by high concentrations of LILE as well as Cl and F (Appendix 4).

Carbonate and apatite from *Group 3* and *Group 4* peridotites were identified based on scanning electron microscopy-energy dispersive spectrometer (SEM-EDS). The SEM-EDS-semi-quantitative data obtained indicate that the carbonates are predominantly calcite with up to ~6 wt.% $MgCO_3$ and ~0.5 wt.% $FeCO_3$, similar to those identified in the same localities by Laurora et al. (2001). Apatite is a F-bearing apatite (F ≈ 3 wt.%, Cl ≈ 0.2 wt.%) found either as included grains within clinopyroxene or interstitial to the primary silicate assemblage.

3.4.6. Petrography and major element composition of base-metal sulfides

Base metals sulfides (with sizes varying from ~ 1 to ~ 500 µm) were identified in all groups, except in *Group 1* peridotites. The distribution of BMS in the peridotite xenoliths is heterogeneous, but generally, up to ten BMS grains were detected in each 9- cm^2 polished thick section. They occur either as: (i) inclusions within silicates (hereafter *included*; *e.g.*, Fig. 9A – D), (2) along grain boundaries between silicates (hereafter *interstitial*; Fig. 9E, F), and (3) embedded within interstitial glass (hereafter *glass-related*; Fig. 9G, H).

Most BMS identified in the *Group 2* lherzolites are *glass-related* and consist of single grains of millerite (NiS), or composite grains made up of pentlandite $(Fe,Ni)_9S_8$ ± Ni-rich mss (Fe_{1-x},$Ni_{1-x}S$) ± chalcopyrite ($CuFeS_2$) (chalcopyrite fraction greater than 20% volume). In addition, Fe-rich mss ± pentlandite *included* within kink-banded olivine and Cpx1 were also identified in the *Group 2* (Figs. 9G, H and 11; Appendix 5). The BMS from the *Group 3* peridotites are Fe-rich mss located either *included* in olivine with undulating extinction, or more commonly *interstitial* to Cpx 2 and Cpx 3 often associated with carbonate or apatite blebs, and sometimes texturally located next to an empty vesicle (Figs. 9C, D, and 11; Appendix 5). In contrast, the BMS from the *Group 4* peridotites are isolated grains of Fe-rich mss with or without pentlandite ± pyrrhotite ($Fe_{1-x}S$) ± cubanite ($CuFe_2S_3$) found *included* in, or *interstitial* to Cpx 4, Cpx 5 and Cpx 6 (Figs. 9G and 11; Appendix 5).

3.4.7. In situ HSE and semi-metal abundances in base-metal sulfides

HSE and chalcophile semi-metal (*i.e.*, As, Se, Sb, Te, Bi, Pb) concentrations in BMS are reported in Appendix 5 and Figure 11 shows the CI chondrite-normalised HSE patterns. Six distinct HSE patterns have been recognised for the BMS populations of the Patagonian mantle xenoliths (Table 2).

A subset of 17 out of 49 BMS exhibit the two types of CI chondrite-normalised HSE patterns reported for the *silicate-enclosed* (*i.e.*, residual; hereafter *Type 1A*) and *interstitial* (*i.e.*, metasomatic; hereafter *Type 2A*) BMS described in peridotite xenoliths elsewhere (Alard et al., 2000, 2002, Griffin et al., 2002, 2004; Aulbach et al., 2004; Powell et al., 2007; Powell and O'Reilly, 2007; Saunders et al., 2015). *Type 1A* BMS exhibit nearly flat to smoothly negative slope from Os to Rh and pronounced negative slope from Pt to Re (Fig. 11A), which is reflected in $(PPGE/IPGE)_n$ ratios between 0.03 and 0.21. They have the highest Os-Ir-Ru but the lowest Au and Re concentrations and consist of Fe-rich mss *included* within primary olivine with deformation textures or within residual clinopyroxene (Cpx1). *Type 2A* BMS have the lowest total HSE concentrations but exhibit the highest Au contents (up to 12 $\mu g.g^{-1}$) (Fig. 11B). These BMS display CI chondrite-normalised HSE patterns characterised by a positive slope ($(PPGE/IPGE)_n$ = 1.91-14.04; Fig. 11B) and consists of isolated grains of Fe-rich mss or Fe-rich mss ± pentlandite ± chalcopyrite ± cubanite. They occur as *interstitial* grains to Cpx2, and Cpx3 in *Group 3* peridotites

(samples TL-01, TL-03, GG-10, GG-13) as well as *included* or *interstitial* grains to Cpx4 and Cpx5 in the *Group 4* peridotites (samples GG-01-A, GG-03, GG-17).

Two sub-types (*Type 1B* and *Type* 2B) of the *Type 1A* and *Type* 2A CI chondrite-normalised HSE patterns have been identified in BMS associated with metasomatic F-apatite and Mg-rich carbonate, and/or empty vesicles (Fig. 9C, D, and F). These BMS occur (i) predominantly as *interstitial* components associated with Cpx3 (*Type 1B*) and (ii) to a lesser extent as *included* grains within Cpx3 (Fig. 6C, D) of the *Group 3* or *included* within Cpx6 of the *Group 4* peridotites (*Type 2B*). The *Type 1B* BMS have similar total HSE contents than the *Type 1A*, with a negative sloped CI chondrite-normalised HSE pattern. In contrast to the *Type 1A*, the *Type 1B* BMS (Fe-rich mss) display a pronounced positive Pd anomaly ($(Pd/Pt)_n$ = 1.8 – 6.4; Fig. 11C). This $(Pd/Pt)_n$ roughly increases with the concentration of Re (up to 6 $\mu g.g^{-1}$) and the chalcophile semi-metals (Fig. 11C, Appendix 5). On the other hand, the *Type 2B* BMS, also associated either with Mg-carbonates, F-apatite blebs or empty vesicles (Fig. 9C, D, and F) exhibit similar to lower total HSE concentrations and distribution to the *Type 2A*. The *Type 2B* BMS (Fe-rich mss ± pentlandite ± pyrrhotite) also display a positive sloped CI chondrite-normalised HSE pattern (Fig. 11D), but differentiates by its suprachondritic $(Os/Ir)_n$ ratio (1.3 – 5.3) as well as by its higher content in chalcophile semi-metals (Fig. 11D, Appendix 5).

The Type 3 BMS comprise isolated grains of millerite and Ni-rich mss ± pentlandite ± chalcopyrite exclusively found in *glass-related* sites in the *Group 2* lherzolites (Fig. 9H). These BMS have total HSE concentrations intermediate between *Type 1B* and *Type 2A* and display flat CI chondrite-normalised HSE patterns (*Type 3A*), sometimes with a marked negative Pt anomaly and a slightly positive Pd anomaly (*Type 3B*) (Fig. 11E, F; Table 2). The semi-metals content in the *Type 3A* and *Type 3B* BMS are somehow intermediate to the BMS described above (Appendix 5).

Figure 12 shows the co-variation between $(Os/Ir)_n$, $(Pt/Pd)_n$ versus S/Se and the Au content versus the S/Te ratios for each BMS type to evaluate the effect of semimetals on the HSE systematics. The *Type 1B* and *Type 2B* S/Se ratios are restricted to a narrow range (~ 1000 - 6000) compared to the *Type 1A* and *Type 2A* that display a wider range of S/Se ratios that extends towards one order of magnitude higher (Fig. 12A). In addition, the *Type 2B* has the highest $(Os/Ir)_n$ ratios at the lowest S/Se ratios (Fig. 12A). Fig. 12B shows that the *Type 1B* and *Type 2B* BMS have the highest $(Pd/Pt)_n$ ratios, which are roughly related to low S/Se ratios. Figure 12C, on the other hand, shows a negative correlation between the Au content and the S/Te ratios of the BMS. The *Type 1B* and *Type 2B* BMS have the lowest S/Te and in the former, the Au content remains relatively low, whereas the latter shows the highest Au values.

3.5. DISCUSSION

3.5.1. Estimation of the degree of partial melting

The suite of peridotite xenoliths analysed in this study range from *strongly depleted* (*Group 1*), *slightly depleted* (*Group 2*), *slightly enriched* (*Group 3*), to *strongly enriched* (*Group 4*) peridotites (Figs. 2, 4, 5). The depleted nature of the *Group 1* and *Group 2* peridotites is suggested by a combination of features including their lack or low modal percentage of clinopyroxene, high Mg# of olivine, the absence of metasomatic phases, and the LREE depletion producing marked positive sloped CI chondrite-normalised REE patterns (Fig. 5). Figures 5A, C, 8A, C show the estimated degree of partial melting that these rocks underwent, computed from their whole-rock

and clinopyroxene REE distribution respectively for the non-modal fractional melting model of a PUM equilibrated in the spinel lherzolite facies. The results obtained using whole-rock data indicate that the *Group 1* peridotites experienced a minimum of 14–18% partial melting, whereas the *Group 2* underwent less than 14% partial melting (Figs. 5A, C). The estimated degree of partial melting is consistent with the low modal percentage of clinopyroxene. In contrast, the results obtained using Cpx1 from the *Group 2* lherzolites indicate non-modal fractional melting of up to ~10% (Fig. 8A). The slight discrepancy observed between the partial melting estimations using the whole-rock and single mineral approach very likely reflect the effect of the interstitial glass in the whole-rock (*e.g.*, Marchesi et al., 2017).

On the other hand, the presence of accessory amphibole, phlogopite, carbonate, and apatite in the *Group 3* and *Group 4* peridotites, indicates that metasomatism has overprinted any record of previous partial melting events. Therefore, partial melting estimations in these rock types can only be assessed by using the trace element distribution in primary clinopyroxene. Lherzolites of the *Group 3* preserve Cpx1 characterised by high Mg#, low Al_2O_3 content and LREE depletion, which is suggestive of a residual origin. Thus, a minimum of 12% degree of partial melting estimated was estimated from Cpx1 of the *Group 3* by comparison with the PUM partial melting model (Fig. 8C).

In contrast, lherzolites and wehrlites from *Group 4* contain only clinopyroxene (Cpx4, Cpx5, and Cpx6) displaying REE and trace element composition characterised by strong LREE enrichment relative the HREE; features clearly inconsistent with a residual origin (Fig. 6E, F) and therefore cannot be used for quantifying the degree of partial melting.

3.5.2. Evidence of modal and cryptic volatile-rich metasomatism

Several lines of evidence indicate strong cryptic and modal metasomatism in the *Group 3* and *Group 4* peridotites including: (1) an assemblage of volatile-rich minerals that include amphibole, phlogopite, apatite, and carbonate often associated with empty vesicles indicating degassing of a volatile-rich fluid/melt (Fig. 3G), (2) LREE enrichment in the whole-rock peridotites and clinopyroxene (Fig. 6C – F), and (3) identification of wehrlites forming after lherzolites.

Modal metasomatism recorded by the formation of apatite and carbonates commonly associated with empty vesicles suggest the infiltration of fluids and/or melts enriched in volatile components (*e.g.*, C, H, F, S, P) and in the most incompatible trace elements (LREE, Sr, Th, U). In the *Group 3* peridotites, the enrichment in the most incompatible trace elements (Fig. 5E, F) and the lower modal abundance of metasomatic minerals indicate that the rocks were modified by the infiltration of a metasomatic agent at very low fluid-melt/rock ratios. The CI chondrite-normalised trace element patterns of these peridotites overlap with the pattern for fertile peridotite xenoliths from Montferrier in France (Fig. 5E), which were interpreted as metasomatised by melts enriched in a volatile component at relatively low fluid-melt/rock ratio (Alard et al., 2011). The Cpx2 from these peridotites display high Mg#, Na_2O and Cr_2O_3 but low TiO_2 and Al_2O_3 as well as LREE enrichment and(Fig. 6C, D), high LILE and negative Nb and Ta anomalies. These features are similar to those reported for mantle xenoliths from East Oman and Cameroon that have been metasomatised by CO_2-rich and Na-bearing mafic silicate melts (Grégoire et al., 2009; Teitchou et al., 2011) as well as by alkali (silica-undersaturated and nepheline normative) basalts as described by Laurora et al. (2001) and Rivalenti et al. (2004) for Gobernador Gregores peridotite xenoliths. In fact, Gobernador Gregores *Group 3* lherzolites (samples GG-05, GG-10, GG-13) exhibit a stronger LREE/HREE fractionation and a strong negative Ti and moderately negative Zr and Hf anomalies, which is also compatible with metasomatism caused by CO_2-rich and Na-bearing mafic

silicate melts at relatively low melt/rock ratios. On the other hand, the Cpx3 from the *Group 3* peridotites in the Tres Lagos has a greater Al_2O_3 and TiO_2 content than Cpx2 and a REE pattern similar to that of the whole-rock, with lower LREE/HREE fractionation than the Cpx2, and without negative anomalies in Ti, Zr, and Hf (Fig. 6C, D). In contrast with the metasomatic imprint of Cpx2, Cpx3 features are consistent with a metasomatism produced by alkali silicate melts at relatively low melt/rock ratios.

Modal and cryptic metasomatism by carbonatite-like melts is better recorded in the *Group 4* lherzolites and wehrlites from Gobernador Gregores. Infiltration of a carbonatite-like melt at high melt/rock ratios in these rocks is suggested by: (1) the higher modal abundance of metasomatic apatite and carbonates associated with amphibole and phlogopite, which were not identified in other metasomatised peridotites (Fig. 3), (2) the modal variation towards wehrlite (Figs. 2 and 4), and (3) the extremely high LREE/HREE fractionation and negative Zr, Hf, and Ti anomalies in whole-rock analyses (Fig. 5G, H; Coltorti et al., 1999). The imprint of evolving carbonatite melts is particularly well recorded in the different types of clinopyroxene identified in the *Group 4* peridotites. Thus, Cpx4 is enriched in Na_2O and characterised by a very high Cr_2O_3 and Mg# and low TiO_2 content, and exhibit a high LREE enrichment, $(La/Yb)_n$, $(Zr/Hf)_n$ and low $(Ti/Eu)_n$, similar to clinopyroxene that typically crystallize from carbonatite-like melts (Fig. 6E, F) (*e.g.*, Akizawa et al., 2017). In contrast, Cpx5 exhibits a similar minor and trace element distribution to Cpx4 (Fig. 6E, F; Appendix 2) but displays a higher SiO_2 and TiO_2 and lower Na_2O content, which suggests the infiltration of a metasomatic melt with a stronger silicate component (Rivalenti et al., 2004). The *Group 4* Cpx6 shows a marked Fe-Ti enrichment accompanied by an increase in Al_2O_3 at distinctly lower Mg# than Cpx4 and Cpx5 (Appendix 2) without negative Hf and Zr anomalies. Thus, Cpx6 features are consistent with a crystallization from late alkaline silicate melts percolating and metasomatising upper mantle peridotites at high melt/rock ratios (Rivalenti et al., 2004), also evidenced by cross-cutting relationships with former silicates (Fig. 3H, I).

In summary, we suggest that the *Group 3* and *Group 4* peridotites preserve the record of metasomatism caused by carbonatite-like melts that evolved towards CO_2-rich mafic silicate melts and finally alkali silicate melts, although at different melt/rock ratios. During an early stage of infiltration at high melt/rock ratios, the carbonatite melt produced a strong modal metasomatism resulting in the crystallization of apatite, carbonates and Cpx4 in the *Group 4* peridotites. Progressive percolation and reaction of this carbonatite agent with the peridotite wall-rock at decreasing melt volume gave rise to melts with stronger volatile and silicate component, resulting in CO_2-rich mafic silicate melt that produced cryptic and modal metasomatism at low and high melt/rock ratios in the *Group 3* and *Group 4* peridotites, recorded in Cpx2 and Cpx5, respectively. Continued evolution of the melt after reaction with the peridotite wall-rock ended in the volatile-rich alkaline silicate melt that produced the in Cpx3 and Cpx6 in the peridotites of the *Group 3* and *Group 4* respectively. These observations are consistent with previous interpretations by Rivalenti et al. (2004) who showed that the metasomatic fingerprints of Gobernador Gregores mantle peridotites are the result of a single metasomatic melt evolving from CO_2-rich nepheline-normative basalts towards silica saturation. Consistently, Hirose (1997), Dasgupta et al. (2006), and Mallik and Dasgupta (2013) experimentally demonstrated the evolution of carbonatite melts towards alkali basalts after percolation and reaction with a peridotite wall-rock whereas Zhang et al. (2017) showed the existence of natural CO_2-rich silicate melts that continuously evolved to alkali basalts in the South China Sea.

3.5.3. Nature of the interstitial glass

As noted above, the *Group 2* lherzolite samples from the Cerro Redondo contain glassy veinlets (< 60 µm) that infiltrate the interstices between pre-existing silicates. Electron microprobe analyses of these veinlets yield analytical totals < 88 % and relatively high contents of SiO_2 (46.7 – 51.7 wt.%), MgO (> 28 wt.%) and Al_2O_3 (7.8 – 13.5 wt.%) (Appendix 4), which may reflect the presence of zeolites. Interstitial glass showing the same microstructural relationships and similar composition have been reported in other peridotite xenoliths equilibrated in the spinel facies (Neumann and Wulff-Pedersen, 1997; Demény et al., 2004; Scambelluri et al., 2009; Miller et al., 2012; González-Jiménez et al., 2014). The latter authors interpreted these textures as a result of (1) breakdown of hydrous minerals due to decompression melting, (2) host basalt infiltration, or (3) metasomatic melts that infiltrated the peridotite prior to the xenolith entrapment and ascent to surface. The glassy veinlets observed in the *Group 2* peridotites could not be explained after breakdown or melting of hydrous phases because these are anhydrous lherzolites and the primitive mantle-normalised trace element patterns of the glassy veinlets are clearly distinct to those formed after the breakdown of hydrous minerals (Fig. 13). Disequilibrium reaction textures (Fig. 2C) in contact with clinopyroxene indicate that this late infiltrating silicate melt was very likely SiO_2 under-saturated. Moreover, the PUM-normalised trace element patterns of the glass analysed here is very distinct to that of the host basalt and more alike to Na-alkali melts (Fig. 13). This is consistent with the observation that the interstitial glass analysed here still preserves a primary mineral assemblage -incompletely reacted olivine and partly corroded pyroxenes together with armalcolite [(Mg, Fe^{2+})Ti_2O_5], ilmenite, feldspar and apatite- that resulted from the evolution of silica under-saturated Na-alkali melts during percolation of the peridotite matrix (Ionov et al., 1999; Grégoire et al., 2000).

3.5.4. HSE mobility in the subcontinental lithospheric mantle beneath southern Patagonia

3.5.4.1. Genesis of "unmodified" Type 1A and Type 2A base-metal sulfides

Type 1A BMS consist of Fe-rich mss higher in Os, Ir, Ru, and Rh and lower in Pt, Pd, and Au, reflected in the CI chondrite-normalised HSE patterns with a marked negative slope ($(PPGE/IPGE)_n$ = 0.24 – 0.68) (Fig. 11A). This signature, in addition to their occurrence as *included* minerals in olivine or residual Cpx1 indicates that these BMS are residues left after melt extraction of the upper mantle peridotite (Alard et al., 2000, 2002; Griffin et al., 2002; Aulbach et al., 2004; Bockrath et al., 2004) (Figs. 6, 11, 12; Appendix 4). Considering that partial melting estimations for these samples is of ~10%, preservation of these BMS is expected because in the mantle BMS are normally exhausted after 12 – 30% partial melting (Lorand and Grégoire, 2006), depending on sulfur abundance, pressure and oxygen fugacity (Mavrogenes and O'Neill, 1999; Jugo et al., 2010). This is also consistent with the experimental results that show the formation of IPGE-rich crystalline mss if the percentage of melting of the peridotite is below 10% (Fonseca et al., 2012). The preservation of residual *Type 1A* sulfides (and Cpx1) in the *Group 3* peridotites is also consistent with metasomatism at low melt/rock ratios that have not completely erased residual signatures of the rock-forming minerals. Figure 10 shows that this type of Fe-rich mss crystallized at ~1000 °C, consistent with the temperature estimated for the re-equilibrium of Cpx1 (Appendix 2).

In contrast, the *Type 2A* BMS are rich in Pt, Pd, and Au relative to Os, Ir, Ru, and Rh ($(PPGE/IPGE)_n$ = 2.1 – 17.1) (Fig. 11B; Appendix 4). They consist of isolated grains of Fe-rich mss or Fe-rich mss ± pentlandite ± cubanite included in or interstitial to olivine or secondary

clinopyroxene (*i.e.*, metasomatised Cpx2, and metasomatic Cpx4 and Cpx5). These BMS may represent blebs of immiscible Fe-Ni-Cu sulfide melt extracted by the incongruent melting of the BMS originally *included* in primary silicates and/or crystallized products by the CO_2-rich mafic silicate melt (Harvey et al., 2010). Later annealing or growth of cooling silicates could also mechanically include some of these *Type 2A* BMS originally located in an *interstitial* position, thus explaining why this type of BMS are sometimes included within olivine grains (Griffin et al., 2002).

3.5.4.2. Reworking of base-metal sulfides by CO_2-phosphate-rich metasomatic agents

The *Type 1B* BMS CI chondrite-normalised HSE pattern resembles that of the *Type 1A*, whereas that of the *Type 2B* resembles the *Type 2A*. However, the BMS *Type 1B* and *Type 2B* have a significantly higher semi-metal elements (As, Se, Sb, Te, Bi, Pb) contents (Appendix 5). This overall increase in the semi-metal content of the BMS corresponds with the higher content of Os, Pd, Au, and Re (Fig. 11C, D). *Type 1B* BMS are Fe-rich mss found interstitial to Cpx3 (metasomatised by volatile-rich alkaline silicate melt) in the *Group 3* peridotites that were affected by metasomatism at low melt/rock ratios. We suggest that these were originally *Type 1A* grains that were reworked in situ and therefore have their original composition modified by interaction with the infiltrating volatile-rich alkaline silicate melt. Such, reworking likely produced a remobilisation during melt-rock interaction, thus explaining why *Type 1B* BMS occur only in an *interstitial* position. This modification also defined a slightly different CI chondrite-normalised HSE pattern characterised by a marked increase in Pd and Re relative to Pt and Au respectively, as well as an increase in the chalcophile semi-metals (Figs 12C, Appendix 5). Crystallization temperatures of these *Type 1B* BMS are similar to those of the *Type 1A* (~1000 °C), also indirectly supporting a subsolidus modification of the *Type 1A* to form the *Type 1B* BMS.

In contrast, *Type 2B* BMS from *Group 3* and *Group 4* peridotites consist of Fe-rich mss ± pentlandite ± pyrrhotite that is commonly associated with metasomatic apatite, carbonate, or newly crystallized Cpx3 or Cpx6. Particularly, the *Type 2B* BMS have systematically suprachondritic $(Os/Ir)_n$ as well as a high $(Pd/Pt)_n$ ratio and Au content. The bleb-like textures and the contacts between the BMS and the apatite and carbonate (Fig. 9C, D) suggest that these BMS may represent molten globules of *Type 2A* BMS removed as partially molten mattes along with bubbles of CO_2- and phosphate-rich melts owing their preferential wetting properties relative to silicate melts (Mungall, 2015). Alternatively, they could be the solid product of immiscible droplets formed by sulfide-carbonate-phosphate once the *Type 2A* BMS were dissolved in the infiltrating melt enriched in sulfur, carbonate and phosphate (Hughes et al., 2017; O'Driscoll et al., 2018). In either case, the Cu-Ni fraction should have been removed during partial melting while the overall signature of HSE of the older *Type 2A* BMS was preserved. The latter highlights that CO_2- and P-rich melts are an effective way of transferring the absolute original HSE abundances of the mantle to the migrating magmas. Indeed, the suprachondritic $(Os/Ir)_n$ and high $(Pd/Pt)_n$ ratios exhibited by the *Type 1B* and *Type 2B* BMS are symptomatic of this volatile-rich metasomatism. In addition, contrary to metasomatic BMS assemblages in mantle peridotites and pyroxenites (Delpech et al., 2012, Saunders et al., 2016) that show elevated S/Se ratios, we found a positive correspondence between Pd and Au, and the total content of semi-metals (Fig. 12) in the *Type 1B* and *Type 2B* BMS. The latter suggests that semi-metals might play a significant role either in mobilizing or fixing the most incompatible HSE (Helmy and Fonseca, 2017), adding complexity to the yet underexplored behaviour of the semi-metal elements in the mantle.

3.5.4.3. Base-metal sulfide remobilisation by late infiltrating Na-rich alkaline melts

The *Type 3A* and *Type 3B* BMS consist of millerite and Ni-rich mss (± pentlandite ± chalcopyrite) that are exclusively found embedded in the interstitial silica under-saturated Na-alkali metasomatic glass of the *Group 2* peridotites. These BMS exhibit CI chondrite-normalised HSE patterns with a nearly flat shape (*Type 3A*), and variable negative Pt and slight positive Pd and Re anomalies (*Type 3B*). Near flat shapes of the CI chondrite-normalised HSE patterns in mantle Ni-Fe-Cu sulfides assemblages are typical of BMS derived from the direct crystallization of sulfide melts segregated by liquid immiscibility from silicate melts (Wang et al., 2009; Lorand et al., 2008, 2010, 2013; González-Jiménez et al., 2014). Metal-sulfide equilibrium in the Ni-Fe-S system (Wood, 1987) indicates that the high-temperature polymorph of millerite α-NiS is stable at temperatures between 1000-1200 °C and a low sulfur fugacity (log fS_2 from -0.5 to 1) relevant for the formation of Na-alkali metasomatic glass. The early crystallization of α-NiS directly from melts can explain the presence of millerite crystals associated or not with other BMS (Fig. 9H; Appendix 4). Moreover, Ni-rich mss ± pentlandite ± chalcopyrite assemblages may also be interpreted as the product of subsolidus re-equilibrium of mss crystallized from immiscible Ni-Fe-Cu rich sulfide melts. Experimental data on the Fe-Ni-Cu system (Craig and Kullerud, 1969; Fleet and Pan, 1994; Ballhaus et al., 2001) shows that mss is the first phase that crystallized from a Fe-Ni-Cu sulfide melt once it was separated by liquid immiscibility from a mafic silicate melt. At 1000 °C, this mss coexists with a Cu-rich melt that may incorporate variable amounts of Ni (Craig and Kullerud, 1969; Ballhaus et al., 2001). As the temperature cools down to T < 600 °C, the mss recrystallized to pentlandite giving rise to assemblages of pentlandite ± chalcopyrite (Appendix 4). We suggest that the *Type 3A* and *Type 3B* BMS are quenched droplets of immiscible sulfide liquid that were transported by the infiltrating silica under-saturated Na-rich alkaline melt just before the eruption of the xenolith. These droplets could be either exsolved upon degassing and quenched due to rapid undercooling of the ascending xenolith. Alternatively, they could represent droplets of immiscible sulfide melt already segregated in from the infiltrating alkaline magma because of melt-rock reactions, thus explaining the common association of these types of BMS with empty vesicles. These empty vesicles could represent former vapour bubbles to which BMS were attached and transported in the upward-migrating melt against their natural tendency to settle due to gravity forces (Bockrath et al., 2004; Holzheid, 2010; Mungall et al., 2015).

The *Type 3* BMS exhibit a slightly positive Pd anomaly as observed in the *Type 1B* and Type *2B* as well as Os/Ir, $(Pt/Pd)_n$ ratios versus S/Se, and Au versus S/Te that overlap that of the other BMS types (*i.e., Type 1A, Type 2A, Type 1B and 2B*; Fig. 12). The latter might indicate a possible heritage by removal of pre-existing BMS of the infiltrated peridotitic rock. The negative Pt anomaly could reflect the exsolution of Pt-rich nano-to-micron scale inclusions during subsolidus recrystallization of the BMS assemblage, despite the fact that these have not been observed (*e.g.*, Luguet et al., 2007; Kogiso et al., 2008; Lorand et al., 2008). The interpretation given above is consistent with the late nature of the late-infiltrating silica under-saturated Na-rich alkali melt and the variably higher $^{187}Re/^{188}Os$ values at lower $^{187}Os/^{188}Os$ ratios of the *Group 2* peridotites, which indicates the recent addition of Re to the peridotites (see the following section).

3.5.4.4. Impact of melt depletion and metasomatism on the bulk-rock HSE and Re-Os systematics

The *Group 1* peridotites exhibit CI chondrite-normalised HSE patterns characterised by an enrichment in Os, Ir, and Ru relative to Pt, Pd, and Re (Fig. 6A), which is consistent with the strongly depleted nature of these peridotites (Fig. 5A, B). The oldest $T_{RD} \approx T_{MA}$ age obtained in this group of peridotites is 1.45 Ga indicative that these peridotite xenoliths sampled volumes of ancient mantle beneath southern Patagonia, such as those previously identified in peridotite xenoliths from Tres Lagos (1.78 Ga; Schilling et al., 2017) and Pali Aike (2.5 Ga, Mundl et al., 2014). Given the

degree of partial melting underwent by these rocks and their low Al_2O_3, the T_{RD} age of 0.34 Ga obtained for the Tres Lagos sample in this group of peridotites could reflect a younger event of partial melting instead of later metasomatism, owing to the similarity of the T_{RD} and T_{MA} ages obtained for this group of samples (Rudnick and Walker, 2009).

The *Group 2* lherzolites display the highest total HSE abundances, whereas their CI chondrite-normalised HSE patterns are near flat, PUM-like with overall Pt, Pd, and Re contents greater than in the *Group 1*, *Group 3*, and *Group 4* peridotites (Fig. 6B). Such HSE enrichment can be explained as a result of the infiltration of the late silica undersaturated Na-rich alkali melt carrying *Type 3A* and *Type 3B* sulfides. A few of the *Type 3* BMS have high concentrations of Re (up to 12 $\mu g.g^{-1}$) (Fig. 11E, F), and thus may have also added enough ^{187}Re to produce the decoupling between the high $^{187}Re/^{188}Os$ and low $^{187}Os/^{188}Os$ that is observed for these group of samples (Fig. 7B), explaining the significant differences between the calculated T_{RD} and T_{MA} ages (Appendix 3). Therefore, the T_{RD} ages of the *Group 2* peridotites (1.13 – 1.23 Ga for Cerro Redondo samples; Fig. 7D; Appendix 3) very likely reflect a minimum age of melt depletion owing the possible ingrowth of ^{187}Os by decay of ^{187}Re from the *glass-related* BMS of the *Type 3A* and *Type 3B*, consistently with their estimated low degrees of partial melting (~ 10%).

The *slightly enriched peridotites* (*Group 3*) display convex upwards shaped CI chondrite-normalised HSE patterns with depletion in Pt and Re and $(Pd/Pt)_n$ between 1.01 and 1.4. These rocks have a large discrepancy between the T_{RD} and T_{MA} ages in the youngest population (offset = 0.1 – 0.9 Ga; Appendix 3) indicating the post-melting metasomatic addition of ^{187}Re, likely along with Pd, thus explaining the higher CI chondrite normalised values of Pd relative to the more compatible Pt. Such ^{187}Re addition could also explain the higher $^{187}Os/^{188}Os$ ratios obtained for the samples with low Al_2O_3 content (Fig. 7A). This is consistent with the preservation of a mixture of different generations of BMS including residual *Type 1A* and metasomatic/metasomatised *Type 1B*¸ *Type 2A, and Type 2B* related to the effect of metasomatism at low melt/rock ratios. Therefore, T_{RD} ages of the *Group 3* peridotites (0.13 – 0.9 Ga; Fig. 7D; Appendix 3) likely reflects the mixture of the different generations of BMS added at different stages (different timing) of metasomatic modification such as *Type 1B* and *Type 2B* (with greater Re content) BMS (Fig. 7B) and later little ^{187}Os ingrowth (Fig. 7C).

The *strongly enriched peridotites* (*Group 4*) from Gobernador Gregores display two types of CI chondrite-normalised HSE patterns. The subset of lherzolites GG-02, GG-07, and GG-14 that experienced mostly CO_2-rich mafic silicate melt metasomatism exhibits convex upward shaped patterns and strong depletion in Os, Pt, Pd and Re. In contrast, the most metasomatised lherzolites (samples GG-03, GG-01-A, GG-17) and wehrlite (sample GG-01-B) display CI chondrite-normalised HSE patterns characterised by stronger enrichment in the PPGE relative to the IPGE (Fig. 6D; Appendix 3). This subset of highly metasomatised rocks contain predominantly *Type 2A* and *Type 2B* BMS formed by volatile-rich alkaline silicate melts and sulfide-carbonate-phosphate immiscibility characterised by higher PPGE contents and Re for the *Type 2B* BMS, which explains the existence of meaningless T_{RD} (*e.g.*, -7.94 and -14.05 Ga) T_{MA} (*e.g.*, 38.02 Ga) values (Appendix 3). Thus, the similar HSE distribution obtained by the whole-rock and individual BMS grains attest the key role of the latter in controlling the budget of metals in these peridotites. Moreover, it highlights that the HSE distribution is the result of the extensive infiltration of volatile-rich alkaline silicate melts, which have interacted with a pre-existing depleted mantle.

3.5.4.5. Mobility of HSE and chalcophile semi-metals in the SCLM beneath southern Patagonia

Figure 14 summarises the sequence of events that have affected the HSE composition of the BMS and their peridotitic host rocks. Partial melting produced a depleted SCLM with: (1) almost no BMS grains with a high content of IPGE in the whole-rock (up to 18% partial melting; *Group 1*), or (2) a slightly depleted mantle with surviving residual *Type 1A* BMS included within silicates (up to 10% partial melting; *Group 2* and *Group 3*) (Stage 1; Fig. 14). In the *Group 3* peridotites, this was followed by metasomatism at low melt/rock ratios. Interaction of these rocks with CO_2-rich mafic silicate melts led to the formation of metasomatic *Type 2A* BMS along with newly formed clinopyroxene (Cpx2) (Stage 2; Fig. 14). The later evolution of the melt towards volatile-rich alkali silicate melts produced a secondary modification of early BMS grains (*Type 1A* and *Type 2A*), giving rise to the Os, Pd, Re and chalcophile semi-metals rich *Type 1B* and *Type 2B* BMS (Stage 3; Fig. 14). Thus, the resulting whole-rock CI chondrite-normalised HSE pattern of the *Group 3* peridotites reflects a mixture of the different BMS-forming processes described above. In the *Group 4* peridotites, the melt depletion event was followed by metasomatism operating at high melt/rock ratios. After such high degree of metasomatic modification by carbonatite to CO_2-rich mafic silicate melts, the residual signatures of the *Type 1A* BMS were erased and the metasomatic *Type 2A* BMS were formed along with newly formed clinopyroxene (Cpx4 and Cpx5) (Stage 2; Fig. 14). Evolution of the melt towards volatile-rich alkali silicate melts and interaction with the peridotite produced a secondary modification of earlier generations of BMS (*Type 2A*) forming the *Type 2B* BMS enriched in Os, Pd, Re and chalcophile semi-metals (Stage 3; Fig. 14). The metasomatic imprint recorded in *Group 4* peridotites is particularly evident in the metasomatised lherzolites and wehrlite (samples GG-03, GG-01-A, GG-01-B, and GG-17), which equilibrated extensively with the percolating melt. This resulted in PPGE rich CI chondrite-normalised HSE patterns (resemblance to the melt) and highly radiogenic $^{187}Os/^{188}Os$ compositions. Finally, the *Group 2* lherzolites were percolated by silica under-saturated Na-alkali melts carrying immiscible Ni-Cu rich sulfide liquids of the *Type 3A* and *Type 3B* which resulted in a strong refertilisation at the whole-rock scale as well as an addition of ^{187}Re which resulted in a high HSE content and large difference between the T_{RD} and T_{MA} values.

3.6. CONCLUSIONS AND IMPLICATIOS FOR METALLOGENY

The peridotite xenoliths from southern Patagonia record a multistage history of depletion and subsequent metasomatism by carbonatite melts that evolved towards volatile and silica-rich compositions after reaction with the peridotite wall rock at variable melt/rock ratios. The volatile-rich alkaline silicate melts are agents that potentially may cause precipitation of BMS enriched in Os, Pd, Au, and Re, acting as an effective agent to remobilise and transport these HSE in the mantle. On the other hand, the infiltration of silica under-saturated Na-alkali melts (now the interstitial glass) carrying HSE-rich Ni-Cu immiscible sulfide droplets through the *Group 2* lherzolites confirm previous experimental results (Ballhaus et al., 2001; Bockrath et al., 2004), highlighting the ability of silicate melts to transport immiscible Ni-Cu rich sulfide melts enriched in HSE. This observation suggests that even at reducing conditions, the transport of BMS (and HSE + Ni + Cu) melts entrained in silicate melts can account as an important process in either (1) the refertilization in HSE of the SCLM, or (2) the scavenging of BMS from the SCLM by ascending melts as for Ni-Cu + PGE magmatic ore deposits (Griffin et al., 2013). Interestingly, the total whole-rock HSE contents of the *Group 2* peridotites is the highest of all the studied samples indicating that in this case, the transport of immiscible sulfide melts promoted the HSE enrichment of a selected domain of the SCLM. The results of this study indicate that although further studies and experimental data are needed, CO_2 and other volatile-rich melts may be important in the redistribution of HSE in the

SCLM and may play an unforeseen role in metallogeny. In addition, we suggest that Na-rich alkaline silicate melts can capture sulfide melts from the SCLM, transport them as entrained droplets and eventually dissolve them into the silicate melt if favorable conditions (*i.e.*, higher sulfur solubility) are reached, resulting in an effective mechanism to produce metal enrichment of mantle-derived magmas.

3.7. BIBLIOGRAPHY

Akizawa, N., Miyake, A., Ishikawa, A., Tamura, A., Terada, Y., Uesigi, K., Takeuchi, A., Arai, S., Tanaka, C., Igami, Y., Suzuki, K., Kogiso, T., 2017. Metasomatic PGE mobilization by carbonatitic melt in the mantle: Evidence from sub-μm-scale sulfide-carbonaceous glass inclusions in Tahitian harzburgite xenolith. Chem. Geol. 475, 87-104.

Alard, O., Griffin, W.L., Lorand, J.-P., Jackson, S.E., O'Reilly, S.Y., 2000. Non-chondritic distribution of the highly siderophile elements in mantle sulfides. Nature 407, 891-894.

Alard, O., Griffin, W.L., Pearson, N.J., O'Reilly, S.Y., 2002. New insights into the Re-Os systematics of sub-continental lithospheric mantle from in situ analysis of sulfides. Earth Planet. Sci. Lett. 203, 651-663.

Alard, O., Luguet, A., Pearson, N.J., Griffin, W.L., Lorand, J-P., Gannoun, A., Burton, K.W., O'Reilly, S.Y., 2005. In situ Os isotopes in abyssal peridotites bridge the isotopic gap between MORBs and their source mantle. Nature 436, 1005-1008.

Alard, O., Lorand, J.-P., Resiberg, L., Bodinier, J.-L., Dautria, J.-M., O'Reilly, S.Y., 2011. Volatile-rich metasomatism in Montferrier xenoliths (Southern France): implications for the abundances of chalcophile and siderophile elements in the subcontinental mantle. J. Petrol. 52, 2009–2045.

Aliani, P., Ntaflos, T., Bjerg, E., 2009. Origin of melt pockets in mantle xenoliths from southern Patagonia, Argentina. J. South Amer. Earth Sci. 28, 419–428.

Aulbach, S., Griffin, W.L., O'Reilly, S.Y., McCandless, T.E., 2004. Genesis and evolution of the lithospheric mantle beneath the Buffalo Head Terrane, Alberta (Canada). Lithos 77, 413-451.

Baker, M.D., Stolper, E.M., 1994. Determining the composition of high pressure melts using diamond aggregates. Geochim. Cosmochim. Acta 58, 2811-2827.

Ballhaus, C., Tredoux, M., Späth, A., 2001. Phase relations in the Fe-Ni-Cu-PGE-S system at magmatic temperature and application to massive sulfide ores of the Sudbury Igneous Complex. J. Petrol. 42 1991–1926.

Becker, H., Horan, M.F., Walker, R.J., Gao, S., Lorand, J.-P., Rudnick, R.L., 2006. Highly siderophile element compositions of the earth's primitive mantle. Geochim. Cosmochim. Acta 70, 4528-4550.

Begg, G.C., Hronsky, J.M.A., Arndt, N.T., Griffin, W.L., O'Reilly, S.Y., Hayward, N., 2010. Lithospheric, cratonic and geodynamic setting of Ni-Cu-PGE sulfide deposits. Econ. Geol. 105:1057–1070.

Bockrath, C., Ballhaus, C., Holzheid, A., 2004. Fractionation of the platinum-group elements during mantle melting. Science 305, 1951–1953.

Coltorti, M., Bonadiman, C., Hinton, R.W., Siena, F., Upton, B.G.J., 1999. Carbonatite metasomatism of the oceanic upper mantle: evidence from clinopyroxenes and glasses in ultramafic xenoliths of Grande Comore, Indian Ocean. J. Petrol. 40, 303-320.

Craig, J.R., Kullerud, G., 1969. Phase relations in the Cu-Fe-Ni-S system and their application to magmatic ore deposits. Econ. Geol., monograph 4, 344-358.

D'Orazio, M., Agostini, S., Innocenti, F., Haller, M.J., Manetti, P., Mazzarini, F., 2001. Slab window-related magmatism from southernmost South america: the late Miocene volcanics from the Estancia Glen cross area (528S, Argentina–Chile). Lithos 57, 67–89.

Dasgupta, R., Hirschmann, M.M., Stalker, K., 2006. Immiscible transition from carbonate-rich to silicate-rich melts in the 3 GPa melting interval of eclogite + CO_2 and genesis of silica-undersaturated ocean island lavas. J. Petrol. 47, 647-671.

Delpech, G., Lorand, J.-P., Grégoire, M., Cottin, J.-Y., O'Reilly, S.Y., 2012. In-situ geochemistry of sulfides in highly metasomatised mantle xenoliths from Kerguelen, southern India Ocean. Lithos 154, 296-314.

Demény, A., Wennemann, T.W., Hegner, E., Nagy, G., Milton, J.A., Embey-Isztin, A., Homonnay, Z., Dobosi, G., 2004. Trace element and C-O-Sr-Nd isotope evidence for subduction-related carbonate-silicate melts in mantle xenoliths (Pannonian Basin, Hungary). Lithos 75, 89-113.

Fischer-Gödde, M., Becker, H., Wombacher, F., 2010. Rhodium, gold and other highly siderophile element abundances in chondritic meteorites. Geochim. Cosmochim. Acta 74, 356-379.

Fleet, M.E., Pan, Y., 1994. Fractional crystallization of anhydrous sulfide liquid in the system Fe-Ni-Cu-S, with application to magmatic sulfide deposits. Geochim. Cosmochim. Acta 58, 3369-3377.

Fonseca, R.O.C., Laurenz, V., Mallmann, G., Luguet, A., Höne, N., Jochum, V., 2012. New constraints on the génesis and long-term stability of Os-rich alloys in the Earth's mantle. Geochim. Cosmochim. Acta 87, 227-242.

Forsythe, R.D., Nelson, E.P., Carr, M.J., Kaeding, M.E., Herve', M., Mpodozis, C., Soffia, J.M., Harambour, S., 1986. Pliocene near-trench magmatism in southern Chile: a possible manifestation of ridge collision. Geology 14, 23–27.

González-Jiménez, J.M., Villaseca, C., Griffin, W.L., O'Reilly S.Y., Belousova, E., Ancochea, E., Pearson, N.J., 2014. Significance of ancient sulfides PGE and Re-Os signatures in the mantle beneath Calatrava, Central Spain. Contrib. Mineral. Petrol. 168, 1047.

Gorring, M.L., Kay, S.M., Zeitler, P.K., Ramos, V.A., Rubiolo, D., Fernandez, M., Panza, J.L., 1997. Neogene Patagonian plateau lavas: Continental magmas associated with ridge collision at the Chile Triple Junction. Tectonics 16, 1-17.

Gorring, M.L., Kay, S.M., 2000. Carbonatite metasomatized peridotite xenoliths from southern Patagonia: implications for lithospheric processes and Neogene plateau magmatism. Contrib. Mineral. Petrol. 140, 55-72.

Gorring, M.L., Kay, S.M., 2001. Mantle processes and sources of Neogene slab window magmas from southern Patagonia, Argentina. J. Petrol. 42, 1067–1094.

Grégoire, M., Lorand, J-P., Cottin, J.Y., Giret, A., Mattielli, N., Weis, D., 1997. Petrology of the Kerguelen mantle xenoliths: Evidence of a refractory oceanic mantle percolated by basaltic melts beneath the Kerguelen Archipielago. Eur. J. Mineral. 9, 1085-1100.

Grégoire, M., Lorand, J-P., O'Reilly, S.Y., Cottin, J.Y., 2000. Armalcolite-bearing, Ti-rich metasomatic assemblages in harzburgitic xenoliths from the Kerguelen Islands: Implications for the oceanic mantle budget of high-field strength elements. Geochim. Cosmochim. Acta 64, 673-694.

Grégoire, M., Langlade, J.A., Delpech, G., Dantas, C., Ceuleneer, G., 2009. Nature and evolution of the lithospheric mantle beneath the passive margin of East Oman: Evidence from mantle xenoliths sampled by Cenozoic alkaline lavas. Lithos 112, 203-2016.

Griffin, W.L., Spetius, Z.V., Pearson, N.J., O'Reilly, S.Y., 2002. In situ Re-Os analysis of sulfide inclusions in kimberlitic olivine: new constraints on depletion events in the Siberian lithospheric mantle. Geochem. Geophys. Geosyst. 3, 11.

Griffin, W.L., Graham, S., O'Reilly, S.Y., Pearson, N.J., 2004. Lithospheric evolution beneath the Kaapvaal Craton: Re-Os systematics of sulfides in mantle-derived peridotites. Chem. Geol. 208, 89-118.

Griffin, W.L., Begg, G.C., O'Reilly, S.Y., 2013. Continental-root control on the genesis of magmatic ore deposits. Nature Geosci. 6, 905-910.

Harvey, J., Gannoun, A., Burton, K.W., Rogers, N.W., Schiano, P., Alard, O., 2010. Selenium, tellurium, arsenic and antinomy contents of primary mantle sulfides. Can. Min. 40, 637-650.

Harvey, J., Gannoun, A., Burton, K.W., Schiano, P., Rogers, N.W., Alard, O., 2010. Unravelling the effects of melt depletion and secondary infiltration on mantle Re-Os isotopes beneath the French Massif Central. Geochim. Cosmochim. Acta 74, 293-320.

Harvey, J., Yoshikawa, M., Hammond, S.J., Burton, K.W., 2012. Deciphering the trace element characteristicis in Kilbourne Hole peridotite xenoliths: melt-rock interaction and metasomatism beneath the Rio Grande rift, SW USA. J. Petrol. 53, 1709-1742.

Harvey, J., König, S., Luguet, A., 2015. The effects of melt depletion and metasomatism on highly siderophile and strongly chalchophile elements: S-Se-Te-Re-PGE systematics of peridotite xenoliths from Kilbourne Hole, New Mexico. Geochim. Cosmochim. Acta 166, 210-233.

Harvey, J., Warren, J.M., Shirey, S.B., 2016. Mantle sulfides and their role in Re-Os and Pb isotope geochronology. Rev. Mineral. Geochem. 81, 579-649.

Hattori, K., Arai, S., Clarke, D.B., 2002. Selenium, tellurium, arsenic and antimony contents of primary mantle sulfides. Can. Min. 40, 637-650.

Helmy, H.M., Fonseca, R.O.C., 2017. The behaviour of Pt, Pd, Cu and Ni in the Se-sulfide system between 1050 and 700°C and the role of Se in platinum-group elements fractionation in sulfide melts. Geochim. Cosmochim. Acta 216, 141-152.

Hirose, K., 1997. Partial melt compositions of carbonated peridotites at 3 GPa and role of CO_2 in alkali-basalt magma generation. Geophys. Res. Lett. 24, 2837-2840.

Holzheid, A., 2010. Separation of sulfide melt droplets in sulfur saturated silicate liquids. Chem. Geol. 274, 127-135

Horan, M.F., Walker, R.J., Morgan, J.W., Grossman, J.N., Rubin, A.E., 2003. Highly siderophile elements in chondrites. Chem. Geol. 196, 27-42.

Hronsky, J.M.A., Groves, D.I., Loucks, R.R., Begg, G.C., 2012. A unified model for gold mineralization in accretionary orogens and implications for regional-scale exploration targeting methods. Miner. Deposita 47, 339-358.

Hughes, H.S.R., McDonald, I., Loocke, M., Butler, I.B., Upton, B.G.J., Faithfull, J.W., 2017. Paradoxical co-existing base metal sulfides in the mantle: the multi-event record preserved in Loch Roag peridotite xenoliths, North Atlantic Craton. Lithos 276, 103-121.

Ionov, D.A., Grégoire, M., Prikhod'ko, V.S., 1999. Feldspar – Ti-oxide metasomatism in off-cratonic continental and oceanic upper mantle. Earth Planet. Sci. Lett. 165, 37-44.

Ionov, D.A., Bodinier, J-L., Mukasa, S.B., Zanetti, A., 2002. Mechanisms and sources of mantle metasomatism: major and trace element compositions of peridotite xenoliths from Spitsbergen in the context of numerical modelling. J. Petrol. 43, 2219-2259.

Jalowitzki, T., Gervasoni, F., Conceiçao, R.V., Orihasgi, Y., Bertotto, G.W., Sumino, H., Schilling, M., Nagao, K., Morata, D., Sylvester, P., 2017. Slab-derived components in the subcontinental lithospheric mantle beneath Chilean Patagonia: Geochemistry and Sr-Nd-Pb isotopes of mantle xenoliths and host basalt. Lithos 292-293, 179-197.

Jugo, P.J., Wilke, M., Botcharnikov, R.E., 2010. Sulfur K-edge XANES analysis of natural and synthetic basaltic glasses: implications for S speciation and S content as function of oxygen fugacity. Geochim. Cosmochim. Acta 74, 5926-5938.

Kogiso, T., Suzuki, T., Suzuki, Y., Shinotsuka, K., Uesugi, K., Takeuchi, A., Suzuki, Y., 2008. Detecting micrometer-scale platinum-group minerals in mantle peridotite with microbeam synchrotron radiation X-ray fluorescence analysis. Geochem. Geophys. Geosyst. 9.

Kullerud, G., Yund, R.A., Moh, G., 1969. Phase relations in the Cu-Fe-S and Cu-Ni-S systems. In: Wilson, H.D.B. (Ed.), Magmatic ore deposits. Econ. Geol. Monogr. 4, 323-343.

Laurora, A., Mazzucchelli, M., Rivalenti, G., Vannucci, R., Zanetti, A., Barbieri, M.A., Cingolani, C., 2001. Metasomatism and melting in carbonated peridotite xenoliths from the mantle wedge: The Gobernador Gregores case (Southern Patagonia). J. Petrol. 42, 69-87.

Lorand, J.-P., Delpech, G., Grégoire, M., Moine, B., O'Reilly, S.Y., Cottin, J.Y., 2004. Platinum-group elements and the multistage metasomatic history of Kerguelen lithospheric mantle (South Indian Ocean). Chem. Geol. 208, 195–215.

Lorand, J.-P., Grégoire, M., 2006. Petrogenesis of base metal sulfide assemblages of some peridotites from the Kaapvaal craton (South Africa). Contrib. Mineral. Petrol. 151, 521-538.

Lorand, J-P., Luguet, A., Alard, O., 2008. Platinum-group elements: a new set of key tracers for the Earth's interior. Elements 4, 247-252.

Lorand, J.-P., Alard, O., Luguet, A., 2010. Platinum-group element micronuggets and refertilization process in the Lherz peridotite. Earth Planet. Sci. Lett. 289, 298–310.

Lorand, J.-P., Luguet, A., Alard, O., 2013. Platinum-group element systematics and petrogenetic processing of the continental upper mantle: A review. Lithos 164-167, 2-21.

Luguet, A., Lorand, J.-P., Seyler, M., 2003. Sulfide petrology and highly siderophile element geochemistry of abyssal peridotites: a coupled study in samples from the Kane Fracture Zone (45°W 23°20 N, MARK Area, Atlantic Ocean). Geochim. Cosmochim. Acta 67, 1553–1570.

Luguet, A., Shirey, S.B., Lorand, J.-P., Horan, M.F., Carlson, R.W., 2007. Residual platinum-group minerals from highly depleted harzburgites of the Lherz massif (France) and their role in HSE fractionation of the mantle. Geochim. Cosmochim. Acta 71, 3082-3097.

Luguet, A., Behrens, M., Pearson, D.G., König, S., Herwartz, D., 2015. Significance of the whole rock Re-Os ages in cryptically and modally metasomatised cratonic peridotites: Constraints from HSE-Se-Te systematics. Geochim. Cosmochim. Acta 164, 441-463.

Luguet, A., Reisberg, L., 2016. Highly siderophile element and 187Os signatures in non-cratonic basalt-hosted peridotite xenoliths: unravelling the origin and evolution of the post-Archean lithospheric mantle. Rev. Mineral. Geochem. 81, 305-367.

Mallik, A., Dasgupta, R., 2013. Reactive infiltration of MORB-eclogite-derived carbonated silicate melt into fertile peridotite at 3 GPa and genesis of alkali magmas. J. Petrol. 54, 2267-2300.

Marchesi, C., Konc, Z., Garrido, C.J., Bosch, D., Hidas, K., Varas-Reus, M.I., Acosta-Vigil, A., 2017. Multi-stage evolution of the lithospheric mantle beneath the westernmost Mediterranean: Geochemical constraints from peridotite xenoliths in the eastern Betic Cordillera (SE Spain). Lithos, 276, 75-89.

Mavrogenes, J., O'Neill, H.S.C., 1999. The relative effects of pressure, temperature and oxygen fugacity on the solubility of sulfide in mafic magmas. Geochim. Cosmochim. Acta 63, 1173-1180.

McDonough, W.F., Sun, S.-s., 1995. The composition of the Earth. Chem. Geol. 120, 223-253.

McInnes, B.I.A., McBridge, J.S., Evans, N.J., Lambert, D.D., Andrew, A.S., 1999. Osmium isotope constrains on ore metal recycling in subduction zones. Science 286, 512-516.

Miller, C., Zanetti., A., Thöni, M., Konzett, J., Klötzli, U., 2012. Mafic and silicat-rich glasses in mantle xenoliths from Wau-en-Namus, Libya: textural and geochemical evidence for peridotite-melt-rock reactions. Lithos 128, 11-26.

Moine, B., Grégoire, M., O'Reilly, S.Y., Delpech, G., Sheppard, S.M.F., Lorand, J.-P., Renac, C., Giret, A., Cottin, J.Y., 2004. Carbonatite melt in oceanic upper mantle beneath the Kerguelen Archipelago. Lithos 75, 239–252.

Mundl, A., Ntaflos, T., Ackerman, L., Bizimis, M., Bjerg, E.A., Hauzenberger, C.A., 2015. Mesoproterozoic and Paleoproterozoic subcontinental lithospheric mantle domains beneath southern Patagonia: isotopic evidence for its connection to Africa and Antarctica. Geology 43, 39–42.

Mungall, J.E., 2015. Physical controls of nucleation, growth and migration of vapor bubbles in partially molten cumulates. In: Charlier, B., Namur, O., Latypov, R., Tegner, C., (eds) Layered Intrusions. Springer Geology, Springer, Dordrecht.

Neumann, E.R., Wulff-Pedersen, E., 1997. The origin of highly silicic glass in mantle xenoliths from the Canary Islands. Journal of PetrologyJ. Petrol. 38, 1513-1539.

Niu, Y., 1997. Mantle melting and melt extraction processes beneath ocean ridges: evidence from abyssal peridotites. J. Petrol. 38, 1047-1074.

Ntaflos, T., Bjerg, E.A., Labudia, C.H., Kurat, G., 2007. Depleted lithosphere from the mantle wedge beneath Tres Lagos, southern Patagonia, Argentina. Lithos 94, 46-65.

O'Driscoll, B., González-Jiménez, J.M., 2016. Petrogenesis of the platinum-group minerals. Rev. Mineral. Geochem. 81, 489-578.

O'Driscoll, B., Walker, R.J., Clay, P.L., Day, J.M.D., Ash, R.D., Daly, J.S., 2018. Length-scales of chemical and isotopic heterogeneity in the mantle section of the Shetland Ophiolite Complex, Scotland. Earth Planet. Sci. Lett. 488, 144-154.

Pankhurst, R. J., Riley, T. R., Fanning, C. M., Kelley, S. P., 2000. Episodic silicic volcanism in Patagonia and the Antarctic Peninsula: chronology of magmatism associated with the break-up of Gondwana. J. Petrol. 41, 605-625.

Pearson, D.G., Canil, D., Shirey, S.B., 2004. Mantle samples included in volcanic rocks: xenoliths and diamonds. In: Carlson, R.W. (Ed.) Treatise of Geochemistry, Vol 2. Amsterdam: Elsevier, 171-275.

Powell, W., O'Reilly, S.Y., 2007. Metasomatism and sulfide mobility in the lithospheric mantle beneath eastern Australia: implications for mantle Re-Os chronology. Lithos 94, 132-147.

Ramos, V.A., Aleman, A., 2000. Tectonic evolution of the Andes. *In*: Tectonic evolution of South America. International Geological Congress, Rio de Janerio, pp. 635-685.

Rivalenti, G., Zanetti, A., Mazzucchelli, M., Vannucci, R., Cingolani, C., 2004. Equivocal carbonatite markers in the mantle xneoliths of the Patagonia backarc: the Gobernador Gregores case (Santa Cruz Province, Argentina). Contrib. Mineral. Petrol. 147, 647-670.

Robinson, J.A.C., Wood, B.J., Blundy, J.D., 1998. The beginning of melting of fertile and depleted peridotite at 1.5 Gpa. Earth Planet. Sci. Lett. 155, 97-111.

Rudnick, R.L., Walker, R.J., 2009. Interpreting ages from Re-Os isotopes in peridotites. Lithos 112S, 1083-1095.

Saunders, J.E., Pearson, N.J., O'Reilly, S.Y., Griffin, W.L., 2015. Sulfide metasomatism and the mobility of gold in the lithospheric mantle. Chem. Geol. 410, 149-161.

Saunders, J.E., Pearson, N.J., O'Reilly, S.Y., Griffin, W.L., 2016. Gold in the mantle: The role of pyroxenites. Lithos 244, 205-217

Scamberulli, M., Vannucci, R., De Stefano, A., Preite-Martinez, M., Rivalenti, G., 2009. CO_2 fluid and silicate glass as monitors of alkali basalt/peridotite interaction in the mantle wedge beneath Gobernador Gregores, Southern Patagonia. Lithos 107, 121-133.

Schilling, M.E., Carlson, R.W., Conceição, R.V., Dantas, C., Bertotto, G.W., Koester, E., 2008. Re-Os isotope constraints on subcontinental lithospheric mantle evolution of southern South America. Earth Planet. Sci. Lett. 268, 89-101.

Schilling, M.E., Carlson, R.W., Tassara, A., Conceição, R.V., Bertotto, G.W., Vásquez, M., Muñoz, D., Jalowitzki, T., Gervasoni, F., Morata, D., 2017. The origin of Patagonia revealed by Re-Os systematics of mantle xenoliths. Precambrian Research 294, 15-32.

Stern, C.R., Frey, F.A., Futa, K., Zartman, R.E., Peng, Z., Kyser, T.K., 1990. Trace-element and Sr, Nd, Pb, and O isotopic composition of Pliocene and Quaternary alkali basalts of the Patagonia Plateau lavas of southernmost South America. Contrib. Mineral. Petrol. 104, 294–308.

Tassara, S., González-Jiménez, J.M., Reich, M., Schilling, M.E., Morata, D., Begg, G., Saunders, E., Griffin, W.L., O'Reilly, S.Y., Grégoire, M., Barra, F., Corgne, A., 2017. Plume-subduction interaction forms large auriferous provinces. Nature Comms. 8:843.

Teitchou, M.I., Grégoire, M., Temdjim, T., Ghogomu, R.T., Ngwa, C., Aka, F.T., 2011. Mineralogical and geochemical fingerprints of mantle metasomatism beneath Nyos volcano (Cameroon volcanic line). Geological Geol. Society Soc. of America. Special paper 478, 193-210.

Van Acken, D., Luguet, A., Pearson, D.G., Nowell, G.M., Fonseca, R.O.C., Nagel. T.J., Schulz, T., 2017. Mesoarchean melting and Neoarchean to Paleoproterozoic metasomatism during the formation of the cratonic mantle keel beneath West Greenland. Geochim. Cosmochim. Acta 203, 37-53.

Walker, R.J., Prichard, H.M., Ishiwatari, A., Pimentel, M., 2002. The osmium isotopic composition of convecting upper mantle deduced from ophiolites chromites. Geochim. Cosmochim. Acta 66, 329-345.

Wang, J., Hattori, K.H., Kilian, R., Stern, C.R., 2007. Metasomatism of sub-arc mantle peridotites below southernmost South America: Reduction of fO2 by slab-melt. Contrib. Mineral. Petrol. 153, 607–624.

Wang, J., Hattori, K.H., Li, J., Stern, C.R., 2008. Oxidation state of Paleozoic subcontinental lithospheric mantle below the Pali Aike volcanic field in southernmost Patagonia. Lithos 105, 98–110.

Wang, K.L., O'Reilly, S.Y., Griffin, W.L., Pearson, N.J., Zhang, M., 2009. Sulfides in mantle peridotites from Penghu Island, Taiwan: melt percolation, PGE fractionation, and lithospheric evolution of South China bloc. Geochim. Cosmochim. Acta 73, 4531-4557.

Widom, E., Kepezhinkas, P., Defant, M., 2003. The nature of metasomatism in the sub-arc mantle wedge: evidence from Re-Os isotopes in Kamchatka peridotite xenoliths. Chem. Geol. 196, 283-306.

Wilshire, H.G., Shervais, J.W., 1975. Al-augite and Cr-diopside ultramafic xenoliths in basaltic rocks from western United States. Physics and Chemistry of the Earth 9, 257-272.

Wood, S.A., 1987. Thermodynamic calculations of the volatility of the platinum group elements (PGE): the PGE content of fluids at magmatic temperatures. Geochim. Cosmochim. Acta 51, 3041-3050.

Zhang, G-L., Chen, L-H., Jackson, M.G., Hofmann, A., 2017. Evolution of carbonated melt to alkali basalt in the South China Sea. Nature Geosci. 10, 229-236.

3.8. FIGURES

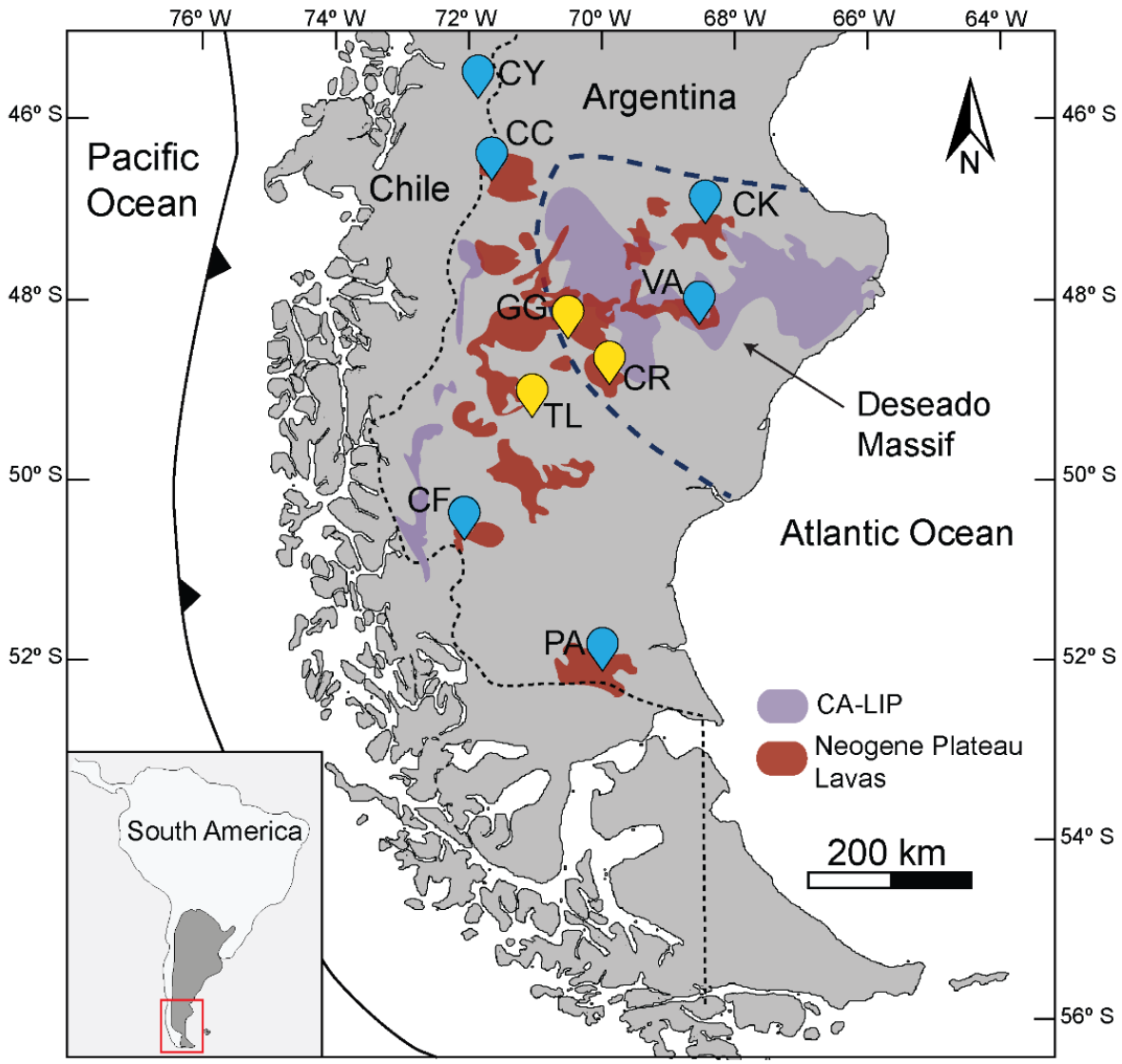

Figure 1. Simplified sketch map of southern South America showing the Neogene Plateau basalts containing mantle xenoliths. The localities studied in this work include Tres Lagos (TL), Gobernador Gregores (GG), and Cerro Redondo (CR). Keys for other volcanic centres containing mantle xenoliths are CY: Coyhaique; CC: Chile Chico; CK: Cerro Clark; VA: Volcán Auvernia; CF: Cerro del Fraile; PA: Pali Aike. CA-LIP: Chon Aike large igneous province.

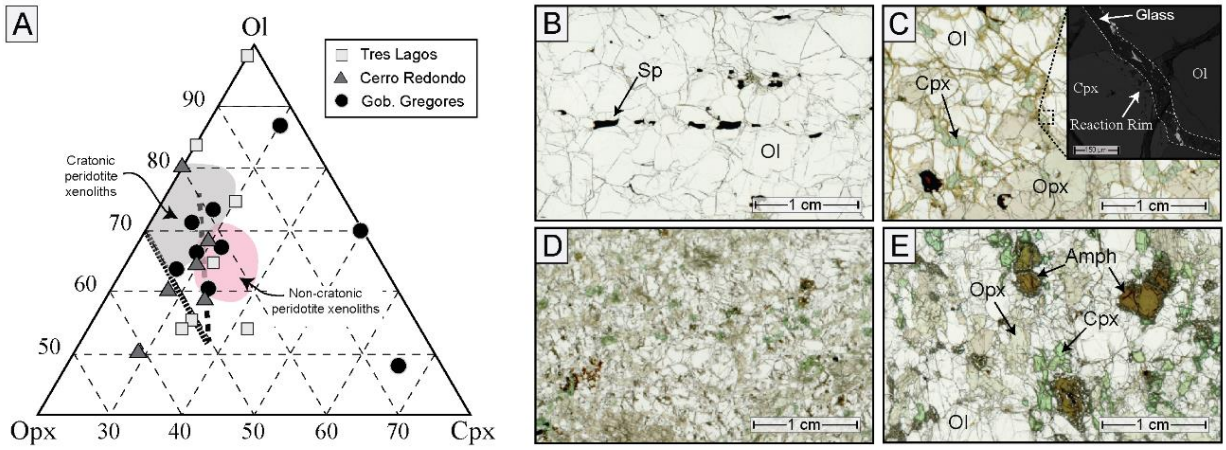

Figure 2. A- Mineral modal abundances estimated for the investigated peridotite xenoliths modified after Harvey et al. (2012). Dashed lines represent the effects upon modal mineralogy of experimental 20% batch melting (large dashed lines) of Baker and Stolper (1994) and the repeated extraction of small batch melts (small dashed lines) of Robinson et al. (1998). Fields for cratonic and non-cratonic peridotite xenoliths are derived from Pearson et al. (2004). **B** to **E-** Thin section scans of representative textures of the investigated mantle xenoliths. **B-** Granular dunite from Tres Lagos showing an alignment of spinel grains. **C-** porphyroblastic lherzolite from Cerro Redondo with abundant interstitial silicate glass. Inset: Backscattered electron image of infiltrating glassy vein cross-cutting the main mineral assemblage and showing reaction zones in contact with clinopyroxene. White dashed lines delimit the infiltrating glassy vein containing BMS, apatites and Ti-oxides. **D-** microgranular lherzolite from Gobernador Gregores. **E-** Amphibole bearing granular lherzolite from Gobernador Gregores.

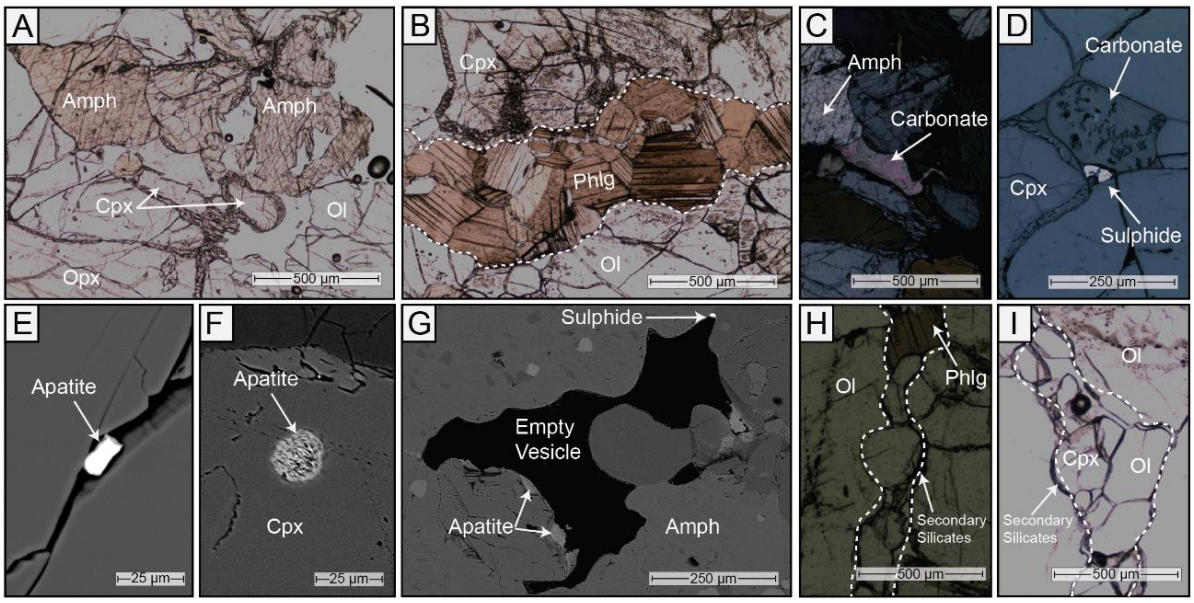

Figure 3. Optical and scanning electron microphotographs of metasomatic minerals recognised in the Patagonian mantle xenoliths. **A-** Plane polarised light image of unreacted amphibole crystals (*Group 4*; Gobernador Gregores). **B-** Plane polarised light image of a phlogopite vein cross-cutting the primary silicate assemblage (*Group 4*; Gobernador Gregores). **C-** Cross polarised image of amphibole and a carbonate melt pocket (*Group 4*; Gobernador Gregores). **D-** Reflected light image of carbonate melt pocket coexisting with a BMS bleb (*Group 3*; Tres Lagos). **E** to **G-** Apatite crystals located interstitial to the silicate matrix (*Group 3*; Tres Lagos) **(E)**, included within clinopyroxene (*Group 3*; Gobernador Gregores) **(F)**, and in contact with an empty vesicle close to a metasomatic amphibole (*Group 4*; Gobernador Gregores).

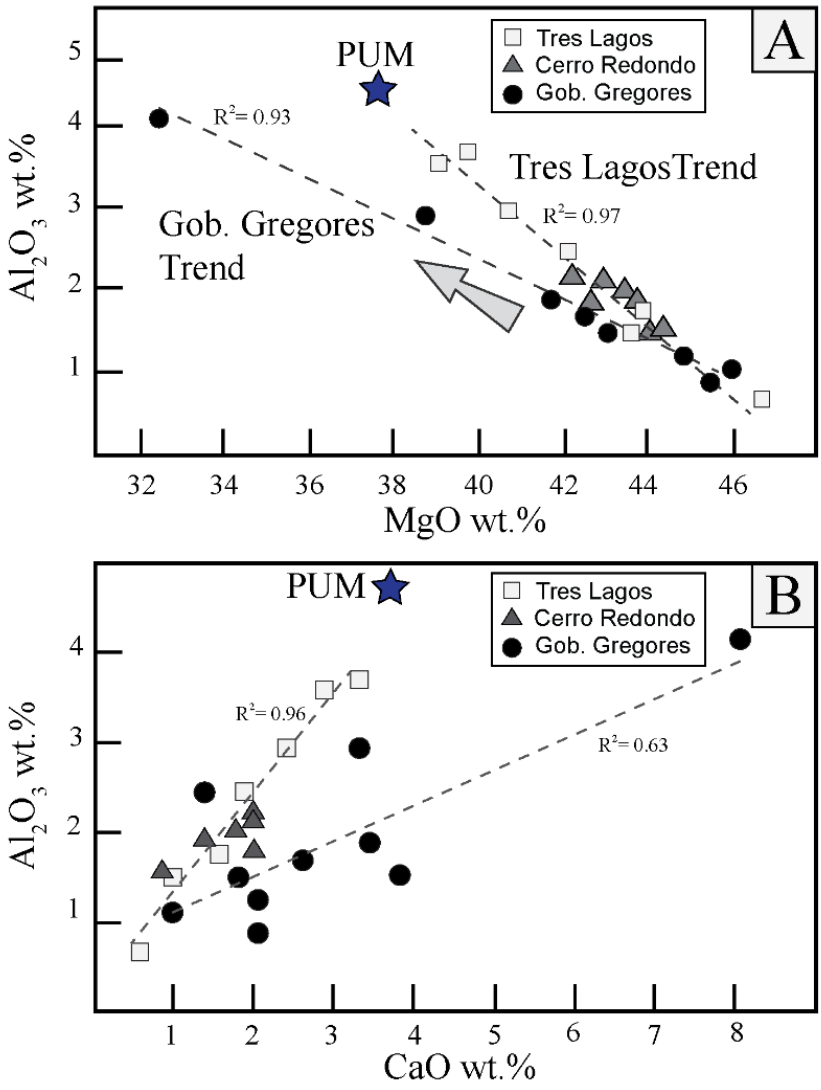

Figure 4. Major element variations for southern Patagonian peridotite xenoliths. Dashed lines correspond to the inferred trends for the variable transformation occurred between the refractory dunite/harzburgites and variably depleted/enriched lherzolites and lherzolites. PUM: Primitive upper mantle (McDonough and Sun, 1995).

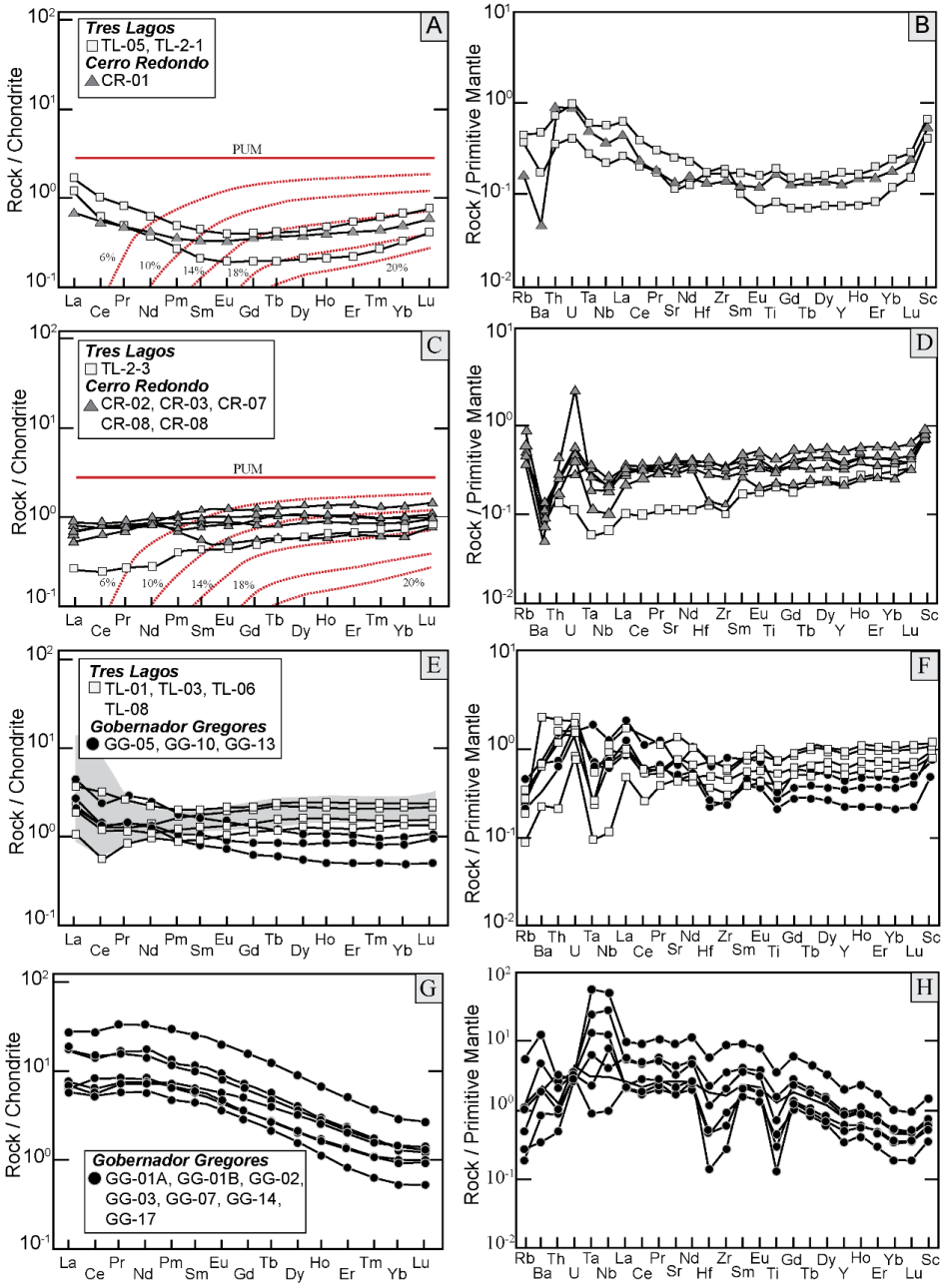

Figure 5. CI chondrite-normalised and primitive mantle-normalised trace element patterns for the whole-rock REE and trace element compositions of the investigated Patagonian peridotite xenoliths. In panels A and C, *Groups 1* and *2* peridotites are compared to curves calculated for non-modal fractional melting of the primitive upper mantle (PUM, McDonough and Sun, 1995) in the spinel lherzolite facies (red dotted lines). [Source and melting; olivine: orthopyroxene: clinopyroxene modal proportions 0.54: 0.28 0.18 and 0.11: 0.59: 0.53, respectively (Niu, 1997; at 1.5 GPa)]. The grey area in (**E**) represent the CI chondrite-normalised REE patterns of peridotite xenoliths metasomatised by volatile-rich melts (Alard et al., 2011). Normalising values after McDonough and Sun (1995).

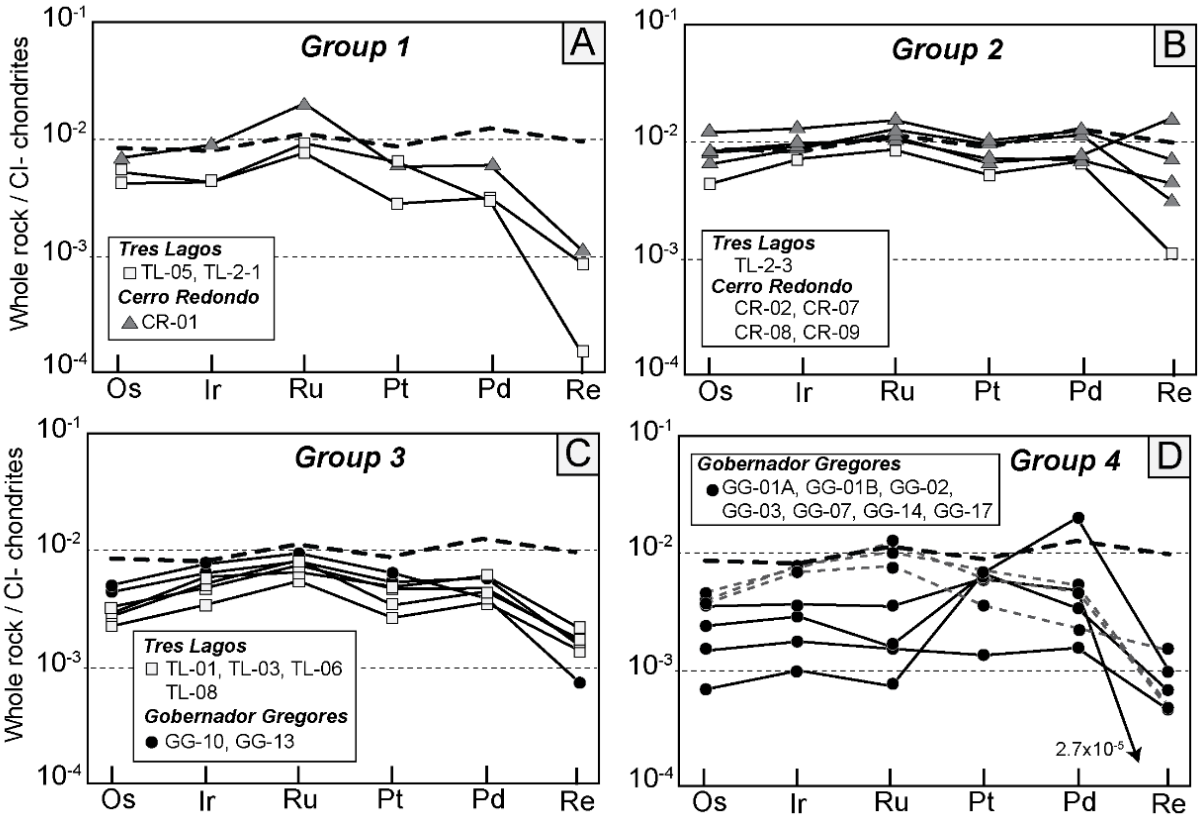

Figure 6. Whole-rock CI chondrite-normalised HSE patterns of the southern Patagonian peridotite xenoliths. Dashed lines in panel 8D are samples GG-02, GG-07, and GG-14. The thick dashed line in all panels is the primitive upper mantle after Becker et al. (2006). Normalising values after Luguet and Reisberg, 2016 (original values from Horan et al. (2003) and Fischer Gödde et al. (2011)).

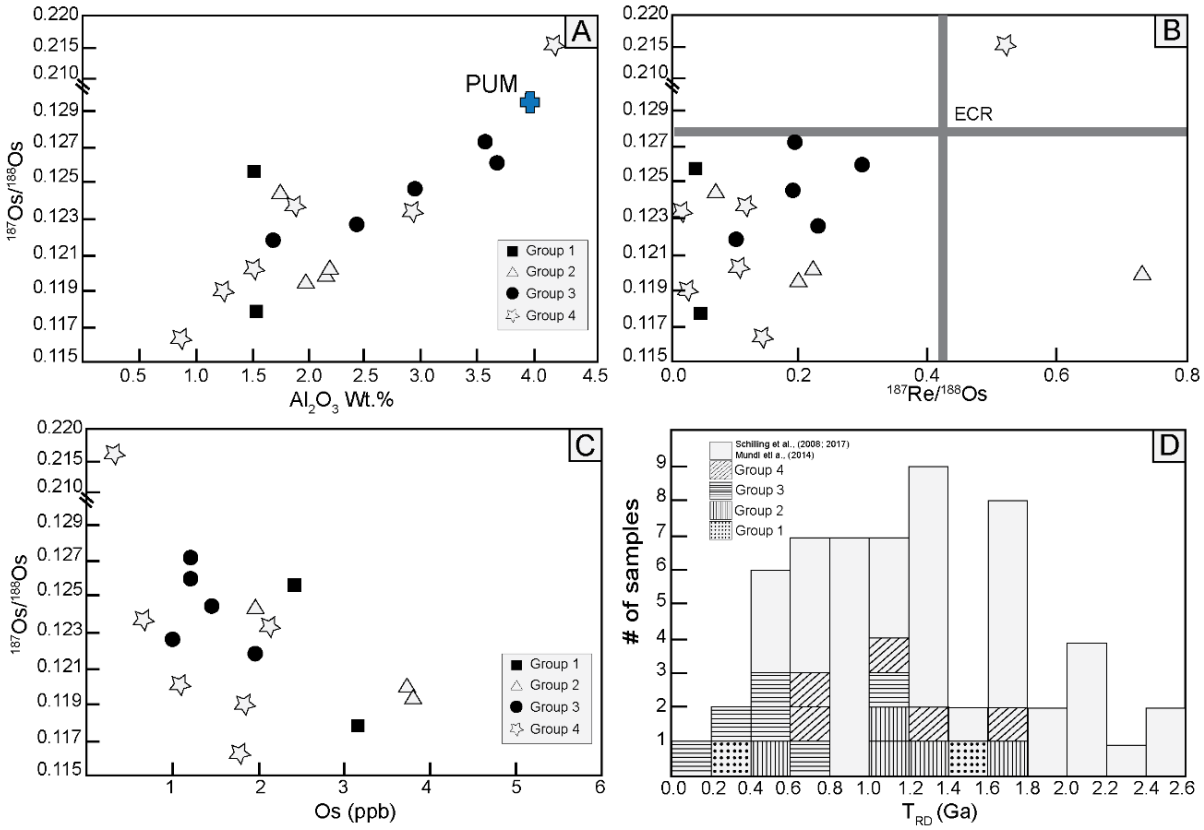

Figure 7. Re-Os isotope data and calculated T_{RD} model ages for whole-rock southern Patagonian peridotite xenoliths. **A-** Co-variation between the Os isotopic composition and the Al_2O_3 wt.% of the whole-rock southern Patagonian peridotite xenoliths. **B-** Plots of $^{187}Re/^{188}Os$ versus $^{187}Os/^{188}Os$ for the whole-rock southern Patagonian peridotite xenoliths. ECR correspond to values of the "Enstatitic Chondritic Reservoir" (Walker et al., 2002). **C-** Co-variation between the Os content and the Os isotopic composition of the whole-rock southern Patagonian peridotite xenoliths. **D-** Histogram of calculated T_{RD} model ages based on the ECR (Walker et al., 2002), comprising 21 Patagonian peridotite xenoliths from this study and those of Mundl et al., (2014) and Schilling et al., (2017).

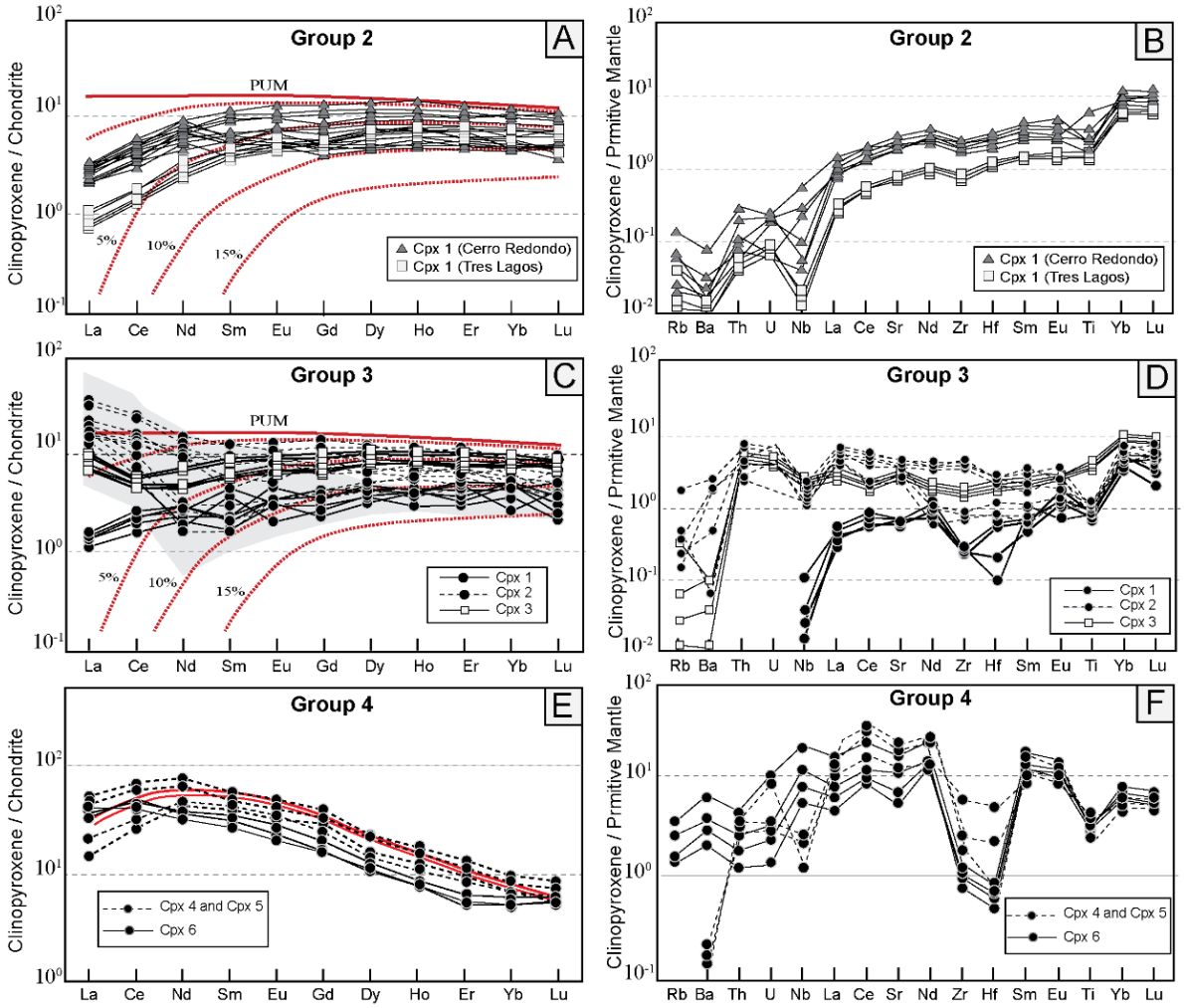

Figure 8. CI chondrite-normalised and primitive mantle-normalised REE and trace element patterns of clinopyroxene from *Group 2* (**A-B**), *Group 3* (**C-D**), and *Group 4* (**E-F**) peridotite xenoliths from southern Patagonia. Panels A and C compare the REE composition of *Group 1* and *3* peridotites to curves calculated for non-modal fractional melting of the primitive upper mantle (PUM, McDonough and Sun, 1995) in the spinel lherzolite facies (red dotted lines). [Source and melting; olivine: orthopyroxene: clinopyroxene modal proportions 0.54: 0.28 0.18 and 0.11: 0.59: 0.53, respectively (Niu, 1997; at 1.5 GPa)]. In figure **C**, the compositional field of clinopyroxene metasomatised by CO_2-rich OIB alkaline melts (Ionov et al., 2002; Grégoire et al., 2009) is shown for comparison. In figure **E**, the red line indicates the pattern for metasomatic clinopyroxene formed after carbonatite metasomatism (Akizawa et al., 2017). Normalising values after McDonough and Sun (1995).

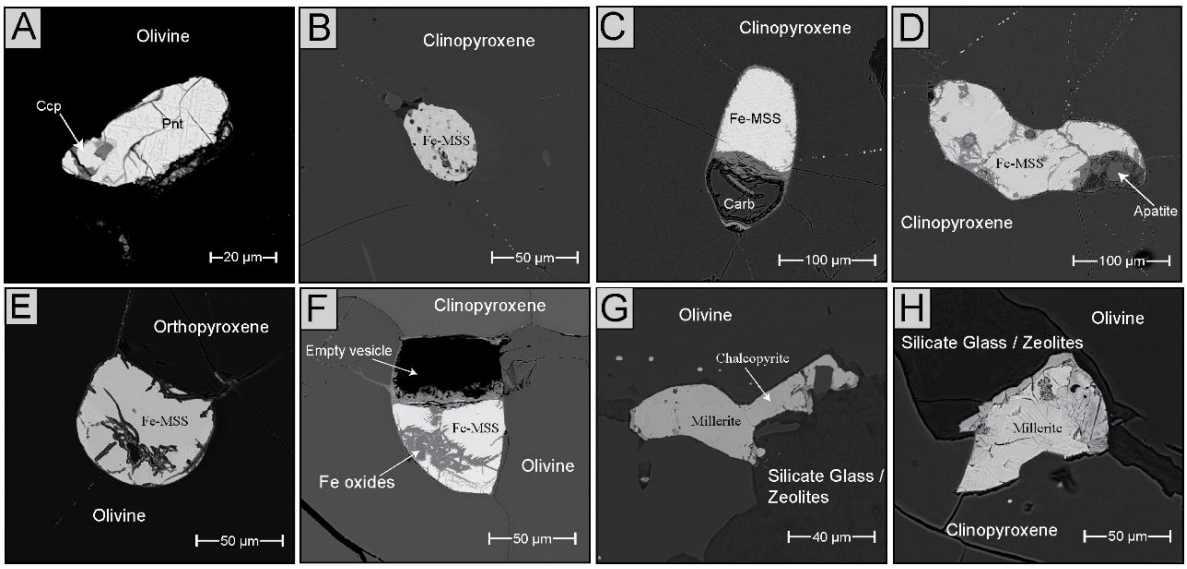

Figure 9. Backscattered electron images of base metal BMS from southern Patagonian peridotite xenoliths. **A-** Sub-rounded BMS *included* within olivine and composed of pentlandite with chalcopyrite exolutions. **B-** Rounded BMS *included* within clinopyroxene and composed of Fe-rich mss with a surrounding trail of µ-sized BMS inclusions. **C, D**- Fe-rich mss with flame-like exolutions of chalcopyrite *included* within clinopyroxene and attached to a bleb of carbonate (**C**) and apatite (**D**). **E-** *Interstitial* grain of pure Fe-mss located between an orthopyroxene and an olivine grain. **F-** *Interstitial* Fe-rich mss located between clinopyroxene and olivine and attached to an empty vesicle. **G, H-** *Glass-related* BMS embedded in silicate glass composed of millerite with micro-textured chalcopyrite exolutions.

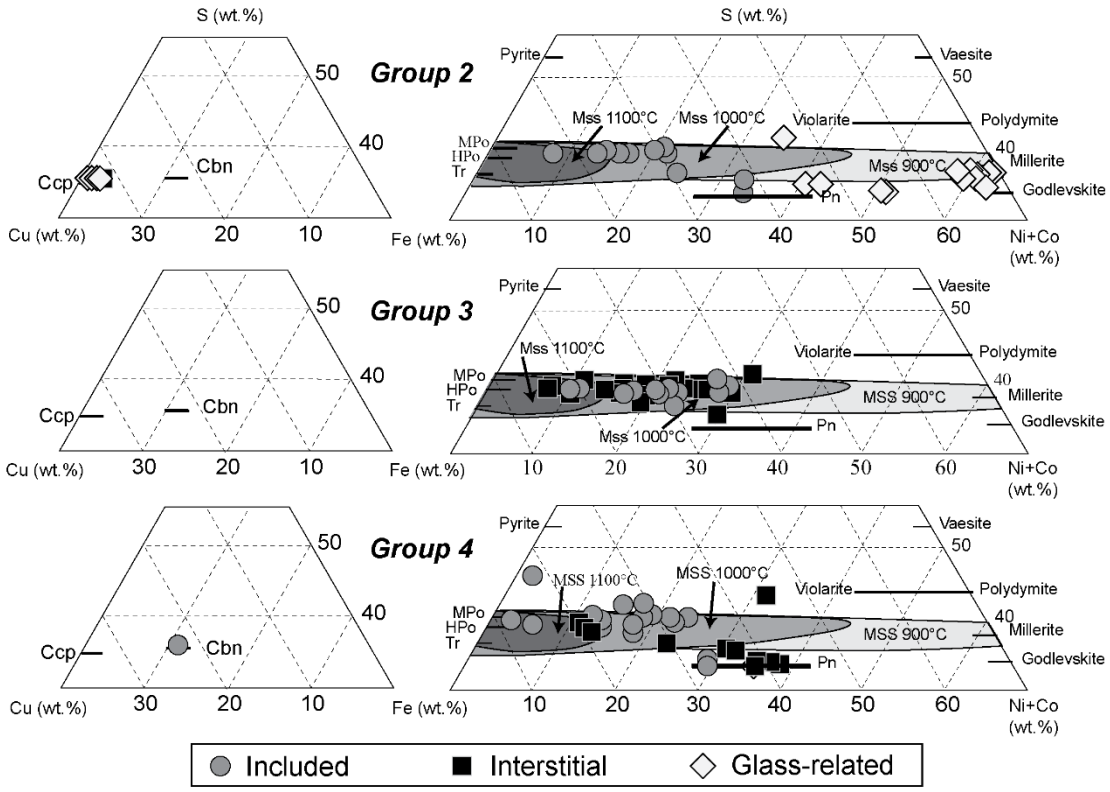

Figure 10. Composition of the BMS from the southern Patagonian peridotite xenoliths in the S - Fe - Ni + Co and S - Fe – Cu systems. Phase relations after Kullerud et al., (1969). A- BMS from *Group 2* samples. B- BMS from *Group 3* samples. C- BMS from *Group 4* samples.

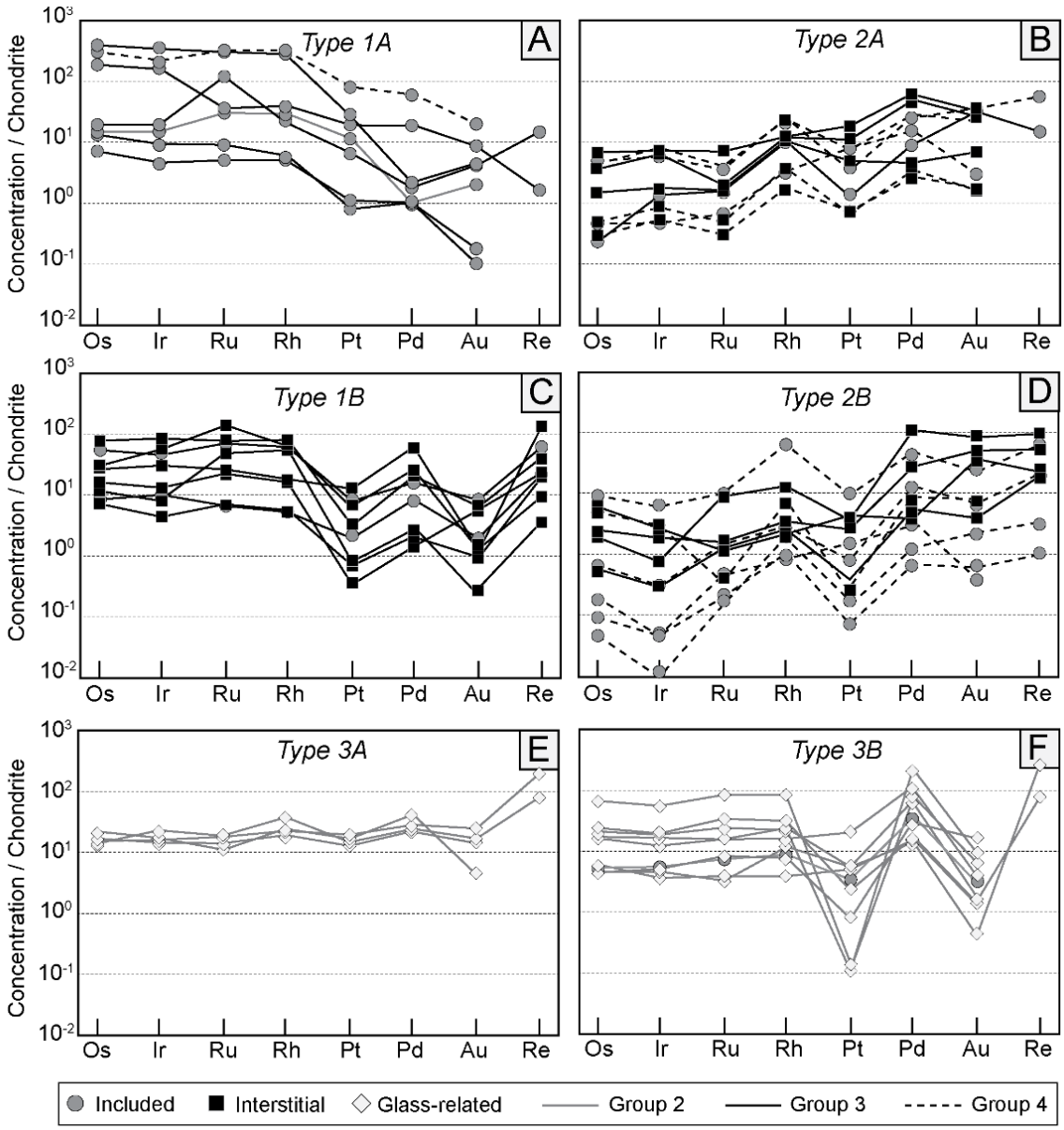

Figure 11. CI chondrite-normalised HSE element patterns of the BMS from southern Patagonian peridotite xenoliths. Normalising values after Luguet and Reisberg, 2016 (original values from Horan et al. (2003) and Fischer Gödde et al. (2011)).

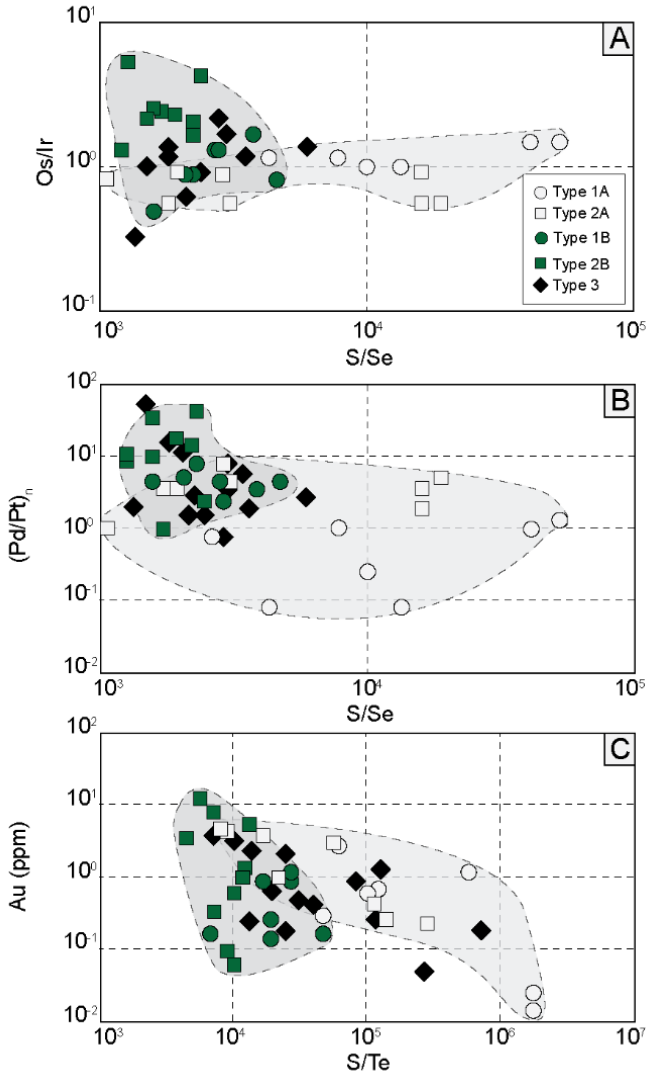

Figure 12. Bivariate plots of the $(Os/Ir)_n$ and $(Pd/Pt)_n$ versus the S/Se ratios of the different types of BMS identified in this study (**A** and **B** respectively). **C-** Correspondance between the Au content and the S/Te ratios of the different types of BMS identified in this study.

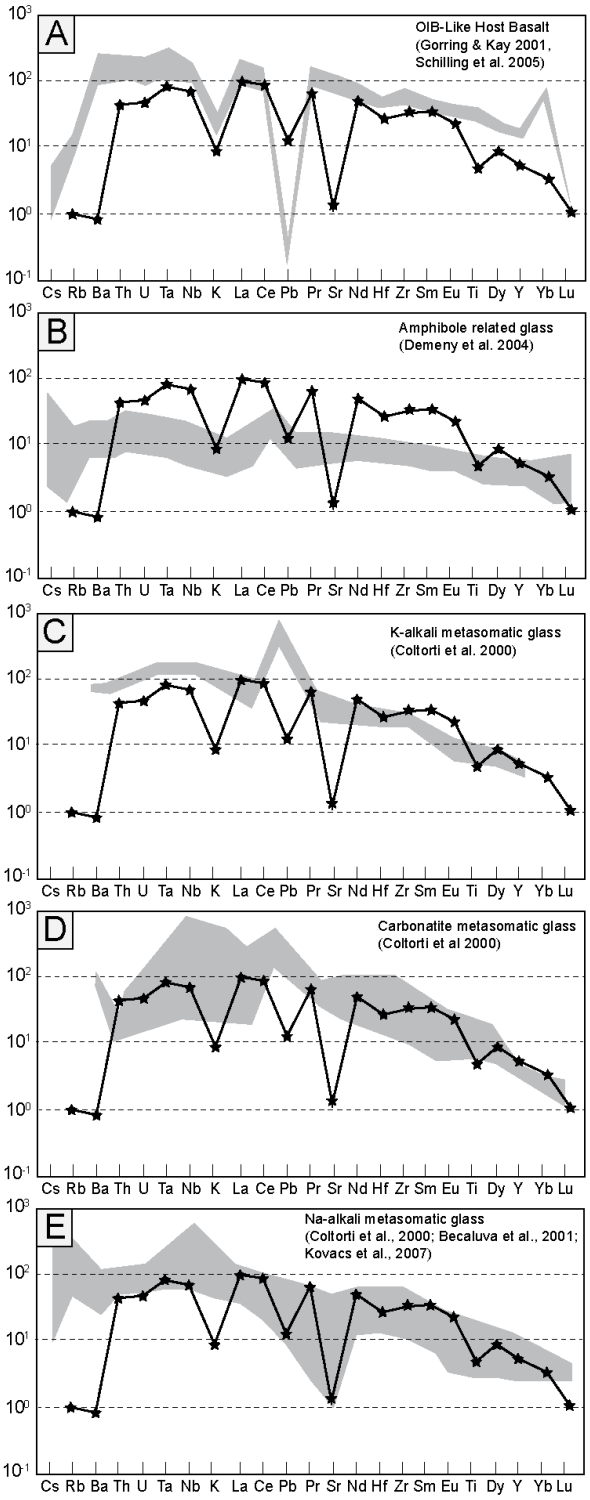

Figure 13. CI chondrite-normalised trace element composition of the interstitial glass in *Group 2* peridotites compared with glasses from mantle xenoliths formed after different possible origins. Normalising values after McDonough and Sun (1995).

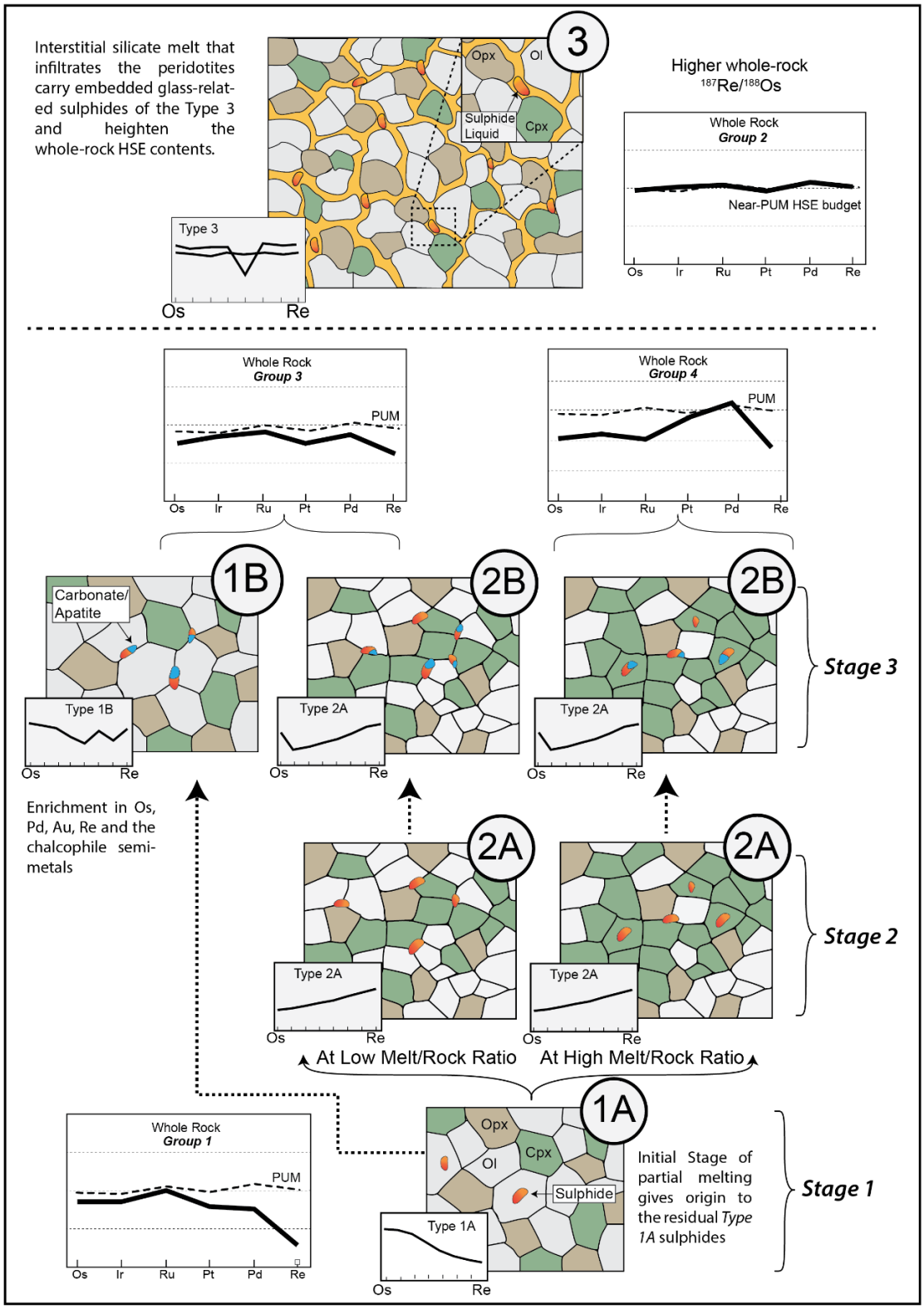

Figure 14. Cartoon showing the likely sequence of events that occurred during the genesis of the different types of BMS defined in this study.

Table 1. Summarised compositional features of the different clinopyroxene types.

	Cpx1		***Cpx2***	***Cpx3***	***Cpx4***	***Cpx5***	***Cpx6***
Group	**2**	**3**	**3**	**3**	**4**	**4**	**4**
Mg#	90.3-93.6	93-94	91.4-92.6	90.5-91.6	92.2-92.6	90.77-92.15	86.7-90.6
Al_2O_3	2.27-7.47	2.72-4.33	4.50-5.50	5.81-6.43	4.13-5.44	5.06-5.82	3.91-8.86
Cr_2O_3	0.87-1.39	0.68-1.45	0.91-1.23	0.64-0.89	2.18-3.20	1.85-2.04	0.70-1.49
TiO_2	0.18-0.72	0.20-0.23	0.19-0.27	0.42-0.58	0.27-0.41	0.07-0.31	0.64-1.06
NaO	0.46-1.62	0.46-0.56	1.36-1.49	1.59-1.77	0.96-0.78	1.32-2.55	0.81-3.52
$(La/Ce)_n$	0.50-0.97	0.60-0.73	1.05-2.22	1.46-1.82	0.56-0.75	0.73-0.80	0.61-1.00
$(La/Yb)_n$	0.02-0.61	0.24-0.53	2.23-3.83	0.83-1.08	1.73-4.30	4.01-4.61	3.63-11.85
$(LREE/HREE)_n$	0.02-0.87	0.27-0.45	0.97-1.94	0.50-0.61	2.07-3.39	3.19-3.46	4.43-8.40

Table 2. Summarised petrographic and compositional features of the different base-metal sulfides.

	Type 1A	***Type 1B***	***Type 2A***	***Type 2B***	***Type 3A***	***Type 3B***
BMS phases	Fe-mss	Fe-mss	Fe-mss ± pnt ± Ccp ± Cb	Fe-mss ± pnt ± py	Ni-mss ± pnt ± ccp	Ni-mss ± pnt ± ccp
Texture	Included	Interstitial **	Included / Interstitial	Included / Interstitial**	Glass-related	Glass-related
Type of Cpx associated	1	3	2, 3, 4, 5	3, 6	-	-
$(PPGE/IPGE)_n$	0.03-0.21	0.03-0.85	1.91-14.04	0.81-8.56	0.68-1.11	0.23-3.25
$(Os/Ir)_n$	0.97-1.51	0.48-1.63	0.16-0.92	1.34-5.34	0.59-1.35	0.30-2.04
$(Pd/Pt)_n$	0.03-3.33	1.81-6.42	0.78-6.80	0.74-34.28	1.21-2.21	0.59-1946.11

*pnt: pentlandite; ccp: Chalcopyrite; cb: Cubanite; py: Pyrrhotite; mill: Millerite

** Attached to a carbonate or apatite bleb, or to a vesicle

3.9. Acknowledgements

We acknowledge Andrew Kerr, Brian O'Driscoll and an anonymous reviewer for comments that significantly improved the first version of this manuscript. This research has been supported by a PhD scholarship from CONICYT (#21170857) to Santiago Tassara and a France-Chile exchange project ECOS-CONICYT CU1501 to JMGJ and MG. Additional funding was provided by Millennium Science Initiative through the Millennium Nucleus for Metal Tracing along Subduction Grant NC130065, the FONDAP project 15090013 "Centro de Excelencia en Geotermia de Los Andes, CEGA" and DID-UACh project #S-2015-52. Financial support for the in-situ analysis of HSE in base-metal sulfides was provided by the Ramón y Cajal Fellowship RYC-2015-17596 and the project CGL2014-55949-R granted by the Spanish "Ministerio de Economía y Competitividad" to JMGJ. Financial support for the Electron Microprobe and the LA-ICPMS analysis performed in Toulouse was provided by CNRS funding to MG. Financial support for LA-ICPMS analysis performed at the University of Chile was provided the CONICYT-Fondequip instrumentation grant EQM120098. We also thank X. Llovet (serveis Científico-Tècnics of the University of Barcelona), M. Leisen and R. Romero (Department of Geology, University of Chile) for their assistance during EPMA and LA-ICP-MS analyses respectively.

CHAPTER 4. THE ROLE OF THE LITHOSPHERIC MANTLE IN THE OXIDATION STATE AND ORE FERTILITY OF ARC MAGMAS

S. Tassara,[1,2]* M. Reich,[1,2] B.A. Konecke,[3] J.M. González-Jiménez,[4]A.C. Simon,[3] D. Morata,[1,2] F. Barra,[1,2] A. Fiege,[5] M. E. Schilling,[6] A. Corgne[6]

[1]*Department of Geology and Andean Geothermal Centre of Excellence (CEGA), FCFM, Universidad de Chile, Santiago 8370450, Chile.*
[2]*Millennium Nucleus for Metal Tracing Along Subduction, Universidad de Chile, Santiago 8370450, Chile.*
[3]*Department of Earth and Environmental Sciences, University of Michigan, Ann Arbor, Michigan 48109, U.S.A.*
[4]*Departamento de Mineralogía y Petrología, Facultad de Ciencias, Universidad de Granada, Granada 180002, Spain.*
[5]*Department of Earth and Planetary Sciences, American Museum of Natural History, New York 10024-5192, U.S.A.*
[6]*Instituto de Ciencias de la Tierra, Facultad de Ciencias, Universidad Austral de Chile, Valdivia 5090000, Chile.*

(*) Corresponding author**:** tassara.carlos.sant@ug.uchile.cl

Keywords**:** Lithospheric Mantle, Arc Magmas, Oxidation State, Apatite, XANES, Gold, Ore Deposits.

4.1. ABSTRACT

The oxidation state of the Earth's mantle exerts a fundamental control on the evolution of arc magmas and underpins models of ore deposit formation in subduction zones. Whether the oxidized nature of arc magmas is inherited from the asthenospheric mantle source or acquired during ascent and differentiation is vigorously debated, limiting our understanding of the mechanisms of extraction of sulphur and metals from the mantle. Here, we used the redox-sensitive behaviour of sulphur in apatite crystallized from quenched alkaline basaltic melts preserved within a peridotite xenolith from southern Patagonia to elucidate the redox evolution of melts during their ascent through the subcontinental lithospheric mantle. Our data reveal that an initially reduced silicate melt (ΔFMQ -2.2 to -1.2) entered the subcontinental lithospheric mantle and was oxidized to ΔFMQ between 0 and 1.2 by reaction with the peridotite wall-rock (ΔFMQ 0 to +0.8). This redox gradient (Δ(ΔFMQ) of up to 3) triggered changes in sulphur speciation and solubility in the silicate melt, boosting the potential of the melt to scavenge ore-metals such as gold. We conclude that high redox gradients in the subcontinental lithospheric mantle can effectively modify the oxidation state of primitive melts and enhance their metallogenic potential, exerting a first-order control on the global-scale localization of crustal provinces endowed with gold deposits.

4.2. INTRODUCTION

The oxidation state of the Earth's mantle is a fundamental parameter on models that attempt to explain the formation of metallogenic provinces on a lithospheric scale (*1-3*). The oxygen fugacity (fO_2), as well as the contents of sulphur and chalcophile and siderophile elements (*i.e.*, Au, Ag, Cu Ni, Os, Ir, Ru, Rh, Pt, Pd, Re; *hereafter* "ore-metals") of primitive melts associated with the formation of giant ore deposits, are frequently attributed to be either inherited directly from their asthenospheric mantle source (*4, 5*), or the result of variable degrees of differentiation and assimilation at crustal levels (*6-10*). In contrast, relatively little attention has been paid to processes occurring in the subcontinental lithospheric mantle (SCLM) that might lead to changes in the oxidation state and composition of ascending magmas after partial melting in the asthenosphere and before they reach crustal levels. For example, Chin *et al.* (*11*) and Griffin *et al.* (*12*) explored the effects of the SCLM on the composition of primary asthenosphere-derived melts during their ascent through the SCLM and concluded that refertilization of the SCLM by metasomatism might be an important process that modifies the composition and fO_2 of ascending melts and fluids. Furthermore, studies have provided evidence that restricted blocks of the SCLM may act as fertile source regions from where ore-metals are tapped by partial melting, fluxed melting, or by interaction with ascending melts (*13, 14*). Despite these advances, the impact and extent of silicate melt-SCLM interaction on the oxidation state of ascending melts that ultimately reach the crust to form ore deposits remains largely underexplored.

Ore-metals and sulphur are stored primarily within accessory base metal sulfides and sulfide liquids in the mantle, and their release and titration into the overriding crust is partially controlled by the oxygen fugacity, fO_2 (*15, 16*). This parameter reflects the oxidation state of the system and is commonly expressed as log units relative to the fayalite-magnetite-quartz mineral buffer (ΔFMQ). Experimental studies have shown that sulfide (S^{2-}) is the dominant oxidation state of sulphur in silicate melts under reducing conditions (ΔFMQ <0). In contrast, at ΔFMQ >2 the melt is dominated by sulfate (S^{6+}) whereas a sharp transition from sulfide towards the more soluble oxidized sulphur is observed around ΔFMQ +1 (*17*). Hence, the formation of oxidized magmas efficiently promotes the titration of sulphur and metals from the mantle, ultimately increasing the ore metal endowment of the overlying crust (*2, 3*). One view suggests that the oxidation state of primary melts in subduction zones and mid-ocean ridges are indistinguishably low (*7-9, 18*), whereas other authors claim that the oxidized nature of arc basalts is inherited from an oxidized asthenospheric mantle source (*1, 5, 19*).

Here, we test these contrasting hypotheses by measuring directly the formal oxidation state(s) of sulphur in magmatic apatite contained within quenched silicate glass entrained in a peridotite xenolith from Patagonia, Argentina that represents a silicate melt that ascended through the SCLM. By combining micro-X-ray absorption near-edge structure (μ-XANES) spectroscopic analysis of sulphur in apatite with petrological and mineralogical data, we show that originally reduced silicate melts that infiltrated a relatively oxidized SCLM re-equilibrated with the surrounding wall-rock resulting in oxidation of the ascending melts, triggering changes in sulphur speciation and solubility. We link this process to the formation of gold and metal-rich magmas in the oxidized portions of the SCLM, providing new insights into how mantle processes may govern the localization of metallogenic provinces.

4.3. SAMPLE BACKGROUND AND REDOX CONSTRAINTS

This study focuses on a lherzolite xenolith, which represents the mantle beneath the world-class El Deseado Massif auriferous province (Supplementary Fig. 1). The Deseado Massif hosts several Au-Ag epithermal deposits associated with calc-alkaline rhyolites, basaltic andesites, and basalts from the late magmatic stages of the Chon Aike Large Igneous Province (CA-LIP) (*20*). The CA-LIP formed during two major periods between 180 to 155 Ma (*21*). The early Jurassic event was related to the thermal impact of the Karoo plume head (~180 Ma), whereas the Middle to Late Jurassic events reflects the influence of active subduction on the western margin of Gondwana (~155 Ma) (*22*). Mantle xenoliths from the SCLM beneath the Deseado Massif were later extruded by extensive Neogene (~3.5 Ma) back-arc plateau volcanism (*23*).

The studied peridotite is a protogranular anhydrous lherzolite equilibrated in the spinel facies at temperatures of 1020 – 1150 °C (*14*). The sample is characterized by the presence of quenched interstitial glass distributed along grain boundaries of the peridotite silicate matrix forming an interconnected network of veinlets (Supplementary Fig. 2). These veinlets contain a mineral assemblage that includes armalcolite, ilmenite, K-feldspar, apatite, Au-bearing sulfides, and native gold particles embedded within a glassy matrix (*14*) (Supplementary Fig. 3). The interstitial glass and associated minerals were interpreted as remnants of a Au-bearing, Na-rich silica-undersaturated melt that infiltrated the peridotite. This melt extracted Ni-Cu sulfide liquids from the surrounding peridotite wall-rock and were physically entrained and transported within the silicate melt through the mantle (*24-26*).

The fO_2 conditions of the oxide-silicate assemblage in the host peridotite were calculated using the methods described by Wood *et al.* (*27*) yielding ΔFMQ values between 0 and +0.8 (Supplementary Table 1 and 2), consistent with redox constraints for most SCLM peridotites reported in the literature (*3, 28*). The oxidation state of the infiltrating silicate melt was determined by using two independent and self-consistent approaches based on the composition of armalcolite and apatite, respectively. Terrestrial occurrences of armalcolite [$(Fe,Mg)Ti_2O_5$] are exclusively associated with metasomatic melts in the upper mantle and high-Ti primitive lavas (*29-32*). Compositional analysis of armalcolite shows that it contains high concentration of Cr (1.73 and 2.16 wt.%) and is among the most MgO-enriched compositions reported in both lunar and terrestrial occurrences (Supplementary Table 3). Stoichiometric calculations indicate that armalcolite has near zero trivalent Fe and Ti concentrations (Supplementary Table 4). Similar compositions were reported for Cr-bearing armalcolite found in the Kerguelen island mantle xenoliths (*30, 32, 33*) (Supplementary Fig. 4). In an attempt to constrain the oxidation state of lunar basalts, Friel *et al.* (*34*) performed experimental studies on the stability of synthetic armalcolite as a function of fO_2 at 1200 °C and 1 atm. This experiment and observations in natural samples (*32*) demonstrated that Cr-rich and near-zero Fe^{3+} variety of armalcolite forms only under reducing conditions (fO_2 between $10^{-9.5}$ and $10^{-10.5}$ bar), *i.e.* ΔFMQ ≈ -2.2 to -1.20 (cf. Figure 4 in (*34*)). In addition, these authors showed that at even lower conditions (fO_2 between $10^{-12.2}$ and $10^{-12.8}$ bar), armalcolite breaks down to form Mg-rich armalcolite plus ilmenite. Based on experimental data, we constrained the oxidation conditions of the infiltrating silicate melt at the time of armalcolite crystallization in the mantle at ΔFMQ ≈ -2.2 to -1.2, whereas the presence of ilmenite suggests ΔFMQ values closer to -2.2 (*34*).

Apatite [$Ca_5(PO_4)_3(F,Cl,OH)$] also occurs embedded within the interstitial silicate glass, commonly forming isolated clusters of crystals of up to ~8 µm in size (Supplementary Fig. 3). The apatite crystals are euhedral and show typical hexagonal and acicular shapes, indicating that it

crystallized from the surrounding melt upon rapid quenching (*35*), possibly during the xenolith eruption (*14*). Electron probe micro-analysis (EPMA) revealed that apatite corresponds to the F-rich end-member (Supplementary Table 5), which suggests a late crystallization from the silicate melt associated with increasing differentiation (*36*). Sulphur concentrations in the analysed apatite are between 40 and 170 µg/g with a few grains showing concentrations below detection limits (~30 µg/g) (Supplementary Table 5). The sulphur µ-XANES spectra of the studied apatite grains revealed two dominant peaks at ~2469.7 eV (sulfide) and ~2481.8 eV (sulfate), indicating that both species were incorporated within the apatite structure (Fig. 1). The integrated S^{6+}/S_{total} peak area ratios were determined following the methodology of Konecke *et al.* (*37*) and range between 0.28 and 0.48 (Supplementary Fig. 4). In order to reduce crystal orientation effects on the relative integrated area of the different peaks of the µ-XANES spectra, several apatite spectra were collected, normalized (*e.g.*, baseline removal and intensity normalization), and then merged (*37*) to obtain an average spectrum representative of the bulk sulphur oxidation state of the studied apatite grains. The averaged integrated S^{6+}/S_{total} peak area can be used to estimate the fO_2 of the infiltrating silicate melt from which apatite crystallized. Experiments performed by Konecke *et al.* (*37*) showed that apatite formed at ΔFMQ = 0 has a S^{6+}/S_{total} ratio of 0.168, whereas apatite that crystallized at ΔFMQ ≈ +1.2 is characterized by a S^{6+}/S_{total} ratio of 0.958. This implies that apatite undergoes a pronounced shift from sulfide- to sulfate-dominated species with changing oxidation conditions, similarly to silicate melts (*17*). The averaged integrated S^{6+}/S_{total} ratio of the studied apatite is ~0.35 (Fig. 1), which indicates that the oxidation state of the infiltrating silicate melt at the time of apatite crystallization was $0 < \Delta FMQ < +1.2$. Given that the S^{6+}/S_{total} ratio and log (fO_2) follow a near linear trend within this range, we infer that the final oxidation state of the silicate melt at apatite formation was around ΔFMQ + 0.5. Considering that an increase in pressure shifts the stability field of sulfide towards more oxidizing conditions (*38*) and inferring that apatite follows a similar trend, we conclude that a ΔFMQ +0.5 represents a minimum fO_2 value for the silicate melt.

4.4. DISCUSSION

The interstitial network of glass veinlets in the peridotite xenolith represents a Na-rich silica undersaturated melt that percolated through the SCLM and quenched during the rapid eruption of the xenolith (*14*). Based on our data, we propose that the mineral assemblage associated with the glassy vein (armalcolite and apatite) records two different oxidation states of the percolating silicate melt, and where armalcolite formed under highly reducing conditions (ΔFMQ -2.2 to -1.2), followed by the later crystallization of apatite crystallization under more oxidizing conditions (ΔFMQ 0 to +1.2).

4.4.1. Melt oxidation in the lithospheric mantle

The armalcolite-bearing silicate melt (ΔFMQ -2.2 to -1.2) infiltrated a relatively more oxidized peridotite (ΔFMQ 0 to +0.8), producing a high redox gradient, *i.e.*, a Δ(ΔFMQ) of near 3 log units between these two components (Fig. 2A). The final redox conditions after oxidation of the reduced silicate melt and reduction of the relatively oxidized peridotite will depend on the mass balance between the more reduced and more oxidized components (*39*). Apatite crystallized from the surrounding silicate melt after the melt-peridotite interaction started, and contains both sulfide and sulfate as evidenced by our µ-XANES data (Fig. 1). The presence of sulfate in apatite requires the reaction between two components, *i.e.*, a highly reduced melt with a S^{6+}/S_{total} ~ 0 and low

sulphur content (*17*) that reacted with a more oxidized and sulfide-bearing peridotite (ΔFMQ 0 to +0.8).

In the SCLM, the oxidation state is governed by minerals that have a high content of Fe^{3+} such as spinel and clinopyroxene (*27*). These two phases are the first minerals to react with the melt when the redox conditions are disturbed, as has been reported during the mixing process between two compositionally distinct magmas (*40*). Clinopyroxene and spinel from the studied peridotite show reaction rims when in contact with the reduced infiltrating silicate melt (Supplementary Fig. 3) indicating a $Fe^{2+} \leftrightarrow Fe^{3+}$ exchange between the peridotite wall-rock and the infiltrating silicate melt, which promotes oxidation of the melt (*41*) (Fig. 2B). Other than Fe, sulphur also has a large oxidation potential (*39*), and an increase in the oxidation state of the melt after melt-peridotite interaction would promote an increase in the sulphur solubility of the infiltrating silicate melt (*42*). Thus, at higher redox and sulphur solubility conditions (*42*), the sulfide liquids entrained in the percolating silicate melt will be partially absorbed and will contribute to achieving higher fO_2 conditions by increasing the oxygen/cation ratio of the melt (*41, 43*) (Fig. 2C). Apatite crystallized from the melt after the melt-peridotite interaction will incorporate both sulfide and sulfate in varying proportions, according to the S^{6+}/S_{total} ratio of the melt; therefore, recording the post-reaction oxidation state of the silicate melt (*37*) (Figs. 1, 2D).

4.4.2. Scavenging sulphur and ore-metals from the lithospheric mantle

The process described above explains the oxidation of silicate melts that ascend through the SCLM with concomitant destabilization of metal-bearing sulfides and incorporation of sulphur. Sulfide breakdown will not only release sulphur but also its contained ore-metals (*16*), such as Au (Fig. 2D), which under certain circumstances could lead to metal enrichment in the silicate melts. The solubility of Au in sulphur-bearing silicate melts is maximized when sulphur is dissolved as both sulfide and sulfate species (*41*) and when the sulfide concentration is near the sulfide-saturated threshold (*44-47*). Figure 3 shows that the estimated fO_2 of the silicate melt after reacting with the peridotite wall-rock is between ΔFMQ 0 and +1.2. Sulphur μ-XANES in apatite indicates that the S^{6+}/S_{total} ratio is ~0.35 and the presence of sulfide liquids within this silicate melt indicates that the melt was once sulfide saturated. These redox conditions are in good agreement with those that maximize Au solubility of sulphur-bearing basaltic melts, determined experimentally by Botcharnikov *et al.* (*44*) at 1050 °C and 200 MPa (Fig. 3), meaning that the highest Au solubility was achieved during redox re-equilibration within the SCLM. In addition, the mineral assemblage associated with the studied melt contains native gold particles included within the sulfides as well as embedded within the quenched glass (*16*). The native gold micro-particles in the sulfides have euhedral and hexagonal forms (*14*) and likely crystallized from the sulfide liquids during desulfurization, after oxidation of the surrounding silicate melt (*26*). Continued oxidation and desulfurization would result in the release of these Au micro-particles into the silicate melt. The Au micro-particles embedded within the glass have irregular shapes (*14*), pointing to partial dissolution in the surrounding melt. This is in good agreement with Au solubility experiments (*44, 48*) and indicates that the studied silicate melt had an enhanced capability for transporting significant amounts of Au (Fig. 3).

In summary, metal-rich sulfide liquids embedded within a reduced silicate melt (*24-26*) may source significant amounts of sulphur and Au due to the transient increase in fO_2 caused by melt-peridotite interaction in the SCLM during melt ascent (Fig. 2).

4.4.3. Impact on the oxidation state of primitive arc magmas

Figure 4 shows a conceptual model that highlights the impact of redox gradients in the mantle on the metallogenic potential of a crustal column in a subduction environment. The occurrence of a high redox gradient between the sub-arc asthenospheric and lithospheric mantle may help reconcile contrasting hypotheses about the origin of the oxidized nature of arc basalts. The oxidation state of the sub-arc mantle has been assessed through the study of peridotite xenoliths and exhumed peridotite bodies, or indirectly through investigation the study of primitive arc basalts. Both peridotite xenoliths (-1.5< ΔFMQ >3.5; (*3*) and references therein) and arc basalts (2< ΔFMQ >4; (*5, 19*)) display a distinctly oxidized nature compared to other tectonic settings. However, the peridotite xenoliths and exhumed peridotite bodies represent the buoyant and rigid upper SCLM, and do not necessarily represent the sub-arc asthenospheric mantle, which is the source of most arc basalts (Fig. 4). On the other hand, primitive arc basalts are not primary magmas *per se*, and the absence of evidence for crustal contamination does not exclude differentiation processes after their formation in the asthenosphere and during ascent throughout the SCLM. Therefore, geochemical tracers such as the V/Sc and Zn/Fe ratios as well as the Fe isotopic composition of primitive basalts are probably the only factual indicators of the original redox signature of melts generated in the sub-arc asthenosphere because they are not modified during post-melting differentiation (*10, 18, 49*) (Fig. 4). V/Sc and Zn/Fe ratios are highly similar between arc basalts and mid-ocean ridge basalts indicating that the oxidation state of both asthenospheric sources is comparable (*i.e.*, FMQ < +0.25; (*18*)). Hence, the redox gradient between the sub-arc asthenospheric and lithospheric mantle can be explained according to the following model.

The SCLM represents a stable, ancient portion of the mantle under the continental crust since its formation in the mid to late Archean due to its positive buoyancy (*50, 51*). The time-integrated flux of metasomatic melt and fluid percolation events through the SCLM changes its chemical composition and leads to the formation of highly oxidized domains, particularly in the sub-arc lithospheric mantle (up to ΔFMQ ~ +3.5; (*3, 52, 53*)) (Fig. 4). In addition, and given that the sub-arc lithospheric mantle has a much longer residence time above a dehydrating slab than the underlying convecting asthenospheric mantle wedge (Fig. 4), it is likely that the sub-arc lithospheric mantle interacted with large amounts of oxidizing melts/fluids, even more than the convecting asthenospheric mantle wedge, which is continuously subject to convective recycling (*54*). This is consistent with recent evidence from sub-arc mantle peridotites that show the presence of slab-derived, oxidized fluids in the lithospheric mantle (*55*), suggesting that slab fluids can migrate over long distances without oxidizing the surrounding asthenospheric mantle. This observation suggests that the sub-arc lithosphere becomes more oxidized with time in comparison to the underlying convecting asthenospheric mantle source of arc magmas (*54*), as evidenced by the oxidized nature of the sub-arc mantle xenoliths (*3*) compared to the more reduced state of the asthenosphere, as revealed by the geochemical signatures of basalts (*7, 18, 49*).

Therefore, if melting of this sub-arc asthenosphere produces a basaltic melt with ΔFMQ ~ 0 (*7, 18, 49*) (Fig. 4), the interaction of this melt with a highly oxidized and sulfide-rich overlying SCLM (*56*) upon ascent will induce redox gradients leading to the oxidation of the ascending silicate melt(s). The more oxidized the SCLM is, the higher the redox gradient (Δ(ΔFMQ)) between the peridotite and the infiltrating silicate melt, and the higher the oxidation state of the resulting silicate melt. This process is an unforeseen mechanism that may contribute to the higher oxidation state of arc lavas, explaining the apparently contradictory evidence between the relatively oxidized

nature of primitive arc basalts and their V/Sc and Fe/Zn ratios (*7, 18*), and the relationship between high-$\delta^{18}O$ of arc basalts and sub-arc SCLM (*57*).

4.5. CONCLUDING REMARKS

In summary, we propose that the oxidation state of primitive arc basalts, as well as their sulphur and ore-metals content, may not be determined entirely by the composition of their asthenospheric mantle source or by crustal assimilation. We argue that high redox gradients in the mantle exert a fundamental role in the formation of oxidized magmas and concomitant sulphur and ore metal extraction. However, it is important to note that our data do not exclude scenarios where the oxidized nature of primitive melts, as well as their high sulphur and metals content, are inherited features from an asthenospheric mantle source, acquired by intracrustal differentiation or contamination, or devolatilization. Rather, our model points to an optimal alignment of common geological processes that occur in different zones of the upper mantle, and helps improve our understanding of metallogenic processes that operate along subduction zones on a global scale.

4.6. BIBLIOGRAPHY

1. Mungall, J.E. Roasting the mantle: Slab melting and the genesis of major Au and Au-rich Cu deposits. *Geology* **30**, 915-918 (2002).
2. Sillitoe, R.H. Major gold deposits and belts of the North and South American Cordillera: distribution, tectonomagmatic settings, and metallogenic considerations. *Economic Geology* **103**, 663-687 (2008).
3. Richards, J.P. The oxidation state, and sulphur and Cu contents of arc magmas: implications for metallogeny. *Lithos* **233**, 27-45 (2015).
4. Carmichael, I.S.E. The redox states of basic and silicic magmas: a reflection of their source regions? *Contributions to Mineralogy and Petrology* **106**, 129-141 (1991).
5. Kelley, K., Cottrell, E. Water and the oxidation state of subduction zone magmas. *Science* **325**, 605-607 (2009).
6. Jenner, F.E., O´Neill, H.St.C., Arculus, R.J., Mavrogenes, J.A. The magnetite crisis in the evolution of arc-related magmas and the initial concentration of Au, Ag, and Cu. *Journal of Petrology* **51**, 2445-2464 (2010).
7. Lee, C-T.A., Luffi, P., Le Roux, V., Dasgupta, R., Albarède, F., Leeman, W.P. The redox state of arc mantle using Zn/Fe systematics. *Nature* **468**, 681-685 (2010).
8. Lee, C-T.A., Luffi, P., Chin, E.J., Bouchet, R., Dasgupta, R., Morton, D.M., Le Roux, V., Yin, Q.Z., Jin, D. Copper systematics in arc magmas and implications for crust-mantle differentiation. *Science* **336**, 64-68 (2002).
9. Tang, M., Erdman, M., Eldridge, G., Lee, C-T.A. The redox "filter" beneath magmatic orogens and the formation of continental crust. *Science Advances* **4**, 5, eaar4444 (2018).
10. Lee, C-T.A., Erdman, M., Yang, W., Ingram, L., Chin, E.J., DePaolo, D. Sulphur isotopic compositions of deep arc cumulates. *Earth and Planetary Science Letters* **500**, 76-85 (2018).
11. Chin, E.J., Lee, C-T.A., Barnes, J.D. Thickening, refertilization, and the deep lithosphere filter in continental arcs: Constraints from major and trace elements and oxygen isotopes. *Earth and Planetary Science Letters* **397**, 184-200 (2014).
12. Griffin, W.L., Huang, J-X., Thomassot, E., Gain, S.E.M., Toledo, V., O'Reilly, S.Y. Super-reducing conditions in ancient and modern volcanic systems: sources and behaviour of carbon-rich fluids in the lithospheric mantle. *Mineralogy and Petrology*, 1-14 (2018).

13. Griffin, W.L., Begg, G.C., O´Reilly, S.Y. Continental-root control on the genesis of magmatic ore deposits. *Nature Geoscience* **6**, 905-910 (2013).
14. Tassara, S., González-Jiménez, J.M., Reich, M., Schilling, M.E., Morata, D., Begg, G.C., Saunders, E., Griffin, W.L., O´Reilly, S.Y., Grégoire, M., Barra, F., Corgne, A. Plume-subduction interaction forms large auriferous provinces. *Nature Communications* **8**, 843 (2017).
15. Jugo, P.J. Sulphur content at sulfide saturation in oxidized magmas. *Geology* **37**, 415-418 (2009).
16. Lorand, J-P., Luguet, A. Chalcophile and siderophile elements in mantle rocks: trace elements controlled by trace minerals. *In*: Harvey, J., Day, J.M.D. (Eds). Highly Siderophile and Strongly Chalcophile Elements in High-Temperature Geochemistry and Cosmochemistry. Reviews in Mineralogy and Geochemistry **81**. The Mineralogical Society of America (2016).
17. Jugo, P.J., Wilke, M., Botcharnikov, R.E. Sulphur K-edge XANES analysis of natural and synthetic basaltic glasses: implications for S speciation and S content as a function of oxygen fugacity. *Geochimica et Cosmochimica Acta* **74**, 5926-5938 (2010).
18. Lee, C-T.A., Leeman, W.P., Canil, D., Li, Z.X.A. Similar V/Sc systematics in MORB and arc basalts: implications for the oxygen fugacities of their mantle source regions. *Journal of Petrology* **46**, 2313-2336 (2005).
19. Evans, K.A. The redox budget of subduction zones. *Earth-Science Reviews* **113**, 11-32 (2012).
20. Schalamuk, I.B., Zubia, M., Genini, A., Fernandez, R.R. Jurassic epithermal Au-Ag deposits of Patagonia, Argentina. *Ore Geology Reviews* **12**, 173-176 (1997).
21. Féraud, G., Alric, V., Fornari, M., Bertrand, H., Haller, M. $^{40}Ar/^{39}Ar$ dating of the Jurassic volcanic province of Patagonia: migrating magmatism related to Gondwana break-up and subduction. *Earth and Planetary Science Letters* **172**, 83-96 (1999).
22. Pankhurst, R.J., Riley, T.R., Fanning, C.M., Kelley, S.P. Episodic silicic volcanism in Patagonia and the Antarctic Peninsula: chronology of magmatism associated with the break-up of Gondwana. *Journal of Petrology* **41**, 605-625 (2000).
23. Rivalenti, G., Mazzucchelli, M., Laurora, A., Ciuffi, S.I.A., Zanetti, A., Vannucci, R., Cingolani, C.A. The backarc mantle lithosphere in Patagonia, South America. *Journal of South American Earth Sciences* **17**, 121-152 (2004).
24. Bockrath, C., Ballhaus, C., Holzheid, A. Fractionation of the platinum-group elements during mantle melting. *Science* **305**, 1951-1953 (2004).
25. Ballhaus, C., Bockrath, C., Wohlgemuth-Ueberwasser, C., Laurenz, V., Berndt, J. Fractionation of the noble metals by physical processes. *Contributions to Mineralogy and Petrology* **152**, 667-684 (2006).
26. Tassara, S., González-Jiménez, J.M., Reich, M., Saunders, E., Luguet, A., Morata, D., Grégoire, M., van Acken, D., Schilling, M.E., Barra, F., Nowell, G., Corgne, A. Highly siderophile elements mobility in the subcontinental lithospheric mantle beneath southern Patagonia. *Lithos* **314-315**, 579-596 (2018).
27. Wood, B.J., Bryndzia, L.T., Johnson, K.E. Mantle oxidation state and its relationship to tectonic environment and fluid speciation. *Science* **248**, 337-345 (1990).
28. Ballhaus, C. Redox states of lithospheric and asthenospheric upper mantle. *Contributions to Mineralogy and Petrology* **114**, 331-348 (1993).
29. Haggerty, S.E. Metasomatic mineral titanates in upper mantle xenoliths. *In*: Mantle Xenoliths (Ed. P.H. Nixon) pp 671-690, John Wiley and Sons (1987).
30. Bowles, J.F.W. Definition and range of naturally occurring minerals with the pseudobrookite structure. *American Mineralogist* **73**, 1377-1383 (1988).

31. Contini, S., Venturelli, G., Toscani, L. Cr-Zr armalcolite-bearing lamproites of Cancarix, SE Spain. *Mineralogical Magazine* **57**, 203-216 (1993).
32. Grégoire, M., Lorand, J-P., O´Reilly, S.Y., Cottin, J.Y. Armalcolite-bearing, Ti-rich metasomatic assemblages in harzburgitic xenoliths from Kerguelen Islands: Implications for the oceanic mantle budget of high-field strength elements. *Geochimica et Cosmochimica Acta* **64**, 673-694 (2000).
33. Haggerty, S.E. Oxide mineralogy in the upper mantle. *In* D.H. Lindsley (Ed.) Oxide minerals: Petrologic and Magnetic Significance. Pp 355-416, *Mineralogical Society of America Publ.* (1991).
34. Friel, J.J., Harker, R.I., Ulmer, G.C. Armalcolite stability as a function of pressure and oxygen fugacity. *Geochimica et Cosmochimica Acta* 41, 403-10 (1977).
35. Piccoli, P.M., Candela, P.A. Apatite in Igneous Systems. *In*: Kohn, M.J., Rakovan., Hughes, J.M. (Eds.), Phosphates: geochemical, geobiological, and materials importance. *Rev. Mineral. Geochem.* 48, 255-292 (2002).
36. Nash, W.P. Phosphate minerals in terrestrial igneous and metamorphic rocks. In: Nriagu, J.O., Moore, P.B. (Eds.), *Phosphate Minerals*. Springer-Verlag, Berlin, p. 442 (1984).
37. Konecke, B.A., Fiege, A., Simon, A.C., Parat, F., Stechern, A. Co-variability of S^{6+}, S^{4+}, and S^{2-} in apatite as a function of oxidation state: Implications for a new oxybarometer. *American Mineralogist* **102**, 548-557 (2017).
38. Matjuschkin, C., Blundy, J.D., Brooker, R.A. The effect of pressure on sulphur speciation in mid-to deep-crustal arc magmas and implications for the formation of porphyry copper deposits. *Contributions to Mineralogy and Petrology* **171**:66 (2016).
39. Evans, K.A., Tomkins, A.G. The relationship between subduction zone redox budget and arc magma fertility. *Earth and Planetary Science Letters* **308**, 401-409 (2011).
40. Fiege, A., Ruprecht, P., Simon, A.C. A magma mixing redox trap that moderates mass transfer of sulphur and metals. *Geochemical Perspectives Letters* **3**, 190-199 (2017).
41. Cooper, R.F., Fanselow, J.B., Poker, D.B. The mechanism of oxidation of a basaltic glass: chemical diffusion of network modifying cations. *Geochimica et Cosmochimica Acta* **60**, 3253-3265 (1996).
42. Jugo, P.J., Luth, R.W., Richards, J.P. An experimental study of the sulphur content in basaltic melts saturated with immiscible sulfide or sulfate liquids at 1300 °C and 1.0 GPa. *Journal of Petrology* **46**, 783-798 (2005).
43. Behrens, H., Gaillard, F. Geochemical aspects of melts: Volatiles and redox behaviour. *Elements* **2**, 275-280 (2006).
44. Botcharnikov, R.E., Linnen, R.L., Wilke, M., Holtz, F., Jugo, P.J., Berndt, J. High gold concentrations in sulfide-bearing magma under oxidizing conditions. *Nature Geoscience* **4**, 112-115 (2011).
45. Zajacz, Z., Candela, P.A., Piccoli, P.M., Wälle, M., Sanchez-Valle, C. Gold and copper in volatile saturated mafic to intermediate magmas: Solubilities, partitioning, and implications for ore deposit formation. *Geochimica et Cosmochimica Acta* **91**, 140-159 (2012).
46. Li, Y., Audétat, A. Partitioning of V, Mn, Co, Ni, Cu, Zn, As, Mo, Ag, Sn, Sb, W, Au, Pb, and Bi between sulfide phases and hydrous basanite melt at upper mantle conditions. *Earth and Planetary Science Letters* **355-356**, 327-340 (2012).
47. Jégo, S., Nakamura, M., Kimura, J-I., Iizuka, Y., Chang, Q., Zellmer, G.F. Is gold solubility subject to pressure variations in ascending arc magmas? *Geochimica et Cosmochimica Acta* **188**, 224-243 (2016).

48. Jégo, S., Pichavant, M. Gold solubility in arc magmas: Experimental determination of the effect of sulphur at 1000 °C and 0.4 GPa. *Geochimica et Cosmochimica Acta* **84**, 560-592 (2012).
49. Dauphas, N., Craddock, P.R., Asimow, P.D., Bennet, V.C., Nutman, A.P., Ohnenstetter, D. Iron isotopes may reveal the redox conditions of mantle melting from Archean to present. *Earth and Planetary Science Letters* **288**, 255-267 (2009).
50. Griffin, W.L., O'Reilly, S.Y., Afonso, J.C., Begg, G.C. The composition and evolution of lithospheric mantle: A re-evaluation and its tectonic implications. *Journal of Petrology* **50**, 1185-1204 (2009).
51. Herzberg, C., Rudnick, R. Formation of cratonic lithosphere: an integrated thermal and petrological model. *Lithos* **149**, 4-15 (2012).
52. McGuire, A.V., Dyar, M.D., Nielson, J.E. Metasomatic oxidation of upper mantle peridotite. *Contributions to Mineralogy and Petrology* **109**, 252-264 (1991).
53. McCammon, C.A., Griffin, W.L., Shee, S.R., O´Neill, H.S.C. Oxidation during metasomatism in ultramafic xenoliths from the Wesselton kimberlite, South Africa: implications for the survival of diamond. *Contributions to Mineralogy and Petrology* **141**, 287-296 (2001).
54. Frost, D.J., McCammon, C.A. The redox state of the Earth´s mantle. *Annual Review of Earth and Planetary Science*s **36**, 389-420 (2008).
55. Bénard, A., Klimm, K., Woodland, A.B., Arculus, R.J., Wilke, M., Botcharnikov, R.E., Shimizu, N., Nebel, O., Rivard, C., Ionov, D.A. Oxidising agents in sub-arc mantle melts link slab devolatilization and arc magmas. *Nature Communications* **9**, 3500 (2018)
56. Rielli, A., Tomkins, A.G., Nebel, O., Brugger, J., Etschmann, B., Zhong, R., Yaxley, G.M., Paterson, D. Evidence of sub-arc mantle oxidation by sulphur and carbon. *Geochemical Perspectives Letters* **3**, 124-132 (2017).
57. Liu, C-Z., Wu, F-W., Chung, S-L., Li, Q-L., Sun, W-D., Ji, W-Q. A 'hidden' ^{18}O-enriched reservoir in the sub-arc mantle. *Scientific Reports* **4**, 4232 (2014).
58. Mathez, E.A. Influence of degassing on oxidation states of basaltic magmas. *Nature* **310**, 371-375 (1984).

4.7. FIGURES

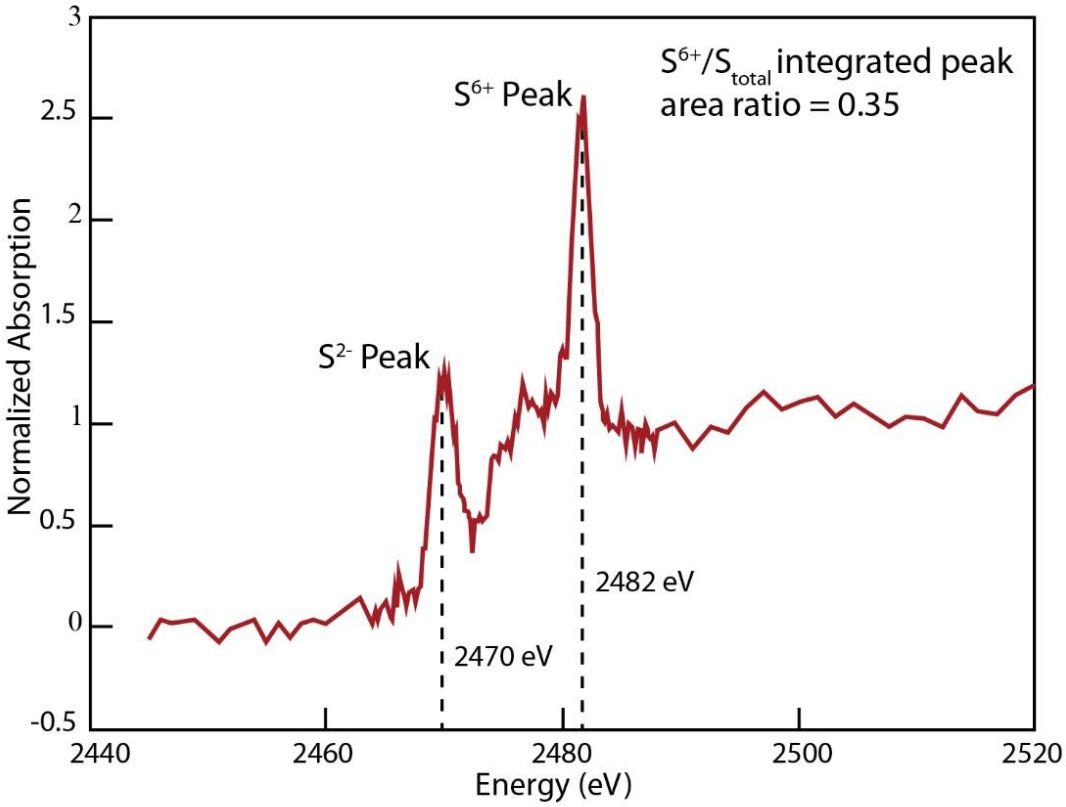

Fig. 1. Sulphur µ-XANES spectra of the studied apatite. Averaged µ-XANES spectra showing the oxidation state of sulphur in apatite crystallized from a silicate melt that percolated through the subcontinental lithospheric mantle in southern Patagonia.

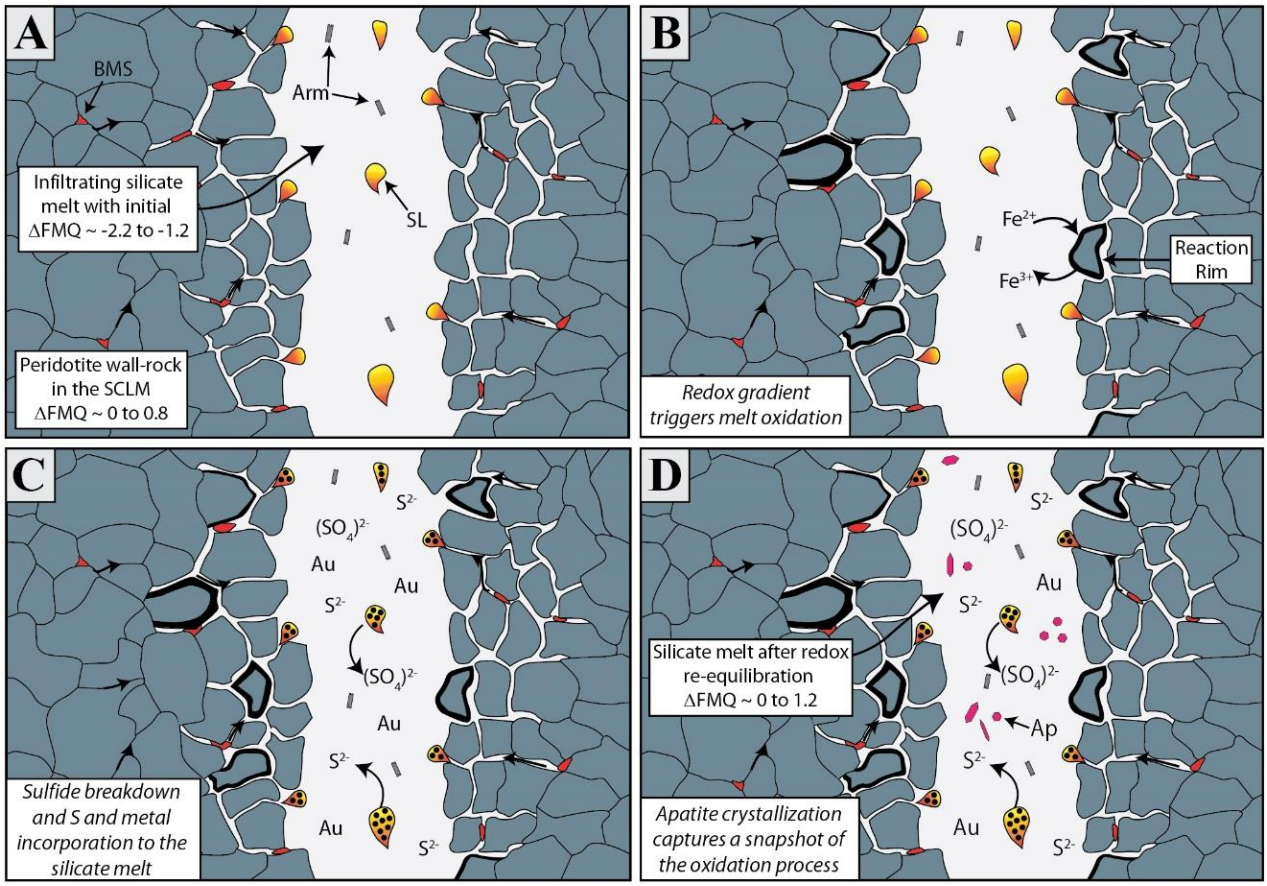

Fig. 2. Mechanisms leading to oxidation of percolating melts and ore metal incorporation. (**A**) The reduced silicate melt enters the subcontinental lithospheric mantle, entraining immiscible sulfide liquids. A redox gradient is generated between the reduced melt and the more oxidized peridotite wall-rock. (**B**) The silicate melt starts to re-equilibrate with the surrounding peridotite wall-rock. (**C**) Increasing oxygen fugacity triggers changes in the sulphur solubility promoting metal sulfide breakdown and release of sulfide, sulfate, and Au into the percolating silicate melt. (**D**) Quenching upon rapid ascent induced apatite crystallization, which records a snapshot of the melt-SCLM interaction process.

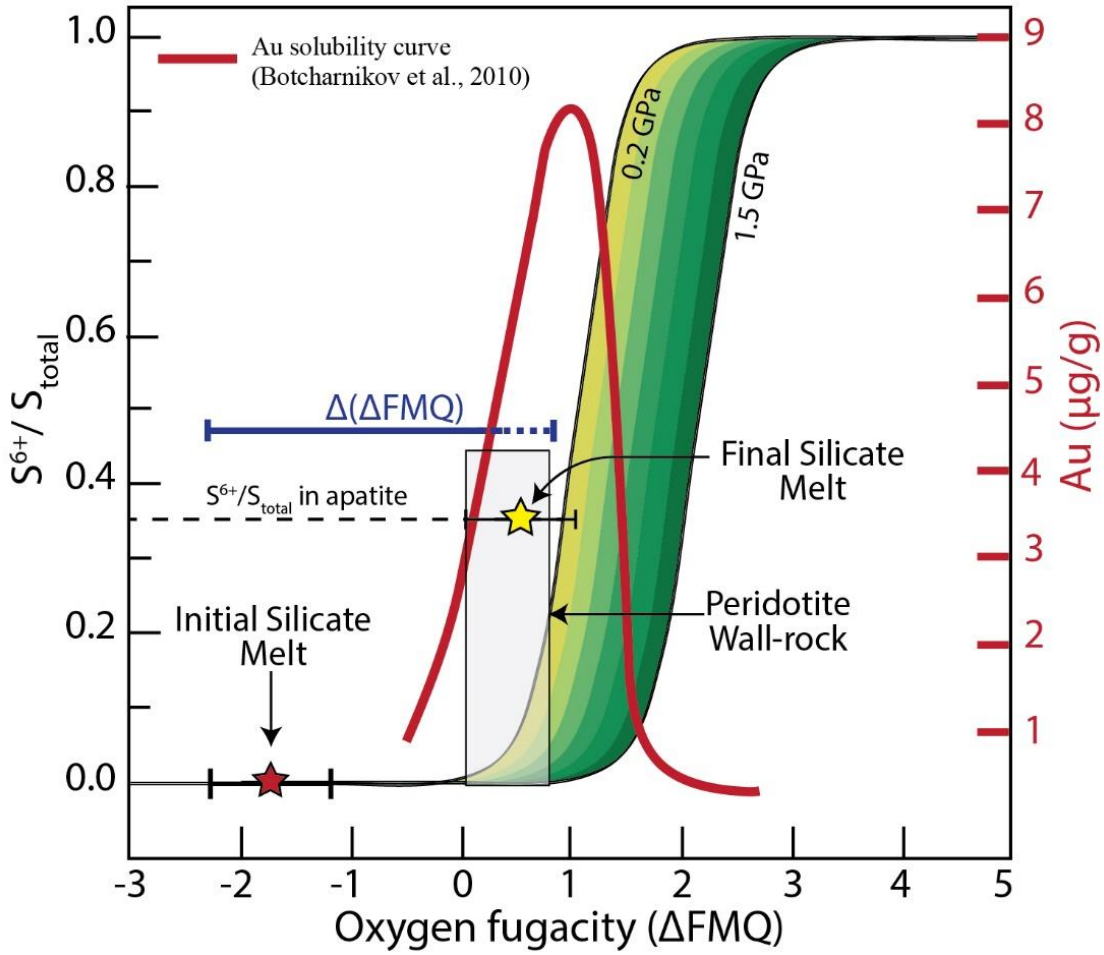

Fig. 3. Redox evolution of the silicate melt and the effect of redox gradients on Au solubility. Plot of S^{6+}/S_{total} vs. oxygen fugacity, expressed log units relative to the fayalite-magnetite-quartz mineral buffer (ΔFMQ). The diagram shows the initial and final redox conditions of the originally reduced silicate melt that interacts with the more oxidized peridotite wall-rock. The green shaded area illustrates the changes in sulfur speciation and solubility in silicate melts with pressure after Jugo *et al.* (*17*) and Matjuschkin *et al.* (*38*). The redox gradient generated between the melt and the peridotite wall-rock, defined as Δ(ΔFMQ), promoted oxidation of the infiltrating melt leading to optimal Au solubility conditions.

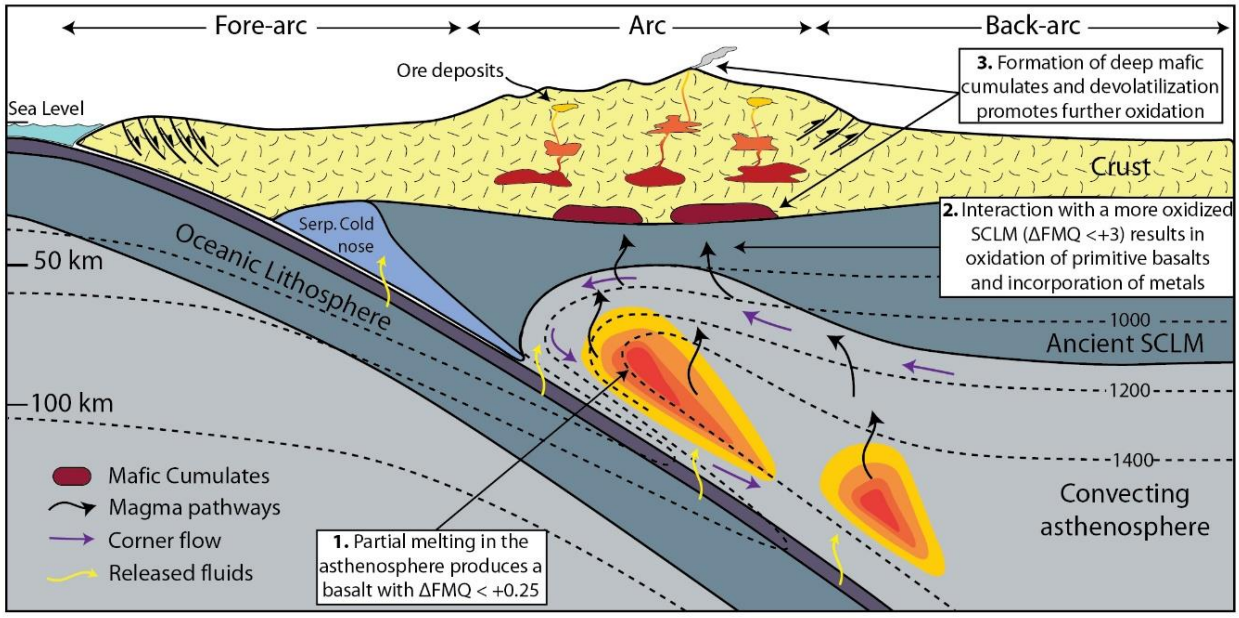

Fig. 4. Redox evolution of silicate melts formed within an arc setting, and its impact on ore deposit formation. The conceptual model aims to highlight the difference between the redox state of the sub-arc asthenospheric and lithospheric mantle. Initial melting in the asthenosphere generates primitive, reduced melts (1). Following ascent and interaction with the more oxidized lithosphere (2) a redox gradient is created, triggering oxidation of the ascending melts and increasing their potential for scavenging sulfur and metals. Later differentiation within the crust (3) through the formation of deep arc cumulates (*9*) and devolatilization (*58*), among other processes, induces further oxidation of arc magmas leading to the formation of ore deposits.

4.8. Acknowledgments

We thank Tony Lanzirotti and Matt Newville for assistance with µ-XANES analyses at the GeoSoilEnviroCars (Sector 13), Advanced Photon Source (APS), Argonne National Laboratory. This study was funded by the Iniciativa Científica Milenio through Millennium Nucleus for Metal Tracing along Subduction Grant NC130065. Additional funding for analytical work was provided by the FONDAP project 15090013 "Centro de Excelencia en Geotermia de Los Andes, CEGA". Santiago Tassara acknowledges CONICYT for support through a Ph.D. scholarship #21170857. This research used resources of the Advanced Photon Source, a U.S. Department of Energy (DOE) Office of Science User Facility operated for the DOE Office of Science by Argonne National Laboratory under Contract No. DE-AC02-06CH11357. The DID-UACh project #S-201505 financed the fieldwork.

4.9. Author contributions

All the authors contributed substantially to the paper as a team including sampling, data acquisition and interpretation, construction of the model, and writing. M.R., D.M., F.B., and J.M.G.-J. conceived and designed the study. EPMA data acquisition was carried out by S.T. and B.A.K., under the supervision of A.C.S. µ-XANES data acquisition was carried out by S.T. and B.A.K., under the supervision of A.F. M.E.S. and A.C. provided the samples. All the authors analysed and discussed the data and revised the manuscript, which was written by S.T. and M.R.

CHAPTER 5. A COMPLEX REDOX RECORD IN PRIMITIVE MELTS FROM THE SOUTHERN ANDES

Tassara, S.[1,2]*, Reich, M.[1,2], Cannatelli, C.[1,2], Konecke, B.A.[3], Kausel, D.[1,2], Morata, D.[1,2], Barra, F.[1,2], Simon, A.C.[3], Fiege, A.[4], Morgado, E.[1,5]

[1]*Department of Geology and Andean Geothermal Center of Excellence (CEGA), FCFM, Universidad de Chile, Plaza Ercilla 803, Santiago, Chile.*
[2]*Department of Earth and Environmental Sciences, University of Michigan, Ann Arbor, Michigan 48109, U.S.A.*
[3]*Institute of Geophysics and Tectonics, School of Earth and Environment, University of Leeds, UK.*
[4]*Department of Earth and Planetary Sciences, American Museum of Natural History, New York 10024-5192, U.S.A.*

(*) Corresponding author: Santiago Tassara
Keywords: melt inclusions, arc basalts, redox, oxygen fugacity, XANES.

5.1. ABSTRACT

The oxygen fugacity (fO_2) of the Earth's upper mantle and its melting products is a parameter of paramount significance controlling the geochemical evolution of arc magmas and their connection with the continental crustal construction and growth. Several studies have focused on the fO_2 archive of peridotite xenoliths, primitive melts in relatively young arc settings, and MORB, leading to complex variations among the different tectonic environments. In contrast, few studies have attempted to examine the early redox history of primitive magmas in mature arcs, thereby limiting our understanding of the nature and evolution of fO_2 during the subduction cycle. Here, we investigate the basaltic tephra from the Los Hornitos monogenetic cones in central-southern Chile, which are among the most primitive materials reported in the Southern Andes (olivine Mg# ≤ 92.5, and Ni ≤ 5000 ppm). These features offer a unique opportunity to explore the fO_2 conditions below the Andean arc by studying olivine phenocrysts and their contained crystal and melt inclusions. We integrated EPMA, LA-ICP-MS, and µ-XANES analyses to constrain the redox conditions recorded in the basaltic tephra by three different and self-reliant methods. First, we determined the fO_2 based on the olivine-spinel equilibrium, yielding values from ΔFMQ +0.4 to +1.4. Second, we constrained the fO_2 conditions of melt inclusions using Fe-XANES data and the redox dependent olivine-melt vanadium partitioning. After correcting for post-entrapment crystallization and diffusive iron loss, the Fe-XANES data indicate that the melt inclusions were trapped at ΔFMQ +2.5 ± 0.5. Results using the olivine-melt vanadium partitioning oxybarometer in melt inclusions are in agreement with Fe-XANES, yielding ΔFMQ values of +2.6 ± 0.3. In order to test the potential effects of other post-entrapment modification of the melt inclusions fO_2 prior to eruption, we assessed the residence time of these magmas using Mg-Fe interdiffusion modelling in olivine. The short residence times (<200 days) compared to vanadium re-equilibration models show that the melt inclusions still preserve the archive of their true entrapment fO_2 conditions. Therefore, we argue that the observed fO_2 differences between the olivine-spinel mineral and the olivine-hosted melt inclusions results from redox processes during the early history of these

magmas in the deep lithosphere, which are yet to be determined. Our data reveals a complex fO_2 history of primitive melts in the southern Andes and open a new avenue of research, while providing a cautionary note on the direct extrapolation of primitive melts fO_2 values to that of their mantle source.

5.2. INTRODUCTION

In the absence of direct samples of the Earth's upper mantle (i.e., peridotite xenoliths), olivine-hosted melt inclusions (MIs) are the closest natural window available to investigate deep magmatic processes. Thus, MIs have received increasing attention for tracing the early geochemical history of primitive magmatic systems (Lowenstern, 1995; Sobolev and Chaussidon, 1996; Shimizu, 1998; Laubier et al., 2007; Kent, 2008; Manzini et al., 2017; Reinhard et al., 2018; Søager et al., 2018; Neave et al., 2018; Bouvier et al., 2019; Howarth et al., 2019; Hanyu et al., 2019).

Recently, olivine-hosted MIs have also been used to explore the oxygen fugacity (fO_2) of their mantle source region, and to evaluate the subsequent post-melting redox history of magmas during storage, differentiation, and ascent (e.g., Kelley and Cottrell, 2012; Hartley et al., 2017; Head et al., 2018). This is of key interest to better constrain, for instance, the fO_2 conditions at which magmas are sourced in the mantle wedge of subduction zones. The predominant view holds that the mantle source region in subduction zones is oxidized due to the reaction with oxidizing fluids derived from the dehydrating slab (Brandon and Draper, 1996; Wood et al., 1990; Parkinson and Arculus, 1999; Kelley and Cottrell, 2009; 2012). An alternative hypothesis proposes that the fO_2 of the mantle source region in subduction zones is undistinguishable from that of mid ocean ridges, suggesting that arc basalts inherit their oxidized nature during differentiation on its way to the surface (Lee et al., 2005; 2010; Dauhpas et al., 2009; Mallmann and O'Neill, 2009; Tang et al., 2018). Despite that, mantle-derived magmas are commonly expected to result in continued oxidation during ascent, crystallization, degassing and assimilation, recent studies on olivine-hosted MIs have traced evidence of progressive reduction along with differentiation (Cottrell and Kelley, 2012; Hartley et al., 2017). This evidence highlights that both source melting and post-melting redox processes controlling the fO_2 signature of arc magmas remains enigmatic, requiring further investigation.

The most direct tracer of fO_2 in a magmatic system is the measurement of the oxidation state of iron (Fe), its most abundant redox-sensitive element (Carmichael, 1991; Condie, 1993; Hofmann, 1988; O'Connor, 1965; Wilke, 2004; Cottrell and Kelley, 2009). Microscale X-ray absorption near edge structure (µ-XANES) spectroscopy allows determining the speciation of Fe in small-sized samples such as MIs. The Fe^{3+}/Fe_{tot} ratio of glasses has been calibrated for a range of compositions and fO_2 (e.g., Berry et al., 2003; Cottrell et al., 2009; Farges et al., 2004; Galoisy et al., 2001; Giuli et al., 2003, 2011, 2012; Knipping et al., 2015; Wilke et al., 2001, 2004; Fiege et al., 2017), making the use of Fe µ-XANES methods particularly useful for tracing the early redox processes in MIs. However, the premise that olivine-hosted MIs behave as closed systems after their entrapment (e.g., Sobolev, 1996; Cherniak, 2010) has been challenged by several studies. Both natural and experimental studies have shown that the MI-host system is open to, at least, post-entrapment diffusion of Fe^{2+} and H^+ that can affect the redox state of the inclusions (Danyushevsky et al., 2000, 2002; Gaetani et al., 2012; Bucholz et al., 2013; Hartley et al., 2015). Therefore, recognizing the extent to which post-entrapment processes affects the fO_2 of a melt inclusion assemblage has become crucial, making their use as tracers of deep redox processes at least

challenging. A more recently developed approach to constrain the fO_2 in olivine-hosted MIs is the redox-dependent partitioning of the multivalent element vanadium (V) between olivine and hydrous basaltic melts (Gaetani and Grove, 1997; Canil and Fedorchouk, 2001; Papike et al., 2013; Laubier et al., 2014; Shihinka et al., 2018). This approach is more robust to post-entrapment modifications because of the trace abundance of V in melts and its generally incompatible behavior in olivine (Shishkina et al., 2018). Therefore, a comparison between various fO_2 approaches, including mineral (e.g., olivine-spinel equilibrium) and melt inclusion-based oxybarometers may offer a unique opportunity to improve our knowledge about the fO_2 conditions of parental melts, and also test the effects of post-entrapment modifications. Such an approach would be particularly relevant to test in a mature arc setting, where redox data of primitive melts are scarce and the nature and evolution of fO_2 during the subduction cycle remains largely unconstrained.

In this study, we explore the redox record of the primitive basaltic eruptive products of Los Hornitos mafic monogenetic vents from the transitional Southern Volcanic Zone in the Andes of south-central Chile. These are among the most primitive materials reported in the Southern Andes, with olivine Mg# of up to ~93 as reported in previous studies (e.g., Salas et al., 2017). We integrate EPMA, LA-ICP-MS, and Fe µ-XANES analyses of olivine and their contained crystal and MIs to determine their fO_2 values by using a combination of three different and independent oxybarometers, namely olivine-spinel equilibrium, the ratio of oxidized to reduced iron in MIs, and the olivine-melt V partition coefficient. Our data reveal significant differences between the fO_2 conditions recorded by the crystal phase assemblage and the olivine-hosted MIs within a single suite of samples. After a detailed assessment of post-entrapment modifications of the MIs and olivine Fe-Mg diffusivity modeling aimed at determining residence times of magmas, our data indicate that the redox evolution of the primitive basaltic magmas of Los Hornitos is more complex than expected. We discuss the possible source and post-melting redox processes that could result in such fO_2 variations and explore its implications for the use of primitive basalts to directly trace their mantle source fO_2 conditions.

5.3. GEOLOGIC BACKGROUND AND SAMPLE MATERIAL

The Southern Volcanic Zone (SVZ) is a ~1400 km long arc segment that limits with the flat-slab subduction segment to the north at ~32° S, and with the subduction of the Chile Ridge towards the south at ~46° S (Fig. 1). The volcanism of the SVZ results from the subduction of the Nazca Plate (convergence velocity of 7 cm/year) beneath the South American continent (DeMets et al., 2010). This segment can be divided into four zones (northern, transitional, central, and southern) based on the geochemistry of the erupted volcanic products, although their precise limits remain uncertain (Sellés et al., 2004; Völker et al., 2011). Within this segment, the abundance of eruptions bringing primitive basaltic material to the surface decreases significantly towards the Northern SVZ, due to an increase in the crustal thickness (Tassara and Echaurren, 2012). However, in the Transitional SVZ (TSVZ) there are still a few examples of monogenetic eruptions containing primitive basalts (Salas et al., 2017). Among these, the Los Hornitos Cones (LHC) comprise two small monogenetic vents located ~9 km south of the Cerro Azul/Quizapu stratovolcano, in the Descabezado Grande Volcanic Field (DGVF), within the Chilean TSVZ (Fig. 1). The eruptive products of the LHC are basaltic lava flows and pyroclastic material. The tephra material is particularly primitive as evidenced by the Mg# of its olivine (Mg# = [MgO/(MgO+FeO)×100] in molar proportions) reaching values of up to ~93 (Salas et al., 2017).

Melt inclusion studies of eruptive products from the SVZ lavas are scarce and have mostly focused on individual stratovolcanoes (e.g., Witter et al., 2004; Zajacz and Halter, 2009; Rea et al., 2009; Watt et al., 2013). For example, data obtained from olivine-hosted MIs were used predominantly to constrain primitive magma compositions and melt generation parameters (e.g., Weller and Stern, 2018). Wehrman et al. (2014), on the other hand, presented a more regional study that aimed to determine the along-strike variability of volatiles in parental melts in the SVZ. These authors included in their regional analysis melt inclusions data from the LHC, indicating a strong subduction component. Their comparative analyses indicated that the olivine-hosted MIs from the LHC are among the most primitive compositions of the SVZ and suffered sulfur and chlorine outgassing. However, it is important to stress out that there are no studies that report fO_2 determinations in MIs of primitive eruptive materials in the SVZ, hampering our understanding of processes that occur on the mantle source of the parental melts.

Here, we examine the basaltic tephra from the explosive stages of the LHC because olivine-hosted inclusions in this material are less susceptible to recrystallization than in basaltic lavas (see Hartley et al., 2017). The tephra material is rich in euhedral olivine phenocrysts that contain abundant Cr-spinel and melt inclusions. Olivine grains were hand-picked and inspected individually for the occurrence of MIs. Detailed petrographic observations revealed that MIs are present in almost all olivine grains from the LHC. The inclusions are colorless to light brown, rounded to elongated and vary in size from 10 to 90 µm (Fig. 2A-C). Except for the smallest MIs (~5 to 10 µm), they always display a shrinkage bubble and commonly, accidental crystals of Cr-spinel. These features are characteristic of olivine-hosted MIs reported in the literature (Cannatelli et al., 2016, and references therein). The MIs commonly occur as isolated inclusions, making it difficult to define melt inclusion assemblages (MIA) genetically related due to the lack of symmetry in olivine. For analysis, the olivine phenocrysts were mounted in epoxy mounts and polished individually until MIs were exposed. MIs were carefully examined and selected to avoid cracks and embayments that could have reset the system after the melt entrapment; also, only MIs completely enclosed within the host crystal and devoid of any evidence of recrystallization were picked for analysis.

5.4. ANALYTICAL METHODS

5.4.1. Electron probe microanalysis (EPMA) and electron backscatter diffraction (EBSD)

The concentrations of major and minor elements in olivine, Cr-spinel, and MIs were quantitatively characterized by wavelength-dispersive spectrometry (WDS) using a CAMECA SX-100 electron microprobe at the University of Michigan in Ann Arbor. An acceleration voltage of 20 kV, a beam current of 10 nA, and a focused beam was used for olivine and Cr-spinel analyses. Counting times of 20 s on the peak and 10 s on the background position were used for all elements. For melt inclusion analysis, an acceleration voltage of 15 kV, a beam current of 5-10 nA, and a beam size of 5 µm was used. Peak counting time of 10 s were used for all elements when analyzing the MIs, excepting 5 s for Na and K. Precautions were taken to prevent electron beam damage of glass (e.g., alkali diffusion and Si, Al burn-in; Morgan and London 2005).

Crystallographic orientations of olivine crystals were determined using electron back-scatter diffraction methods (EBSD; Prior et al., 1999). These data were used in diffusion modelling, considering the fact the Fe-Mg diffusivity depends on the crystallographic orientation of olivine crystals. The EBSD data was obtained using a FEI Quanta 650 field emission scanning electron

microscope (FESEM) equipped with a Nordlys EBSD camera at the School of Earth and Environment, University of Leeds, UK.

5.4.2. Micro X-ray absorption near edge structure spectroscopy (µ-XANES)

In situ XANES analyses at the Fe *K*-edge were performed at the GSECARS 13-ID-E beamline of the Advanced Photon Source (APS), Argonne National Laboratory (Illinois, U.S.A.). The beamline covers an energy range of 2.4 to 28 keV and uses a set of Kirkpatrick-Baez (KB) focusing mirrors that result in a 2 µm × 1 µm (µ-XANES) focused beam, allowing for high spatial resolution. Energy selection was achieved using a Si (111) channel cut monochromator. The energy of the first derivative peak of Fe metal foil was set to the F K-edge energy of 7110.75 eV as determined by Kraft et al. (1996). All spectra were collected in fluorescence mode from 7062 to 7308 eV with a counting time per point of 1-2 s and step sizes of 3 eV from 7062 to 7107 eV; 0.1 eV from 7107 to 7137 (pre-edge); 2 eV from 7137 to 7308 eV. We emphasize that the fluorescence mode was chosen due to the nature of the samples which did not allow for transmission mode. All µ-XANES data were corrected for detector dead time and self-absorption. The XANES spectra were processed and calibrated according to the method described by Fiege et al. (2017).

5.4.3. Laser ablation inductively coupled plasma mass spectrometry (LA-ICP-MS)

The concentration of trace elements (La, Ce, Nd, Sm, Eu, Gd, Dy, Ho, Er, Yb, Lu, Rb, Ba, Th, U, Sr, Zr, Hf, Ti, Ni, and V) in olivine and MIs were obtained by laser ablation inductively coupled plasma mass spectrometry (LA-ICP-MS), using a ArF excimer laser 193 nm (Photon Machines Analyte G2) coupled to a quadrupole ICP-MS (ThermoFisher Scientific iCAPQ) at the Mass Spectrometry Laboratory of the Andean Geothermal Center of Excellence (CEGA), Universidad de Chile, Santiago. The counting time for one analysis was typically 180 s (60 s on gas blank to establish background and 120 s for data collection), unless limited by the small volume of material for the case of the MIs. The diameter of the laser beam was 12-40 µm, the frequency 7 Hz, and 4 J/cm2 of laser fluence. A maximum of 15 unknowns were bracketed by the measurement of two external standards: the NIST SRM 610 (primary) and the USGS BHVO2G (secondary). The secondary standard was repetitively analyzed and treated as an unknown, yielding both precision and the accuracy better than 10% for the analytical session. The data reduction was carried out using the Iolite software (Woodhead et al., 2007; Paton et al., 2011); Si or Al contents - determined by EMPA – were used as internal standards. Detection limits and standard errors for each element are presented in Appendixes 2 and 4.

5.4.4. Oxygen fugacity determination

We assessed the fO_2 values of the basaltic tephra material from LHC via three different and independent methods. The first one involves the olivine-spinel equilibrium, which is one of the most common approaches to estimate the redox state of upper mantle and basaltic rocks. The foundation of this oxybarometer relies on the presence of both Fe^{2+} and Fe^{3+} in spinel (Irvine, 1965), and several models have been developed over the years (O´Neill and Wall, 1987; Mattioli and Wood, 1988; Ballhaus et al., 1991). We used the model of Ballhaus et al. (1991), based on the olivine-orthopyroxene-spinel equilibrium, to constrain the fO_2 of the melts that produced the tephra material from LHC. This model is also applicable to orthopyroxene-undersaturated systems, at the risk of increasing the uncertainty in up to ~0.2 log units, as long as $X_{Fe}^{ol} < 0.15$ (Ballhaus et al., 1991). Temperature was calculated using the Fe-Mg spinel-olivine equilibrium thermometer

(Ballhaus et al., 1991), and pressure was assumed to be 1 GPa, resembling crustal pressures estimated for the TSVC (Tassara and Echaurren, 2012). The second redox meter takes into account the oxidation state of Fe (Fe^{2+} vs. Fe^{3+}) in the MIs to determine fO_2. The Fe^{3+}/Fe_{tot} ratios of the studied MIs were obtained using Fe µ-XANES following the procedure of Fiege et al. (2017), and the fO_2 values were translated to log units with respect to the FMQ buffer using equation 7 of Kress and Carmichael (1991), at 1200°C and 0.1 GPa. The third approach involves olivine-melt redox dependent vanadium (V) partitioning. V can be present as 2+, 3+, 4+, and 5+, although the states 3+ and 4+ prevail in natural magmatic systems (Borisov et al., 1987; Sutton et al., 2005). In Fe-Mg silicates, V^{4+} is more incompatible compared to V^{3+}. Therefore, rising fO_2 will increase the V^{4+}/V^{3+} ratio of the melt, modifying the partition coefficient of V between the silicates and the melt. We used the calibration of Shishkina et al. (2018) to determine the fO_2 in the MIs based on their V content measured using LA-ICP-MS. This method is based on the fO_2-dependent partitioning of V between olivine and melt ($D_V^{Ol/melt}$) and was calibrated at temperatures between 1025 and 1150 °C, and pressures between from 0.1 to 0.3 GPa (Shishkina et al., 2018).

5.5. RESULTS

5.5.1. Olivine composition

Olivine was the only significant silicate crystal phase recovered from the tephra material at LHC. The olivine phenocrysts are colorless to greenish-colored, euhedral to subhedral, and vary in size from ~150 to 1500 µm (Fig. 2A, B). Excluding a few smaller crystals (< 200 µm), olivine phenocrysts always host tens of µm-sized Cr-spinel mineral inclusions. The composition of the olivine cores hosting the Cr-spinel inclusions vary from 46.6 to 52.5 wt% MgO (Mg# from 87.6 to 92.5, with an average value of 91.1; Appendix 1). Selected in-situ trace element data of olivine obtained by LA-ICP-MS are presented in Appendix 2. Nickel concentrations ranges from 1360 to 5190 ppm and correlate positively with Mg# values. The most primitive olivine crystals have Ni contents slightly higher than those expected from simple melting of a peridotite source at a given Mg# (Herzberg, 2011), although they follow a typically low Ni fractionation trend (Appendix 1). The CaO concentration was determined by EPMA due to ^{40}Ca interference with ^{40}Ar during LA-ICP-MS analysis, and is slightly lower (1100 – 1700 ppm) than expected for olivine crystallized from peridotite-derived melts (Sobolev et al., 2007). The Fe/Mn ratios range between 41.8 and 58.9 (Appendix 2) and are also consistently lower than olivine derived from peridotite melts (Sobolev et al., 2007). The Cr content (148 – 590 ppm) correlates positively with Ni (R^2 = 0.64) and Al (R^2 = 0.5). The Al concentration of olivine (72 – 202 ppm) correlates positively with Ni (R^2 = 0.47) and negatively with Mn (R^2 = 0.33) (Appendix 2).

5.5.2. Cr-spinel composition

Cr-spinel inclusions occur as reddish to dark-brown euhedral crystals, ranging in size from 3 to 10 µm, commonly forming clusters of up to 10 crystals within olivine (Fig. 2A, B). A set of 21 Cr-spinel inclusions were analyzed, as well as their respective olivine hosts (Appendix 3). They show a narrow compositional range with Cr# varying from 63.5 to 74.1 (Cr# = Cr/(Cr+Al)×100, mol.%). These Cr# values are similar to Cr-spinels with the highest Cr# reported in the literature, underscoring their highly primitive nature (e.g., Kamchatka picrobasalts, Cr# = 60 - 80, Portnyagin et al., 2005). The Mg# of the Cr-spinel inclusions varies from 40.4 to 60.3 mol.%, even within the narrow range of Mg# content of the host olivine (Appendix 3). The Cr# of the spinel correlates

negatively with its Fe^{3+} contents (R^2 = 0.56; Fe^{3+} calculated based on perfect stoichiometry). There is no clear correlation between the Mg# of the Cr-spinel inclusions and the Mg# of their olivine hosts.

5.5.3. Melt inclusions composition

The major and minor element concentrations of the olivine-hosted MIs (normalized to a water free basis) can be found in Appendix 1. The measured MgO concentration range from 4.5 to 9.8 wt.%, and the SiO_2 concentrations vary from 46.4 and 54.9 wt.%. The FeO_{tot} and K_2O contents are 5.2-9.6 wt.% and 0.4- 1.2 wt.%, respectively. Major elements concentration versus the MgO content show no correlation for FeO_{tot} (R^2 = 0.04); Al_2O_3 and TiO_2, on the other hand, show a weak positive correlation with decreasing MgO (R^2 of 0.12 and 0.15, respectively). CaO decreases with increasing FeO_{tot} (R^2 = 0.32) and increases with increasing Al_2O_3 (R^2 = 0.51), whereas alkalis also show a weakly positive correspondence with increasing Al_2O_3 (R^2 = 0.14). The non-normalized total oxide wt.% of the analyzed MIs range from 94 to 99.78, likely due to the presence of significant amounts of water (Wehrman et al., 2014; Salas et al., 2017). Sulfur concentrations are widely variable, ranging from ~550 to ~3740 ppm, and Cl varies between 770 and 2278 ppm (average 1σ: 30 and 25 ppm respectively), as commonly reported in arc magmas (Wallace 2005; Straub and Layne 2003). Chlorine concentrations show a weak positive correlation with sulfur (R^2 = 0.32). Post-entrapment modifications and the recalculated composition of the MIs are addressed and discussed in section 4.5.

The trace element composition of the MIs is presented in Appendix 4 and their primitive upper mantle (PUM) normalized patterns (McDonough & Sun, 1995) are displayed in Figure 4. All analyzed inclusions show similar trace element contents, and distribution patterns are typical of those of arc magmas. They have relatively flat PUM-normalized patterns, particularly for the most incompatible elements, with concentrations lower than the average N-MORB (Fig. 3). The most notorious aspects of the trace element composition are the strongly positive Sr and Pb anomalies, and negative anomalies for Nb and Ta (Fig. 3), similar to those reported for primitive arc basalts (Smith and Jagoutz, 2017). An enrichment in large-ion lithophile elements (LILE, Ba, and Sr) is observed, and shows a good correspondence with K contents. The La/Yb ratios are relatively low and vary between 2.5 and 6.5, whereas the Rb/Yb ratios can be as high as 17.15 (Fig. 3).

When compared to the global composition of primitive arc magmas, the major and trace element signature of the olivine-hosted MIs studied here resembles those of primitive calc-alkaline basalts from intra-oceanic arcs such as from New Zealand, Aleutians, and the Solomon Islands (Sorbadere et al., 2011; Smith and Jagoutz, 2017).

5.5.4. Iron µ-XANES analysis of melt inclusions

A total of 45 melt inclusion Fe µ-XANES spectra were collected. Based on the shape of the post-edge region of the acquired spectra, a total of ten spectra that were clearly devoid of olivine host contamination were used to calculate their Fe^{3+}/Fe_{tot} ratio (Fig. 4). Although the Fe^{3+}/Fe_{tot} ratio can be slightly affected by melt composition and temperature (Kress and Carmichael 1991; Morreti 2005), Fiege et al. (2017) have recently provided empirical calibrations for basaltic glasses that allow to accurately calculate fO_2 from the Fe^{3+}/Fe_{tot} data obtained at the GSECARS 13-ID-E beamline of the Advanced Photon Source (APS). The calculated centroid energy of the pre-edge (Fig. 4) has been shown to be a function of the Fe^{2+} and Fe^{3+} relative contributions, where the weighted centroid changes gradually from Fe^{2+}- to Fe^{3+}-dominated with increasing oxidation state

of felsic to basaltic melts (e.g., Berry et al., 2003; Cottrell et al., 2009; Fiege et al., 2017). We used the recently described methods of Fiege et al. (2017) to fit and calibrate the measured spectra. The Fityk software (Wojdyr 2010) was used to fit the background spectra through a combination of exponentially modified Gaussian and linear functions and, subsequently, adding Gaussian functions to fit the background-corrected pre-edge peak. Fityk provides the intensity peak and area of each Gaussian, which were used to calculate the centroid energy position. We used the basaltic glass data of Fiege et al. (2017) as check standards for the data processing and calculation of the Fe^{3+}/Fe_{tot} ratios, leading to identical results within error. The measured Fe^{3+}/Fe_{tot} ratios of the studied MIs range from 0.37 to 0.49 (average 0.437 ± 0.05, 1σ) (Appendix 2). The effects of post entrapment modifications on the Fe^{3+}/Fe_{tot} ratios of the MIs are discussed below.

5.5.5. Post-entrapment modification of melt inclusions

The assumption that MIs behave as closed systems after their entrapment in a crystal host renders its potential to trace the composition of near-primary melts in volcanic systems (e.g., Sobolev, 1996; Cherniak, 2010). However, several studies have highlighted that post-entrapment processes can significant modify the original composition of the melt (e.g., Danyushevsky et al., 2000, 2002). In the particular case of olivine-hosted MIs, post-entrapment crystallization (PEC) is a near ubiquitous process altering the composition of the originally trapped melt (Hartley et al., 2017). During cooling of the melt inclusion-olivine system, olivine can crystallize at expense of the melt in the inclusion forming a rim along their walls, lowering the Mg# of the theoretical olivine in equilibrium with the remaining melt, and resulting in disequilibrium with the olivine host (Fig. 5). In addition to PEC, post-entrapment diffusive modifications reported in olivine hosted MIs include both hydration and dehydration (Chen et al., 2011; Gaetani et al., 2012; Hartley et al., 2015), loss of volatiles such as sulfur and CO_2 (Bucholz et al., 2013), and diffusive Fe^{2+} loss (Danyushevsky et al., 2000, 2002). In turn, the Mg# gradient within the newly formed rim of olivine after PEC can trigger and/or enhance Fe^{2+} loss (Danyushevsky et al., 2000, 2002). This process involves diffusive loss of Fe from the inclusion and gain of Mg, leading to a decrease in the total Fe content (Danyushevsky et al., 2000) (Fig. 5). Given the highly incompatible behavior of Fe^{3+} in olivine, both PEC and Fe^{2+} loss will increase the Fe^{3+}/Fe_{tot} ratio of the inclusion, significantly altering the original fO_2 of the trapped melt. Thus, assessing the extent to which this process occurred is fundamental before addressing the valence state of Fe in olivine-hosted MIs.

The MIs studied here are clearly in disequilibrium with their olivine host, as the Mg# of the olivine in equilibrium with the melt is significantly lower than our measured values for the host (Appendix 1). Figure 6 shows that PEC was certainly in part responsible of this disequilibrium. We modelled the reverse crystallization of the olivine rims to add them back to the inclusions using the Petrolog3 software (Danyushevsky and Plechov, 2011). The olivine equilibrium model of Ford et al. (1983) was used, and Fe^{3+} was assuming to be perfectly incompatible within olivine. The studied MIs have undergone variable PEC, ranging from 1.6 to 18.2 % by weight. However, this correction does not allow to determine the original composition of the inclusion if Fe^{2+} loss also occurred. For example, as explained by Laubier et al. (2012), if an inclusion is trapped at ~1300°C and cools to ~1200°C, PEC will happen. If the system is kept at ~1200°C enough time, the Mg# gradient between the melt inclusion and the olivine host will promote further diffusion of Fe out of the inclusion. The overall result of the combined processes could result in a melt inclusion with lower FeO concentration, but still in equilibrium with the host (Fig. 5). If olivine continues to grow within the inclusion, then the Mg# of the olivine in equilibrium will decrease. Correcting for PEC using reverse crystallization would thus result in the composition of the low-FeO inclusion in

equilibrium with the host, but not that of the originally trapped melt. To identify this effect, the composition of the inclusion is compared with that of the whole rock and/or the modelled liquid lines of descent. Figure 7 shows binary plots comparing the PEC-corrected composition of the MIs to the bulk rock data of Salas et al. (2017), and the liquid lines of descent modelled in Petrolog3 at ΔFMQ+1 and 1 kbar. The covariations presented in Figure 7 are consistent with fractional crystallization of olivine exclusively, implying that all the analyzed inclusions were trapped well before plagioclase and clinopyroxene started to crystallize. This might be the effect of high-water content in the melts, suppressing plagioclase crystallization by stabilizing the Ab component in the melt (e.g., Yoder, 1969; Sisson and Grove, 1993). However, Figure 7D also shows that the Fe content of the MIs at a given MgO value is systematically lower than expected from the modelled liquid line of descent and the whole rock data, particularly at lower MgO contents.

The above described features are indicative of significant Fe^{2+} loss in addition to PEC. The lower FeO content of the inclusions caused by Fe^{2+} loss has two main effects on its composition: (1) it will increase the relative concentration of all other major elements in the melt inclusion and (2) it will significantly increase its Fe^{3+}/Fe_{tot} ratio. Whereas (1) is not of great relevance for the purposes of this study, (2) is critical and needs corrections. Laubier et al. (2012) corrected the diffusive Fe^{2+} loss of olivine-hosted MIs based on correlations between trace elements and FeO contents. However, our trace element data do not show a similar trend, precluding the use of this method. Danyushevsky et al. (2000), on the other hand, proposed a correction based on eliminating any FeO variations that may have been originally present (i.e., defining a constant FeO content for the inclusions). To avoid this problem, we chose to use an alternative solution by virtually projecting the measured FeO content of the MIs to the FeO predicted by the liquid line of descent. The corrected data is presented in Appendix 1. We discuss the effects of this correction on the original Fe^{3+}/Fe_{tot} ratios in the next section.

5.5.6. Redox state constraints

The calculated fO_2 of the LHC basaltic tephra material using the olivine-spinel equilibrium model of Ballhaus et al. (1991) yield ΔFMQ values between +0.4 and +1.4 (mean +0.9 ± 0.43, 1σ) (Table 1, Appendix 3). The uncertainty in the ΔFMQ values were calculated as the propagated error from the calculations of each of the variables involved in the equation, including the EPMA data, the stoichiometric Fe^{3+} content estimated for Cr-spinel, and the equilibrium temperature (Davis et al., 2017). The calculated uncertainty increases when the Cr-spinel composition has low ferric concentrations, as noticed by Davis et al. (2017) (Appendix 3). These data show that the primitive melts from LHC are up to ~1.5 ΔFMQ units more oxidize that mid-ocean-ridge-basalts (MORBs), which usually record ΔFMQ values between -0.1 and +0.3 (Cottrell and Kelley, 2011; O'Neill et al., 2018; Zhang et al., 2018). The slightly oxidizing conditions recorded in LHC are characteristic of typical arc magmas (ΔFMQ: +1 - +2) (Richards, 2015).

The calculated fO_2 of the MIs using the Fe μ-XANES redox meter yield ΔFMQ values between +2.4 and +3.4 after the PEC correction, and between +1.9 to +3.3 (mean +2.5 ± 0.5, 1σ) when diffusive Fe^{2+} corrections were applied after the PEC correction (Table 2, Appendix 2). The effect of PEC on the original Fe^{3+}/Fe_{tot} ratio of the MIs was corrected using the procedure described by Hartley et al. (2017), which consists of diluting the Fe^{3+} measured by XANES by the calculated extent of PEC of each melt inclusion and then re-calculating the Fe^{3+}/Fe_{tot} ratio accordingly (Appendix 2). The correction for diffusive Fe^{2+} loss (Danyushevsky et al., 2000, 2002) was performed after the PEC correction, and consisted on adding the lost Fe^{2+} back to the inclusion according to the calculated liquid lines of descent, (Fig. 7D; Table 2).

Finally, we calculated the fO_2 of the MIs using the olivine-melt V partitioning redox meter, yielding similar results than the Fe µ-XANES. The fO_2 values estimated using this method ranged from ΔFMQ +2.2 to +3.3 (mean 2.6 ± 0.3, σ) (Table 3), calculated using the equation 5 from Shishkina et al. (2018), after obtaining the $D_V^{Ol/melt}$ for 21 different melt inclusion-olivine host pairs. The *D* values can be slightly affected by PEC, and therefore were corrected according to the degree of PEC of each melt inclusion.

5.6. DISCUSSIONS

The MIs trapped in Mg-rich olivine crystals from the LHC basaltic tephra display major and trace element trends that are indicative of olivine fractionation (Fig. 7). These trends suggest that the studied MIs constitute a genetically related suite and underline their highly primitive nature. Their trace element chemistry (Fig. 3) emphasizes the characteristic patterns of hydrous and LILE rich magmas formed after melting of an initially depleted MORB-type mantle source (low HREE) and the addition of slab-derived components (Smith and Jagoutz, 2017). Thus, the results presented here allow further exploring the redox record of typical primitive melts that have suffered little differentiation in a mature arc setting.

5.6.1. Assesing fO_2 differences at LHC

The fO_2 data at LHC indicate a difference in the redox state calculated using mineral equilibria vs. MIs. The olivine-spinel oxybarometer yield ΔFMQ values at +0.9 ± 0.4 (Table 1), while MIs Fe µ-XANES and olivine-melt V partitioning redox meter yield consistently higher values at ΔFMQ +2.5 ± 0.5 (Table 2) and 2.6 ± 0.3 (Table 3), respectively. Changes in the intensive variables of magmas affect the fO_2 estimations derived from its Fe^{3+}/Fe_{tot} ratio (Kress and Carmichael, 1991). However, increasing pressure from 0.1 to 1 GPa or decreasing pressure by 200 °C only results in an increase of ~0.15 log units with respect to the FMQ buffer, which is insignificant when considering the range of fO_2 values obtained and the associated errors.

Therefore, a ~1.5 log unit discrepancy in the fO_2 values might represent either an artifact resulting of post-entrapment oxidation affecting the MIs, or evidence of two different stages of redox evolution recorded in the mineral phases and melt inclusion assemblages. In addition to the PEC and Fe^{2+} loss corrections (see section 4.5), there are other post-entrapment diffusive processes that add further complications to the proper interpretation of fO_2 determinations in olivine-hosted MIs. Among these, the diffusive exchange of H^+ and Fe^{3+} with the external host and/or melt may have an impact on the redox state of the melt inclusion (Rowe et al., 2007; Gaetani et al., 2012; Gaetani et al., 2012; Bucholz et al., 2013; Hartley et al., 2015, 2017). In the next paragraphs, we discuss the potential effect of post-entrapment diffusive modification of MIs to assess the reliability of our fO_2 determinations based on Fe µ-XANES and olivine-melt V partitioning.

The degree to which post-entrapment diffusive modification processes can re-equilibrate the composition and/or oxidation state of an olivine-hosted melt inclusion, obliterating the original entrapment conditions, largely depends on the degree to which certain elements can be exchanged between the melt and host, or through the host. High diffusivities in the host crystal, higher partition coefficients between host crystal and melt, higher temperature, and smaller-sized host crystals and MIs enhance the re-equilibration (Qin et al., 1992). Iron can re-equilibrate almost completely with the surrounding melt on timescales of hours to days at magmatic temperature (Gaetani et al., 2012; Bucholz et al., 2013). Even with the commonly expected magma ascent and eruption simplicity of

monogenetic vents, timescales of hours to days is relatively very short considering that some systems record residence times of ~15 years (Johnson et al., 2008). Conversely, vanadium occurs at trace concentrations in the melt, has a much lower partition coefficient in olivine, and has also lower diffusivity than Fe in olivine, making it more robust to post-entrapment diffusive modifications (Qin et al., 1992).

It is important to note that the fO_2 values obtained for the MIs using Fe µ-XANES and $D_V^{Ol/melt}$ data corrected for PEC and Fe loss, and PEC, respectively, are consistent between each other. This means that, regardless of the specific mechanism, if post-entrapment diffusive re-equilibration processes altered the original fO_2, it occurred over long time scales that resulted in the obliteration of both the V concentration and the Fe^{3+}/Fe_{tot} ratio of the MIs. One way to evaluate this effect involves calculating the degree of V re-equilibration that can occur over time. We used to the model of Qin et al. (1992) to estimate V re-equilibration timescales under different ΔFMQ conditions. A melt inclusion with a diameter of 80 µm and an olivine host of 800 µm was used, consistent with our samples, and the V diffusivity $D_V^{Ol/melt}$ data was taken from Spandler et al. (2010) and Shishkina et al. (2018), respectively. Figure 8 shows the results of the modelling, suggesting that a significant V re-equilibration (~80%) will occur after two years at ΔFMQ = 0, and after four years at ΔFMQ = +2. In contrast, complete V re-equilibration will occur only after approximately five years. At higher fO_2's, the inclusion will take even longer to re-equilibrate (Fig. 8). It is important to highlight that the V diffusivity data of Spandler et al. (2010) was obtained at 1300°C and therefore the re-equilibration times can be considered as conservative.

Our second approach involved assessing whether post-entrapment modifications could have sufficiently re-equilibrated V concentrations within the olivine-hosted MIs. Necessarily, V diffusion timescales would have needed to be longer than the residence time of magma prior to eruption. We calculated residence times by means of Mg-Fe diffusion modelling on olivine crystal rims. Iron and Mg concentration profiles were measured in 8 olivine crystals from the LHC tephra material using EMPA. All the olivine crystals used for diffusion modelling were carefully selected according to the criteria described in Costa et al. (2008) and Shea et al. (2015). Two 1D traverse measurements in one crystal plane were used for verifying the obtained timescales (Fig. 9) from single olivine crystals (Shea et al., 2015), also ensuring that the diffusion-related gradients were not associated with crystal growth (Costa et al., 2008). To obtain high-resolution traverses, we coupled the EMPA measurements with the backscattered electron (BSE) images and back-scattered electron diffraction data (BSED). This method has been used successfully in previous studies (e.g., Martin et al., 2008; Hartley et al., 2016; Morgado et al., 2017; Pankhurst et al., 2018), and allows obtaining diffusion data irrespective of the crystallographic orientation of the olivine crystal section in the sample. We calculated the uncertainties in diffusion coefficient and consequent magmatic timescales following the procedure of Kahl et al. (2015). This method considers errors in the calculated temperature, fO_2, and activation energy. Calculations were made for a temperature range between 1100 to 1160 °C, and a pressure of 2 kbar at ΔFMQ = +1. Modelled results obtained solving Fick's second law for each profile diffusion coefficient resulting from its crystallographic orientation and obtained according to Philibert (1991). The calculated residence time yielded scales varying from 13 to 102 days (uncertainty of up to ~100 days), which can extend up to 204 days considering changes resulting from increasing pressure to values as high as 1.5 GPa. In Figure 9, two diffusion profiles yielding 38 and 52 days are shown.

Using these data, we proceeded to compare the time scales needed for V re-equilibration with time scales of magmatic residence. As seen in Figure 8, the calculated times of residence of the

LHC magma in the crust (<204 days) is far too short compared to the 2 years needed for significant vanadium re-equilibration to occur (~80%) at ΔFMQ = 0. Therefore, our modelled data confirm that the $D_V^{Ol/melt}$ were not significantly affected by post-entrapment diffusive re-equilibration processes. This result strongly suggests that the fO_2 values calculated using V partitioning data and Fe µ-XANES are representative of the original redox state of the MIs and differ from the fO_2 recorded in the mineral phase assemblage. The potential implications are discussed in the next section.

5.6.2. Two different redox conditions recorded in the LHC magmas?

Primitive basaltic melts have been widely used to constrain the oxidation state of the mantle (Evans, 2012). However, the ability of primitive melts to record the oxidation state of their mantle source has been questioned (e.g., Lee et al., 2005, 2010). It is likely that, if primary basaltic melts evolve from its original fO_2 condition on their way towards the surface, the calculated fO_2 of magmas would not be directly representative of their mantle source. It is commonly assumed that because of the primitive nature of some basalts, differentiation could have not significantly altered their original (primary) redox conditions. However, only a few studies have attempted to constrain the effects of magmatic differentiation on the redox state of primitive magmas (Kelley and Cottrell, 2012; Hartley et al., 2017), and none of them on mature arc settings.

The oxidation state of the LHC magmas recorded by the olivine-spinel equilibrium shows relatively common conditions for arc magmas, i.e., slightly more oxidized than MORBs (Fig. 10). However, the fO_2 recorded by the melt inclusion assemblage are up to ~1.5 orders of magnitude more oxidized, even when considering the error associated to each method (Fig. 10). Considering that post-entrapment processes did not significantly alter the melt inclusion redox meters, one alternative is that the fO_2 data at LHC record two different stages of redox evolution. Petrographic evidence shows that several MIs trapped accidental Cr-spinel crystals (Fig. 6B), suggesting that some of the MIs could have been formed during a later stage of magmatic evolution. Under this scenario, our data are indicative of magmatic oxidation from ΔFMQ = +0.9 ± 0.43 during the equilibration of olivine and Cr-spinel, to ΔFMQ = +2.5 ± 0.5 during the entrapment of the MIs. Oxidation of primitive arc magmas during ascent can be caused by assimilation of the more oxidized crustal rocks, which can remain unnoticed in primitive arc melts (Smith and Jagoutz, 2017). Although we cannot quantify this effect, we expect it to be relatively minor considering the short magmatic residence times calculated for the LHC eruptive products using Mg-Fe diffusion models in olivine (<204 days). Magma oxidation can also result from early crystallization of Fe^{2+}-bearing phases such as olivine and Cr-spinel, increasing the Fe^{3+}/Fe_{tot} ratio of the remaining melt. In the LHC, it is likely that crystallization of both olivine and Cr-spinel could have increased the Fe^{3+}/Fe_{tot} ratio of the remaining melt, given that both mineral phases have lower Fe^{3+}/Fe^{2+} ratios than the silicate melt (Appendix 1 and 3). Another possibility is related to sulfur degassing during ascent and storage. Sulfur outgassing occurs predominantly as SO_2, whereas the S redox equilibria in basaltic melts will be modulated by S^{6+} and/or S^{2-} species (Oppenheimer, 2003; Wallace, 2005; Metrich et al., 2009; Jugo et al., 2010). Considering the fact that the LHC MIs were among the most affected by degassing of the entire SVZ (Wehrman et al., 2014) and that calculated fO_2's point to predominantly S^{6+} species (Jugo et al., 2010), it is possible that S degassing might have bear an influence on oxidation of the remaining melt. However, the devolatilization of 1000 ppm of S^{6+} can result in the oxidation of 0.2% Fe^{2+} to Fe^{3+}, which translates to a variation in the fO_2 of the magmas of only ΔFMQ ~0.3, upon composition. Therefore, the effect of S degassing may not have been considerable but is worth exploring in future studies.

The differences in fO_2 at LHC may have resulted from a combination of the abovementioned processes rather than a single factor. However, the extent of such processes remains unknown and therefore there is insufficient evidence to explain the reportedly large redox variations. One further aspect is worth mentioning here: the large gradients in fO_2 recorded in the LHC eruptive products occurred despite the very low degree of geochemical evolution of the studied melts (i.e., Mg# of the studied olivine between 87.7 and 92.5). The Mg# of olivine is commonly used to determine whether a magma is sufficiently primitive to be in equilibrium with a peridotite source (e.g., Evans, 2012). However, our observations show that even at high Mg# and apparent equilibrium with a peridotite source, the redox state of primitive arc magmas may vary significantly, raising a cautionary note on the direct use of primitive arc melts as tracers of fO_2 of the subarc mantle.

An important question that arises from the previous discussion is *how can the melt fO_2 increase significantly while maintaining equilibrium with a peridotite source?* The answer to this question is not trivial and might be obscured by our relative lack of knowledge of the processes that affect magmas from their formation in the asthenosphere until they reach the crust – that is, during their ascent throughout the subcontinental lithospheric mantle (SCLM). The SCLM is the most stable and long-lived portion of the lithosphere (Griffin et al., 2009; Herzberg and Rudnick, 2012). It has a history that records the imprint of several episodes (and styles) of metasomatism, resulting in a complex geochemistry. Furthermore, it is known that sub-arc mantle xenoliths are relatively oxidized (e.g., Richards, 2015), pointing to an oxidized SCLM beneath arcs. It is possible that the SCLM might be even more oxidized than the underlying asthenospheric wedge, considering the fact that it has a longer residence time above the convective mantle undergoing continuous recycling by corner flow. Upon ascent, primitive magmas formed in the asthenosphere must break their way through the SCLM to reach the crust. Therefore, if magmas react with a more oxidized peridotite wall-rock during their ascent across the SCLM, they might oxidize while maintaining their primary -or near primary- Fe/Mg equilibrium. Quoting Kress and Charmichael (1991): "*... unless the ascending melt encounters wall rocks with substantially different ΔFMQ along its path, there will be little chemical driving force for oxygen diffusion into or out of the melt phase ... Consequently, the oxidation state of a melt that ascends as a closed system will reflect the oxidation state of its source region*". Thus, we suggest that ascending melts interacting with a more oxidized SCLM as an open system with respect to fO_2 could potentially explain some of the apparently contradictory evidence concerning the redox state of the mantle source of primitive melts, opening new avenues in the investigation of the redox state of arc magmas.

5.7. CONCLUSIONS

In this study, we explored the redox record of the basaltic tephra from Los Hornitos cones in central-southern Chile, which are among the most primitive materials reported in the Southern Volcanic Zone of the Andes with Mg# and Ni up to 92.5 and 5000 ppm, respectively. Oxygen fugacity data obtained from mineral equilibria and melt inclusion assemblages yielded significant differences in the calculated redox conditions. Olivine-spinel oxybarometry yielded fO_2 values ranging from ΔFMQ +0.9 ± 0.4, while the olivine-hosted MIs record uniformly more oxidizing conditions. fO_2 values calculated based on in-situ Fe µ-XANES analyses show values from ΔFMQ +2.5 ± 0.5, in agreement with the calculated fO_2 values based on the olivine-melt vanadium partitioning (ΔFMQ +2.6 ± 0.3). Our analysis of this discrepancy suggests that the fO_2 values of the LHC primitive melts were most likely imprinted during two different stages of redox evolution, regardless of post-entrapment modifications of the MIs. Based on our data, we suggest that the reported fO_2 gradient between the olivine-spinel and the MIs may result from a combination redox

processes in the deep lithosphere. We propose that the early the crystallization of olivine and Cr-spinel, and to lesser extent sulfur degassing, may have contributed to trigger the oxidation of the residual melt. Furthermore, we propose that oxidation of arc magmas during their ascent across the subcontinental lithospheric mantle may have also contributed to their oxidized nature while maintaining its apparent equilibrium with a peridotite source. Finally, our results show that fO_2 variations recorded in primitive arc melts may be more common than previously thought, and regardless of the mechanisms leading to the observed differences, they provide a cautionary note on the interpretation of calculated fO_2 values.

5.8. BIBLIOGRAPHY

Ballhaus, C., Berry, R.F. and Green, D.H. (1991) High pressure experimental calibration of the olivine-orthopyroxene-spinel oxygen geobarometer: implications for the oxidation state of the upper mantle. Contributions to Mineralogy and Petrology **107**, 2279-2302.

Bénard, A., Klimm, K., Woodland, A.B., Arculus, R.J., Wilke, M., Botcharnikov, R.E., Shimizu, N., Nebel, O., Rivard, C. and Ionov, D. (2018) Oxidising agents sub-arc mantle melts link slab devolatilization and arc magmas. Nature Communications 9, 3500.

Berry, A.J., O'Neill, H.St.C., Jayasuriya, K.D., Campbell, S.J. and Foran, G.J. (2003) XANES calibrations for the oxidation state of iron in a silicate glass. American Mineralogist 88, 967-977.

Borisov, A.A., Kadik, A.A., Zharkova, Y.V. and Kalinichenko, N.V. (1987) Effects of oxygen fugacity on the ration between valency forms of vanadium in magmas. Geochemistry international **24**, 111-116. (translated from Geokhimiya 6, 892-897).

Bouvier, A-S., Manzini, M., Rose-Koga, E.F., Nichols, A.R.L. and Baumgartner, L.P. (2019) Tracing of Cl input into the sub-arc mantle through the combined analyses of B, O and Cl isotopes in MIs. Earth and Planetary Science Letters **507**, 30-39.

Brandon, A.D. and Draper, D.S. (1996) Constraints on the origin of the oxidation state of mantle overlying subduction zones: An example from Simcoe, Washington, USA. Geochimica et Cosmochimica Acta **60**, 1739-1749.

Bucholz, C.E., Gaetani, G.A., Behn, M.D. and Shimizu, N. (2013) Post-entrapment modification of volatiles and oxygen fugacity in olivine-hosted MIs. Earth and Planetary Science Letters **374**, 145-155.

Canil, D. and Fedortchouk, Y. (2001) Olivine-liquid partitioning of vanadium and other trace elements, with applications to modern and ancient picrites. Canadian Mineralogist **39**, 319–330.

Cannatelli, C., Doherty, A.L., Esposito, R., Lima, A. and De Vivo, B. (2016) Understanding a volcano through a droplet: a melt inclusion approach. Journal of Geochemical Exploration **171**, 4-19.

Carmichael, I.S.E. (1991) The redox states of basaltic and silicic magmas: a reflection of their source regions? Contributions to Mineralogy and Petrology **106**, 129-141.

Chen, Y., Provsot, A., Schiano, P. and Cluzel, N. (2011) The rate of water loss from olivine-hosted MIs. Contributions to Mineralogy and Petrology **162**, 397-411.

Cherniak, D.J. (2010) REE diffusion in olivine. American Mineralogist 95, 362-368.

Condie, K.C. (1993) Chemical composition and evolution of the upper continental crust: contrasting results from surface samples and shales. Chemical Geology **104**, 1-37.

Costa, F., Dohmen, R. and Chakraborty, S. (2008) Time scales of magmatic processes from modeling the zoning patterns of crystals. Reviews in mineralogy and Geochemistry **69**, 545-594.

Cottrell, E. and Kelley, K.A. (2011) The oxidation state of Fe in MORB glasses and the oxygen fugacity of the upper mantle. Earth and Planetary Science Letters **305**, 270-282.

Cottrell, E., Kelley, K.A., Lanzirotti, A. and Fischer, R.A. (2009) High-precision determination of iron oxidation state in silicate glasses using XANES. Chemical Geology **268**, 167-179.

Danyushevsky, L.V. and Plechov, P. (2011) Petrolog3: integrated software for modeling crystallization processes. Geochemistry, Geophysics and Geosystems **12**, 1-32.

Danyushevsky, L.V., Della-Pasqua, F.N. and Sokolov, S. (2000) Re-equilibration of MIs trapped by magnesian olivine phenocrysts from subduction-related magmas: petrological implications. Contrib. Mineral. Petrol. **138**, 68–83.

Danyushevsky, L.V., McNeill, A.W. and Sobolev, A.V. (2002) Experimental and petrological studies of MIs in phenocrysts from mantle-derived magams: an overview of techniques, advantages and complications. Chemical Geology **183**, 5-24.

Dauphas, N., Craddock, P.R., Asimow, P.D., Bennett, V.C., Nutman, A.P. and Ohnenstetter, D. (2009) Iron isotopes may reveal the redox conditions of mantle melting from Archean to Present. Earth and Planetary Science Letters **288**, 255-267.

Davis, F.A., Cottrell, E., Birner, S.K., Warren, J.M. and Lopez, O.G. (2017) Revisiting the electron microprobe method of spinel-olivine-orthopyroxene oxybarometry applied to spinel peridotites. American Mineralogist **102**, 421-435.

DeMets, C., Gordon, R. and Argus, D.F. (2010) Geologically current plate motion. Geophysical Journal International **181**, 1-80.

Evans, K.A., Elburg, M. and Kamenetsky, V.S. (2012) Oxidation state of the subarc mantle. Geology **40**, 783-786.

Farges, F., Lefrère, Y., Rossano, S., Berthereau, A., Calas, G. and Brown, G.E. (2004) The effect of redox state on the local structural environment of iron in silicate glasses: a combined XAFS spectroscopy, molecular dynamics, and bond valence study. Journal of Non-Crystalline solids **344**, 176-188.

Fiege, A., Ruprecht, P., Simon, A.C., Bell, A.S., Göttlicher, J., Newville, M., Lanzirotti, T. and Moore, G. (2017) Calibration of Fe XANES for high-precision determination of Fe oxidation state in glasses: Comparison of new and existing results obtained at different synchrotron radiation sources. American Mineralogist **102**, 369-380.

Ford, C.E., Russel, D.G., Craven, J.A. and Fisk, M.R. (1983) Olivine-liquid equilibria: Temperature, pressure and composition dependence of the crystal/liquid cation partition coefficients for Mg, Fe^{2+}, Ca and Mn. Journal of Petrology **24**, 256-266.

Gaetani, G. and Grove, T. (1997) Partitioning of moderately siderophile elements among olivine, silicate melt, and sulfide melt: Constraints on core formation in the Earth and Mars. Geochimica et Cosmochimica Acta **61**, 1826-1846.

Gaetani, G.A., O'Leary, J.A., Shimizu, N., Bucholz, C.E. and Newville, M. (2012) Rapid reequilibration of H_2O and oxygen fugacity in olivine-hosted MIs. Geology **40**, 915-918.

Galoisy, L., Calas, G. and Arrio, M.A. (2001) High-resolution XANES spectra of iron in minerals and glasses: Structural information from the pre-edge region. Chemical Geology **174**, 307-319.

Giuli, G., Alonso-Mori, R., Cicconi, M.R., Paris, E., Glatzel, P., Eeckhout, S.G. and Scaillet, B. (2012) Effect of alkalis on the Fe oxidation state and local environment in peralkaline rhyolitic glasses. American Mineralogist **97**, 468-475.

Giuli, G., Paris, E., Hess, K.U., Dingwell, D.B., Cicconi, M.R., Eeckhout, S.G., Fehr, K.T. and Valenti, P. (2011) XAS determination of the Fe local environment and oxidation state in phonolite glasses. American Mineralogist 96, 631-636.

Giuli, G., Paris, E., Pratesi, G., Koeberl, C. and Cipriani, C. (2003) Iron oxidation state in the Fe-rich layers and silica matrix of Libyan Desert Glass: A high-resolution XANES study. Meteroritics and Planetary Science **38**, 1171-1186.

Griffin, W.L., O'Reilly, S.Y., Afonso, J.C. and Begg, G.C. (2009) The composition and evolution of the lithospheric mantle: A re-evaluation and its tectonic implications. Journal of Petrology **50**, 1185-1204.

Hanyu, T., Shimizu, K., Ushikubo, T., Kimura, J-I., Chang, Q., Hamada, M., Ito, M., Iwamori, H. and Ishikawa, T. (2019) Tiny droplets of ocean island basalts unveil Earth's deep chlorine cycle. Nature Communications **10**, 60.

Hartley, M.E., Neave, D.A., Maclennan, J., Edmonds, M. and Thordarson, T. (2015) Diffusive over-hydration of olivine-hosted MIs. Earth and Planetary Science Letters **425**, 168-178.

Hartley, M.E., Shorttle, O., Maclennan, J., Moussallam, Y. and Edmonds, M. (2017) Olivine-hosted MIs as an archive of redox heterogeneity in magmatic systems. Earth and Planetary Science Letters **479**, 192-205.

Head, E., Lanzirotti, A., Newville, M. and Sutton, S. (2018) Vanadium, sulfur, and iron valences in MIs as a window into magmatic processes: A case study at Nyamuragira volcano, Africa. Geochimica et Cosmochimica Acta **226**, 149-173.

Herzberg, C. (2011) Identification of source lithology in the Hawaiian and Canary Islands: implications for origins, Journal of Petrology **52**, 113–146.

Herzberg, C. and Rudnick, R. (2012) Formation of cratonic lithosphere: an integrated thermal and petrological model. Lithos **149**, 4-15.

Hickey-Vargas, R., Holbik, S., Tormey, D., Frey, F.A. and Moreno Roa, H. (2016) Basaltic rocks from the Andean Southern Volcanic Zone: Insights from the comparison of along-strike and small-scale geochemical variations and their sources. Lithos **258-259**, 115-132.

Hofmann, A.W. (1988) Chemical differentiation of the Earth: The relationship between mantle, continental crust, and oceanic crust. Earth and Planetary Science Letters **90**, 297-314.

Howarth, G.H. and Büttner, S.H. (2019) New constraints on archetypal South African kimberlite petrogenesis from quenched glass-rich MIs in olivine megacrysts. Gondwana Research **68**, 116-126.

Irvine, T.N. (1965) Chromian spinel as a petrogenetic indicator. Part I. Theory. Can. J. Earth. Sci. **2**, 648-671.

Johnson, E.R., Wallace, P.J., Cashman, K.V., Delgado-Granados, H. and Kent, A.J.R. (2008) Magmatic volatile contents and degassing-induced crystallization at Volcán Jorullo, Mexico: implications for melt evolution and the plumbing systems of monogenetic volcanoes. Earth and Planetary Science Letters **269**, 478-487.

Jugo, P.J., Wilke, M. and Botcharnikov, R.E. (2010) Sulphur K-edge XANES analysis of natural and synthetic basaltic glasses: implications for S speciation and S content as a function of oxygen fugacity. Geochimica et Cosmochimica Acta 74, 5926-5938.

Kelley, K.A. and Cottrell, E. (2009) Water and the oxidation state of subduction zone magmas. Science **325**, 605-607.

Kelley, K.A. and Cottrell, E. (2012) The influence of magmatic differentiation on the oxidation state of Fe in a basaltic arc magma. Earth and Planetary Science Letters **329-330**, 109-121.

Kent, A.J.R. (2008) MIs in basaltic and related volcanic rocks. Reviews in Mineralogy and Geochemistry **69**, 273-331.

Knipping, J.L., Behrens, H., Wilke, M., Göttlicher, J., and Stabile, P. (2015) Effect of oxygen fugacity on the coordination and oxidation state of iron in alkali bearing silicate melts. Chemical Geology **411**, 143–154.

Kraft, S., Stümpel, J., Becker, P. and Kuetgens, U. (1996) High resolution X-ray absorption spectroscopy with absolute energy calibration for the determination of absorption edge energies. Review of Scientific Instruments **67**, 681–687.

Kress, V.C., Carmichael, I.S.E. (1991) The compressibility of silicate liquids containing Fe2O3 and the effect of composition, temperature, oxygen fugacity and pressure on their redox states. Contributions to Mineralogy and Petrology 108, 82-92.

Laubier, M., Gale, A. and Langmuir, C. (2012) Melting and Crustal Processes at the FAMOUS segment (Mid-Atlantic Ridge): New Insights from Olivine-hosted MIs from multiple samples. Journal of Petrology **53**, 665-698.

Laubier, M., Grove, T.L. and Langmuir, C.H. (2014) Trace element mineral/melt partitioning for basaltic and basaltic andesitic melts: An experimental and laser ICP-MS study with application to the oxidation state of mantle source regions. Earth and Planetary Science Letters **392**, 265–278.

Laubier, M., Schiano, P., Doucelance, R., Ottolini, L. and Laporte D. (2007) Olivine-hosted MIs and melting processes beneath the FAMOUS zone (Mid-Atlantic-Ridge). Chemical Geology **240**, 129-150.

Lee, C-T.A., Leeman, W.P., Canil. D. and Li, Z-X.A. (2005). Similar V/Sc systematics in MORB and arc basalts: implications for the oxygen fugacities of their mantle source regions. Journal of Petrology **46**, 2313-2336.

Lee, C-T.A., Luffi, P., Le Roux, V., Dasgupta, R., Albaréde, F. and Leeman, W.P. (2010) The redox state of arc mantle using Zn/Fe systematics. Nature **468**, 681-685.

Lowenstern, J.B. (1995) Application of silicate MIs to the study of magmatic volatiles. In: J.F.H. Thompson (Ed). Magmas, fluids, and ore deposits. Mineralogical Society of Canada **23**, 71-99.

Mallmann, G. and O'Neill, H.S.C. (2009) The crystal/melt partitioning of V during mantle melting as a function of oxygen fugacity compared with some other elements (Al, P, Ca, Sc, Ti, Cr, Fe, Ga, Y, Zr and Nb). Journal of Petrology **50**, 1765-1794.

Manzini, M., Bouvier, A-S., Barnes, J.D., Bonifacie, M., Rose-Koga, E.F., Ulmer, P., Métrich, N., Bardoux, G., Williams, J., Layne, G.D., Straub, S., Baumgartner, L.P. and John, T. (2017) SIMS chlorine isotope analyses in MIs from arc settings. Chemical Geology **449**, 112-122.

Mattioli, G.S. and Wood, B.J. (1988) Magnetite activities across the MgAl2O4-Fe3O4 spinel join, with application to thermobarometric estimates of upper mantle oxygen fugacity. Contributions to Mineralogy and Petrology **98**, 148-162.

McDonough, W.F. and Sun, S.-s. (1995) The composition of the earth. Chemical Geology 120, 223-253.

Metrich, N., Berry, A.J., O'Neill, H.St.C. and Susini, J. (2009) The oxidation state of sulfur in synthetic and natural glasses determined by X-ray absorption spectroscopy. Geochimica et Cosmochimica Acta 73, 2382-2399.

Moretti, R. (2005) Polymerisation, basicity, oxidation state and their role in ionic modelling of silicate melts. Annals of Geophysics **48**, 583-608.

Morgan, G.B. and London, D. (2005) Effect of current density on the electron microprobe analysis of alkali aluminosilicate glasses. American mineralogist **90**, 1131-1138.

Neave, D.A., Shorttle, Ol., Oeser, M., Weyer, S. and Kobayashi, K. (2018) Mantle-derived trace element variability in olivines and their MIs. Earth and Planetary Science Letters **483**, 90-104.

O'Connor, J.T. (1965) A classification for quartz-rich igneous rocks based on feldspar ratios. U.S. Geological Survey Professional Paper B **525**, 79-84.

O'Neill, H.S.C. and Wall, V.J. (1987) The olivine-orthopyroxene-spinel oxygen geobarometer, the nickel precipitation curve, and the oxygen fugacity of the Earth's upper mantle. Journal of Petrology **28**, 1169-1191.

O'Neill, H.SC., Berry, A.J. and Mallmann, G. (2018) The oxidation state of iron in Mid-Ocean Ridge Basaltic (MORB) glasses: Implications for their petrogenesis and oxygen fugacities. Earth and Planetary Science Letters **504**, 152-162.

Oppenheimer, C. (2003) Volcanic degassing, treatise on geochemistry, 123-166.

Papike, J.J., Burger, P.V., Bell, A.S., Le, L., Shearer, C.K., Sutton, S.R., Jones, J. and Newville, M. (2013) Developing vanadium valence state oxybarometers (spinel-melt, olivine-melt, spinel-olivine) and V/(Cr+Al) partitioning (spinel-melt) for martian olivine-phyric basalts. American Mineralogist **98**, 2193–2196.

Parkinson, I.J. and Arculus, R.J. (1999) The redox state of subduction zones: insights from arc-peridotites. Chemical Geology **160**, 409-423.

Paton, C., Hellstrom, J., Paul, B., Woodhead, J. and Hergt, J. (2011) Iolite: Freeware for the visualization and processing of mass spectrometric data. Journal of Analytical Atomic Spectrometry.

Philibert, J., 1991. Atom Movements, Diffusion and Mass Transport in Solids. *Les éditions de Physique*, Les Ulis, France, p. 577.

Portnyagin, M.V., Plechov, P.Y., Matveev, S.V., Osipenko, A.B. and Mironov, N.L. (2005) Petrology of avachites, high-magnesian basalts of Avachinsky volcano, Kamchatka: I. General characteristics and composition of rocks and minerals. Petrology 13, 99–121.

Prior, D.J., Boyle, A.P., Brenker, F., Cheadle, M.C., Day, A., López, G., Peruzzio, L., Potts, G.J., Reddy, S., Spiess, R., Timms, N.E., Trimby, P., Wheeler, J. and Zetterström, L. (1999) The application of electron backscatter diffraction and orientation contrast imaging in the SEM to textural problems in rocks. American Mineralogist **84**, 1741–1759.

Qin, Z., Lu, F. and Anderson, A.T.Jr. (1992) Diffusive reequilibration of melt and fluid inclusions. American Mineralogist **77**, 565-576.

Rea, J.C., Varekamp, J.C., Mandeville, C., Goss, A.R. and Colvin, A. (2009) Regional magmatic setting of Callaqui Volcano, (S-Andes Chile). Abstrac, Portland GSA annual meeting, 33-14.

Reinhard, A.A., Jackson, M.G., Koornneef, J.M., Rose-Koga, E.F., Blusztajn, J., Konter, J.G., Koga, K.T., Wallace, P.J. and Harvey, J. (2018) Sr and Nd isotopic compositions of individual olivine-hosted MIs from Hawai'i and Samoa: Implications for the origin of isotopic heterogeneity in MIs from OIB lavas. Chemical Geology **495**, 36-49.

Richards, J.P. (2015) The oxidation state, and sulfur and Cu contents of arc magmas: implications for metallogeny. Lithos **233**, 27-45.

Rowe, M.C., Kent, A.J.R. and Nielsen, R.L. (2007) Determination of sulfur speciation and oxidation state of olivine hosted MIs. Chemical Geology **236**, 303-322.

Salas, P.A., Rabbia, O.M., Hernández, L.B. and Ruprecht, P. (2017). Mafic monogenetic vents at the Descabezado Grande volcanic field ((35.5°S–70.8°W): the northernmost evidence of regional primitive volcanism in the Southern Volcanic Zone of Chile. International Journal of Earth Sciences **106**, 1107-1121.

Schmidt, M.W. and Jagoutz, O. (2017) The global systematics of primitive arc melts. Geochemistry, Geophysics, Geosystems **18**, 2817-2854.

Sellés, D., Rodríguez, C., Dungan, M.A., Naranjo, J.A. and Gardeweg, M. (2004) Geochemistry of Nevado de Longaví volcano (36.2 ºS): a compositionally atypical arc volcano in the Southern Volcanic Zone of the Andes. Revista Geologica de Chile **31**, 293–315.

Shea, T., Costa, F., Krimer, D. and Hammer, J.E. (2015) Accuracy of timescales retrieved from diffusion modeling in olivine: a 3D perspective. American Mineralogist **100**, 2026-2042.

Shimizu, N. (1998) The geochemistry of olivine-hosted MIs in a FAMOUS basalt ALV519-4-1. Physics of the Earth and Planetary Interiors **107**, 183-201.

Shishkina, T., Portnyagin, M., Botcharnikov, R.E., Almeev, R.R., Simonyan, A.V., Garbe-Schönberg, D., Schuth, S., Oeser, M. and Holtz, F. (2018) Experimental calibration and implications of olivine-melt vanadium oxybarometry for hydrous basaltic arc magmas. American Mineralogist 103, 369-383.

Sisson, T.W. and Grove, T.L. (1993) Experimental investigations of the role of H_2O in calc-alkaline differentiation and subduction zone magmatism. Contributions to Mineralogy and Petrology **113**, 143-166.

Søager, N., Portnyagin, M., Hoernle, K., Holm, P.M. and Garbe-Schönberg, D. (2018) Lithos **310-311**, 225-240.

Sobolev, A.V. and Chaussidon, M. (1996) H2O concentrations in primary melts from supra-subduction zones and mid-ocean ridges: implications for H2O storage and recycling in the mantle. Earth and Planetary Science Letters **137**, 45-55.

Sobolev, A.V., Hofmann, A.W., Kuzmin, D.V., et al. (2007) The amount of recycled crust in sources of mantle-derived melts. Science **316**, 412–417.

Sorbadere, F., Schiano, P., Metrich, N. and Garaebiti, E. (2011) Insights into the origin of primitive silica-undersaturated arc magmas of Aoba volcano (Vanuatu arc). Contributions to Mineralogy and Petrology **162**, 995-1009.

Spandler, C. and O'Neill, H.St.C. (2010) Diffusion and partition coefficients of minor and trace elements in San Carlos olivine at 1300°C with some geochemical implications. Contributions to Mineralogy and Petrology **159**, 791–818.

Sutton, S.R., Karner, J., Papike, J., Delaney, J.S., Shearer, C., Newville, M., Eng, P., Rivers, M. and Dyar, M.D. Vanadium K edge XANES of synthetic and natural basaltic glasses and application to microscale oxygen barometry. Geochimica et Cosmochimica Acta **69**, 2333-2348.

Straub S.M. and Layne G.D. (2003) The systematics of chlorine, fluorine, and water in Izu arc front volcanic rocks: implications for volatile recycling in subduction zones. Geochim Cosmochim Acta **67**, 4179–4203.

Tang, M., Erdman, M., Eldridge, G. and Lee, C-T.A. (2018) The redox "filter" beneath magmatic orogens and the formation of continental crust. Science advances **4**, eaar4444.

Tassara, A. and Echaurren, A. (2012) Anatomy of the Andean subduction one: three-dimensional density model upgraded and compared against global-scale models. Geophysical Journal International 189, 161-168.

Volker, D., Kutterolf, S. and Wehrmann, H. (2011) Comparative mass balance of volcanic edifices at the Southern Volcanic Zone of the Andes between 33ºS and 44ºS. Journal of Volcanology and Geothermal Research **205**, 114-129.

Wallace, P.J. (2005) Volatiles in subduction zone magmas: concentrations and fluxes based on MIs and volcanic gas data. Journal of Volcanology and Geothermal Research **140**, 217–240.

Wallace, P.J. (2005) Volatiles in subduction zone magmas: concentrations and fluxes based on melt inclusion and volcanic gas data. Journal of Volcanology and Geothermal Research 140, 217-240.

Wehrmann, H., Hoernle, K., Jacques, G., Garbe-Schonberg, D., Schuman, K., Mahlke, J. and Lara, L.E (2014). Volatile (sulphur and chlorine), major, and trace element geochemistry of mafic to intermediate tephras from the Chilean Southern Volcanic Zone (33–43°S). International Journal of Earth Sciences **103**, 1945-1962.

Weller, D.J. and Stern, C.R. (2018) Along-strike variability of primitive magmas (major and volatile elements) inferred from olivine-hosted MIs, southernmost Andean Southern Volcanic Zone, Chile. Lithos **296-299**, 233-244.

Wilke, M., Partzsch, G.M., Bernhardt, R. and Lattard, D. (2004) Determination of the iron oxidation state in basaltic glasses using XANES at the *K*-edge. Chemical Geology **220**, 143-161.

Witter, J.B., Kress, V.C., Delmelle, P. and Stix, J. (2004) Volatile degassing, petrology, and magma dynamics of the Villarica Lava Lake, Southern Chile. Journal of Volcanology and Geothermal Research **34**, 303-337.

Wojdyr, M. (2010) Fityk: a general-purpose peal fitting program. Journal of Applied Crystallography **43**, 1126-1128.

Wood, B.J., Bryndzia, L.T. and Johnson, K.E. (1990) Mantle oxidation-state and its relationship to tectonic environment and fluid speciation. Science **248**, 337-345.

Woodhead, J., Hellstrom, J., Hergt, J., Greig, A. and Maas, R. (2007) isotopic and elemental imaging of geological material by laser ablation inductively coupled plasma mass spectrometry

Yoder, H.S., Jr. (1969) Calc-alkalic andesites: experimental data bearing on the origin of their assumed characteristics. In: Proceedings of the Andesite Conference. Oreg., Dep. Geol. Miner. Ind., Bull. **65**, 77-89.

Zajacz, Z. and Halter, W. (2009) Copper transport by high temperature, sulfur-rich magmatic vapor: evidence from silicate melt and vapor inclusions in a basaltic andesite from the Villarica volcano (Chile). Earth and Planetaru Science Letters **282**, 115-121.

Zhang, H.L., Cottrell, E., Solheid, P., Kelley, K., Hirschmann, M.M. (2018) Determination of $Fe^{3+}/\Sigma Fe$ of XANES basaltic glass standards by Mössbauer spectroscopy and its application to the oxidation state of iron in MORB. Chemical Geology **479**, 166-175.

Hartley, M.E., Morgan, D.J., Maclennan, J., Edmonds, M. and Thordarson, T. (2016) Tracking timescales of short-term precursors to large basaltic fissure eruptions through Fe-Mg diffusion in olivine. Earth and Planetary Science Letters 439, 58-70.

Martin, V. M., Morgan, D. J., Jerram, D. A., Caddick, M. J., Prior, D. J. and Davidson, J. P. (2008) Bang! Month-scale eruption triggering at Santorini volcano. Science **321**, 1178-1178.

Morgado, E., Parada, M. A., Morgan, D. J., Gutiérrez, F., Castruccio, A. and Contreras, C. (2017) Transient shallow reservoirs beneath small eruptive centres: Constraints from Mg-Fe interdiffusion in olivine. Journal of Volcanology and Geothermal Research **347**, 327-336.

Pankhurst, M. J., Morgan, D. J., Thordarson, T. and Loughlin, S. C. (2018) Magmatic crystal records in time, space, and process, causatively linked with volcanic unrest. Earth and Planetary Science Letters **493**, 231-241.

Kahl, M., Chakraborty, S., Pompilio, M. and Costa, F. (2015) Constraints on the nature and evolution of the magma plumbing system of Mt. Etna Volcano (1991–2008) from a combined thermodynamic and kinetic modelling of the compositional record of minerals. Journal of Petrology **56**, 2025-2068.

5.9. FIGURES

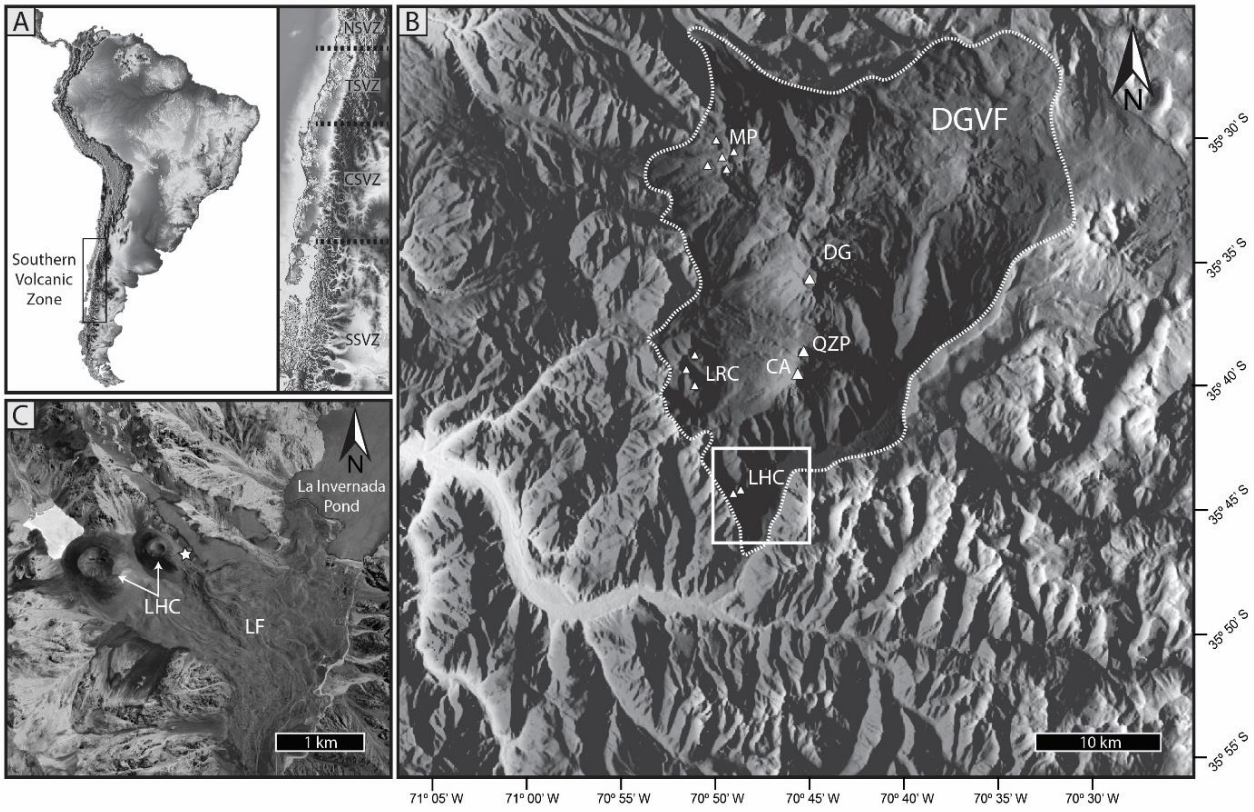

Figure 1. (A) Location of the transitional southern volcanic zone (TSVZ) in the Chilean Andes, South America. (B) Distribution of the main volcanic edifices in the Descabeazdo Grande Volcanic Field (DGVF) within the TSVZ. MP: Manantial Pelado; DG: Descabezado Grande; QZP: Quizapu: CA: Cerro Azul; LRC: La Resolana cones; LHC: Los Hornitos cones. (C). Inset in (B) closer view of the LHC and location of the simple site.

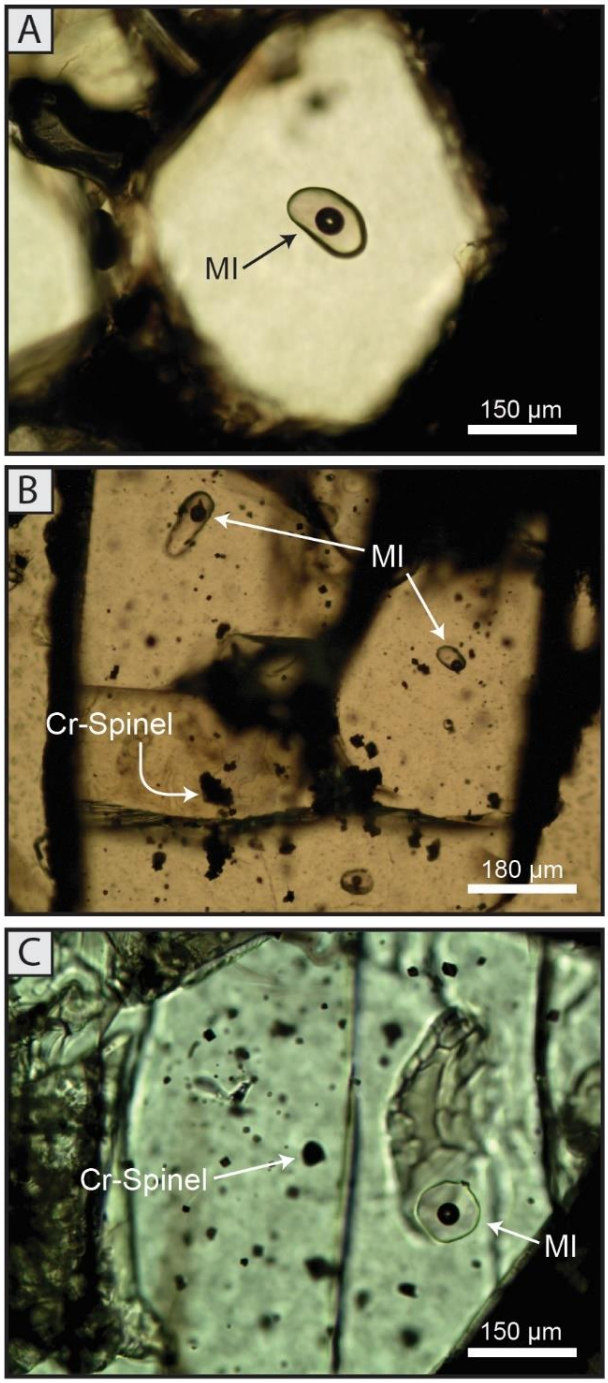

Figure 2. Plane polarized light images of olivine-hosted MIs from the LHC basaltic tephra. (A) MIs selected for study are commonly located in the center of olivine phenocrysts and far from any fracture and/or embayment, and devoid of any signs of recrystallization. (B) and (C) show typical occurrences of MIs, along with tens of Cr-spinel crystals within the same olivine host.

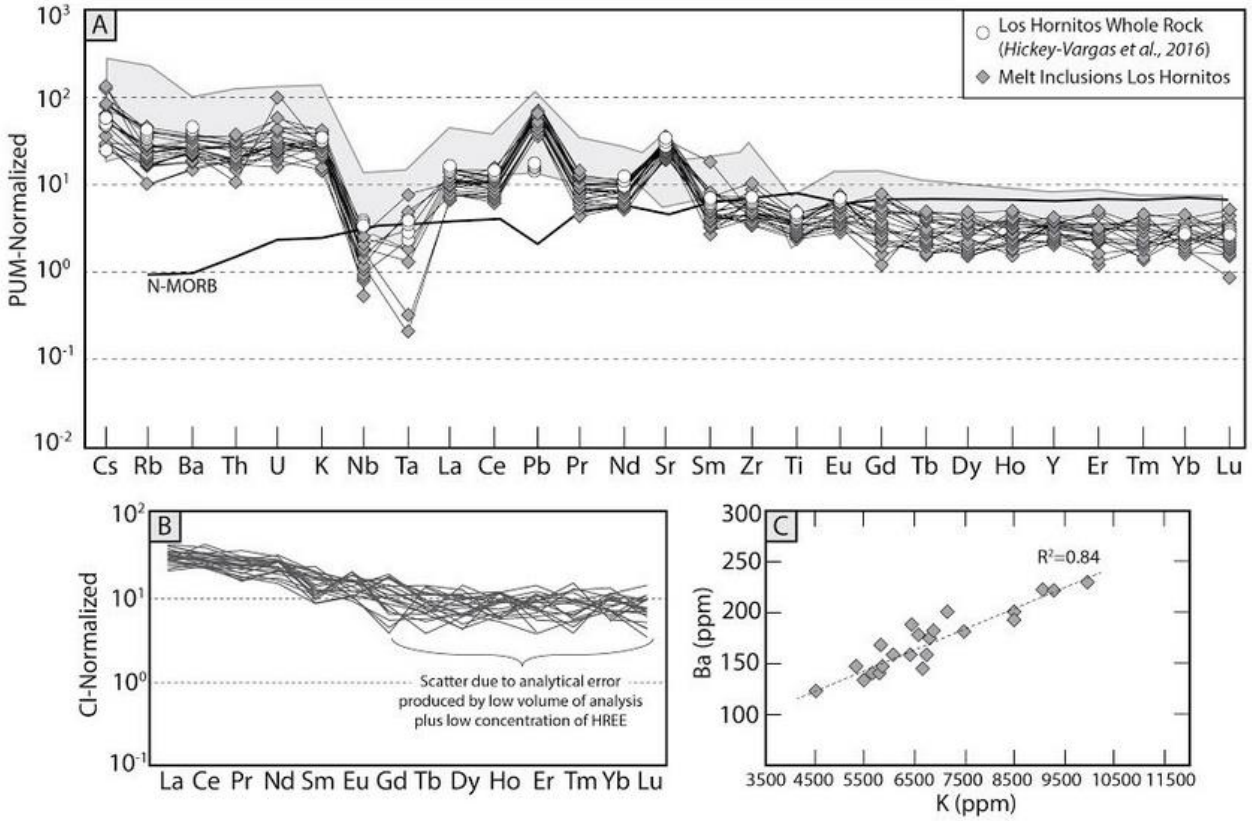

Figure 3. Trace element composition of the studied olivine-hosted MIs. (A) Primitive upper mantle (PUM)-normalized trace element data obtained by LA-ICP-MS. Bulk rock geochemical data of the LHC and volcanic products of the Descabezado Grande Volcanic Field are shown for comparison (shaded field; Hickey-Vargas et al., 2016). N-MORB field after McDonough and Sun (1995). (B) Rare earth element (REE) data of olivine-hosted MIs determined by LA-ICP-MS methods. (C) Melt inclusion Ba vs. K bivariant plot, showing a typical of arc magmas signature influenced by a slab fluid component.

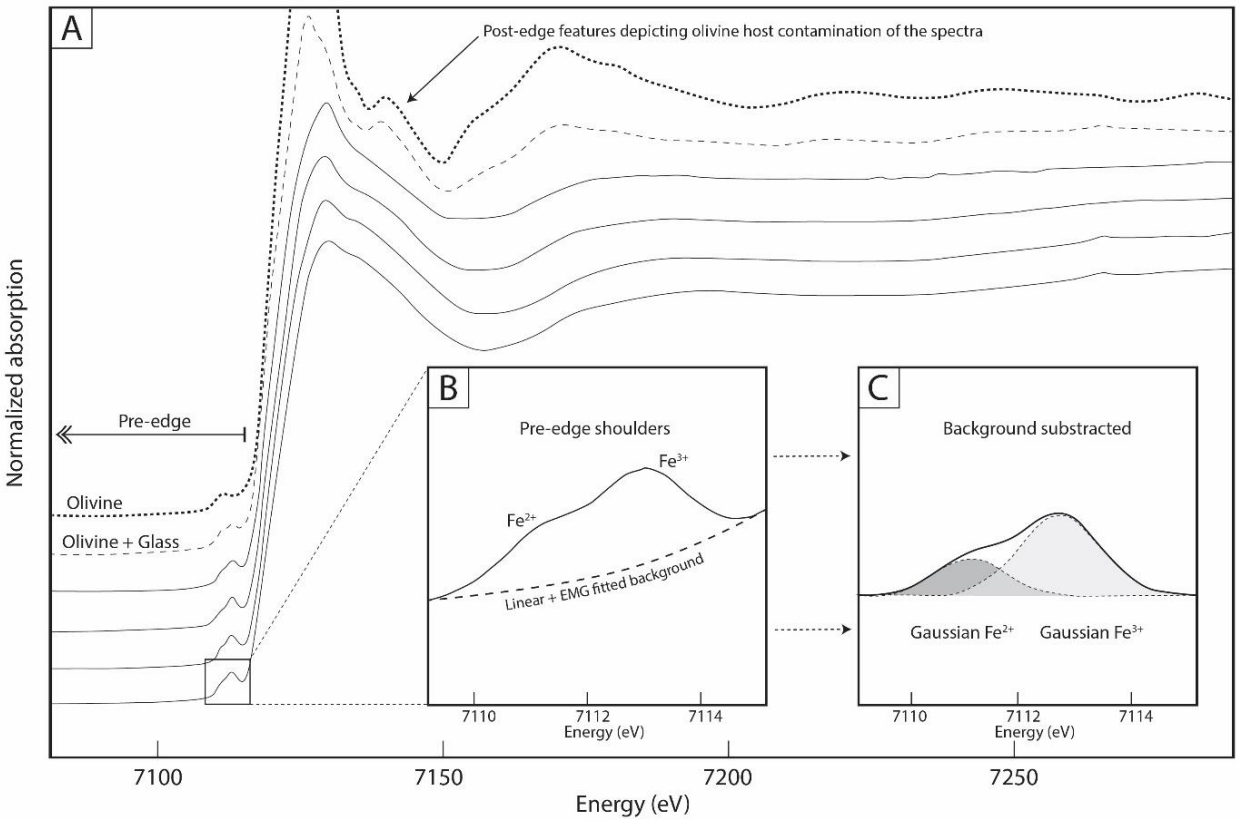

Figure 4. (A) Representative Fe □-XANES spectra of MIs from LHC showing their principal features. The spectra of olivine and olivine-melt inclusion mixture is also shown to underline the importance of checking the quality of the spectra. Host-contaminated melt inclusion spectra display post-edge features typical of olivine. (B) and (C) illustrate the fitting procedure where the fitted background is subtracted from the pre-edge region of the spectra (B). The position of the centroid energy is calculated afterwards based on the area and peak center of each of the gaussians applied to the Fe^{2+} and Fe^{3+} shoulders respectively (C).

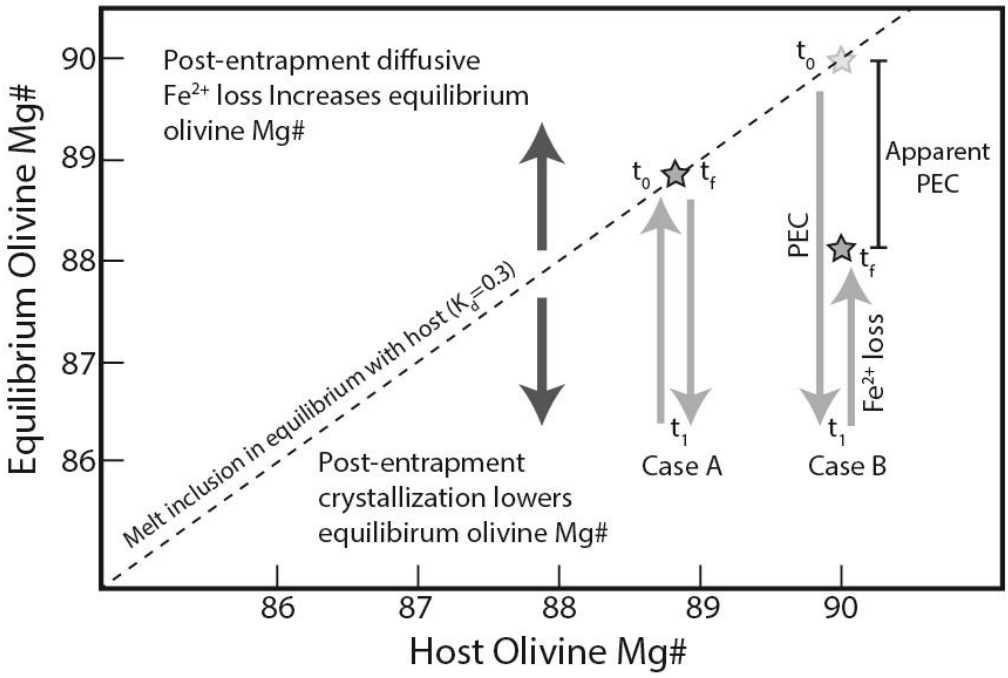

Figure 5. Comparison of the Mg# of olivine in equilibrium with the melt inclusion (see BSE image in Fig. 6A) against the Mg# of the olivine host. The diagram shows the different effects of post-entrapment crystallization (PEC) and post-entrapment Fe^{2+} loss on the Mg# of olivine. PEC will reduce the Mg# of equilibrium olivine, plotting below the equilibrium (K_d=0.3; dashed line). In contrast, Fe^{2+} loss will increase the Mg# of equilibrium olivine, plotting above the equilibrium line. Case A illustrates the scenario where significant Fe^{2+} loss occurred after PEC, resulting in a melt inclusion in equilibrium with its olivine host yet with lower FeO content than the original trapped melt. Case B shows the case where the melt inclusion underwent significant PEC followed by little Fe^{2+} loss, resulting in a Fe/Mg disequilibrium where Fe-loss could remain unnoticed.

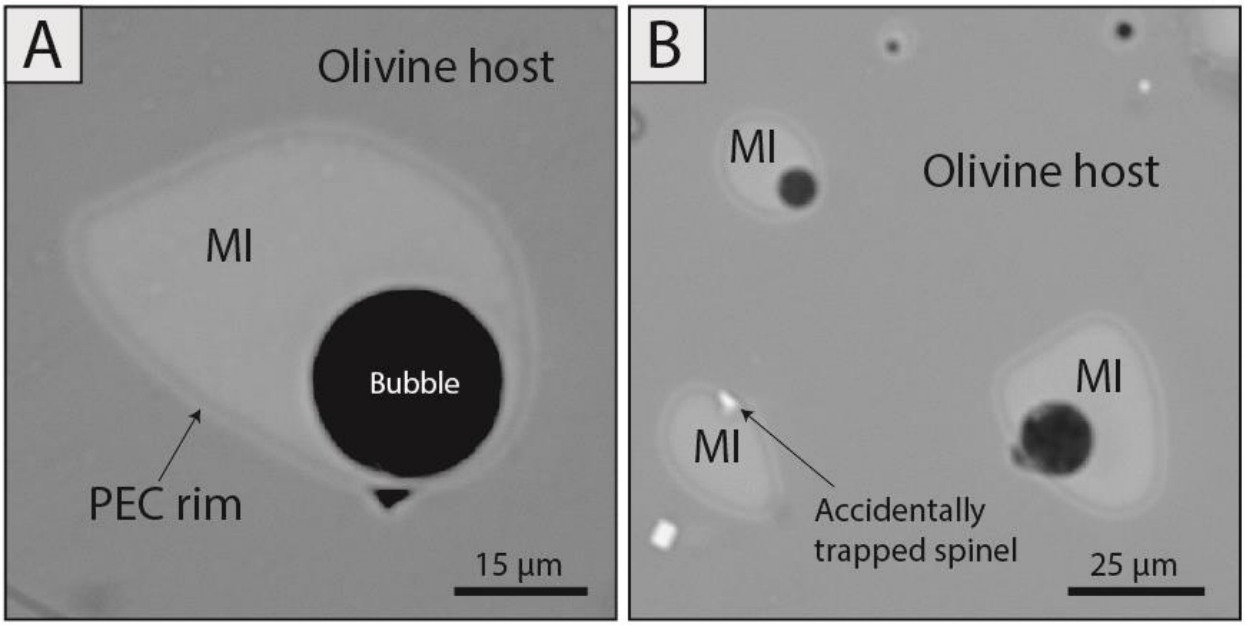

Figure 6. Backscattered electron (BSE) images of olivine-hosted MIs from the LHC basaltic tephra. (A) Example of a melt inclusion showing a PEC rim of olivine ("equilibrium olivine") around its wall. (B) Melt inclusion assemblage also showing PEC rims, and accidentally trapped Cr-spinel crystals.

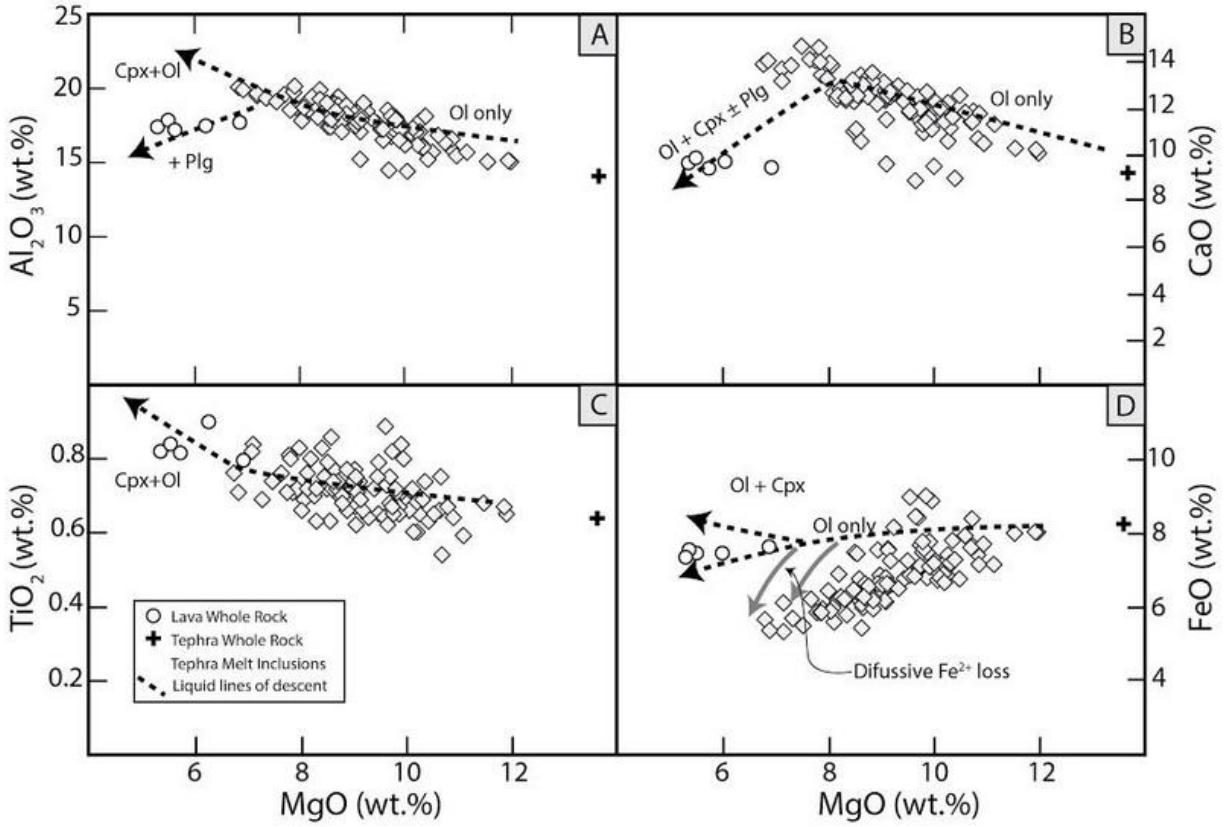

Figure 7. Major element variations of the studied suite of olivine-hosted MIs. The composition of the bulk volcanic products of the LHC from Salas et al. (2017) are shown for comparison, along with the calculated liquid lines of descent. (A), (B), and (C) show variations that are consistent with olivine fractionation, depicting the primitive nature of the inclusions. Bulk rock compositions are consistent with further fractionation of clinopyroxene ± plagioclase. (D) shows that the PEC corrected composition of the inclusions deviates significantly from the predicted liquid line of descent. This underlines the effect of post-entrapment Fe^{2+} loss from the inclusions.

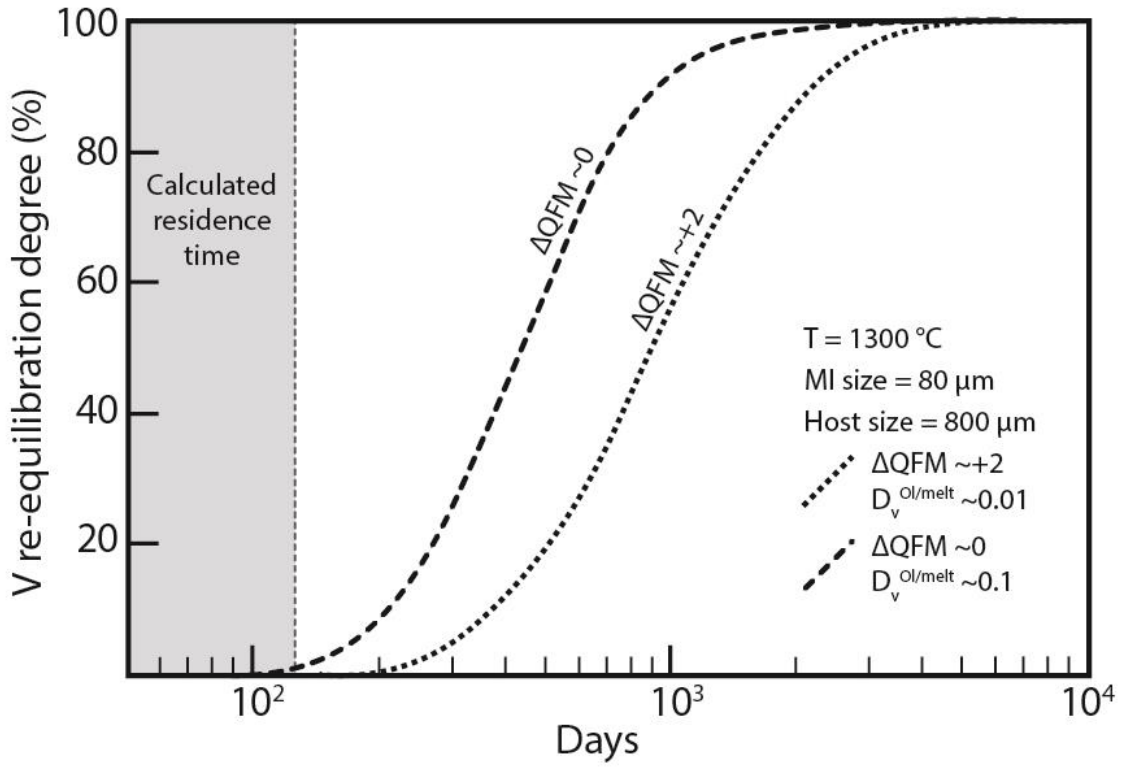

Figure 8. Vanadium (V) re-equilibration timescales between olivine-hosted MIs and carrier melt at 1300 °C and variable fO_2 conditions. Calculations were based on the model by Qin et al. (1992) and modified after Shishkina et al., (2018). The residence time of the LHC magma prior to eruption, calculated using Mg-Fe diffusion in olivine (Fig. 9), is shown for comparison. The data highlights that residence time (<200 years) was significantly short for V to re-equilibrate.

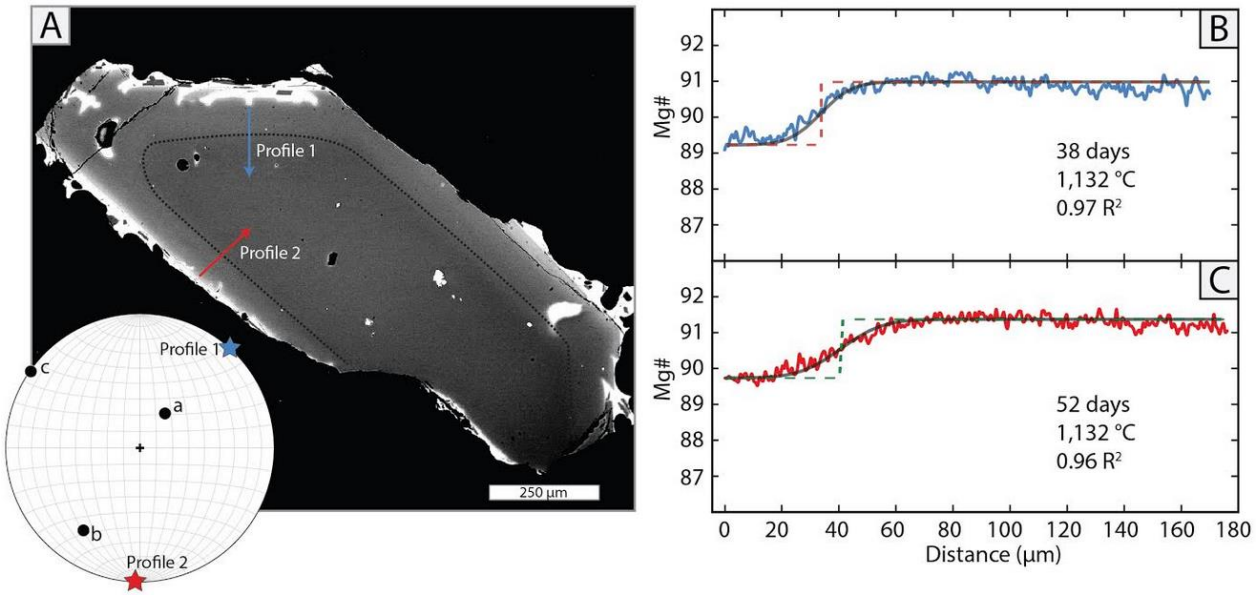

Figure 9. BSE image of an olivine phenocryst (A) and high-resolution Mg profiles showing timescales calculated using diffusion methods (B, C). The crystallographic orientation (axis a, b, and c) and traverse directions projected onto the stereographic lower hemisphere are shown in (A). (B) and (C) show the Mg# content (Mg#=100*Mg/(Mg+Fe), in mol) of the high-resolution profiles calculated from BSE grayscale calibrated profile plotted against distance. Colored lines: BSE profiles; solid dark line: best fit diffusion model (highest coefficient determination, R^2) between BSE profile and the Mg# content measured; dashed line: initial forsterite profile.

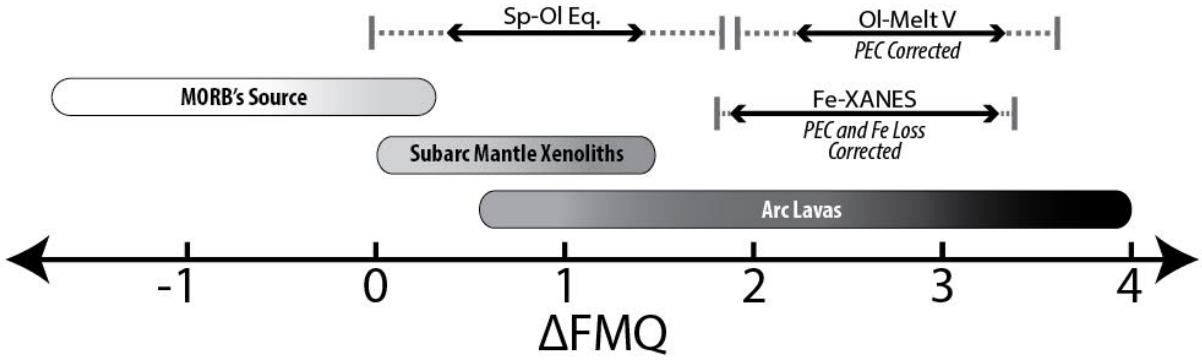

Figure 10. Calculated fO_2 values for the magmatic products of the LHC using olivine-spinel oxybarometry and melt inclusion redox meters (V partitioning and Fe □-XANES). As a comparison, the typical range of fO_2 for MORB, sub-arc mantle xenoliths, and arc lavas are shown (after Bénard et al., 2018; and references therein).

Table 1. Summary of data used in the estimation of fO_2 based on the olivine-spinel equilibrium.

Crystal #	MgO	SiO_2	Al_2O_3	FeO	MnO	NiO	Cr_2O_3	CaO	TiO_2	Total	T (K)	ΔFMQ*	2σ
Sp-17	12.31	0.10	13.82	24.16	0.37	0.09	45.99	0.03	0.41	97.31	1332	1.25	0.324
Ol-17	47.60	41.13	0.00	11.86	0.16	0.17	0.04	0.15	0.00	101.13			
Sp-26	14.16	0.11	13.64	16.71	0.33	0.19	52.82	0.02	0.23	98.24	1354	0.41	0.816
Ol-26	49.47	41.42	0.02	9.13	0.14	0.32	0.04	0.15	bdl	100.72			
Sp-32	14.21	0.11	13.61	16.79	0.34	0.19	52.88	0.01	0.24	98.43	1359	0.44	0.794
Ol-32	49.54	41.47	0.01	9.12	0.15	0.33	0.04	0.15	bdl	100.85			
Sp-54	14.81	0.09	14.74	18.43	0.32	0.20	48.15	0.01	0.37	97.16	1390	1.36	0.417
Ol-54	50.62	40.44	0.04	8.44	0.14	0.39	0.06	0.15	bdl	100.31			
Sp-27	14.32	0.11	13.56	16.81	0.34	0.20	52.50	0.02	0.24	98.12	1374	0.55	0.721
Ol-27	49.39	41.49	0.02	9.01	0.14	0.34	0.04	0.15	bdl	100.59			
Sp-47	14.21	0.10	13.56	18.02	0.34	0.19	50.41	0.01	0.30	97.18	1332	1.15	0.534
Ol-47	50.48	41.16	0.01	8.32	0.13	0.41	0.08	0.13	0.00	100.75			
Sp-51	14.81	0.09	15.59	18.67	0.33	0.21	47.17	0.02	0.39	97.30	1365	1.39	0.418
Ol-51	51.03	40.93	0.03	8.47	0.11	0.39	0.07	0.15	0.02	101.22			
Sp-14	14.20	0.12	13.50	16.81	0.32	0.19	52.24	0.02	0.26	97.69	1361	0.56	0.744
Ol-14	49.30	41.47	0.02	8.91	0.13	0.34	0.04	0.16	bdl	100.39			
Average Std. Dev. (Sp)	0.13	0.02	0.14	0.22	0.02	0.02	0.20	0.01	0.02				
Average Std. Dev. (Ol)	0.24	0.30	0.04	0.16	0.02	0.02	0.05	0.02	0.02				

*Calculated based on Ballhaus et al. (1991) at 1 GPa.

Table 2. Summary of data used in the estimation of fO_2 based on the Fe-XANES analyses.

Inclusion #	Centroid Energy (eV)	Fe^{3+}/Fe_{tot}	PEC (%)	Fe^{3+}/Fe_{tot} (PEC-corrected)	FeO*	FeO (Lost by diffusion)	Fe_2O_3 (Recalculated)	FeO (Recalculated)	$\Delta FMQ^{\downarrow}$
3	7112.455	0.4986	13.08	0.4334	7.94	---	3.86	4.54	3.3
4	7112.300	0.4540	13.18	0.3942	7.93	---	3.52	4.87	2.9
5	7112.451	0.4971	12.15	0.4367	7.93	---	3.90	4.53	3.2
6	7112.144	0.4030	5.97	0.3789	7.93	0.686	3.05	5.19	2.4
7	7112.314	0.4168	10.07	0.3748	7.94	0.292	3.19	5.08	2.5
21	7112.253	0.3813	7.37	0.3532	7.92	0.437	2.94	5.27	2.2
28	7112.270	0.3915	4.10	0.3754	7.86	1.608	2.61	5.52	1.9
34	7112.426	0.4823	3.26	0.4666	7.88	1.241	3.44	5.77	2.8
37	7112.336	0.3822	4.33	0.3657	7.87	1.424	2.62	5.51	1.9
38	7112.336	0.4295	9.74	0.3877	7.94	0.788	3.08	5.17	2.4

*FeO: Calculated according to the modelled liquid line of descent; $^{\downarrow}$Based on Kress and Carmichael (1991) at 1200°C and 1 Kb

Table 3. Vanadium concentration of MIs and their olivine host data used for the olivine-melt vanadium oxybarometry.

Inclusion #	Vanadium in Melt		V in Olivine	$D_V^{Ol/melt}$	ΔFMQ
	Measured	PEC-corrected			
43	320	294	4.7	0.016	2.2
62	309	292	4.4	0.015	2.3
103	299	271	4.2	0.015	2.2
91	302	292	4.2	0.014	2.3
55	276	247	3.7	0.015	2.3
110	198	178	2.6	0.015	2.3
92	241	228	3.1	0.014	2.4
76	280	263	3.5	0.013	2.4
1	274	245	3.3	0.014	2.4
102	304	266	3.5	0.013	2.4
47	278	270	3.2	0.012	2.6
72	325	297	3.5	0.012	2.6
31	314	298	3.4	0.011	2.6
32	318	278	3.4	0.012	2.5
106	259	245	2.6	0.011	2.7
90	305	296	3.0	0.010	2.8
19	270	252	2.3	0.009	2.9
40	297	270	2.4	0.009	3.0
3	265	230	2.1	0.009	2.9
8	311	297	2.0	0.007	3.3
Average Std. Dev.		20	1		~0.3

5.10. ACKNOWLEDGEMENTS

This study was funded by the Iniciativa Científica Milenio, through grant "Millennium Nucleus for Metal Tracing along Subduction". Additional support was provided by the FONDAP project 15090013 "Centro de Excelencia en Geotermia de Los Andes, CEGA", and CONICYT-FONDEQUIP grants EQM120098 and EQM140009. We thank Tony Lanzirotti and Mat Newville for assistance with µ-XANES analyses at the GeoSoilEnviroCars (Sector 13), Advanced Photon Source (APS), Argonne National Laboratory. We are also grateful to Owen Neill for assistance during EPMA acquisition, to Mathieu Nielsen and Rurik Romero for assistance during LA-ICP-MS analysis, and to Gerd Siefeld for assistance and guidance during fieldwork. Santiago Tassara acknowledges CONICYT for support through a Ph.D. scholarship #21170857. This research used resources of the Advanced Photon Source, a U.S. Department of Energy (DOE) Office of Science User Facility operated for the DOE Office of Science by Argonne National Laboratory under Contract No. DE-AC02-06CH11357.

CHAPTER 6. CONCLUSIONS

Several lines of evidence suggest that the formation and spatial occurrence of ore deposits in the crust is controlled by the distribution of deep-seated fertile reservoirs. The subcontinental lithospheric mantle (SCLM) has been invoked as a suitable candidate to hold such enriched reservoirs, because of its complex and long history of melt depletion and metasomatism. However, several aspects remained mostly unknown, motivating this thesis. For example: (i) the nature of the metasomatic agents and the mechanisms leading to metal enrichment in the SCLM were not fully constrained; (ii) the magma-SCLM interactions were under-investigated from a metallogenic perspective, and most importantly, (iii) no direct connection was reported between an enriched reservoir in the SCLM and the formation of a metallogenic province in the overlying crust. Some of these aspects have been highly debated over the years while some others have been overlooked, hampering our knowledge about the role of the SCLM on the formation of ore deposits and metallogenic provinces.

This thesis tackled some of these issues by focusing primarily on ultramafic xenoliths that sample the SCLM from beneath the Deseado Massif auriferous province in southern Patagonia. In addition, olivine-hosted melt inclusions from highly primitive basalts from the southern Andes were studied to address this scientific problem from an additional perspective.

Chapter 2 documents the first occurrence of native gold particles in peridotite xenoliths carried to the surface by basaltic lavas from depths of ~50 km. The xenoliths sample the SCLM below the Deseado Massif, providing a unique link between a gold-rich reservoir in the mantle and a world-class auriferous province. Petrographic, mineralogical, and geochemical data were used to develop a new model for the formation of the Deseado Massif gold province that is consistent with the well-known geological history of southern Patagonia. It is proposed that an initial stage of mantle-plume activity during the break-up of Gondwana resulted in gold refertilization of the SCLM. The later emplacement of a subduction zone that provided the necessary fluids to efficiently promote the titration of gold from the mantle to the crust, resulting in the formation of several epithermal Au-Ag deposits during the Jurassic.

Chapter 3 explores the mechanisms of mobility of the highly siderophile elements (HSE: Os, Ir, Ru, Rh, Pt, Pd, Au, and Re) in the SCLM that could potentially lead to the formation of a metalogenically fertile reservoir. The HSE geochemistry of the peridotite xenoliths was studied and linked to episodes of partial melting and metasomatism. This chapter shows that the SCLM beneath southern Patagonia records a complex multistage history of melt depletion and subsequent metasomatism operated by agents of variably composition and melt/rock ratios. Each metasomatic style had a particular fingerprint on the petrography and geochemistry of the base metal sulfides controlling the budget of HSE. In particular, it is demonstrated that the two most effective agents in the remobilization of HSE in the upper mantle are: (i) volatile-rich alkaline silicate melts, which selectively transport Os, Pd, Au, and Re; and (ii) Ni-Cu rich immiscible sulfide liquids physically entrained in alkaline silicate melts, which are capable of remobilizing all the HSE because of their strong partitioning into the sulfide phases. This chapter highlights that several generations of BMS result from the percolation of variable metasomatic agents into the SCLM, providing valuable insights to understand the mechanisms leading to HSE refertilization in the SCLM.

Chapter 4 deepens our understanding of the mechanisms leading to ore fertility of magmas. The chapter explores the effect of redox gradients in the mantle, and how these processes may enhance the extraction of sulfur and gold from an enriched SCLM reservoir. The approach involved

using in-situ synchrotron-based techniques to constrain changes in the oxidation state of sulfur recorded in mantle apatite. XANES data showed the presence of both sulfides (S^{-2}) and sulfate (S^{+6}) in apatite crystallized from an apparently initially reduced silicate melt in the upper mantle. These data provide evidence of progressive oxidation of the silicate melts during their ascent across the SCLM. It is proposed that the redox gradient between the ascending silicate melts and the SCLM peridotite wall-rock triggered changes in sulfur speciation and solubility in the silicate melt, enhancing its potential to scavenge HSE from the SCLM. This chapter highlights that substantial and heretofore unrecognized redox gradients may exist between ascending primitive magmas and a more oxidized SCLM, exerting a fundamental control on the oxidation state and ore fertility of magmas.

Chapter 5 provides an alternative view of redox processes in the mantle by focusing on olivine-hosted melt inclusions from highly primitive basalts in the southern Andes. The aim of this work is to investigate the redox evolution of the most primitive melts reported in the southern Andes. This chapter uses synchrotron-based techniques (i.e., XANES) and major and trace element geochemistry of melt inclusions, silicates, and associated oxides to assess the oxidation state of the eruptive products of the Los Hornitos cones in south-central Chile. The data shows that despite the relatively minor petrogenetic evolution of these primitive melts, they have suffered significant post-melting changes in their oxidation state. The presence of two different redox states recorded in the melt inclusions and oxide assemblages, respectively, provide compelling evidence of a complex redox evolution of the melts. This study has implications for understanding the origin of the oxidized nature of arc magmas, a key parameter controlling ore fertility, emphasizing the role of post-melting modifications during ascent across the lithosphere in controlling its oxygen fugacity.

Overall, this thesis allowed to grasp at the inner working of Earth's mantle during metallogenesis. The observations and geochemical data point to an enriched SCLM domain as the primary sources for gold in the metallogenic province of El Deseado Massif in southern Patagonia. It is proposed that enriched domains of the SCLM might be relatively durable and store gold (and silver) over large periods until a later remobilization event releases the stored metals. It is also suggested that redox gradients between ascending magmas and the SCLM peridotite wall-rock can trigger an increase in the sulfur and metals solubility of magmas, promoting the efficient extraction of the ore metals from fertile SCLM domains. These studies are relevant to our understanding of mantle dynamics and how the SCLM plays an important role in the genesis of ore deposits. A predictive understanding of the relationships between ore systems, mantle melting, and lithosphere-scale tectonics are thus relevant to mineral exploration and provide a framework for better understanding the global-scale localization of blocks of continental crust highly endowed with ore deposits.

Supplementary Information for

THE ROLE OF THE SUBCONTINENTAL LITHOSPHERIC MANTLE IN METALLOGENESIS

By

CARLOS SANTIAGO TASSARA

ADVISOR:
DIEGO MORATA CÉSPEDES

CO-ADVISOR:
MARTIN REICH MORALES

COMMITTEE:
FERNANDO BARRA PANTOJA
CLAUDIA CANNATELLI
MANUEL E. SCHILLING

A.1. SUPPLEMENTARY INFORMATION FOR CHAPTER 2

Analytical methods

Field Emission scanning electron microscopy (FE-SEM)

All sulfides and gold particles were imaged using a JEOL JSM-7100 field emission scanning electron microscope (FE-SEM) at the Serveis Cientificotècnics, University of Barcelona, Spain; and a QUANTA 650 FEG environmental scanning electron microscope (E-SEM) at the Instituto Andaluz de Ciencias de la Tierra (IACT), University of Granada, Spain. Both the FE-SEM and E-SEM are equipped with SE, BSE and EDS detectors. Accelerating voltage was 20 kV and beam current optimised for a sufficient number of counts for each EDS analysis.

Electron microprobe analyses (EMPA)

The major and minor element composition of silicates was determined using a field emission Cameca SXFive electron microprobe at the Raimond Castaing Center, Toulouse University. The operating conditions were: accelerating voltage 15 kV; beam current 20 nA; analysed surface is around 2x2 μm^2. The following standards were used: albite (Na), periclase (Mg), corundum (Al), sanidine (K), Wollastonite (Ca, Si), pyrophanite (Mn, Ti), hematite (Fe), Cr_2O_3 (Cr), NiO (Ni), sphalerite (Zn) and V metal (V).

Sulfide mineral chemical analyses were performed with a five-channel JEOL JXA-8230 electron microprobe at the Serveis Cientificotècnics, University of Barcelona, Spain. The operating conditions were: accelerating voltage 20kV, beam current 20 nA, and a 5 μm beam diameter. The following standards were used: pyrite (S, Fe), Ni metal (Ni), chalcopyrite (Cu), Co metal (Co) and sphalerite (Zn).

Laser ablation inductively coupled plasma mass spectrometry (LA-ICP-MS)

Concentrations of trace elements in clinopyroxene were determined in situ by laser ablation inductively coupled plasma mass spectrometry (LA-ICP-MS) using a NewWave Research UP213 laser coupled to an Agilent 7500 ICP-MS instrument (Raimond Castaing Center, Université Paul Sabatier – Toulouse III, France). NIST 610 and NIST 612 glass standards were used to calibrate relative element sensitivities. Each analysis was normalised using the Ca content determined by electron microprobe. A beam diameter of 50 μm and a scanning rate of 20μm s^{-1} was used. Typical theoretical detection limits range from 10 to 20 ppb for all the elements analysed.

Trace element concentrations of sulfides were carried out in the Geochemical Analysis Unit (GaU) at CCFS/GEMOC, Macquarie University, Sydney using LA-ICP-MS. Helium was used as the carrier gas, which was blended with Ar prior to introduction into the plasma. The laser-ablation system was operated at 5 Hz with an average beam energy 6.9 mJ per pulse. Sulphur, determined by EMP, was used as an internal standard for quantifying the trace element abundances. A quenched NiS (PGE-A: Alard et al., 2000, 2002), doped with selected chalcophile and siderophile elements was used as an external calibration standard. Detection limits for LA-ICP-MS analyses are calculated as average background concentrations plus three standard deviations. Average detection limits for Au and PGE are: Au (0.008 ppm); Os (0.08 ppm); Ir (0.01 ppm); Ru (0.03 ppm); Rh (0.006 ppm); Pt (0.03 ppm) and Pd (0.04 ppm).

Estimations of Pressure and Temperature

Pressure and temperature were estimated using iterative calculations based on P-sensitive thermometers and T-sensitive barometers from the following studies: Wood and Banno (1973), Brey and Khöler (1990), and Putirka (2008). The results are summarised in the table below.

Pressure and Temperature conditions on the studied samples		
	Equilibration Pressures (GPa)	**Equilibration Temperatures (°C)**
Brey and Kholer (1990)	1.5	1,068
	1.5	1,020
	1.5	1,114
Putirka (2008)	1.3	1,068
	1.1	1,020
	1.7	1,114
Wood and Banno (1973)	1.5	1,121
	1.5	1,113
	1.5	1,149

Supplementary Table S1. Summary of the thermobarometers used in the P-T estimation of the equilibrium conditions of the primary assemblage and their results.

Sulfide major and trace element composition

N°	Phase	S	Fe	Co	Ni	Cu	Zn	Total
1	Chalcopyrite	34.65	29.76	0.04	0.55	34.21	<DL	99.21
2	Chalcopyrite	34.88	29.26	0.05	0.85	34.13	0.02	99.64
3	Chalcopyrite	34.79	29.83	0.04	0.21	34.70	0.01	99.58
4	Chalcopyrite	34.48	29.48	0.04	0.53	34.66	0.02	99.21
5	Millerite	34.51	4.87	0.66	59.04	0.27	0.01	99.47
6	Millerite	35.34	2.77	0.36	61.58	0.17	<DL	100.50
7	Millerite	35.04	1.40	0.14	62.36	0.32	<DL	99.76
8	Millerite	35.13	1.38	0.14	62.27	0.32	0.03	99.74
9	MSS	33.02	24.14	0.30	42.09	0.14	<DL	99.68
10	MSS	32.66	14.97	0.18	50.20	0.59	<DL	98.60
11	Pentlandite	33.19	24.69	0.42	40.03	0.20	<DL	98.53
12	Pentlandite	33.23	26.99	0.56	39.09	0.03	<DL	99.91
13	Pentlandite	38.87	36.05	0.30	24.58	0.06	<DL	99.86
14	Pentlandite	33.14	27.14	0.63	39.23	0.09	<DL	100.22
15	Pentlandite	32.99	27.32	0.55	38.91	0.11	<DL	99.88
16	Pentlandite	33.20	26.62	0.56	39.09	0.06	<DL	99.53
17	Pentlandite	33.47	24.14	0.49	39.15	1.20	<DL	98.45

Supplementary Table S4. Major-element composition of sulfides embedded in the metasomatic late vein. <DL: below detection limit. All values are in wt.%.

N°	1	2	3	4	5	6	7	8	9
Os	1.83	81.54	281.99	2.20	2.95	83.44	25.22	27.47	23.51
DL	0.06	0.06	0.04	0.06	0.06	0.23	0.00	0.07	0.07
Ir	0.96	67.34	135.55	0.13	8.16	32.80	12.12	12.05	11.38
DL	0.01	0.01	0.00	0.01	0.00	0.03	0.01	0.01	0.01
Ru	0.48	33.43	72.06	2.51	13.70	32.27	12.49	12.44	12.10
DL	0.01	0.02	0.00	0.00	0.00	0.06	0.00	0.02	0.02
Rh	0.22	8.25	15.59	1.42	3.63	7.44	2.10	2.94	1.80
DL	0.00	0.00	0.00	0.00	0.00	0.01	0.00	0.00	0.00
Pt	14.07	258.85	3.66	0.00	0.88	31.33	2.18	0.30	0.06
DL	0.01	0.03	0.02	0.00	0.02	0.08	0.03	0.03	0.02
Pd	15.91	41.97	43.41	2.49	28.97	38.02	0.06	32.63	0.62
DL	0.01	0.01	0.00	0.01	0.00	0.05	0.02	0.02	0.01
Au	0.67	5.96	4.40	0.00	0.00	3.54	0.02	0.37	0.05
DL	0.01	0.01	0.00	0.01	0.00	0.02	0.01	0.01	0.01
Ag	0.70	23.09	162.96	49.31	42.90	64.24	0.10	3.22	2.44
DL	0.02	0.01	0.01	0.02	0.01	0.05	0.01	0.01	0.01
∑PGE	33.46	491.38	552.26	8.75	58.29	225.30	54.17	87.83	49.46
Total	34.83	520.43	719.62	58.06	101.19	293.08	54.28	91.42	51.95

Supplementary Table S5. Noble metal content of sulfides from Patagonian mantle xenoliths obtained by LA-ICP-MS. <DL: below detection Limit. All values are in ppm.

Estimation of Oxygen Fugacity

		A	B	C
Olivine	**XFe**	0.09	0.09	0.09
	XMg	0.91	0.91	0.91
Orthopyroxene	**XM1 (Fe)**	0.09	0.09	0.09
	XM2 (Fe)	0.08	0.09	0.08
Spinel	**Fe^{3+}**	0.04	0.06	0.08
	Fe^{2+}	0.19	0.22	0.19
	log a(Fe_3O_4)	-2.01	-1.84	-1.48
Temperature (°C)		1,020 1,149	1,020 1,149	1,020 1,149
ΔFMQ		-0.03 0.24	0.44 0.71	0.97 1.25

Supplementary Table S6. Summary of the data used in the oxygen fugacity conditions estimation for three different equilibrated assemblages (A, B and C) for the minimum and maximum temperatures estimated from the thermometers mentioned above.

The fO_2 conditions of the sample were calculated using the following reaction equilibrium:

$6\ Fe_2SiO_4$ (in olivine) + O_2 = $Fe_2Si_2O_6$ (in orthopyroxene) + $2\ Fe_3O_4$ (in spinel)

The Fe^{3+} contents in spinel was calculated from electron microprobe analyses assuming perfect stoichiometry. Thus, the Fe^{3+} content was converted to activities of magnetite (Fe_3O_4) in spinel using the formula below provided by Nell and Wood (1991):

$\log a(Fe_3O_4 \text{ in Sp}) = \log((Fe^{2+})*Fe^{3+})^2/4) + 1/T\ [406\ (Al)^2 + 653\ (Mg)*(Al) + 299\ (Cr)^2 + 199\ (Al)*(Cr) + 346\ (Mg)*(Cr)]$

The terms in parentheses refer to total atomic concentrations of Mg, Fe^{2+}, Fe^{3+}, Cr and Al in spinel on a four-oxygen basis. K is temperature in Kelvin.

Therefore, $\Delta\log fO_2$(FMQ) at a given pressure (in bar) and temperature (in K) is given by the following equation:

$\Delta\log fO_2(FMQ) = \log(fO_2) - \log(fO_2)_{FMQ} = 220/T + 0.35 - 0.0369\ P/T - 12\ \log X_{Fe}Ol - 2620(X_{Mg}Ol)^2/T + 3\log[X_{Fe}M1)Opx * (X_{Fe}M2)Opx] + 2\ \log a(Fe_3O_4 \text{ in Sp})$

$\Delta\log fO_2$(FMQ) is fO_2 relative to FMQ buffer, P in bar, T in Kelvin, $X_{Fe}Ol$ and $X_{Mg}Ol$ refer to the atomic ratio of $Fe^{2+}/(Mg+Fe^{2+})$ and $Mg/(Mg+Fe^{2+})$ in olivine respectively.

($X_{Fe}M1$)Opx and ($X_{Fe}M2$)Opx refer to the atomic fractions of Fe in the M1 and M2 sites of orthopyroxene, and were calculated following the methods in Wood et al. (1990).

a(Fe_3O_4 in Sp) is activity of magnetite, Fe_3O_4, in spinel.

Trace and REE content of clinopyroxene

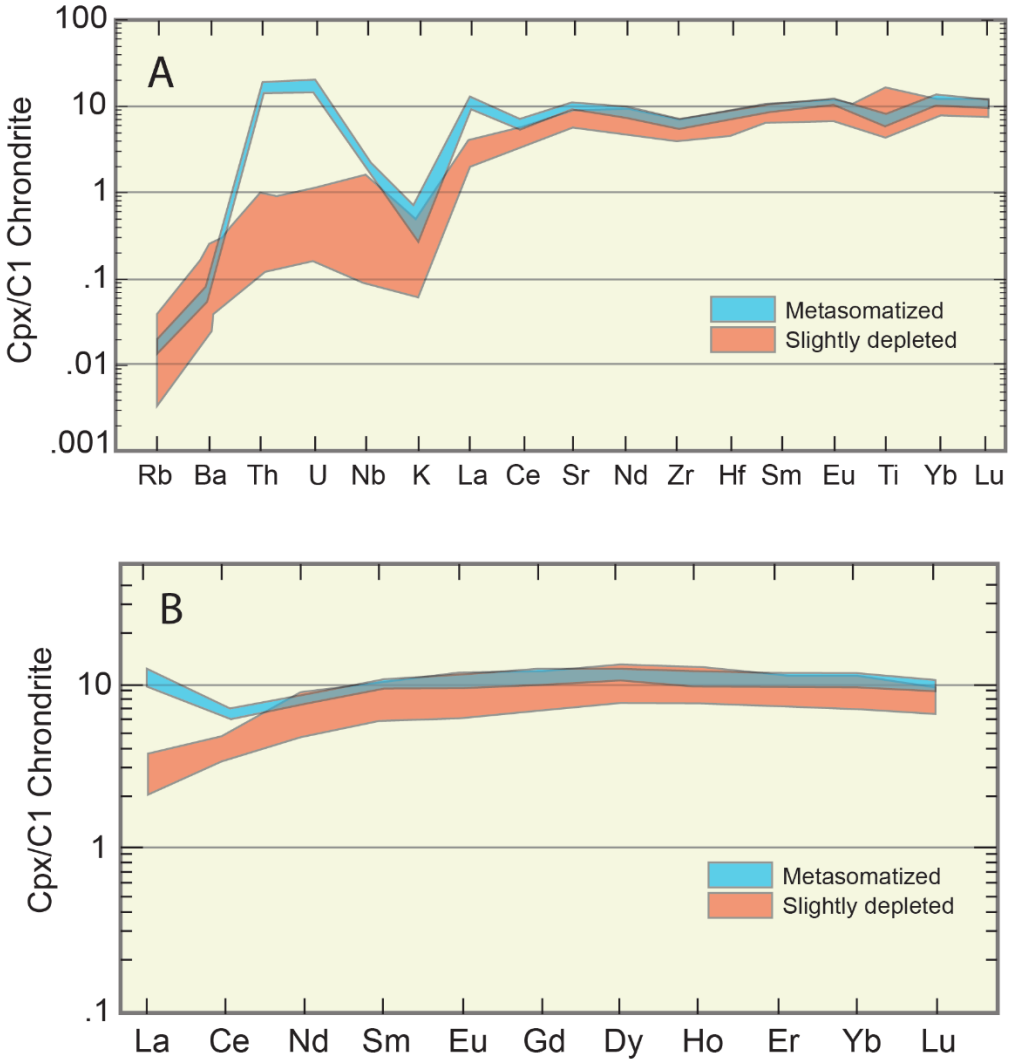

Supplementary Figure S1. Chondrite-normalized trace and REE patterns from clinopyroxenes from Cerro Redondo mantle xenolith reflecting at least two generations of the silicate primary assemblage. Normalizing values are from McDonough and Sun (1995).

Au/Ag Ratios of mantle sulfides and epithermal Au-Ag deposits

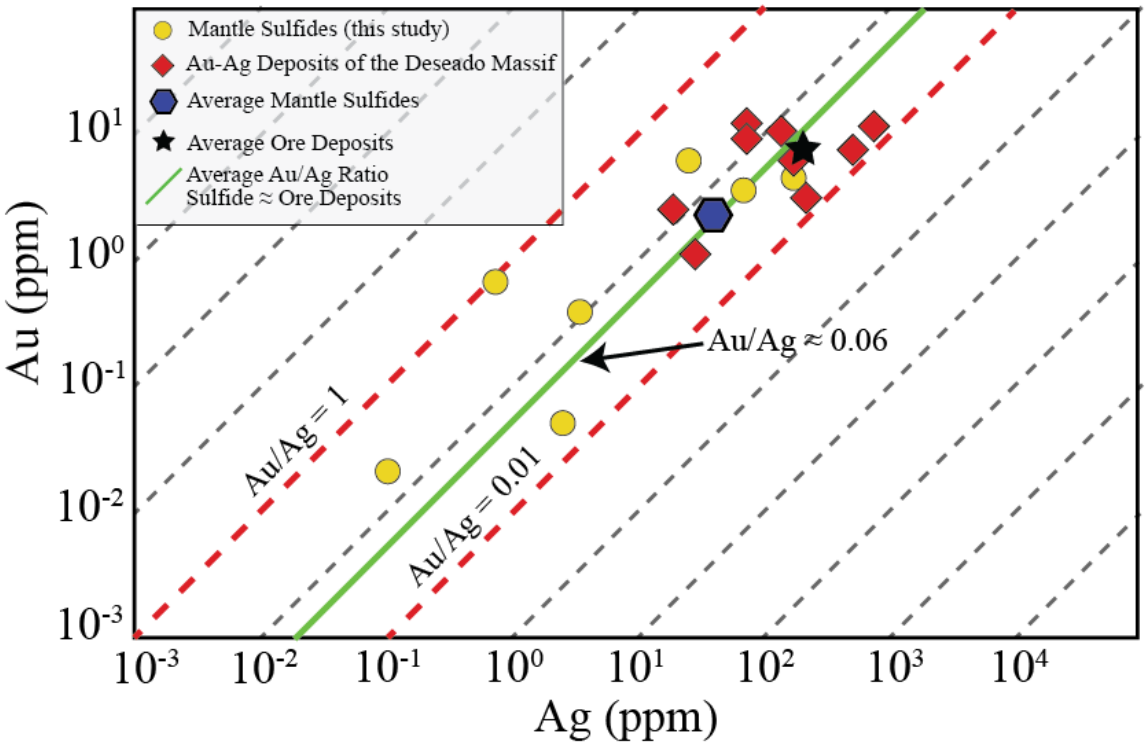

Supplementary Figure S2. Au versus Ag contents of mantle sulfides and epithermal Au-Ag deposits of the Deseado Massif. Dotted lines are constant Au/Ag ratios. Mantle sulfide values from this study (Supplementary Table S5). Epithermal Au-Ag grades taken from Schalamuk et al. (1997); Echavarría et al. (2005); Permuy Vidal et al. (2016); and technical reports from the Mining Companies (links provided in the references).

Supplementary Figure S2 shows the Au/Ag ratios of mantle sulfides in the late infiltrating melt (glassy vein), and the bulk Au/Ag ratios of the epithermal Au-Ag deposits in the Deseado Massif.

Overall, the bulk Au/Ag ratios of the epithermal deposits in the Deseado Massif are between 0.01 and 0.18, while the Au/Ag ratios of the mantle sulfides vary from 0.02 to 0.95. Thus, the Au/Ag ratios of the epithermal deposits and the sulfides are similar within two orders of magnitude at the most.

Supplementary figure S2 points out that the mantle sulfides may exert an important control on the economic metal ratios of epithermal ore deposits of the Deseado Massif.

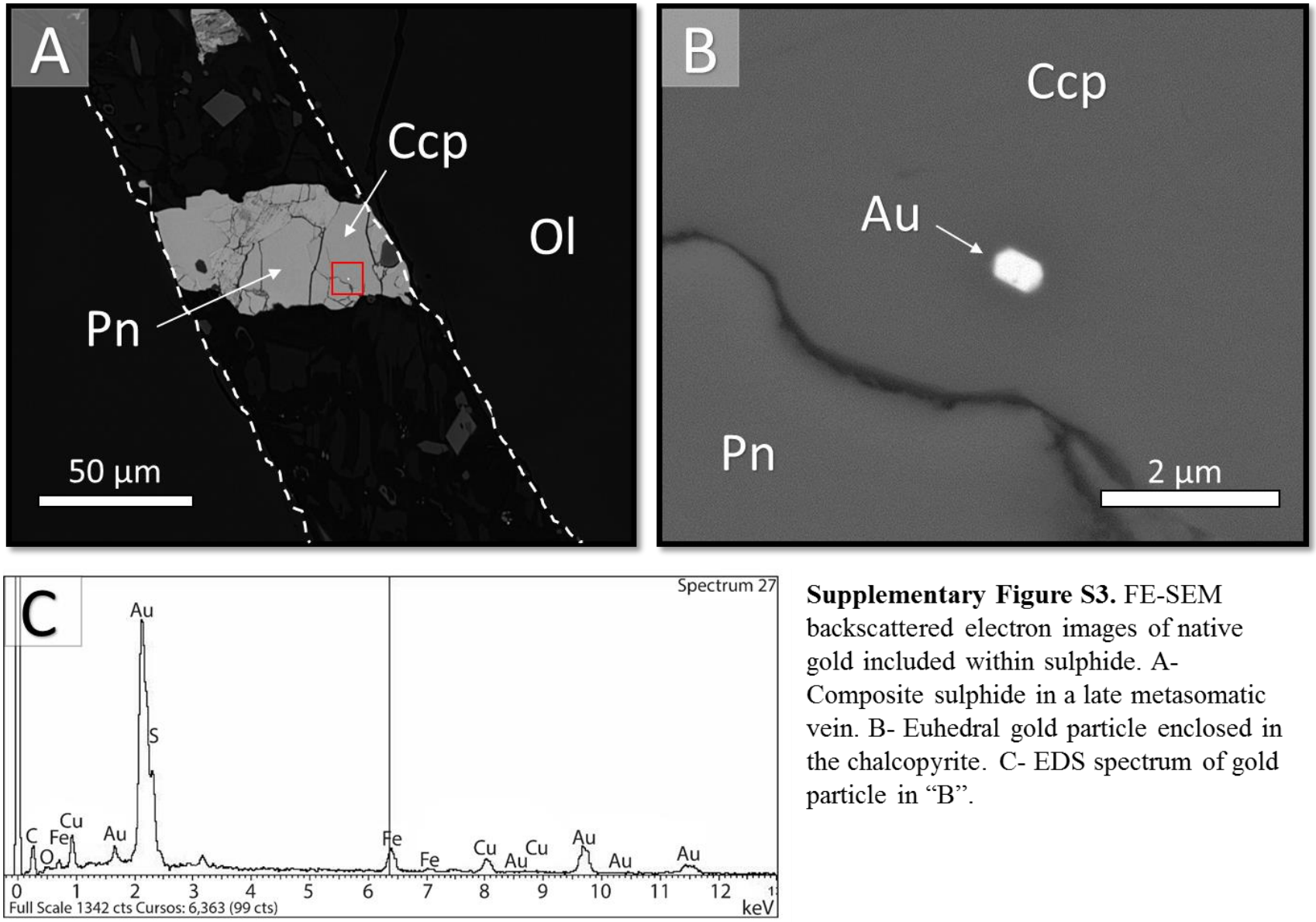

Supplementary Figure S3. FE-SEM backscattered electron images of native gold included within sulphide. A- Composite sulphide in a late metasomatic vein. B- Euhedral gold particle enclosed in the chalcopyrite. C- EDS spectrum of gold particle in "B".

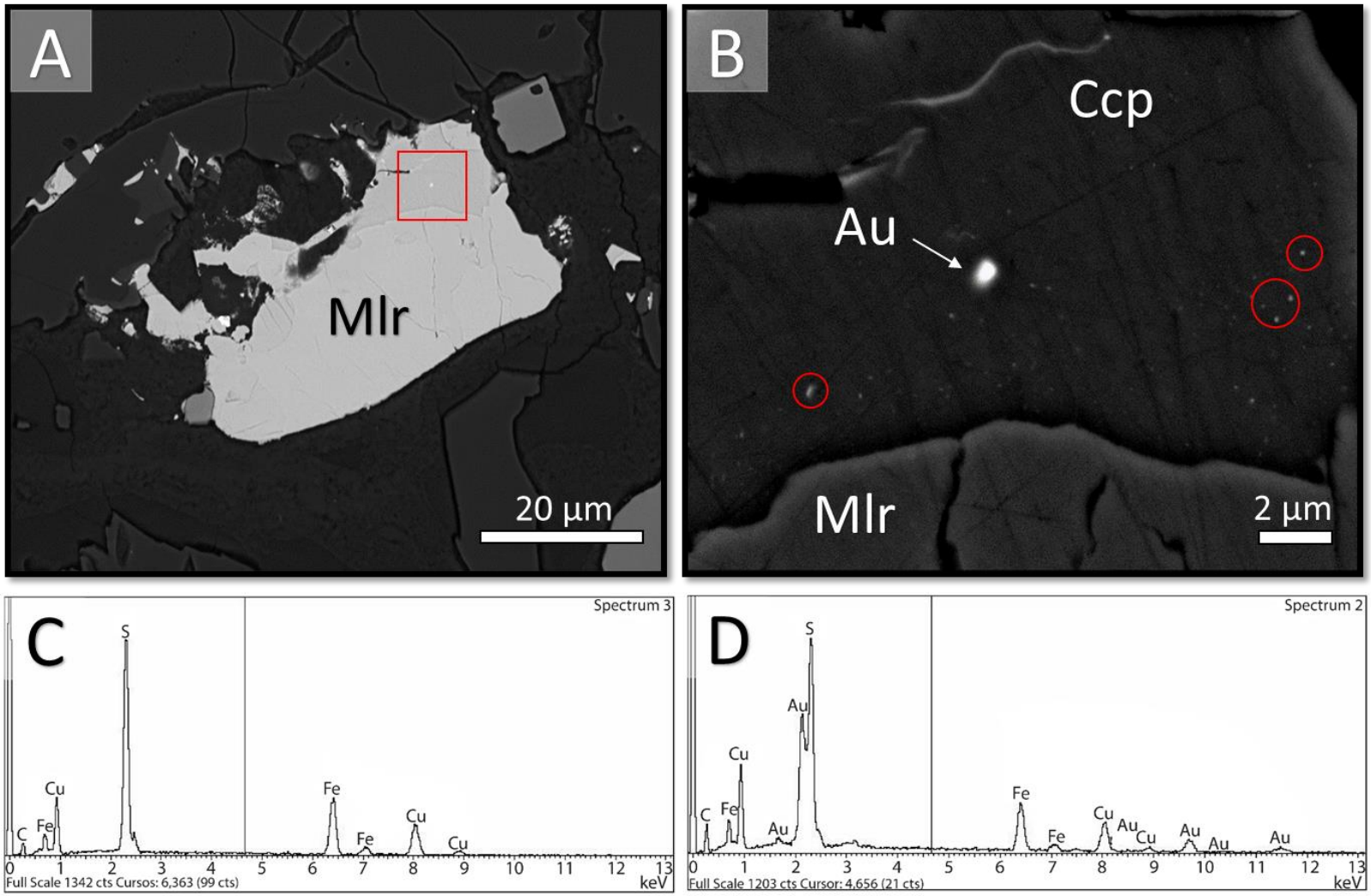

Supplementary Figure S4. FE-SEM backscattered electron images of gold included within sulphide. A- Composite sulphide containing gold particles embedded in a glassy groundmass. B- The inset (red square) in "A" shows a native gold particle (centre) and arrangement of gold nanoparticles within chalcopyrite. C, D- EDS spectrum of the gold particle and surrounding matrix respectively.

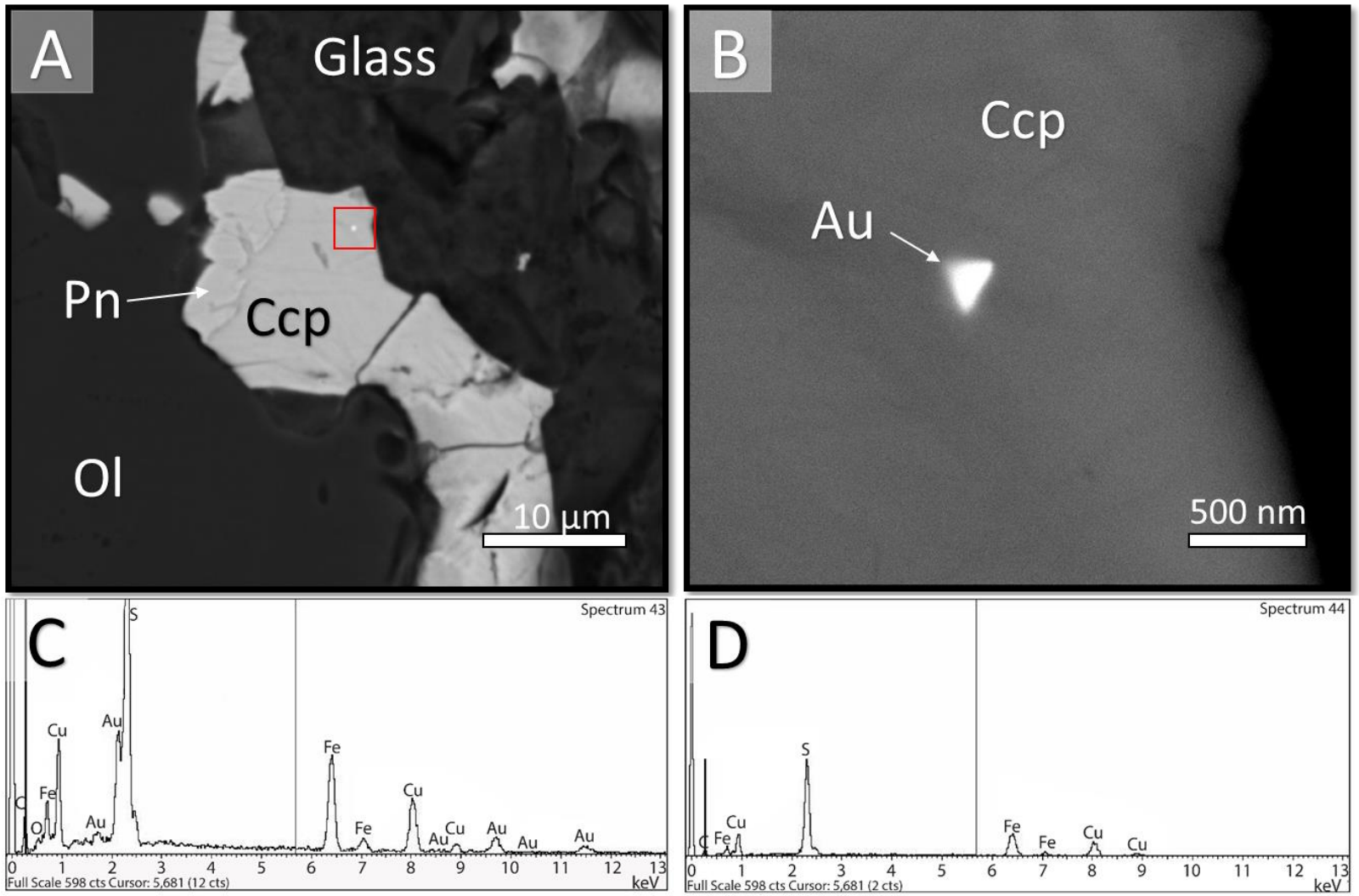

Supplementary Figure S5. FE-SEM backscattered electron images of gold included within sulphide. A- Composite sulphide grain enclosed within devitrified glass in contact with host silicate. B- The inset (red square) in "A" shows a triangular native gold particle enclosed within the chalcopyrite. C,D- EDS spectrum of gold particle in "B" and surrounding matrix respectively.

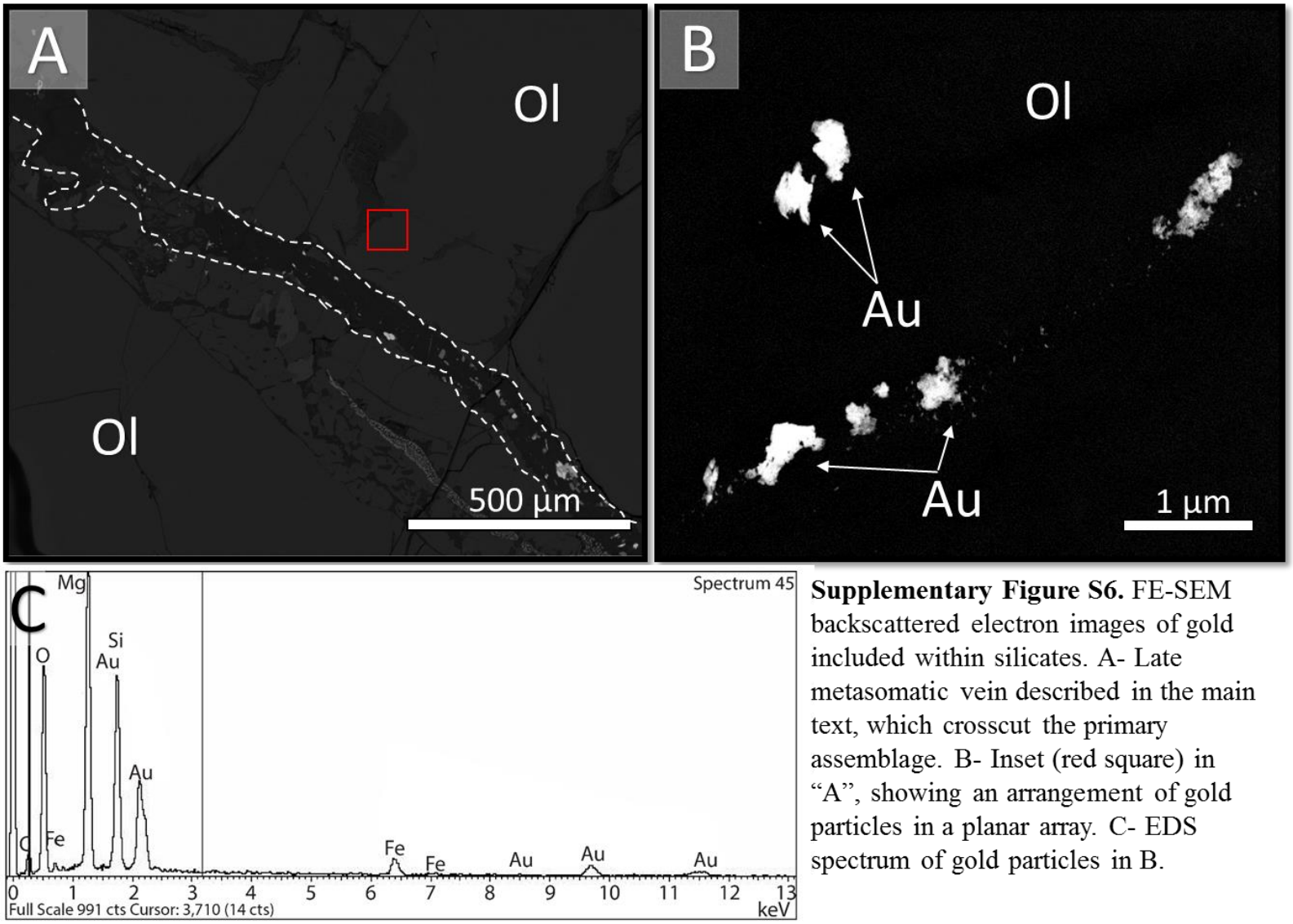

Supplementary Figure S6. FE-SEM backscattered electron images of gold included within silicates. A- Late metasomatic vein described in the main text, which crosscut the primary assemblage. B- Inset (red square) in "A", showing an arrangement of gold particles in a planar array. C- EDS spectrum of gold particles in B.

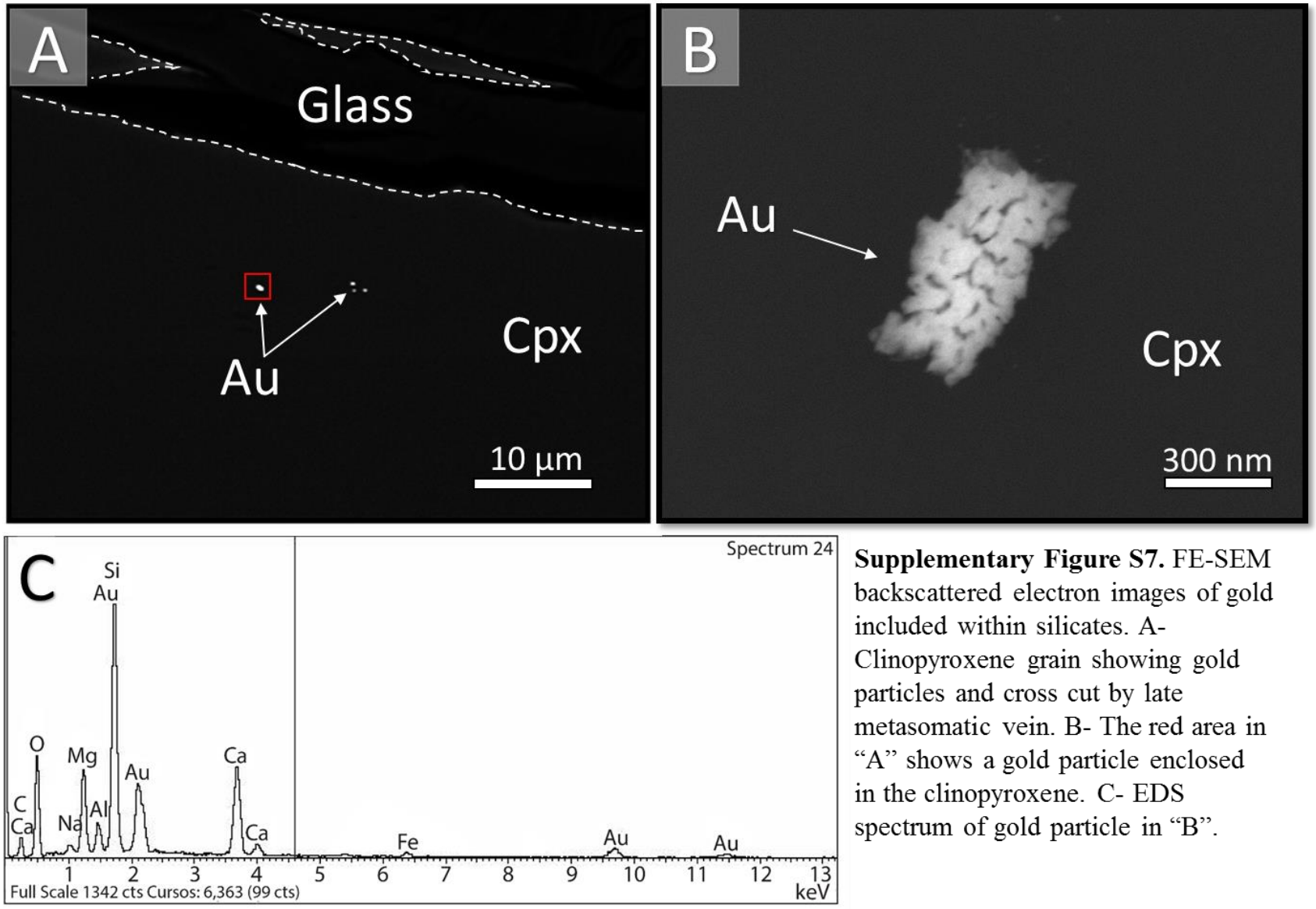

Supplementary Figure S7. FE-SEM backscattered electron images of gold included within silicates. A- Clinopyroxene grain showing gold particles and cross cut by late metasomatic vein. B- The red area in "A" shows a gold particle enclosed in the clinopyroxene. C- EDS spectrum of gold particle in "B".

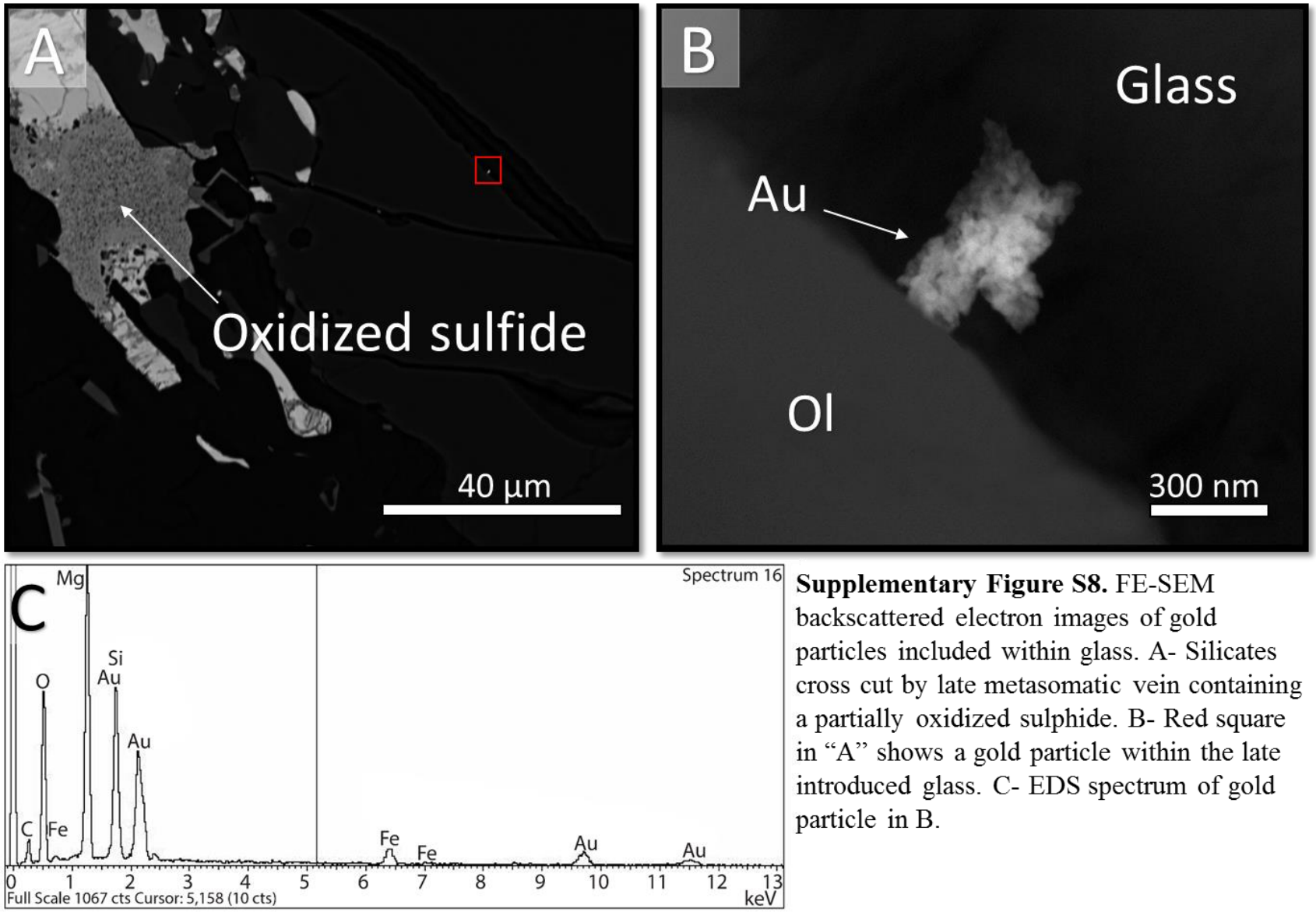

Supplementary Figure S8. FE-SEM backscattered electron images of gold particles included within glass. A- Silicates cross cut by late metasomatic vein containing a partially oxidized sulphide. B- Red square in "A" shows a gold particle within the late introduced glass. C- EDS spectrum of gold particle in B.

SUPPLEMENTARY INFORMATION REFERENCES

Alard, O., Griffin, W.L., Lorand, J.P., Jackson, S.E. and O´Reilly, S.Y. Non-chondritic distribution of the highly siderophile elements in mantle sulfides. Nature 407, 891-894 (2000).

Brey, G.P. and Köhler, T. Geothermobarometry in Four-phase Lherzolites II. New Thermobarometers, and Practical Assessment of Existing Thermobarometers. Journal of Petrology 35, 1353-1378 (1990).

Echavarría, L.E., Schalamuk, I.B. and Etcheverry, R.O. Geologic and tectonic setting of Deseado Massif epithermal deposits, Argentina, based on El Dorado-Monserrat. Journal of South American Earth Sciences 19, 415-432 (2005).

Kulerud, G., Yund, R.A. and Moh, G. Phase relations in Fe-Ni-S, Cu-Fe-S and Cu-Ni-S systems. Economic Geology 61, 323-343 (1996).

Nell, J., and Wood, B.J. High-temperature electrical measurements and thermodynamic properties of Fe_3O_4-$FeCr_2O_4$-$MgCr_2O_4$-$FeAl_2O_4$ spinels. American Mineralogist 76, 406-426 (1991).

McDonough, W.F. and Sun S.-s. The composition of the Earth. Chemical Geology 120, 223-253 (1995).

Schalamuk, I.B., Zubia, M., Genini, A. and Fernandez, R.R. Jurassic epithermal Au_Ag deposits of Patagonia, Argentina. Ore Geology Reviews 12, 173-176 (1997).

Permuy Vidal, C., Guido, D.M., Moreira, P., Ríos, F.J., Melgarejo, J.C. Características metalogenéticas de Eureka West, principal clavo mineralizado de la veta Eureka, Distrito Cerro Negro, Macizo del Deseado. Revista de la Asociación Geológica Argentina 73, 64-77 (2016).

Putirka, K., 2008, Thermometers and Barometers for Volcanic Systems. Minerals, Inclusions and Volcanic Processes, Reviews in Mineralogy and Geochemistry, Mineralogical Society of America 69, 61-120 (2008).

Withney, D.L. and Evans B. W. Abbreviations for names of rock-forming minerals. American Mineralogist 95, 185-187 (2010).

Wood, B.J., and Banno, S. Garnet-orthopyroxene and orthopyroxene-clinopyroxene relationships in simple and complex systems. Contributions to Mineralogy and Petrology 42, 109-124 (1973).

Wood, B.J., Bryndiza, L.T. and Johnson, K.E. Mantle oxidation state and its relationship to tectonic environment and fluid speciation. Science, 238, 337-345 (1990).

McEwen Mining Inc. San José Mine – Argentina. Resources and Reserves. (Accessed May 20, 2016, at http://www.mcewenmining.com/Operations/Reserves-and-Resources/default.aspx).

Goldcorp Inc. Reserves and Resources Notes 2016. (Available at http://s1.q4cdn.com/038672619/files/doc_downloads/2017/Reserves_Resources_Notes_2016.pdf)

Patagonia Gold PLC. Projects, Reserves and Resources. (Accessed May 20, 2016, at http://www.patagoniagold.com/projects/reserves-and-resources/)

Yamana Gold Inc. 2016 Mineral Resources. (Accessed May 20, 2016, at http://www.yamana.com/English/portfolio/reserves-and-resources/default.aspx)

A.2. SUPPLEMENTARY INFORMATION FOR CHAPTER 3

Analytical Methods

Whole-rock major and trace elements

Major element determination by X-Ray Fluorescence (XRF)

Whole-rock major and trace elements were analysed at the Peter Hooper GeoAnalytical Lab, Washington State University, USA (Appendix 2). For this, fresh chips of the sample were hand-picked and a standard volume of chips (approximately 28 g) was grounded in a swing mill with tungsten carbide surfaces for 2 minutes. Then, 3.5 g of the sample powder was weighed into a plastic mixing jar with 7.0 g of spec pure dilithium tetraborate ($Li_2B_4O_7$) and mixed for ten minutes. The mixtures were transferred into graphite crucibles and loaded into a muffle furnace. After fusion, graphite crucibles were removed from the oven and allowed to cool. Each fusion glass bead was reground in the swingmill for 35 seconds, the glass powder then replaced in the graphite crucibles and re-fused for 5 minutes. Following the second fusion, the cooled beads are labelled with an engraver, their lower flat surface is ground on 600 silicon carbide grit, finished briefly on a glass plate (600 grit with alcohol) to remove any metal from the grinding wheel, washed in an ultrasonic cleaner, rinsed in alcohol and wiped dry. The glass beads are then ready to be loaded into the XRF spectrometer. The concentrations of 27 chemical elements were determined by comparing the X-ray intensity for each element in the whole-rock peridotite with the intensity for two beads each of nine USGS standards (PCC-1, BCR-1, BIR-1, DNC-1, W-2, AGV-1, GSP-1, G-2, and STM -1), using the values recommended by Govindaraju (1994) and two beads of pure vein quartz were used as blanks for all elements except Si. The intensities for all elements are corrected automatically for line interference and absorption effects due to all the other elements using the fundamental parameter method.

Trace element determination by ICP-MS

Powdered whole-rock peridotite samples were mixed with an equal amount of lithium tetraborate flux (typically 2 g), placed in a carbon crucible and fused at 1000° C in a muffle furnace for 30 minutes. After cooling, the resultant fusion bead was briefly ground in a carbon-steel ring mill and a 250 mg aliquot was transfered into a 30 ml, screw-top Teflon PFA vial for subsequent dissolution. The acid dissolution consisted of a first evaporation with HNO_3 (2 ml), HF (6 ml), and $HClO_4$ (2 ml) at 110° C. After evaporating to dryness, the sample is wetted and the sides of the vial were rinsed with a small amount of water before a second evaporation with $HClO_4$ (2 ml) at 160° C. After the second evaporation, samples were brought into solution by adding approximately 10 ml of water, 3 ml HNO_3, 5 drops H_2O_2, and 2 drops of HF and warmed on a hot plate until a clear solution was obtained. The sample was then transferred to a clean 60 ml HDPE bottle diluted up to a final weight of 60 g with de-ionized water. Solutions were analysed on an Agilent model 4500 ICP-MS and were diluted by an additional factor 10 at the time of analysis using Agilent's Integrated Sample Introduction System (ISIS).

Determination of HSE and $^{187}Os/^{188}Os$ composition in whole-rock samples

To determine the HSE concentrations and the $^{187}Os/^{188}Os$ compositions of the southern Patagonia peridotites, 1 g of whole-rock powder was spiked with a mixed HSE spike (^{185}Re, ^{106}Pd, ^{195}Pt, ^{191}Ir, ^{190}Os) and digested using 7.5 ml inverse aqua regia (2:1 14 N HNO_3: 10 N HCl) in an Anton Paar HP-Asher at 220ºC and 100 - 130 bars for 13.5 h. Such high pressures are optimal to achieve a complete attack and dissolution of all the HSE-bearing phases, especially refractory platinum group minerals (PGM) such as laurite and HSE alloys (Meisel and Moser, 2004). After

digestion, Os was extracted from the inverse aqua regia solution using 7 ml of $CHCl_3$ and back-extracted into 9 N HBr (Cohen and Waters, 1996). Further purification of Os was achieved by microdistilling the Os-H_2SO_4-dichromate solution into a 20 µL drop 9 N HBr at 80ºC for 2 h.

The inverse aqua regia fraction left over after Os solvent extraction and containing the remaining HSE was dried down and desilicified at 100 ºC for 24 h using 4 ml of 24 N HF and 1ml of 14N HNO_3 to efficiently dissolve the remaining silicate phases that may contain minor proportion of Re (Luguet et al., 2007; Mallmann et al., 2007; Ishikawa et al., 2014). After final equilibration in 10ml of 0.5 N HCl, the HSE are separated from the matrix using the BioRad AG8 X1 resin 100-200 mesh, following the original procedure of Pearson and Woodland (2000).

Osmium concentrations and $^{187}Os/^{188}Os$ ratios were measured on the secondary electron multiplier of the Thermo-Finnifan Triton N-TIMS at the Northern Centre for Isotopic and Elemental Tracing (NCIET), Department of Earth Sciences, University of Durham (UK), following the procedure described by Dale et al. (2008). During the measurement sessions, aliquots of 100-1000 pg Os of the DROsS standard solution were run 6 times and gave a mean $^{187}Os/^{188}Os$ of 0.160704 ±648 (2sd). This is in excellent agreement with the values (0.160924±4, n=8) obtained by Luguet et al. (2008) on 10 – 100 ng aliquots analysed in Faraday mode on the same thermal ionisation mass spectrometer. The lower reproducibility of our DROsS measurements (2‰ vs. 0.024‰) is likely linked to the smaller amount of DROsS standard solution run during this study.

Platinum, Ir, Re, Ru and Pd were analysed at the Steinmann Institute on a Thermo Scientific Element XR SF-ICP-MS using either a cyclonic spray chamber (Ir, Pt, Re) or an ESI Apex dessolvation unit (Ru and Pd) as introduction systems. Mass fractionation and oxide production (specifically on Ir, Pt, Pd and Cd) were estimated by analysing respectively a 1 ppb HSE Standard Solution and 1 ppb Hf, Y-Zr and Mo standard solutions at the beginning, middle point and end of each analytical session.

The average total procedural blanks (n=4 except for Os n=2) are 2pg Os, 1pg Ir, 114 pg Ru, 11pg Pt, 25pg Pd and 6pg Re. All procedural blanks were substracted from each sample analysis. Multiple analyses of the international UB-N peridotite standard (SARM-CRPG) reveal precision of 2% (2sd) for Pd, 11-19% for Pt, Ru and Os, 32% for Ir and 74% for Re. Similar precision have been obtained for Pt, Ru and Os by Meisel and Moser (2004) and Fischer-Gödde et al. (2011) (Table 1). Furthermore, although our reproducibility for Re analyses of UB-N appear to be among, -if not-, the lowest reported one over the past 15 years, low Re precision (35%) was already reported by Fischer-Gödde et al. (2011). Apart from Pd, these multiple determinations of HSE concentrations in the UB-N peridotite standard are less precise than those of Luguet et al. (2015), who used the same chemical and analytical procedures but analysed a different batch of the UB-N standard. Interestingly, the $^{187}Os/^{188}Os$ composition (n=4) of UB-N yield a reproducibility of 0.4%, in excellent agreement with the precision obtained by Meisel and Moser (2004), Becker et al. (2006); Fischer-Gödde et al. (2011) and Luguet et al. (2015), although the average $^{187}Os/^{188}Os$ obtained during the course of this study is systematically 0.2-0.7 % lower than the values published in the literature. When compared to previously published HSE concentrations for UB-N, our HSE concentrations differ by less than 6% for Pt and Pd, by less 14% for Os, Ru and Re and by between 5- and 21% for Ir, rather independently of the relative precision on the HSE concentrations. On this basis as well as (i) considering the well-known heterogeneity previously highlighted among the UB-N HSE concentrations by Fischer-Gödde et al. (2011) and Meisel and Moser (2004) between and within UB-N batches and (ii) considering the fact that contrasting precision for the UB-N replicates were obtained from the same laboratory but on different UB-N powder batches, it is very

likely that the large scatter observed among the UB-N HSE concentrations result from a strong nugget effect, rather than reflecting procedural and/or analytical issues.

A minimum estimate of the timing of melt depletion of the peridotites can be obtained from the $^{187}Os/^{188}Os$ of the sample at the time of eruption and comparing this to the mantle evolution model. The time at which the mantle had this $^{187}Os/^{188}Os$ composition is referred to as the T_{RD} model age, or "Re-depletion" age (Walker et al., 1989). Otherwise, the time of melt depletion of peridotites can be determined by using the measured Re/Os and calculating when the sample had an $^{187}Os/^{188}Os$ matching that of an undifferentiated model mantle (Walker et al., 1989). This model age, referred as T_{MA} (Luck and Allègre, 1984, Shirey and Walker, 1998) relies on the immobility of Re after the melting event, which can be a problem for those xenoliths that suffered subsequent melt infiltration. In this work, model ages were calculated relative to the $^{187}Os/^{188}Os$ evolution of Enstatite Chondrites (present-day $^{187}Os/^{188}Os$=0.12809±0.00085 (2σ), $^{187}Re/^{188}Os$=0.421, Walker et al., 2002). The quoted uncertainties on T_{MA} and T_{RD} model ages include the uncertainties in the measured $^{187}Os/^{188}Os$ and $^{187}Re/^{188}Os$, calculated according to the equation of Sambridge and Lambert (1997).

Table 1: Highly siderophile elements concentrations and ^{187}Os isotopic compositions of procedural blanks and the UBN international standard material.

	$^{187}Os/^{188}Os$	1se	Os (ppb)	Ir (ppb)	Ru (ppb)	Pt (ppb)	Pd (ppb)	Re (ppb)
Total procedual Blanks								
This study (N=5 except Os: n=2 and $^{187}Os/^{188}Os$: n==1)								
Average	0.1273	0.0018	0.002	0.001	0.114	0.011	0.025	0.006
2 sd			0.002	0.002	0.202	0.016	0.027	0.010
International Standard UB-N								
This Study (HP-asher + desilicification)								
	0.12734	0.00010	3.12	2.84	6.07	7.30	6.07	0.084
	0.12678	0.00014	3.13	n.a.	n.a.	n.a.	n.a.	n.a.
	0.12687	0.00012	2.88	2.11	5.08	6.70	6.02	0.234
	0.12688	0.00012	3.34	3.00	5.80	7.71	6.17	0.190
	n.a.	n.a.	3.69	3.08	6.10	7.38	6.13	0.205
Average	0.12696		3.23	2.76	5.76	7.27	6.10	0.178
2 sd	0.00050		0.88	0.88	0.95	0.85	0.13	0.135
Fisher-Gödde et al. (2010) batch b (N=5) (HP-asher)								
Average	**0.12733**		**3.56**	**3.10**	**6.57**	**7.12**	**5.91**	**0.188**
2 sd	0.00068		0.47	0.25	0.69	0.73	0.45	0.066
Fisher-Gödde et al. (2010) batch c (N=5) (HP-asher)								
Average	**0.12726**		**3.34**	**2.90**	**6.10**	**7.20**	**5.79**	**0.179**
2 sd	0.00042		0.21	0.16	0.46	1.27	0.43	0.041
Meisel and Moser (2004) (N=14, except Os N=8) (HP-asher)								
Average			**3.71**	**3.38**	**6.30**	**7.42**	**6.11**	**0.206**
2 sd			0.52	0.42	0.58	0.60	0.36	0.010

N: Number of analyses, sd: standard deviation. HPA refers to High-Pressure Digestion using HP-Asher, HP-CT refers to high-pressure digestion in Carius Tubes.

In situ major and trace element determination of silicates and glass

Major element determination by electron microprobe

The concentrations of major and minor elements in silicates and glass were analysed using a field emission cameca SXFive electron microprobe at the Raimond Castaing Center, CNRS-Toulouse University. The operating conditions were: accelerating voltage 15 kV; beam current 20 nA; the analysed surface was around 4 μm^2. The following standards were used: albite (Na), periclase (Mg), corundum (Al), Sanidine (K), wollastonite (Ca, Si), pyrophanite (Mn, Ti), hematite (Fe), Cr_2O_3 (Cr), NiO (Ni), sphalerite (Zn) and Vanadium metal (V). Elements were counted for 10 s on the peak and 5 s on each background position. To reduce alkali loss during glass analysis,

we lowered the beam current to 10 nA, and the beam was defocused to 10 µm. The results are listed in Appendix 4.

Trace element determination by laser ablation inductively coupled plass mass spectrometry

The concentration of lithophile trace elements (La, Ce, Nd, Sm, Eu, Gd, Dy, Ho, Er, Yb, Lu, Rb, Ba, Th, U, Sr, Zr, Hf, Ti, Ni, and V) in silicate and glass were analysed in situ by laser ablation inductively coupled plasma mass spectrometry (LA-ICP-MS), using a NewWave Research UP213 laser coupled to an Agilent 7500 ICP-MS instrument at GET laboratory, Observatorie Midi-Pyrénées, Toulouse, France, and with an ArF excimer laser 193 nm (Photon Machine Analyte G2) coupled with an iCapQ ICP-MS (ThermoFisher) at the CEGA mass spectrometer laboratory, University of Chile, Santiago, Chile. The counting time for one analysis was typically 180 s (60 s on gas blank to establish background and 120 s for data collection). The diameter of the laser beam was around 40 µm, the frequency 7 Hz, and 4 J/cm2 of laser fluence. A maximum of 10 unknowns were bracketed by the measurement of two external standards: the NIST SRM 610 (primary) and the USGS BCR-2G (secondary). The secondary standard is repetitively analysed as an unknown indicating both precision and the accuracy better than 10% for a given analytical session. The data reduction was carried out with Iolite software (Woodhead et al., 2007; Paton et al., 2011) for the sample using either the Ca or Mg contents -determined by electron microprobe- as internal standards. For the trace element composition of the glasses, the AMS software was used. AMS allows the normalisation of the material analysed to 100% oxide, a valid approximation if all the elements that contribute to the composition are measured. Detection limits for each element are in the range of 10 to 60 ppb except for Sc and V (100 ppb) and Ti (2 ppm), Ni and Cr (0.7 ppm).

In situ major and trace element concentrations in base metal sulfides

Major element determination by electron microprobe

Major element compositions of base metal BMS were performed using a five-channel JEOL JXA-8230 electron microprobe at the Serveis Cientificotècnics, University of Barcelona, Spain. The operating conditions were: accelerating voltage 20 kV, beam current 20 nA and a 5 µm beam diameter. The following standards were used: pyrite (S, Fe), Ni metal (Ni), chalcopyrite (Cu), Co metal (Co) and sphalerite (Zn). The results are listed in Appendix 2.

Trace element determination by laser ablation inductively coupled plass mass spectrometry

Selected individual BMS grains with diameters greater than 50 µm were analysed for its trace element composition (Os, Ir, Ru, Rh, Pt, Pd, Au, Re, Ag, As, Se, Cd, Sb, Te, Pb and Bi) following the methodology of Alard et al. (2000; 2002) and Saunders et al. (2015, 2016). The analyses were carried out on an Agilent 7700cx ICP-MS coupled with a Photon Machines Excite 193 nm ArF excimer laser ablation system at the Geochemical Analysis Unit (GaU) at CCFS/GEMOC, Macquarie University, Sydney, Australia. Data were corrected and processed using the GLITTER^{TM} software (Griffin et al., 2008), which allows for the cleanest part of the time-resolved spectrum to be selected, avoiding inclusion phases and host silicate phases. Helium was used as the carrier gas, which was blended with Ar prior to introduction into the plasma. The laser ablation system was operated at 5 Hz with laser energy of 5.7 J/cm^2. A quenched NiS (PGE-A: Alard et al., 2000, 2002), doped with selected chalcophile and siderophile elements was used as an external calibration standard for all elements except Sb. A chalcophile glass (IMER-2) was used for calibration of Sb concentrations. The accuracy of calibration was assessed using BCR-2 and IMER-2 glasses as unkowns. Detection limits for LA-ICP-MS analyses are calculated as average

background concentrations plus three standard deviations. The results, including a limit of detection for each element and standard deviations, are provided in Appendix 3.

Sulphur, determined by EMP, was used as an internal standard for all LA-ICP-MS analyses of sulfides to quantify the trace-element abundances. Sulphur was used because the difference in S content between typical mantle sulfides (*e.g.* (Ni,Fe)0.8S to (Ni,Fe)1.2S) is 30% relative compared to approximately 300% for Ni and 2000% for Cu in typical mantle sulfides (Alard et al., 2000; Alard et al., 2002; Aulbach et al., 2004; Aulbach et al., 2012; Bulanova et al., 1996; Delpech et al., 2012; Griffin et al., 2002; Guo et al., 1999; Lorand and Alard, 2001; Wang et al., 2009; Saunders et al., 2015; 2016). Therefore, error magnification will be minimised by using sulphur rather than one of the other major elements to quantify the trace-element concentrations.

SUPPLEMENTARY INFORMATION REFERENCES

Alard, O., Griffin, W.L., Lorand, J.-P., Jackson, S.E., O'Reilly, S.Y., 2000. Non-chondritic distribution of the highly siderophile elements in mantle sulfides. Nature 407, 891-894.

Alard, O., Griffin, W.L., Pearson, N.J., O'Reilly, S.Y., 2002. New insights into the Re-Os systematics of sub-continental lithospheric mantle from in situ analysis of sulfides. Earth Planet. Sci. Lett. 203, 651-663.

Aulbach, S., Griffin, W.L., O'Reilly, S.Y., McCandless, T.E., 2004. Genesis and evolution of the lithospheric mantle beneath the Buffalo Head Terrane, Alberta (Canada). Lithos 77, 413-451.

Aulbach, S., Stachel, T., Seitz, H.-M. and Brey, G. P., 2012. Chalcophile and siderophile elements in sulfide inclusions in eclogitic diamonds and metal cycling in a Paleoproterozoic subduction zone. Geochim. Cosmochim. Acta 93, 278-299.

Becker, H., Horan, M.F., Walker, R.J., Gao, S., Lorand, J.-P., Rudnick, R.L., 2006. Highly siderophile element compositions of the earth's primitive mantle. Geochim. Cosmochim. Acta 70, 4528-4550.

Bulanova, G. P., Griffin, W. L., Ryan, C. G., Shestakova, O. Y. and Barnes, S. J., 1996. Trace elements in sulfide inclusions from Yakutian diamonds. Contrib. Mineral. Petrol. 124, 111-125.

Cohen, A.S., Waters, F.G., 1996. Separation of osmium from geological materials by solvent extraction for analysis by thermal ionization mass spectrometry. Analytica Chimica Acta 332, 269-275.

Dale, C.W., Luguet, A., Macpherson, C.G., Pearson, D.G., Hickey-Vargas, R., 2008. Extreme platinum-group element fractionation and variable Os isotope compositions in Philippine Sea Plate basalts: tracing mantle source heterogeneity. Chemical Geology 248, 213-238.

Delpech, G., Lorand, J.-P., Grégoire, M., Cottin, J.-Y., O'Reilly, S.Y., 2012. In-situ geochemistry of sulfides in highly metasomatised mantle xenoliths from Kerguelen, southern India Ocean. Lithos 154, 296-314.

Fischer-Gödde, M., Becker, H., Wombacher, F., 2010. Rhodium, gold and other highly siderophile element abundances in chondritic meteorites. Geochim. Cosmochim. Acta 74, 356-379.

Fischer-Gödde, M., Becker, H., Wombacher, F., 2011. Rhodium, gold and other highly siderophile elements in orogenic peridotites and peridotite xenoliths. Chemical Geology 280, 365-383.

Govindaraju, K., 1994, Geostandards Newsletter, 18, Special Issue, 1-158.

Griffin, W., Powell, W., Pearson, N. and O'Reilly, S., 2008. GLITTER: data reduction software for laser ablation ICP-MS. Laser Ablation-ICP-MS in the Earth Sciences. Mineralogical Association of Canada Short Course Series 40, 204-207.

Griffin, W.L., Spetius, Z.V., Pearson, N.J., O'Reilly, S.Y., 2002. In situ Re-Os analysis of sulfide inclusions in kimberlitic olivine: new constraints on depletion events in the Siberian lithospheric mantle. Geochemistry, Geosphysics, Geosystems 3, 11.

Guo, J., Griffin, W. L. and O'Reilly, S. Y., 1999. Geochemistry and Origin of Sulfide Minerals in Mantle Xenoliths: Qilin, Southeastern China. Journal of Petrology 40, 1125-1149.

Ishikawa, A., Senda, R., Suzuki, K., Dale, C.W., Meisel, T., 2014. Re-evaluating digestión methods for highly siderophile element and ^{187}Os isotope analyses: evidence from geological reference materials. Chemical Geology 384, 27-56.

Lorand, J.-P. and Alard, O., 2001. Platinum-group element abundances in the upper mantle: new constraints from in situ and whole-rock analyses of Massif Central xenoliths (France). Geochim. Cosmochim. Acta 65, 2789-2806.

Luck, J.M., Allègre, C.J., 1984. ^{187}Re-^{187}Os investigation in sulfide from Cape Smith komatiite. Earth Planet. Sci. Lett. 68, 205-208.

Luguet, A., Behrens, M., Pearson, D.G., König, S., Herwatz, D., 2015. Significance of the whole rock Re-Os ages in cryptically and modally metasomatised cratonic peridotites: Constraints from HSE-Se-Te systematics. Geochim. Cosmochim. Acta 164, 441-463.

Luguet, A., Nowell, G.M., Pearson, D.G., 2008. 184Os/188Os and 186Os/188Os measurements by negative thermal ionization mass spectrometry (NTIMS): effects of interfering element and mass fractionation corrections on data accuracy and precision. *In* Highly Siderophile Element Geochemistry Special Issue (eds. Luguet, A., Pearson, D.G., Selby, D., Brenan, J., Meisel, T.). Cheimcal Geology 248, 342-362.

Luguet, A., Shirey, S.B., Lorand, J.-P., Horan, M.F., Carlson, R.W., 2007. Residual platinum-group minerals from highly depleted harzburgites of the Lherz massif (France) and their role in HSE fractionation of the mantle. Geochim. Cosmochim. Acta 71, 3082-3097.

Mallmann, G., O'Neil, H., C., St., 2007. The effect of oxygen fugacity on the partitioning of Re between crystals and silicate melts during mantle melting. Geochim. Cosmochim. Acta 71, 2837-2857.

Meisel, T., Moser, J., 2004. Reference materials for geochemical PGE analysis: new analytical data for Re, Rh, Pd, Os, Ir, Pt and Re by isotope dilution ICP-MS in 11 geological reference materials. Chemical Geology 208, 319–338.

Paton, C., Hellstrom, J., Paul, B., Woodhead, J., Hergt, J., 2011. "Iolite: Freeware for the visualization and processing of mass spectrometric data". Journal of Analytical Atomic Spectrometry.

Pearson, D.G., Woodland, S.J., 2000. Solvent extraction/anion exchange separation and determination of PGEs Os, Ir, Pt, Pd, Ru and Re-Os isotopes in geological samples by isotope dilution ICP-MS. Chemical Geology 165, 87-107.

Sambridge, M., Lambert, D.D., 1997. Propagating errors in decay equations: examples from the Re-Os isotopic system. Geochim. Cosmochim. Acta 61, 3019-3024.

Saunders, J.E., Pearson, N.J., O'Reilly, S.Y., Griffin, W.L., 2015. Sulfide metasomatism and the mobility of gold in the lithospheric mantle. Chemical Geology 410, 149-161.

Saunders, J.E., Pearson, N.J., O'Reilly, S.Y., Griffin, W.L., 2016. Gold in the mantle: The role of pyroxenites. Lithos 244, 205-217.

Shirey, S.B., Walker, R.J., 1998. Re-Os isotopes in cosmochemistry and high-temperature geochemistry. Ann. Rev: Earth Planet. Sci. Lett. 26, 423-500.

Walker, R.J., Carlson, R.W., Shirey, S.B., Boyd, F.R., 1989. Os, Sr, Nd and Pb isotope systematics of the southern African peridotite xenoliths: implications for the chemical evolution of the subcontinental mantle. Geochim. Cosmochim. Acta 53, 1583-1595.

Walker, R.J., Prichard, H.M., Ishiwatari, A., Pimentel, M., 2002. The osmium isotopic composition of convecting upper mantle deduced from ophiolites chromites. Geochim. Cosmochim. Acta 66, 329-345.

Wang, K.L., O'Reilly, S.Y., Griffin, W.L., Pearson, N.J., Zhang, M., 2009. Sulfides in mantle peridotites from Penghu Island, Taiwan: melt percolation, PGE fractionation, and lithospheric evolution of South China bloc. Geochim. Cosmochim. Acta 73, 4531-4557.

Woodhead, J., Hellstrom, J., Hergt, J., Greig, A., Mass, R., 2007. Isotopic and elemental imaging of geological materials by laser ablation Inductively Coupled Plasma mass spectrometry. Journal of Geostandards and Geoanalytical Research 31, 331-343.

Referred to as "Appendix 2" in Chapter 3. Whole-rock major and trace element data of the studied xenoliths.

Label		CR-01	CR-02	CR-03	CR-07	CR-08	CR-09
Group		I	II	II	II	II	II
Lithotype		Harzburgite	Lherzolite	Lherzolite	Lherzolite	Lherzolite	Lherzolite
Primary Modal abundances (%)	Ol	80	50	68	59	60	64
	Opx	20	41	22	27	32	26
	Cpx	0	9	10	14	8	10
Major Element Composition (wt. %)	SiO_2	44.99	45.55	44.99	44.85	45.77	44.87
	TiO_2	0.03	0.04	0.06	0.05	0.05	0.07
	Al_2O_3	1.53	1.77	1.93	1.98	2.18	2.15
	FeO	8.08	7.83	7.74	7.64	7.55	7.78
	MnO	0.13	0.13	0.12	0.12	0.12	0.13
	MgO	44.40	42.61	43.68	43.53	42.25	42.93
	CaO	0.84	2.03	1.44	1.74	2.00	2.01
	Na_2O	0.00	0.02	0.04	0.07	0.07	0.05
	K_2O	0.00	0.00	0.00	0.00	0.00	0.00
	P_2O_5	0.00	0.03	0.01	0.02	0.00	0.01
	Total	100.00	100.00	100.00	100.00	100.00	100.00
	Mg#	90.74	90.65	90.96	91.03	90.89	90.78
Eq. Temperature	T (°C)	962	1023	1114	1016	1041	1039
Trace Element Composition (ppm)	Ni	2179.0	2380.2	2309.0	2399.5	2191.0	2292.8
	Cr	2641.0	3120.7	2557.8	2929.4	2943.4	2364.0
	Sc	8.3	11.1	9.1	9.9	11.6	11.9
	Ti	327.3	391.4	557.2	537.8	520.7	686.7
	V	40.7	58.0	48.6	48.6	58.2	54.7
	Ba	6.6	6.8	7.0	6.3	7.0	9.2
	Rb	0.8	1.0	1.3	1.4	1.0	1.5
	Sr	3.1	7.1	5.1	6.4	3.9	6.1
	Zr	6.5	6.8	8.1	8.1	8.2	7.4
	Y	0.7	1.6	1.6	2.0	1.5	2.4
	Nb	0.0	0.0	0.3	0.0	0.0	0.0
	Ga	1.8	2.0	8.7	2.1	6.7	2.3
	Zn	45.1	45.6	44.5	48.3	42.4	43.1
	Pb	0.0	1.7	0.0	0.4	0.0	0.0
	La	0.0	0.0	6.3	0.0	0.0	0.0
	Ce	0.0	3.8	0.3	0.0	1.1	0.0
	Th	0.6	1.6	0.4	0.6	0.0	0.7
	Nd	1.3	2.4	0.9	2.6	2.2	0.7
	U	0.0	0.3	0.6	0.4	0.3	0.6
	sum tr.	5267.9	6073.6	5577.1	6021.3	5812.5	5504.1
	in %	0.5	0.6	0.6	0.6	0.6	0.6

Label		CR-01	CR-02	CR-03	CR-07	CR-08	CR-09
Group		**I**	**II**	**II**	**II**	**II**	**II**
Lithotype		**Harzburgite**	**Lherzolite**	**Lherzolite**	**Lherzolite**	**Lherzolite**	**Lherzolite**
Trace Element Composition Normalized After CI Carbonaceous Chondrite of McDonough and Sun (1995)	La	0.7	0.7	0.8	0.9	0.8	0.5
	Ce	0.6	0.8	0.8	0.8	0.7	0.6
	Pr	0.5	0.8	0.8	0.9	0.7	0.7
	Nd	0.4	0.8	0.9	1.0	0.8	0.9
	Sm	0.3	0.6	0.8	1.0	0.7	1.1
	Eu	0.3	0.5	0.8	1.0	0.8	1.2
	Gd	0.3	0.5	0.8	1.0	0.8	1.2
	Tb	0.4	0.6	0.8	1.0	1.0	1.2
	Dy	0.4	0.6	0.8	1.0	1.1	1.3
	Ho	0.4	0.6	0.9	1.0	1.0	1.3
	Er	0.4	0.6	0.8	1.0	1.0	1.4
	Tm	0.4	0.6	0.8	0.9	0.9	1.2
	Yb	0.5	0.6	0.9	1.0	1.0	1.3
	Lu	0.6	0.8	0.9	0.9	1.1	1.4
	Ba	40.2	26.9	11.1	25.7	19.5	16.4
	Th	1.1	0.8	0.8	0.7	0.7	0.5
	Nb	5.6	4.9	4.3	4.8	5.9	2.5
	Y	22.0	33.3	48.3	56.6	57.0	74.1
	Hf	1.5	1.5	3.4	3.8	2.8	4.0
	Ta	0.4	0.4	0.3	0.3	0.5	0.2
	U	0.3	0.4	1.8	0.4	0.2	0.3
	Pb	6.9	7.7	11.3	9.6	9.8	7.4
	Rb	8.7	10.4	8.3	18.9	9.8	13.1
	Cs	0.3	0.3	0.4	0.2	0.2	1.3
	Sr	100.3	274.2	226.6	271.0	199.2	272.2
	Sc	339.3	474.4	391.7	416.8	473.9	490.9
	Zr	58.4	48.0	113.7	129.5	97.8	124.4
	La/Yb	1.6	1.1	0.9	0.9	0.8	0.4

Label		TL-01	TL-2-1	TL-2-3	TL-03	TL-05	TL-06	TL-08
Group		**III**	**I**	**II**	**III**	**I**	**III**	**III**
Lithotype		**Lherzolite**	**Harzburgite**	**Lherzolite**	**Lherzolite**	**Dunite**	**Lherzolite**	**Lherzolite**
Primary Modal abundances (%)	Ol	65	84	75	55	98	54	54
	Opx	23	16	15	31	2	24	33
	Cpx	12	0	10	14	0	22	13
Major Element Composition (wt. %)	SiO_2	44.83	43.62	45.04	45.10	45.28	45.96	45.28
	TiO_2	0.12	0.02	0.04	0.07	0.04	0.12	0.09
	Al_2O_3	3.67	0.66	1.76	2.43	1.52	3.57	2.94
	FeO	8.00	8.38	7.72	8.15	8.26	8.03	8.24
	MnO	0.13	0.13	0.12	0.13	0.13	0.13	0.13
	MgO	39.70	46.64	43.74	42.13	43.76	39.14	40.75
	CaO	3.33	0.55	1.56	1.88	1.00	2.87	2.39
	Na_2O	0.19	0.00	0.00	0.07	0.00	0.17	0.15
	K_2O	0.00	0.00	0.00	0.00	0.01	0.00	0.00
	P_2O_5	0.03	0.01	0.00	0.04	0.01	0.01	0.03
	Total	100.00	100.00	100.00	100.00	100.00	100.00	100.00
	Mg#	89.85	90.84	90.99	90.21	90.42	89.68	89.81
Eq. Temperature	T (°C)	967	1020	963	925	1025	922	1008
Trace Element Composition (ppm)	Ni	2051.3	2487.8	2246.0	2174.1	2197.9	1928.2	2084.2
	Cr	2868.0	2219.7	3464.6	2367.8	2993.3	2636.2	2640.8
	Sc	16.4	7.5	10.7	10.7	11.5	15.7	12.6
	Ti	1183.4	160.5	360.5	661.6	368.1	1233.3	906.1
	V	81.3	26.3	48.9	55.7	41.3	77.8	64.9
	Ba	16.3	7.5	7.3	6.5	10.1	11.6	6.8
	Rb	0.7	1.0	1.1	1.5	1.0	2.1	1.5
	Sr	21.8	2.1	2.1	7.3	5.3	13.3	12.2
	Zr	10.4	7.0	6.8	8.2	6.0	10.3	8.8
	Y	4.1	0.7	1.1	1.7	0.8	2.5	2.3
	Nb	0.1	0.0	0.8	0.8	0.3	1.0	0.7
	Ga	2.4	3.3	2.1	2.8	2.9	2.7	3.1
	Cu	15.0	2.5	4.4	7.5	4.7	12.0	21.2
	Zn	51.3	49.1	49.2	46.4	46.7	50.5	49.9
	Pb	0.0	0.0	0.8	2.1	0.0	1.8	0.7
	La	0.0	0.0	0.0	0.1	0.0	1.4	0.6
	Ce	6.4	0.8	0.0	4.2	2.9	0.0	0.4
	Th	1.7	0.8	0.0	0.0	1.1	0.6	0.8
	Nd	3.7	2.3	0.3	3.7	0.8	0.0	3.8
	U	0.0	0.7	0.0	1.8	0.3	1.1	0.1
	sum tr.	6334.2	4979.6	6206.8	5364.5	5695.1	6002.1	5821.6
	in %	0.6	0.5	0.6	0.5	0.6	0.6	0.6

Label		TL-01	TL-2-1	TL-2-3	TL-03	TL-05	TL-06	TL-08
Group		**III**	**I**	**II**	**III**	**I**	**III**	**III**
Lithotype		**Lherzolite**	**Harzburgite**	**Lherzolite**	**Lherzolite**	**Dunite**	**Lherzolite**	**Lherzolite**
Trace Element Composition Normalized After CI Carbonaceous Chondrite of McDonough and Sun (1995)	La	3.9	1.2	0.3	1.1	1.7	2.3	2.1
	Ce	3.1	0.6	0.2	0.6	1.0	1.4	1.2
	Pr	2.5	0.5	0.3	0.9	0.8	1.3	1.2
	Nd	2.2	0.4	0.3	1.0	0.6	1.5	1.1
	Sm	1.9	0.3	0.4	0.9	0.5	1.8	1.3
	Eu	2.3	0.2	0.4	1.0	0.4	1.9	1.3
	Gd	2.2	0.2	0.4	1.2	0.4	2.1	1.4
	Tb	2.4	0.2	0.5	1.2	0.4	2.3	1.6
	Dy	2.4	0.2	0.6	1.3	0.4	2.3	1.7
	Ho	2.5	0.2	0.6	1.3	0.4	2.3	1.7
	Er	2.4	0.2	0.7	1.3	0.5	2.1	1.7
	Tm	2.5	0.3	0.7	1.4	0.6	2.2	1.6
	Yb	2.3	0.3	0.7	1.4	0.7	2.2	1.6
	Lu	2.5	0.4	0.8	1.5	0.8	2.3	1.6
	Ba	494.2	11.3	-9.1	53.1	128.9	153.6	166.6
	Th	5.6	2.9	0.4	0.6	2.5	4.1	3.8
	Nb	25.9	9.5	1.6	2.7	14.6	16.1	20.9
	Y	140.1	12.9	34.6	76.6	28.9	125.4	90.1
	Hf	6.9	2.0	1.3	3.5	1.9	7.0	4.8
	Ta	0.3	0.7	0.1	0.1	0.8	0.3	0.6
	U	1.4	0.7	0.1	0.6	0.8	1.0	1.5
	Pb	5.7	5.8	7.6	5.8	8.2	8.8	7.5
	Rb	3.9	3.9	3.2	1.9	10.7	5.4	6.9
	Cs	0.1	0.1	0.2	0.0	0.3	0.3	0.1
	Sr	943.3	87.3	82.5	310.2	207.1	539.7	511.6
	Sc	632.6	281.7	427.1	447.2	445.9	585.6	533.6
	Zr	211.4	84.6	40.5	111.1	70.8	208.1	161.9
	La/Yb	1.6	4.8	0.4	0.8	2.9	1.1	1.3

Label		GG-01-A	GG-01-B	GG-02	GG-03	GG-05	GG-07	GG-10	GG-13	GG-14	GG-17
Group		**IV**	**IV**	**IV**	**IV**	**III**	**IV**	**III**	**III**	**IV**	**IV**
Lithotype		**Lherzolite**	**Wherlite**	**Lherzolite**	**Lherzolite**	**Lherzolite**	**Lherzolite**	**Lherzolite**	**Lherzolite**	**Lherzolite**	**Lherzolite**
Primary Modal abundances (%)	Ol	48	70	87	67	73	64	71	60	68	70
	Opx	6	0	3	24	19	29	23	26	21	5
	Cpx	46	30	10	9	8	8	6	14	12	25
Major Element Composition (wt. %)	SiO_2	42.67	45.78	41.96	44.42	43.78	44.76	44.90	45.18	43.47	42.65
	TiO_2	0.32	0.71	0.08	0.06	0.04	0.27	0.05	0.05	0.02	0.12
	Al_2O_3	1.88	4.13	0.86	1.49	1.10	2.93	1.68	2.43	1.24	1.50
	FeO	8.89	7.13	9.06	7.83	8.05	9.43	7.98	7.95	7.97	8.30
	MnO	0.14	0.12	0.15	0.13	0.12	0.15	0.13	0.13	0.13	0.14
	MgO	41.98	32.45	45.45	44.03	45.92	38.73	42.61	42.69	44.71	42.89
	CaO	3.46	8.09	2.08	1.79	0.96	3.31	2.59	1.39	2.08	3.80
	Na_2O	0.46	1.16	0.29	0.16	0.00	0.33	0.06	0.15	0.29	0.49
	K_2O	0.13	0.35	0.04	0.00	0.00	0.04	0.00	0.01	0.04	0.05
	P_2O_5	0.08	0.06	0.04	0.10	0.01	0.06	0.01	0.02	0.04	0.06
	Total	100.00	100.00	100.00	100.00	100.00	100.00	100.00	100.00	100.00	100.00
	Mg#	89.38	89.03	89.94	90.93	91.04	87.98	90.49	90.54	90.90	90.20
Eq. Temperature	T (°C)	961	1076	918	962	982	915	1065	-	811	782
Trace Element Composition (ppm)	Ni	2193.5	1553.6	2294.2	2252.7	2563.8	1843.2	2141.7	2204.2	2334.7	2318.3
	Cr	2031.0	4591.8	1615.2	3667.2	2074.2	2857.3	3083.7	3006.5	2216.2	2739.6
	Sc	10.5	24.9	6.2	11.0	7.4	10.9	12.4	10.4	9.8	12.3
	Ti	3157.8	7131.8	800.7	584.4	360.7	2665.9	485.3	519.3	237.4	1182.1
	V	64.2	145.9	34.2	48.2	34.1	65.7	56.6	48.6	33.0	55.6
	Ba	38.1	96.8	17.2	8.9	9.9	20.6	10.5	10.2	19.7	23.5
	Rb	2.8	3.6	1.4	1.6	0.8	1.5	1.5	0.4	0.8	2.8
	Sr	90.4	183.6	41.3	33.6	7.2	51.7	7.7	10.1	43.0	63.6
	Zr	45.2	98.4	18.5	11.1	7.1	23.0	7.1	11.5	8.1	27.5
	Y	4.4	10.4	3.0	3.9	0.4	5.1	1.6	2.0	2.5	3.4
	Nb	20.2	35.1	8.5	0.7	0.6	2.6	0.0	0.3	5.7	3.1
	Ga	3.4	5.8	1.8	3.9	1.0	6.1	2.0	3.6	1.1	2.1
	Cu	7.2	7.0	31.9	4.3	5.5	12.5	6.7	6.0	15.7	3.1
	Zn	65.7	49.6	57.5	54.9	48.0	72.3	47.7	50.7	52.4	49.6
	La	0.0	9.4	1.9	0.0	1.1	6.0	2.7	0.0	0.0	6.2
	Ce	12.8	21.9	6.1	0.0	4.4	5.0	1.4	0.1	2.4	6.6
	Th	0.6	1.3	0.0	0.7	0.0	1.1	0.4	0.7	0.7	0.0
	Nd	8.8	17.3	4.9	3.3	0.0	4.3	3.0	0.0	1.7	6.8
	U	0.7	0.0	0.8	1.0	0.0	0.1	1.6	0.6	0.0	2.5
	sum tr.	7757.3	13988.1	4945.5	6691.5	5128.2	7655.5	5874.0	5885.1	4986.2	6508.8
	in %	0.8	1.4	0.5	0.7	0.5	0.8	0.6	0.6	0.5	0.7

Referred to as "Appendix 3" in Chapter 3. Whole-rock HSE and Re-Os isotope composition data of the studied xenoliths

Sample		$^{187}Os/^{188}Os$	2se	Os (ppb)	Ir (ppb)	Ru (ppb)	Pt (ppb)	Pd (ppb)	Re (ppb)	Os_N/Ir_N	Ru_N/Ir_N	Pt_N/Ir_N	Pd_N/Ir_N	Pd_N/Pt_N	Re_N/Pd_N	T_{RD} (Ga)	T_{MA} (Ga)
Group 1 Peridotites																	
CR-01	0.04600	0.117794	0.00031	3.18	3.78	bdl	5.09	3.45	0.03	0.77	-	0.65	0.67	1.04	0.14	1.45	1.63
TL-05	0.03619	0.125722	0.000115	2.43	1.81	4.81	2.54	1.86	0.02	1.23	1.79	0.68	0.76	1.12	0.16	0.34	0.37
TL-2-1	0.01193	n.a.	n.a.	1.94	1.78	5.86	5.63	1.68	0.01	1.00	2.21	1.52	0.70	0.46	0.05	-	-
Group 2 Peridotites																	
CR-02	0.18160	n.a.	n.a.	2.94	3.72	8.22	8.37	6.73	0.11	0.72	1.48	1.08	1.34	1.23	0.26	-	-
CR-07	0.19555	0.119411	0.000251	3.80	4.07	6.48	6.28	4.02	0.16	0.85	1.07	0.74	0.73	0.98	0.61	1.23	2.27
CR-08	0.21842	0.120119	0.000188	5.52	5.48	9.75	8.91	6.90	0.26	0.92	1.19	0.78	0.93	1.19	0.58	1.13	2.32
CR-09	0.72769	0.119908	0.000043	3.76	3.84	7.03	5.85	4.31	0.58	0.89	1.23	0.73	0.83	1.13	2.10	1.16	-1.63
TL-2-3	0.06601	0.124494	0.000054	1.98	3.00	5.37	4.69	3.87	0.03	0.60	1.20	0.75	0.95	1.27	0.11	0.51	0.61
Group 3 Peridotites																	
TL-01	0.29245	0.126023	0.000199	1.23	2.44	3.92	4.16	3.37	0.08	0.46	1.08	0.82	1.02	1.24	0.35	0.30	0.96
TL-03	0.22749	0.122626	0.000144	1.01	1.40	3.34	2.25	1.99	0.05	0.66	1.60	0.77	1.05	1.35	0.38	0.78	1.67
TL-06	0.18959	0.127191	0.000124	1.22	2.15	5.10	2.97	2.52	0.05	0.52	1.59	0.67	0.87	1.30	0.30	0.13	0.24
TL-08	0.18678	0.124566	0.000186	1.48	1.96	4.59	4.00	2.64	0.06	0.69	1.57	0.98	1.00	1.01	0.34	0.50	0.90
GG-10	0.09921	0.121757	0.000132	1.99	2.61	4.98	4.65	3.30	0.04	0.70	1.28	0.86	0.93	1.09	0.20	0.90	1.17
GG-13	0.03552	n.a.	n.a.	2.28	3.18	5.81	5.49	2.17	0.02	0.65	1.23	0.83	0.50	0.61	0.12	-	-
Group 4 Peridotites																	
GG-01-A	0.11217	0.123755	0.000158	0.67	0.73	0.95	1.16	0.87	0.02	0.83	0.87	0.76	0.88	1.15	0.28	0.62	0.84
GG-01-B	0.5204	0.215985	0.000191	0.31	0.41	0.45	6.07	11.57	0.03	0.68	0.73	7.12	20.82	2.93	0.05	-14.05	38.02
GG-02	0.13968	0.116330	0.000115	1.81	3.11	4.93	3.11	1.29	0.05	0.53	1.06	0.48	0.31	0.64	0.65	1.66	2.46
GG-03	0.00294	n.a.	n.a.	1.61	1.53	2.18	5.34	2.72	0.00	0.96	0.95	1.67	1.31	0.78	0.01	-	-
GG-07	0.01339	0.123417	0.000087	2.12	3.16	8.52	5.28	2.69	0.01	0.61	1.81	0.80	0.63	0.78	0.03	0.66	0.69
GG-14	0.02061	0.118995	0.000077	1.84	3.32	6.36	6.22	3.07	0.01	0.50	1.29	0.90	0.68	0.76	0.04	1.28	1.35
GG-17	0.10265	0.120210	0.000151	1.09	1.20	0.94	5.80	1.91	0.02	0.83	0.52	2.32	1.17	0.50	0.19	1.12	1.47

Referred to as "Appendix 4" in Chapter 3. Major and Trace element composition of silicates and glass.

		Major Element Composition (wt.%)												
Group	**Phase**	**Na2O**	**Al2O3**	**SiO2**	**K2O**	**CaO**	**MnO**	**FeO**	**MgO**	**TiO2**	**Cr2O3**	**NiO**	**Total**	**Mg#**
Group 2	Cpx1	1.13	4.41	52.52	BDL	22.38	0.08	1.95	15.18	0.23	1.21	0.03	99.11	93.28
Group 2	Cpx1	0.96	3.81	52.93	BDL	22.23	0.09	2.04	15.77	0.22	1.17	0.14	99.36	93.25
Group 2	Cpx1	1.07	4.14	52.65	0.05	22.23	0.05	1.97	15.65	0.22	1.15	0.01	99.18	93.40
Group 2	Cpx1	0.86	3.79	52.71	BDL	22.77	0.04	2.13	15.98	0.18	1.04	0.07	99.57	93.06
Group 2	Cpx1	1.12	4.45	52.46	0.02	22.06	0.11	1.94	15.07	0.20	1.26	0.06	98.74	93.27
Group 2	Cpx1	0.87	3.34	53.06	0.01	22.54	0.05	2.09	15.77	0.19	0.87	0.08	98.86	93.09
Group 2	Cpx1	1.13	4.27	52.75	0.01	22.17	0.09	1.92	15.45	0.18	1.21	0.05	99.22	93.50
Group 2	Cpx1	0.46	2.27	53.02	BDL	22.48	0.01	2.53	17.23	0.53	1.39	0.13	100.04	92.40
Group 2	Cpx1	1.09	4.70	52.50	BDL	22.61	0.03	1.92	15.20	0.23	1.31	0.05	99.63	93.38
Group 2	Cpx1	0.96	4.05	52.79	0.02	22.55	0.07	2.05	15.66	0.23	1.18	0.03	99.59	93.16
Group 2	Cpx1	1.33	4.96	52.14	BDL	21.43	0.06	2.40	15.56	0.33	1.24	0.09	99.55	92.05
Group 2	Cpx1	1.62	5.57	52.58	BDL	21.19	0.07	1.96	15.06	0.32	1.37	BDL	99.74	93.18
Group 2	Cpx1	1.39	5.31	52.01	0.01	21.50	0.08	2.21	15.33	0.32	1.26	0.04	99.45	92.53
Group 2	Cpx1	1.32	5.76	52.34	BDL	21.85	0.07	2.10	14.99	0.43	1.07	0.07	99.98	92.71
Group 2	Cpx1	1.44	7.47	50.87	0.03	19.09	0.06	3.02	15.72	0.59	1.11	0.10	99.49	90.26
Group 2	Cpx1	1.51	6.71	51.47	0.02	19.88	0.07	2.94	15.47	0.72	0.95	0.05	99.80	90.37
Group 2	Cpx1	1.26	5.52	52.30	BDL	21.32	0.03	2.28	15.27	0.45	1.08	0.08	99.59	92.28
Group 2	Cpx1	1.28	6.44	51.37	BDL	19.49	0.10	2.89	15.67	0.63	1.08	0.02	98.97	90.62
Group 2	Cpx1	1.23	5.42	52.24	BDL	22.01	0.12	2.02	14.89	0.44	0.98	0.05	99.40	92.92
Group 3	Cpx1	0.51	2.97	52.92	0.02	23.71	0.07	1.90	16.73	0.23	0.82	0.05	99.93	94.00
Group 3	Cpx1	0.46	2.85	53.41	0.01	22.25	0.08	2.26	17.98	0.21	0.68	0.04	100.23	93.43
Group 3	Cpx1	0.56	3.74	52.44	0.01	23.33	0.08	2.01	16.63	0.22	1.16	0.03	100.20	93.64
Group 3	Cpx1	0.54	2.72	53.00	0.02	23.44	0.05	1.96	17.05	0.21	0.74	0.05	99.78	93.94
Group 3	Cpx1	0.47	4.33	51.37	0.02	22.65	0.08	2.28	16.88	0.20	1.45	0.05	99.77	92.96
Group 3	Cpx2	1.49	4.61	53.43	0.01	20.60	0.09	2.40	16.48	0.23	1.16	0.05	100.55	92.46
Group 3	Cpx2	1.42	4.54	53.02	0.02	20.73	0.08	2.33	16.43	0.19	1.23	0.03	100.01	92.64
Group 3	Cpx2	1.41	4.57	52.83	0.01	20.59	0.08	2.44	16.50	0.21	1.17	0.04	99.86	92.35
Group 3	Cpx2	1.36	4.50	52.87	0.01	20.70	0.07	2.33	16.41	0.21	1.18	0.05	99.68	92.62

Group	Phase	Na2O	Al2O3	SiO2	K2O	CaO	MnO	FeO	MgO	TiO2	Cr2O3	NiO	Total	Mg#
Group 3	Cpx2	1.36	4.51	52.77	0.01	20.72	0.09	2.39	16.44	0.21	1.11	0.04	99.65	92.47
Group 3	Cpx2	1.47	5.47	52.65	BDL	20.50	0.09	2.46	15.89	0.24	1.10	0.04	99.90	92.01
Group 3	Cpx2	1.45	5.35	52.59	0.01	20.62	0.08	2.69	15.98	0.24	0.95	0.05	100.00	91.38
Group 3	Cpx2	1.46	5.47	52.42	0.02	20.66	0.11	2.56	15.92	0.24	1.06	0.04	99.95	91.72
Group 3	Cpx2	1.46	5.48	52.56	0.02	20.61	0.07	2.59	16.02	0.26	1.02	0.04	100.15	91.70
Group 3	Cpx2	1.46	5.37	52.59	0.02	20.67	0.09	2.53	16.00	0.24	0.92	0.04	99.93	91.85
Group 3	Cpx2	1.43	5.29	52.51	0.01	20.62	0.11	2.64	16.06	0.26	0.93	0.05	99.91	91.56
Group 3	Cpx2	1.43	5.36	52.49	0.02	20.68	0.09	2.53	16.09	0.27	0.91	0.05	99.91	91.90
Group 3	Cpx2	1.44	5.43	52.54	0.02	20.62	0.08	2.54	15.99	0.26	0.92	0.04	99.88	91.81
Group 3	Cpx2	1.44	5.50	52.39	0.01	20.63	0.09	2.56	15.95	0.25	0.99	0.05	99.85	91.74
Group 3	Cpx2	1.42	5.34	52.36	0.01	20.63	0.09	2.56	16.00	0.26	0.96	0.05	99.69	91.77
Group 3	Cpx3	1.61	6.43	51.92	BDL	20.15	0.10	2.59	14.64	0.58	0.64	0.07	98.72	90.98
Group 3	Cpx3	1.67	6.11	52.29	BDL	20.39	0.08	2.65	14.88	0.56	0.68	0.02	99.31	90.91
Group 3	Cpx3	1.71	6.28	51.13	0.01	20.25	0.07	2.70	14.72	0.58	0.68	0.05	98.18	90.67
Group 3	Cpx3	1.59	6.30	52.03	BDL	20.20	0.09	2.66	14.89	0.54	0.67	0.01	98.98	90.90
Group 3	Cpx3	1.61	6.20	52.25	0.04	20.19	0.06	2.69	15.14	0.55	0.73	0.06	99.51	90.93
Group 3	Cpx3	1.62	6.31	52.06	BDL	20.27	0.09	2.63	14.99	0.55	0.71	0.09	99.32	91.04
Group 3	Cpx3	1.76	6.19	50.05	0.01	20.24	0.11	2.56	15.05	0.55	0.70	0.04	97.27	91.28
Group 3	Cpx3	1.77	6.14	52.06	0.02	20.22	0.07	2.68	14.92	0.57	0.70	0.01	99.14	90.85
Group 3	Cpx3	1.61	5.96	51.94	0.03	20.17	0.08	2.61	14.77	0.57	0.68	0.06	98.48	90.98
Group 3	Cpx3	1.63	6.18	52.09	0.02	20.01	0.17	2.69	14.80	0.52	0.70	0.09	98.90	90.74
Group 3	Cpx3	1.73	6.32	52.35	BDL	20.13	0.09	2.74	15.15	0.55	0.70	0.03	99.77	90.79
Group 3	Cpx3	1.69	6.06	52.51	0.03	20.13	0.09	2.63	15.14	0.44	0.85	0.07	99.64	91.12
Group 3	Cpx3	1.68	5.96	52.41	BDL	19.81	0.10	2.54	15.19	0.44	0.86	0.05	99.04	91.42
Group 3	Cpx3	1.69	5.90	52.70	0.01	19.95	0.07	2.71	15.09	0.42	0.84	0.06	99.42	90.84
Group 3	Cpx3	1.67	6.25	52.36	BDL	20.27	0.13	2.60	15.00	0.43	0.78	0.03	99.52	91.15
Group 3	Cpx3	1.69	5.96	52.60	0.05	20.18	0.13	2.52	15.02	0.47	0.78	0.04	99.44	91.39
Group 3	Cpx3	1.65	6.14	52.45	0.03	20.04	0.08	2.64	15.11	0.46	0.76	0.02	99.38	91.07
Group 3	Cpx3	1.71	5.87	52.13	0.01	20.13	0.03	2.66	14.97	0.47	0.89	0.06	98.91	90.95
Group 3	Cpx3	1.76	5.81	52.32	BDL	20.23	0.10	2.73	14.96	0.46	0.86	0.04	99.27	90.73
Group 3	Cpx3	1.73	6.10	52.44	0.02	20.18	0.07	2.56	14.95	0.45	0.81	0.05	99.35	91.23

Group	Phase	Na2O	Al2O3	SiO2	K2O	CaO	MnO	FeO	MgO	TiO2	Cr2O3	NiO	Total	Mg#
Group 3	Cpx3	1.67	6.10	52.64	BDL	20.00	0.07	2.57	14.93	0.46	0.83	0.04	99.31	91.21
Group 3	Cpx3	1.67	6.00	52.62	BDL	20.34	0.09	2.65	15.05	0.47	0.80	0.05	99.75	91.00
Group 3	Cpx3	1.64	5.99	52.51	0.03	19.82	0.10	2.62	15.12	0.47	0.85	0.03	99.19	91.15
Group 4	Cpx4	0.62	4.77	51.04	BDL	22.25	0.08	2.23	15.64	0.32	2.41	0.09	99.44	92.61
Group 4	Cpx4	0.63	4.13	51.37	BDL	21.81	0.08	2.34	16.36	0.27	2.18	0.10	99.28	92.56
Group 4	Cpx4	0.68	5.04	50.86	0.01	22.02	0.09	2.29	15.37	0.32	2.64	0.04	99.36	92.29
Group 4	Cpx4	0.76	5.38	49.84	BDL	22.25	0.08	2.29	15.13	0.40	3.20	0.09	99.42	92.17
Group 4	Cpx4	0.78	5.44	49.71	0.01	22.21	0.08	2.21	15.36	0.41	3.16	0.08	99.45	92.54
Group 4	Cpx5	1.32	5.82	51.17	0.01	20.13	0.08	2.39	15.73	0.31	2.04	0.06	99.06	92.15
Group 4	Cpx5	2.53	5.06	53.46	0.02	19.03	0.13	2.58	15.06	0.07	1.90	0.08	99.91	91.22
Group 4	Cpx5	2.55	5.08	53.29	BDL	19.00	0.11	2.63	15.08	0.07	1.88	0.02	99.71	91.08
Group 4	Cpx5	2.49	5.07	53.53	0.01	18.71	0.05	2.70	14.90	0.09	1.85	0.06	99.45	90.77
Group 4	Cpx6	2.31	5.38	52.97	0.01	18.68	0.07	3.48	15.27	0.64	1.24	0.03	100.08	88.68
Group 4	Cpx6	0.81	3.91	51.26	0.01	21.97	0.11	3.34	15.83	1.06	1.49	0.08	99.87	89.41
Group 4	Cpx6	2.54	6.17	52.71	BDL	18.27	0.10	3.47	15.00	0.80	1.31	0.06	100.41	88.52
Group 4	Cpx6	2.43	6.10	52.86	0.01	18.45	0.11	3.52	15.00	0.79	1.30	0.09	100.66	88.37
Group 4	Cpx6	2.38	7.17	51.67	0.02	18.23	0.09	3.94	14.46	0.87	1.00	0.20	100.01	86.76
Group 4	Cpx6	3.52	8.86	53.92	0.21	16.26	0.10	3.80	13.89	0.87	0.87	0.16	102.46	86.70
Group 4	Cpx6	2.50	8.01	50.93	0.01	18.61	0.12	3.57	14.14	1.02	0.95	0.01	99.86	87.61
Group 4	Cpx6	2.42	7.81	51.18	BDL	18.26	0.12	3.68	14.20	0.94	0.91	0.03	99.55	87.31
Group 4	Cpx6	2.47	7.76	51.09	BDL	18.58	0.09	3.52	14.08	0.90	1.19	0.07	99.76	87.69
Group 4	Cpx6	2.32	7.71	51.32	0.01	18.60	0.13	3.70	14.45	0.91	0.72	0.05	99.91	87.43
Group 4	Cpx6	2.39	8.00	51.04	BDL	18.70	0.08	3.71	14.05	1.01	0.82	0.09	99.88	87.10
Group 4	Cpx6	2.38	7.93	51.34	0.02	18.50	0.10	3.72	14.44	0.99	0.70	0.04	100.15	87.39

Group	Phase	Na2O	Al2O3	SiO2	K2O	CaO	MnO	FeO	MgO	TiO2	Cr2O3	NiO	Total	Mg#
Group 1	Opx	0.02	2.89	56.22	BDL	0.26	0.13	5.11	34.80	0.03	0.45	0.07	99.98	92.39
Group 1	Opx	BDL	3.11	55.39	BDL	0.54	0.17	5.21	34.63	0.04	0.55	0.06	99.71	92.22
Group 1	Opx	BDL	3.21	56.28	BDL	0.31	0.11	5.05	34.27	0.07	0.48	0.08	99.86	92.36
Group 1	Opx	BDL	3.14	55.89	BDL	0.57	0.15	5.45	34.31	0.02	0.29	0.1	99.93	91.82
Group 2	Opx	BDL	3.53	55.72	BDL	0.50	0.11	5.67	32.96	0.04	0.65	0.08	99.26	91.21
Group 2	Opx	0.03	3.84	55.27	0.02	0.36	0.16	5.77	33.07	0.05	0.69	0.11	99.36	91.09
Group 2	Opx	BDL	3.25	55.93	BDL	0.30	0.16	5.83	33.38	0.04	0.54	0.10	99.55	91.07
Group 2	Opx	0.02	3.25	55.59	BDL	0.35	0.17	5.75	33.22	0.03	0.60	0.05	99.08	91.14
Group 2	Opx	0.02	2.95	55.57	0.01	0.45	0.18	5.51	33.19	0.06	0.47	0.12	98.58	91.49
Group 2	Opx	0.02	3.22	55.48	BDL	0.53	0.18	5.81	33.10	0.06	0.57	0.07	99.08	91.03
Group 2	Opx	0.03	3.06	56.23	BDL	0.42	0.08	5.51	33.96	0.07	0.35	0.15	99.90	91.66
Group 2	Opx	0.10	4.50	55.29	0.04	1.26	0.15	5.63	32.26	0.13	0.62	0.12	100.11	91.08
Group 2	Opx	0.07	3.70	55.97	0.01	0.63	0.14	5.53	33.28	0.07	0.56	0.09	100.07	91.47
Group 2	Opx	0.06	3.11	56.35	BDL	0.35	0.10	5.59	33.54	0.07	0.27	0.10	99.60	91.46
Group 2	Opx	0.04	3.22	56.15	0.01	0.41	0.11	5.58	33.14	0.06	0.54	0.07	99.32	91.38
Group 2	Opx	0.04	3.16	55.92	0.01	0.43	0.19	5.62	33.10	0.06	0.54	0.09	99.16	91.31
Group 2	Opx	0.06	3.13	55.80	BDL	0.35	0.15	5.60	33.14	0.04	0.48	0.04	98.81	91.34
Group 3	Opx	BDL	3.06	55.83	0.02	0.50	0.18	5.55	32.97	0.07	0.44	0.10	98.74	91.37
Group 3	Opx	0.09	4.16	54.94	0.01	0.70	0.12	5.95	32.11	0.10	0.33	0.12	98.63	90.59
Group 3	Opx	0.10	4.20	55.26	BDL	0.73	0.12	6.18	31.94	0.11	0.32	0.13	99.08	90.21
Group 3	Opx	0.14	4.22	54.71	BDL	0.68	0.18	6.22	32.01	0.08	0.31	0.09	98.65	90.17
Group 3	Opx	0.12	4.14	54.83	0.01	0.78	0.14	6.20	32.17	0.12	0.33	0.12	98.98	90.24
Group 3	Opx	0.11	4.06	54.77	0.01	0.70	0.13	6.04	31.88	0.11	0.32	0.10	98.22	90.40
Group 3	Opx	0.11	4.28	54.87	BDL	0.68	0.17	6.16	32.22	0.12	0.30	0.13	99.05	90.32
Group 3	Opx	0.11	4.20	55.62	0.02	0.65	0.14	6.01	32.39	0.09	0.38	0.11	99.71	90.58
Group 3	Opx	0.09	4.24	55.39	0.01	0.67	0.10	5.93	32.44	0.07	0.38	0.05	99.38	90.70
Group 3	Opx	0.11	4.21	55.60	0.01	0.71	0.17	6.11	32.46	0.08	0.38	0.07	99.97	90.45
Group 3	Opx	0.12	3.98	55.34	0.04	0.75	0.11	6.20	32.51	0.13	0.36	0.07	99.63	90.33
Group 3	Opx	0.14	4.11	55.31	0.02	0.70	0.13	5.97	32.31	0.10	0.36	0.04	99.19	90.61
Group 3	Opx	0.13	4.09	55.65	0.01	0.68	0.13	6.17	32.53	0.10	0.32	0.07	99.96	90.39

Group	Phase	Na2O	Al2O3	SiO2	K2O	CaO	MnO	FeO	MgO	TiO2	Cr2O3	NiO	Total	Mg#
Group 3	Opx	0.12	4.22	55.49	0.03	0.71	0.21	6.04	32.21	0.10	0.36	0.06	99.59	90.49
Group 3	Opx	0.11	4.09	55.44	BDL	0.71	0.13	6.09	32.32	0.09	0.37	0.12	99.49	90.44
Group 3	Opx	0.14	4.09	55.49	0.02	0.78	0.10	5.99	32.53	0.07	0.41	0.03	99.69	90.64
Group 3	Opx	0.10	4.01	55.55	BDL	0.67	0.17	6.14	32.55	0.09	0.39	0.18	99.90	90.44
Group 3	Opx	0.11	4.00	55.70	BDL	0.67	0.15	6.09	32.50	0.08	0.39	0.17	99.87	90.48
Group 3	Opx	0.09	3.99	55.35	BDL	0.73	0.15	6.03	32.33	0.08	0.38	0.07	99.20	90.53
Group 3	Opx	0.09	3.41	56.66	0.02	0.66	0.12	5.53	34.44	0.06	0.55	0.10	101.62	91.73
Group 3	Opx	0.09	3.42	56.25	0.01	0.70	0.14	5.52	34.40	0.07	0.56	0.08	101.25	91.74
Group 3	Opx	0.09	3.41	56.19	0.01	0.67	0.14	5.53	34.34	0.04	0.55	0.11	101.08	91.72
Group 3	Opx	0.09	3.42	56.16	0.01	0.68	0.13	5.55	34.29	0.06	0.54	0.09	101.03	91.68
Group 3	Opx	0.08	3.45	55.88	0.01	0.69	0.13	5.45	34.10	0.07	0.52	0.08	100.47	91.78
Group 3	Opx	0.09	3.37	56.09	0.01	0.68	0.14	5.51	34.21	0.06	0.55	0.09	100.80	91.71
Group 3	Opx	0.08	3.41	56.11	0.01	0.68	0.13	5.47	34.22	0.06	0.51	0.11	100.79	91.77
Group 3	Opx	0.03	3.98	54.77	0.01	0.60	0.14	6.15	33.58	0.07	0.70	0.09	100.12	90.68
Group 3	Opx	0.09	4.05	55.76	0.02	0.65	0.12	5.78	33.86	0.06	0.48	0.09	100.97	91.26
Group 3	Opx	0.10	4.05	55.84	0.02	0.67	0.15	5.83	33.56	0.06	0.47	0.10	100.84	91.12
Group 3	Opx	0.09	3.97	55.76	0.01	0.67	0.12	5.79	33.92	0.07	0.46	0.10	100.97	91.25
Group 3	Opx	0.08	4.04	55.66	0.01	0.67	0.12	5.84	33.70	0.07	0.45	0.09	100.74	91.14
Group 3	Opx	0.11	3.92	55.70	0.01	0.72	0.13	5.77	33.75	0.06	0.41	0.11	100.70	91.25
Group 3	Opx	0.09	4.05	55.64	0.01	0.66	0.14	5.84	33.77	0.05	0.48	0.11	100.86	91.15
Group 3	Opx	0.09	4.07	55.57	0.01	0.68	0.14	5.80	33.75	0.07	0.46	0.10	100.73	91.20
Group 4	Opx	0.14	4.48	54.35	0.01	0.77	0.21	6.93	31.80	0.18	0.59	0.03	99.54	89.11
Group 4	Opx	0.15	3.86	54.89	BDL	0.89	0.19	6.82	31.69	0.18	0.54	0.08	99.28	89.23
Group 4	Opx	0.16	3.84	55.09	0.01	0.85	0.11	6.70	31.60	0.18	0.56	0.03	99.13	89.38
Group 4	Opx	0.18	4.86	54.57	BDL	0.81	0.12	6.97	31.24	0.20	0.51	0.09	99.56	88.88
Group 4	Opx	0.18	4.43	55.03	BDL	0.81	0.13	6.91	31.52	0.19	0.54	0.10	99.88	89.05
Group 4	Opx	0.19	4.29	54.45	BDL	0.90	0.16	6.97	31.47	0.19	0.76	0.10	99.47	88.95
Group 4	Opx	0.22	3.67	55.23	BDL	0.92	0.16	6.88	32.08	0.16	0.60	0.08	100.06	89.26
Group 4	Opx	0.07	2.03	57.20	0.01	0.48	0.10	5.61	34.57	0.06	0.38	0.09	100.60	91.66
Group 4	Opx	0.13	2.89	56.00	BDL	0.83	0.19	6.73	32.23	0.12	0.45	0.10	99.75	89.52
Group 4	Opx	0.16	3.44	55.59	0.03	0.85	0.17	6.96	32.14	0.17	0.49	0.10	100.13	89.17

		Na2O	Al2O3	SiO2	K2O	CaO	MnO	FeO	MgO	TiO2	Cr2O3	NiO	Total	Mg#
Group 1	Ol	BDL	0.004	41.21	BDL	0.04	0.10	8.59	49.57	BDL	0.02	0.41	99.93	91.14
Group 1	Ol	BDL	0.01	40.95	BDL	0.03	0.09	8.65	50.31	BDL	0.01	0.36	100.40	91.20
Group 1	Ol	BDL	0.003	41.17	BDL	0.01	0.12	8.74	49.94	BDL	0.02	0.43	100.44	91.06
Group 1	Ol	BDL	0.002	41.31	BDL	0.07	0.06	8.41	50.50	BDL	0.01	0.37	100.74	91.46
Group 2	Ol	BDL	BDL	41.41	0.01	0.12	0.13	8.61	48.87	BDL	0.02	0.41	99.57	91.01
Group 2	Ol	BDL	0.003	41.28	0.02	0.05	0.11	8.75	48.78	BDL	0.00	0.36	99.36	90.86
Group 2	Ol	0.02	0.04	40.85	BDL	0.13	0.12	8.71	49.27	BDL	0.02	0.36	99.54	90.98
Group 2	Ol	0.03	0.05	41.31	BDL	0.09	0.16	8.91	49.27	0.01	0.04	0.42	100.28	90.79
Group 2	Ol	BDL	0.03	40.67	0.01	0.12	0.13	9.17	48.71	0.03	0.03	0.44	99.33	90.45
Group 2	Ol	BDL	BDL	41.04	0.04	0.13	0.19	8.65	49.41	BDL	0.02	0.36	99.87	91.06
Group 2	Ol	BDL	0.03	41.06	0.05	0.12	0.14	8.80	48.64	0.01	0.02	0.40	99.35	90.79
Group 2	Ol	BDL	0.04	41.30	BDL	0.07	0.12	8.79	48.42	BDL	0.00	0.34	99.10	90.76
Group 2	Ol	BDL	BDL	41.08	BDL	0.11	0.13	8.74	48.80	BDL	0.00	0.42	99.29	90.87
Group 2	Ol	BDL	0.01	40.69	0.04	0.03	0.09	8.68	48.89	BDL	0.01	0.43	98.94	90.95
Group 2	Ol	BDL	0.02	40.66	BDL	0.07	0.14	8.55	49.05	BDL	0.01	0.38	98.88	91.10
Group 2	Ol	0.02	BDL	40.92	0.02	0.01	0.09	8.61	49.09	BDL	0.02	0.35	99.13	91.04
Group 2	Ol	BDL	0.01	41.30	BDL	0.02	0.14	8.64	48.86	BDL	0.00	0.39	99.38	90.97
Group 2	Ol	0.02	BDL	41.13	BDL	0.06	0.15	8.64	48.65	BDL	0.00	0.38	99.04	90.95
Group 2	Ol	BDL	0.03	41.12	0.01	BDL	0.11	8.70	48.85	0.01	0.01	0.40	99.24	90.92
Group 2	Ol	BDL	0.03	41.58	0.03	BDL	0.12	8.56	48.94	BDL	0.01	0.44	99.72	91.07
Group 2	Ol	BDL	BDL	41.09	0.03	0.05	0.10	8.48	48.99	BDL	0.01	0.36	99.15	91.15
Group 2	Ol	BDL	0.01	41.24	0.02	0.03	0.13	8.72	49.33	BDL	0.00	0.46	99.95	90.98
Group 3	Ol	BDL	0.01	41.07	0.04	0.04	0.18	8.60	48.40	BDL	0.01	0.38	98.72	90.94
Group 3	Ol	0.02	0.03	41.11	0.01	0.07	0.16	9.68	48.66	BDL	0.01	0.29	100.12	89.97
Group 3	Ol	BDL	0.02	40.95	BDL	0.05	0.15	9.88	48.73	0.02	0.04	0.37	100.32	89.79
Group 3	Ol	0.02	0.05	40.84	0.03	0.05	0.13	9.87	48.62	0.03	0.02	0.36	100.06	89.78
Group 3	Ol	0.03	0.04	41.14	BDL	0.01	0.14	9.42	48.51	BDL	0.02	0.42	99.74	90.18
Group 3	Ol	0.03	0.01	40.77	0.03	0.06	0.11	9.35	48.11	BDL	0.02	0.39	98.88	90.17
Group 3	Ol	BDL	0.03	40.75	0.02	0.03	0.15	9.27	48.27	BDL	0.00	0.38	98.92	90.27
Group 3	Ol	BDL	BDL	40.58	0.02	0.06	0.14	9.27	48.14	BDL	0.01	0.42	98.63	90.26
Group 3	Ol	BDL	0.02	41.51	0.01	0.06	0.21	9.58	49.03	0.01	0.00	0.33	100.79	90.12

Group	Phase	Na2O	Al2O3	SiO2	K2O	CaO	MnO	FeO	MgO	TiO2	Cr2O3	NiO	Total	Mg#
Group 3	Ol	BDL	BDL	40.97	0.02	0.08	0.08	9.81	48.86	0.02	0.04	0.39	100.27	89.88
Group 3	Ol	BDL	0.02	41.44	BDL	0.08	0.19	9.80	48.78	BDL	0.01	0.43	100.74	89.87
Group 3	Ol	BDL	BDL	40.82	0.01	0.04	0.16	9.72	47.74	BDL	0.00	0.39	98.88	89.75
Group 3	Ol	BDL	0.01	40.63	BDL	0.06	0.16	9.79	47.64	BDL	0.00	0.38	98.70	89.66
Group 3	Ol	BDL	0.03	40.98	0.02	0.01	0.11	9.77	47.86	BDL	0.01	0.37	99.15	89.73
Group 3	Ol	BDL	0.03	40.74	BDL	0.07	0.14	9.38	47.92	BDL	0.03	0.49	98.89	90.10
Group 3	Ol	BDL	0.02	40.99	0.01	0.05	0.15	9.76	48.09	BDL	0.00	0.39	99.48	89.78
Group 3	Ol	BDL	BDL	41.10	0.01	0.07	0.13	9.71	48.03	BDL	0.00	0.37	99.50	89.82
Group 3	Ol	0.02	0.01	40.94	0.01	0.06	0.10	9.44	48.43	0.01	0.00	0.38	99.41	90.15
Group 3	Ol	0.02	BDL	41.64	0.01	0.05	0.14	9.41	48.24	BDL	0.01	0.36	99.88	90.13
Group 3	Ol	BDL	0.03	41.16	BDL	0.08	0.15	9.41	48.17	BDL	0.01	0.32	99.42	90.12
Group 3	Ol	0.02	0.04	40.98	BDL	0.07	0.12	9.58	48.32	BDL	0.02	0.37	99.52	89.99
Group 3	Ol	BDL	0.14	41.18	0.03	0.09	0.15	9.66	47.97	BDL	0.01	0.32	99.56	89.85
Group 3	Ol	BDL	0.04	40.92	0.02	0.06	0.13	9.60	48.21	BDL	0.01	0.38	99.39	89.95
Group 3	Ol	BDL	BDL	41.66	0.01	0.06	0.09	8.74	51.03	0.02	0.01	0.37	101.99	91.24
Group 3	Ol	BDL	BDL	41.30	0.01	0.04	0.13	8.62	50.76	0.01	0.02	0.36	101.26	91.31
Group 3	Ol	BDL	0.01	41.14	0.01	0.05	0.12	8.72	50.79	BDL	0.01	0.37	101.22	91.21
Group 3	Ol	BDL	0.001	41.22	0.01	0.06	0.11	8.64	50.46	0.01	0.02	0.37	100.91	91.23
Group 3	Ol	BDL	BDL	41.12	0.01	0.04	0.12	8.75	50.57	BDL	0.01	0.41	101.04	91.15
Group 3	Ol	BDL	0.01	41.29	0.01	0.04	0.14	8.71	50.55	BDL	0.02	0.41	101.18	91.19
Group 3	Ol	0.02	0.01	41.35	0.01	0.05	0.10	8.75	50.44	BDL	0.02	0.38	101.13	91.13
Group 3	Ol	BDL	BDL	41.18	0.01	0.01	0.13	9.16	50.27	0.01	0.00	0.39	101.17	90.72
Group 3	Ol	BDL	BDL	41.22	0.01	0.01	0.15	9.24	50.30	BDL	0.01	0.37	101.30	90.66
Group 3	Ol	BDL	BDL	41.10	BDL	0.01	0.12	9.03	50.24	BDL	0.00	0.39	100.90	90.84
Group 3	Ol	BDL	BDL	41.19	BDL	0.01	0.14	9.20	50.15	BDL	0.01	0.36	101.07	90.67
Group 3	Ol	BDL	BDL	41.14	0.01	0.03	0.14	9.08	49.99	BDL	0.00	0.36	100.77	90.75
Group 3	Ol	BDL	BDL	41.09	0.01	0.02	0.13	9.10	50.21	0.01	0.00	0.36	100.93	90.78
Group 3	Ol	BDL	BDL	41.20	0.01	0.01	0.15	9.17	50.30	BDL	0.01	0.36	101.22	90.72
Group 3	Ol	BDL	BDL	41.02	0.01	0.02	0.13	9.11	50.29	0.01	0.00	0.37	100.96	90.78
Group 3	Ol	0.02	0.003	41.26	0.01	0.05	0.15	9.17	50.38	BDL	0.01	0.39	101.44	90.74
Group 3	Ol	BDL	0.01	41.29	0.01	0.05	0.12	9.09	50.38	BDL	0.00	0.39	101.37	90.80

Group	Phase	Na2O	Al2O3	SiO2	K2O	CaO	MnO	FeO	MgO	TiO2	Cr2O3	NiO	Total	Mg#
Group 3	Ol	BDL	0.005	41.32	0.01	0.05	0.13	9.01	50.20	0.01	0.01	0.37	101.13	90.85
Group 3	Ol	BDL	0.01	41.23	0.01	0.06	0.16	9.02	50.29	BDL	0.01	0.37	101.15	90.86
Group 3	Ol	BDL	0.01	41.25	0.01	0.05	0.11	9.09	50.18	BDL	0.01	0.40	101.10	90.78
Group 3	Ol	BDL	0.01	41.41	0.02	0.05	0.12	9.03	50.20	BDL	0.02	0.40	101.30	90.83
Group 3	Ol	BDL	0.003	41.30	0.01	0.06	0.15	9.06	50.19	BDL	0.01	0.38	101.18	90.80
Group 3	Ol	BDL	0.01	41.12	0.02	0.05	0.14	9.10	50.27	0.01	0.02	0.35	101.08	90.78
Group 3	Ol	BDL	0.003	41.15	0.02	0.06	0.12	9.06	50.18	BDL	0.00	0.39	100.98	90.81
Group 3	Ol	BDL	0.002	41.21	0.01	0.05	0.12	9.05	50.35	BDL	0.02	0.39	101.20	90.84
Group 3	Ol	BDL	0.01	41.27	0.01	0.06	0.13	9.04	50.23	BDL	0.01	0.37	101.15	90.83
Group 3	Ol	BDL	BDL	40.89	0.01	0.05	0.13	9.08	50.18	BDL	0.01	0.38	100.73	90.79
Group 3	Ol	BDL	0.002	41.10	0.01	0.05	0.14	9.06	50.25	BDL	0.03	0.36	101.02	90.81
Group 3	Ol	BDL	0.01	41.12	0.01	0.06	0.13	9.10	50.22	BDL	0.01	0.37	101.03	90.77
Group 3	Ol	BDL	0.01	41.23	0.01	0.06	0.13	9.12	50.25	0.01	0.02	0.37	101.22	90.76
Group 3	Ol	BDL	0.01	41.20	0.01	0.06	0.13	9.05	50.05	BDL	0.01	0.38	100.92	90.79
Group 3	Ol	BDL	0.01	41.15	0.01	0.06	0.13	9.18	50.37	BDL	0.01	0.38	101.31	90.72
Group 4	Ol1	0.02	0.001	40.84	BDL	0.04	0.15	10.14	48.17	0.03	0.01	0.32	99.72	89.44
Group 4	Ol1	0.02	BDL	40.77	0.03	0.03	0.21	9.99	48.37	BDL	0.02	0.33	99.83	89.62
Group 4	Ol1	BDL	0.03	41.08	BDL	0.07	0.20	10.01	48.44	0.03	0.02	0.38	100.31	89.61
Group 4	Ol1	0.04	BDL	40.87	BDL	0.06	0.13	10.20	48.23	0.02	0.02	0.40	99.96	89.40
Group 4	Ol1	BDL	0.02	40.88	0.02	0.11	0.17	10.07	48.15	0.01	0.00	0.34	99.80	89.50
Group 4	Ol1	BDL	0.02	40.46	BDL	0.07	0.16	10.78	47.71	0.02	0.01	0.39	99.61	88.76
Group 4	Ol1	0.02	BDL	40.79	BDL	0.10	0.19	10.76	47.48	0.02	0.00	0.34	99.69	88.73
Group 4	Ol1	0.02	0.01	40.86	BDL	0.07	0.15	10.66	47.57	0.02	0.00	0.33	99.69	88.83
Group 4	Ol1	BDL	0.02	40.77	0.03	0.04	0.15	10.97	47.09	0.03	0.00	0.30	99.51	88.45
Group 4	Ol1	0.03	0.03	40.54	BDL	0.09	0.13	10.85	47.43	0.01	0.03	0.35	99.62	88.63
Group 4	Ol1	BDL	0.02	40.76	0.02	0.06	0.12	11.19	46.98	0.01	0.01	0.34	99.52	88.22
Group 4	Ol1	0.03	0.02	41.09	BDL	0.07	0.18	11.17	47.47	0.01	0.02	0.32	100.39	88.34
Group 4	Ol1	BDL	0.03	40.80	0.03	0.11	0.14	11.11	47.51	0.01	0.01	0.26	100.00	88.41
Group 4	Ol1	0.03	0.05	41.03	BDL	0.07	0.07	11.13	47.56	0.04	0.02	0.32	100.33	88.39
Group 4	Ol1	BDL	0.02	40.72	0.03	0.11	0.13	11.13	46.94	0.01	0.02	0.36	99.46	88.26
Group 4	Ol1	BDL	0.05	40.54	0.01	0.04	0.12	11.32	47.17	0.01	0.00	0.30	99.55	88.14

Group	Phase	Na2O	Al2O3	SiO2	K2O	CaO	MnO	FeO	MgO	TiO2	Cr2O3	NiO	Total	Mg#
Group 4	Ol1	BDL	0.04	40.56	BDL	0.04	0.13	11.36	47.06	0.02	0.00	0.34	99.56	88.07
Group 4	Ol2	BDL	0.02	40.96	0.02	0.11	0.12	7.66	49.44	BDL	0.13	0.30	98.80	92.00
Group 4	Ol2	BDL	0.04	41.16	BDL	0.10	0.14	7.70	50.32	BDL	0.12	0.31	99.93	92.10
Group 4	Ol2	0.02	0.02	41.37	0.03	0.15	0.13	7.80	50.41	0.03	0.13	0.25	100.37	92.01
Group 4	Ol2	BDL	0.03	41.31	0.02	0.16	0.12	7.75	50.37	0.02	0.15	0.27	100.20	92.06
Group 4	Ol2	BDL	0.01	41.32	BDL	0.04	0.10	8.87	49.20	0.02	0.02	0.36	99.94	90.82
Group 4	Ol2	BDL	0.01	40.74	0.03	0.04	0.16	8.95	49.48	0.03	0.02	0.34	99.88	90.79
Group 4	Ol2	0.02	0.003	40.77	0.01	0.07	0.15	8.65	49.15	BDL	0.03	0.38	99.24	91.01
Group 4	Ol2	0.04	0.02	40.92	BDL	0.02	0.12	8.88	49.45	BDL	0.03	0.35	99.82	90.85
Group 4	Ol2	BDL	0.03	40.83	BDL	0.03	0.09	8.85	49.38	BDL	0.02	0.32	99.58	90.86
Group 4	Ol2	0.02	0.01	40.63	BDL	0.07	0.18	8.90	49.62	0.01	0.01	0.40	99.91	90.86

		Na2O	Al2O3	SiO2	K2O	CaO	MnO	FeO	MgO	TiO2	Cr2O3	NiO	Total	Mg#
Group 4	Phlog	0.67	17.39	37.88	9.19	0.05	0.03	3.94	21.62	2.11	1.14	0.24	94.24	90.73
Group 4	Phlog	0.66	17.26	38.00	9.24	0.05	0.02	3.99	21.55	2.12	1.12	0.22	94.23	90.60
Group 4	Phlog	0.68	17.10	38.01	9.39	0.00	0.04	3.94	21.73	2.08	1.13	0.24	94.33	90.77
Group 4	Phlog	0.67	17.03	38.25	9.26	0.03	0.03	4.03	21.36	2.21	1.68	0.25	94.79	90.44
Group 4	Phlog	0.66	17.38	37.66	9.78	0.01	0.05	4.13	21.25	2.15	1.65	0.02	94.75	90.16
Group 4	Phlog	0.67	17.51	38.25	8.52	0.04	0.06	3.95	21.82	2.07	1.39	0.32	94.59	90.79
Group 4	Phlog	0.69	17.53	38.16	8.96	0.01	0.05	4.08	21.61	2.06	1.17	0.70	95.03	90.42
Group 4	Amph	2.62	14.85	42.71	2.01	11.05	0.07	3.97	17.30	1.28	1.38	0.09	97.33	88.60
Group 4	Amph	2.51	14.32	42.93	2.03	11.02	0.07	4.07	17.91	1.33	1.43	0.12	97.73	88.69
Group 4	Amph	2.84	15.00	42.51	2.16	11.08	0.09	3.95	17.46	1.16	1.33	0.05	97.64	88.74

Trace Elements (All values in ppm)

Group	Phase	Rb	Sr	Zr	Nb	Ba	La	Ce	Nd	Sm	Eu	Gd	Dy	Ho	Er	Yb	Lu	Hf	Th	U
Group 2	Cpx1	0.02	55.73	5.96	0.07	BDL	0.67	3.13	3.73	0.79	0.28	0.80	1.12	0.26	0.73	0.77	0.11	0.21	BDL	0.00
Group 2	Cpx1	0.01	56.10	6.14	0.07	BDL	0.64	3.08	3.45	0.92	0.29	0.91	1.04	0.24	0.72	0.78	0.10	0.22	BDL	BDL
Group 2	Cpx1	0.05	54.70	6.20	0.06	BDL	0.59	2.92	3.85	0.86	0.26	0.92	1.13	0.26	0.73	0.76	0.10	0.21	BDL	BDL
Group 2	Cpx1	0.44	53.13	6.04	0.08	0.04	0.54	2.59	2.97	0.68	0.26	0.72	1.07	0.23	0.66	0.66	0.12	0.18	BDL	BDL
Group 2	Cpx1	0.10	55.00	5.85	0.08	0.06	0.61	3.07	3.35	0.81	0.29	0.81	1.17	0.22	0.74	0.68	0.11	0.22	0.01	BDL
Group 2	Cpx1	0.10	55.00	5.85	0.08	BDL	0.61	3.07	3.35	0.81	0.29	0.81	1.17	0.22	0.74	0.68	0.11	0.22	0.01	BDL
Group 2	Cpx1	0.03	52.65	6.48	0.05	BDL	0.57	2.83	3.25	0.72	0.25	0.86	1.10	0.26	0.82	0.75	0.12	0.22	BDL	BDL
Group 2	Cpx1	0.02	46.41	17.20	0.21	BDL	0.85	2.65	2.73	1.12	0.43	1.94	2.45	0.54	1.58	1.52	0.21	0.52	0.01	0.01
Group 2	Cpx1	BDL	17.68	8.10	BDL	BDL	0.23	0.99	1.36	0.67	0.30	0.92	1.53	0.34	0.88	0.87	0.14	0.31	BDL	BDL
Group 2	Cpx1	BDL	15.73	8.82	BDL	BDL	0.17	0.89	1.33	0.71	0.26	0.93	1.38	0.30	0.97	0.95	0.15	0.31	BDL	BDL
Group 2	Cpx1	0.03	42.31	17.75	0.24	0.12	0.72	2.40	2.57	1.02	0.39	1.86	2.36	0.50	1.51	1.45	0.22	0.60	0.01	0.00
Group 2	Cpx1	0.71	31.95	42.90	0.52	0.62	0.26	0.69	0.89	0.69	0.50	1.79	5.92	1.80	7.11	10.92	1.79	0.50	0.08	0.07
Group 2	Cpx1	0.02	42.73	16.23	0.23	0.09	0.84	2.71	2.67	1.06	0.43	1.63	2.24	0.51	1.46	1.43	0.20	0.50	0.02	0.00
Group 2	Cpx1	0.02	52.33	26.32	0.04	0.11	0.74	2.94	3.80	1.64	0.62	2.41	3.17	0.66	1.87	1.72	0.25	0.84	0.01	0.00
Group 2	Cpx1	0.01	41.30	24.03	0.03	0.09	0.56	2.44	3.62	1.55	0.60	2.41	2.94	0.65	1.91	1.76	0.25	0.79	0.01	0.01
Group 2	Cpx1	0.01	48.08	24.30	0.02	0.08	0.71	2.80	3.61	1.44	0.60	2.17	2.87	0.60	1.75	1.69	0.23	0.81	0.01	0.00
Group 2	Cpx1	0.02	46.79	27.37	0.03	0.12	0.67	2.71	3.40	1.45	0.57	2.23	2.91	0.65	1.92	1.81	0.26	0.91	0.00	0.00
Group 2	Cpx1	0.04	46.08	26.50	0.03	0.20	0.63	2.66	3.64	1.51	0.60	2.32	3.02	0.65	1.90	1.74	0.25	0.88	0.01	BDL
Group 2	Cpx1	0.01	49.14	27.02	0.04	0.09	0.64	2.69	3.58	1.45	0.64	2.22	3.06	0.68	1.94	1.85	0.25	0.92	0.01	0.00
Group 3	Cpx1	BDL	15.29	3.25	BDL	BDL	0.38	1.54	0.96	0.83	0.19	1.05	1.32	0.23	0.82	0.49	0.12	0.15	BDL	BDL
Group 3	Cpx1	BDL	16.80	3.61	BDL	BDL	0.38	1.61	1.35	0.34	0.18	0.87	1.06	0.22	0.57	0.77	0.09	0.05	BDL	BDL
Group 3	Cpx1	0.35	14.27	3.46	0.08	BDL	0.31	1.33	0.93	0.44	0.11	0.86	0.98	0.26	0.67	0.88	0.13	0.03	BDL	BDL
Group 3	Cpx1	0.15	14.71	3.03	BDL	BDL	0.33	1.37	1.51	0.30	0.20	0.74	1.13	0.23	0.69	0.70	0.13	0.18	BDL	BDL
Group 3	Cpx1	0.47	12.19	2.85	0.01	BDL	0.27	0.97	1.20	0.21	0.19	0.59	0.92	0.16	0.47	0.59	0.05	0.06	BDL	BDL
Group 3	Cpx2	0.09	74.50	9.16	0.61	0.08	4.34	5.77	1.41	0.45	0.19	0.86	1.26	0.31	0.78	0.77	0.09	0.33	0.43	0.09
Group 3	Cpx2	0.19	63.60	8.66	0.63	0.06	3.78	4.41	1.04	0.19	0.23	0.61	1.00	0.36	0.65	0.80	0.08	0.25	0.30	0.07
Group 3	Cpx2	0.21	54.70	7.42	0.68	BDL	2.65	3.50	0.85	0.61	0.10	0.55	0.95	0.22	0.84	0.78	0.06	0.13	0.30	0.07
Group 3	Cpx2	0.48	55.60	8.26	0.74	0.02	2.91	3.61	1.22	0.31	0.17	0.70	1.07	0.20	0.73	0.80	0.08	0.22	0.19	0.03
Group 3	Cpx2	0.17	50.80	7.57	0.68	0.12	3.06	3.65	0.73	0.24	0.21	0.79	1.26	0.32	0.93	0.70	0.13	0.23	0.22	0.09

Group	Phase	Rb	Sr	Zr	Nb	Ba	La	Ce	Nd	Sm	Eu	Gd	Dy	Ho	Er	Yb	Lu	Hf	Th	U
Group 3	Cpx2	0.64	71.90	35.70	1.02	BDL	3.14	7.61	3.94	0.65	0.42	1.39	1.48	0.25	0.90	0.85	0.09	0.63	0.34	0.08
Group 3	Cpx2	1.08	92.00	46.10	0.92	0.03	5.55	10.67	4.11	1.49	0.44	1.89	2.15	0.56	1.31	0.99	0.09	0.64	0.67	0.12
Group 3	Cpx2	0.11	79.10	45.80	0.95	BDL	3.74	7.81	4.54	0.84	0.28	2.00	1.66	0.37	1.03	1.14	0.15	0.73	0.37	0.15
Group 3	Cpx2	0.19	83.10	41.30	0.93	0.08	3.44	8.36	4.57	1.13	0.41	1.22	1.59	0.36	1.20	0.71	0.18	0.73	0.47	0.15
Group 3	Cpx2	0.96	81.10	40.50	0.77	0.03	3.53	8.71	5.00	0.65	0.37	1.71	1.69	0.40	1.13	0.89	0.09	0.67	0.43	0.18
Group 3	Cpx2	BDL	81.00	39.80	1.16	BDL	3.98	8.59	4.80	1.18	0.43	0.96	1.81	0.46	1.11	0.94	0.13	0.80	0.61	0.10
Group 3	Cpx2	0.43	80.80	43.20	1.08	0.07	4.14	8.37	5.26	1.24	0.52	1.21	2.50	0.44	1.25	1.23	0.11	0.70	0.44	0.17
Group 3	Cpx2	0.14	87.60	45.60	1.21	0.09	4.56	9.37	5.40	1.21	0.55	2.00	2.14	0.45	1.43	0.84	0.15	0.52	0.64	0.08
Group 3	Cpx2	0.29	85.90	43.00	0.95	0.07	4.15	8.83	4.25	1.17	0.40	1.43	2.17	0.40	1.38	1.05	0.12	0.67	0.56	0.12
Group 3	Cpx2	1.08	85.30	44.30	1.29	0.03	5.23	10.15	4.44	1.14	0.51	1.61	1.75	0.34	1.22	0.99	0.12	0.60	0.62	0.09
Group 3	Cpx3	BDL	79.78	23.86	0.61	0.17	2.82	4.01	3.69	1.49	0.60	2.36	2.98	0.66	1.93	1.84	0.26	0.87	0.53	0.13
Group 3	Cpx3	BDL	80.39	23.50	0.58	BDL	2.85	4.09	3.70	1.41	0.60	2.34	3.07	0.68	1.89	1.78	0.26	0.85	0.50	0.13
Group 3	Cpx3	BDL	79.96	23.64	0.59	0.10	2.86	4.21	3.86	1.52	0.61	2.37	3.07	0.65	1.88	1.85	0.24	0.87	0.54	0.14
Group 3	Cpx3	BDL	76.47	23.94	0.58	BDL	2.68	3.87	3.74	1.50	0.63	2.18	3.04	0.67	1.88	1.86	0.26	0.81	0.50	0.12
Group 3	Cpx3	0.02	76.09	23.35	0.55	0.19	2.61	3.84	3.66	1.56	0.62	2.25	3.02	0.64	1.82	1.84	0.25	0.82	0.49	0.12
Group 3	Cpx3	0.01	76.69	23.50	0.57	0.24	2.60	3.91	3.78	1.50	0.60	2.33	2.96	0.68	1.84	1.78	0.27	0.83	0.50	0.12
Group 3	Cpx3	BDL	72.98	22.91	0.58	0.17	2.42	3.51	3.48	1.43	0.59	2.27	3.02	0.65	1.84	1.73	0.26	0.79	0.45	0.11
Group 3	Cpx3	BDL	75.03	23.81	0.58	0.12	2.47	3.65	3.61	1.42	0.62	2.28	3.02	0.64	1.90	1.80	0.25	0.83	0.46	0.13
Group 3	Cpx3	0.02	73.75	22.66	0.56	0.18	2.43	3.67	3.61	1.48	0.59	2.11	2.89	0.63	1.82	1.67	0.25	0.80	0.44	0.12
Group 3	Cpx3	0.01	72.54	22.26	0.50	BDL	2.36	3.43	3.42	1.48	0.54	2.29	2.91	0.63	1.76	1.70	0.24	0.79	0.44	0.12
Group 3	Cpx3	0.03	72.94	22.29	0.54	0.15	2.46	3.68	3.58	1.42	0.57	2.16	2.98	0.62	1.78	1.64	0.24	0.78	0.45	0.11
Group 3	Cpx3	BDL	67.26	18.83	1.73	0.16	2.03	3.27	2.54	1.06	0.45	1.79	2.43	0.53	1.57	1.61	0.22	0.63	0.49	0.10
Group 3	Cpx3	BDL	66.36	18.10	1.64	0.09	1.98	3.17	2.45	1.04	0.42	1.60	2.33	0.53	1.49	1.48	0.20	0.57	0.45	0.10
Group 3	Cpx3	BDL	67.09	17.99	1.60	BDL	2.03	3.26	2.50	1.02	0.44	1.69	2.35	0.51	1.48	1.49	0.23	0.57	0.44	0.11
Group 3	Cpx3	0.02	65.89	18.26	1.61	0.16	1.96	3.21	2.50	1.08	0.51	1.77	2.42	0.52	1.54	1.51	0.21	0.65	0.42	0.10
Group 3	Cpx3	0.01	66.43	18.02	1.59	0.12	1.94	3.11	2.43	1.07	0.47	1.69	2.36	0.52	1.53	1.43	0.21	0.60	0.44	0.10
Group 3	Cpx3	BDL	67.10	18.31	1.66	0.14	1.96	3.16	2.36	1.02	0.42	1.68	2.30	0.53	1.51	1.40	0.23	0.61	0.44	0.10
Group 3	Cpx3	BDL	66.31	18.15	1.62	0.15	1.99	3.24	2.41	1.05	0.42	1.65	2.28	0.51	1.48	1.38	0.21	0.62	0.44	0.10
Group 3	Cpx3	0.07	62.02	18.39	1.53	0.86	1.99	3.50	2.56	0.98	0.44	1.67	2.20	0.51	1.47	1.38	0.20	0.69	0.40	0.11
Group 3	Cpx3	0.24	71.97	18.29	1.86	0.71	2.14	3.34	2.51	0.94	0.45	1.66	2.24	0.50	1.41	1.38	0.23	0.60	0.49	0.10
Group 3	Cpx3	0.02	66.03	18.17	1.66	0.34	1.99	3.20	2.41	1.00	0.45	1.66	2.30	0.53	1.50	1.41	0.20	0.61	0.43	0.10

Group	Phase	Rb	Sr	Zr	Nb	Ba	La	Ce	Nd	Sm	Eu	Gd	Dy	Ho	Er	Yb	Lu	Hf	Th	U
Group 3	Cpx3	0.02	64.24	17.88	1.61	0.12	1.93	3.13	2.44	1.01	0.41	1.54	2.27	0.51	1.40	1.41	0.22	0.62	0.42	0.09
Group 3	Cpx3	0.05	63.97	17.68	1.74	0.83	1.96	3.15	2.35	1.05	0.47	1.47	2.34	0.51	1.37	1.60	0.20	0.66	0.45	0.09
Group 4	Cpx4	0.91	120.64	8.98	4.22	15.56	3.46	16.12	19.39	5.85	1.80	5.79	3.93	0.69	1.54	1.36	0.23	0.15	0.11	0.03
Group 4	Cpx4	2.19	296.56	14.05	13.89	41.47	11.26	38.65	27.13	7.89	2.55	7.34	4.76	0.93	2.00	1.78	0.31	0.23	0.36	0.22
Group 4	Cpx4	1.32	237.74	11.60	10.37	35.55	6.85	23.63	22.58	6.35	1.89	5.96	4.14	0.77	1.66	1.55	0.27	0.18	0.19	0.11
Group 4	Cpx4	2.42	387.48	15.78	16.45	50.38	12.34	42.82	34.97	8.51	2.74	7.80	5.63	0.97	2.17	2.03	0.36	0.26	0.42	0.25
Group 4	Cpx4	3.66	346.65	17.30	18.12	61.15	13.06	45.51	36.14	9.16	3.02	8.11	5.91	1.03	2.28	2.15	0.41	0.31	0.50	0.33
Group 4	Cpx5	2.71	232.01	12.44	11.36	36.96	10.94	35.16	29.45	7.21	2.12	6.86	4.85	0.85	1.76	1.61	0.29	0.20	0.29	0.40
Group 4	Cpx5	2.31	244.87	15.96	16.99	53.33	12.24	39.98	32.21	7.79	2.41	7.25	5.26	0.91	1.95	1.85	0.38	0.29	0.38	0.25
Group 4	Cpx5	0.36	111.17	10.31	9.54	25.71	7.79	27.67	25.44	6.96	1.95	6.19	4.03	0.76	1.55	1.32	0.25	0.21	0.16	0.05
Group 4	Cpx5																			
Group 4	Cpx6	2.23	318.00	26.50	0.31	5.96	10.89	38.81	22.49	5.22	1.31	5.01	3.34	0.58	1.43	1.09	0.17	1.22	0.27	0.13
Group 4	Cpx6	2.96	333.00	84.60	6.16	6.41	9.34	32.25	33.35	8.45	2.76	6.71	3.76	0.63	1.24	1.11	0.19	0.96	0.20	0.05
Group 4	Cpx6	2.13	351.00	56.80	1.84	0.95	19.60	54.41	22.66	4.98	1.45	2.97	2.15	0.36	1.01	1.17	0.15	0.79	0.35	0.26
Group 4	Cpx6	0.86	273.00	67.00	1.64	3.61	7.01	29.81	18.85	5.12	1.51	3.07	2.10	0.31	1.05	1.31	0.16	1.41	0.32	0.11
Group 4	Cpx6	3.32	356.00	63.20	1.86	2.37	16.50	42.35	29.05	6.68	1.77	4.12	2.45	0.38	1.12	1.12	0.18	1.09	0.15	0.41
Group 4	Cpx6	5.45	478.00	45.63	1.56	4.78	16.74	46.61	34.66	8.13	2.22	4.56	3.21	0.49	1.36	0.96	0.15	0.65	0.41	0.07
Group 4	Cpx6	3.96	349.00	30.20	1.83	6.25	13.04	41.25	32.66	7.89	2.04	4.26	2.85	0.45	1.21	1.26	0.20	0.88	0.35	0.17
Group 4	Cpx6	4.41	344.00	49.40	0.85	2.13	18.62	54.04	38.14	7.11	2.36	5.85	3.86	0.51	1.41	1.41	0.21	0.77	0.28	0.35
Group 4	Cpx6	1.01	296.00	59.00	1.45	4.17	10.06	36.15	25.84	6.33	1.56	3.17	2.16	0.31	0.95	1.21	0.13	0.85	0.41	0.32
Group 4	Cpx6	3.79	319.00	25.60	0.26	5.55	9.98	32.47	21.93	4.98	1.25	2.89	1.93	0.29	0.87	0.95	0.11	1.15	0.21	0.11
Group 4	Cpx6	1.26	282.00	61.00	1.42	4.56	11.23	38.06	22.87	5.84	1.86	3.76	2.71	0.47	1.19	1.15	0.20	0.93	0.35	0.26
Group 4	Cpx6	5.01	421.00	42.45	1.32	4.52	14.79	43.17	32.17	7.88	2.15	4.35	3.07	0.52	1.31	1.33	0.20	0.58	0.35	0.10

Interstitial Glass

	Major Element Composition Obtained by EMPA (wt.%)												
Element	**Na2O**	**Al2O3**	**SiO2**	**K2O**	**CaO**	**MnO**	**FeO**	**MgO**	**TiO2**	**Cr2O3**	**NiO**	**ZnO**	**Total**
	0.185	11.03	38.863	0.036	0.909	0.072	6.737	27.216	0.012	0.024	0.262	BDL	85.346
	0.085	2.803	41.466	0.097	0.512	0.056	9.201	30.419	BDL	BDL	BDL	BDL	84.639
	0.09	5.959	38.212	0.025	0.257	0.091	10.079	30.492	0.005	0.045	0.24	BDL	85.495
	0.061	8.219	41.349	0.012	0.626	0.069	0.309	33.386	0.225	0.005	0.037	0.114	84.412
	0.093	8.79	42.471	0.026	0.945	0.04	1.481	30.483	0.206	BDL	0.085	BDL	84.62

Referred to as "Appendix 5" in Chapter 3. Composition of base metal sulfides

Sample ID	BMS bleb Nº	Texture	Phase	Major Element Composition (wt.%)						Calculated At.%						
				S	Fe	Co	Ni	Cu	Total	S	Fe	Co	Ni	Cu	Total	M/S
Group 2 Samples																
CR-08	1	Glass-Related	Millerite	35.07	3.87	0.79	60.09	0.19	100.01	49.64	3.14	0.61	46.47	0.13	100.00	1.01
		Glass-Related	Millerite	35.70	4.07	0.77	60.56	0.47	101.56	49.74	3.25	0.58	46.10	0.33	100.00	1.01
		Glass-Related	Millerite	35.06	3.85	0.79	60.79	0.33	100.82	49.33	3.11	0.61	46.73	0.23	100.00	1.03
		Glass-Related	Millerite	35.42	5.30	0.75	59.91	0.08	101.46	49.44	4.24	0.57	45.68	0.06	100.00	1.02
		Glass-Related	Millerite	35.73	4.09	0.85	60.55	0.10	101.31	49.86	3.27	0.64	46.16	0.07	100.00	1.01
CR-02	2	Glass-Related	Pentlandite	33.86	24.12	0.57	40.30	1.61	100.46	47.80	19.52	0.44	31.08	1.15	100.00	1.09
		Glass-Related	Chalcopyrite	35.37	29.63	0.06	0.57	33.69	99.32	50.73	24.36	0.05	0.45	24.38	100.00	0.97
		Glass-Related	Millerite	33.05	3.51	0.01	62.35	0.39	99.31	47.67	2.90	0.01	49.13	0.28	100.00	1.10
CR-02	3	Glass-Related	Millerite	35.63	2.67	0.78	61.85	0.22	101.15	49.84	2.14	0.59	47.27	0.15	100.00	1.01
		Glass-Related	Millerite	35.39	2.61	0.78	61.63	0.39	100.81	49.72	2.10	0.60	47.30	0.28	100.00	1.01
CR-03	4	Glass-Related	Millerite	35.24	2.62	0.81	60.81	0.76	100.24	49.78	2.12	0.62	46.93	0.54	100.00	1.01
		Glass-Related	Millerite	35.32	2.16	0.52	62.49	0.33	100.82	49.64	1.74	0.40	47.99	0.23	100.00	1.01
		Glass-Related	Millerite	35.43	3.78	0.87	59.87	1.40	101.35	49.55	3.03	0.67	45.74	0.99	100.00	1.02
CR-08	5	Included	Fe-Mss	38.53	43.18	0.18	16.61	0.03	98.53	53.17	34.16	0.14	12.52	0.02	100.00	0.88
CR-07	6	Glass-Related	Pentlandite	33.28	22.87	0.75	41.59	0.54	99.03	47.67	18.78	0.58	32.55	0.39	100.00	1.10
		Glass-Related	Pentlandite	33.00	22.98	0.78	41.61	0.13	98.51	47.55	18.98	0.61	32.75	0.10	100.00	1.10
		Glass-Related	Ni-Mss	33.12	15.37	0.44	49.41	0.37	98.72	47.75	12.70	0.35	38.92	0.27	100.00	1.09
CR-03	7	Glass-Related	Millerite	34.77	1.50	0.57	62.75	0.11	99.70	49.48	1.22	0.44	48.78	0.08	100.00	1.02
		Glass-Related	Millerite	26.86	1.23	0.16	70.88	0.16	99.29	40.42	1.06	0.13	58.27	0.12	100.00	1.47
		Glass-Related	Pentlandite	33.17	25.55	0.67	40.23	0.07	99.68	47.26	20.87	0.52	31.31	0.05	100.00	1.12
CR-07	8	Glass-Related	Pentlandite	33.23	26.99	0.56	39.09	0.03	99.91	47.21	21.98	0.43	30.34	0.02	100.00	1.12
		Glass-Related	Fe-Mss	38.87	36.05	0.30	24.58	0.06	99.86	53.13	28.25	0.22	18.36	0.04	100.00	0.88
		Glass-Related	Pentlandite	33.14	27.14	0.63	39.23	0.09	100.22	47.00	22.06	0.48	30.39	0.06	100.00	1.13
CR-02	9	Glass-Related	Pentlandite	32.99	27.32	0.55	38.91	0.11	99.88	46.95	22.29	0.43	30.25	0.08	100.00	1.13
		Glass-Related	Pentlandite	33.20	26.62	0.56	39.09	0.06	99.53	47.33	21.75	0.43	30.44	0.04	100.00	1.11
		Glass-Related	Chalcopyrite	34.22	29.44	0.04	0.55	33.78	98.03	49.98	24.65	0.03	0.44	24.90	100.00	1.00

Sample ID	BMS bleb Nº	Texture	Phase	Major Element Composition (wt.%)						Calculated At.%						
				S	Fe	Co	Ni	Cu	Total	S	Fe	Co	Ni	Cu	Total	M/S
CR-08	10	Glass-Related	Millerite	35.34	2.77	0.36	61.58	0.17	100.22	49.79	2.24	0.28	47.40	0.12	100.00	1.00
		Glass-Related	Chalcopyrite	34.21	29.26	0.05	0.85	34.13	98.51	49.65	24.35	0.04	0.68	25.00	100.00	1.01
		Glass-Related	Millerite	34.51	4.87	0.66	59.04	0.27	99.36	49.23	3.98	0.52	46.01	0.20	100.00	1.03
CR-07	11	Glass-Related	Millerite	35.04	1.40	0.14	62.36	0.32	99.26	49.80	1.14	0.11	48.42	0.23	100.00	1.00
		Glass-Related	Millerite	35.13	1.38	0.14	62.27	0.32	99.25	49.90	1.12	0.11	48.33	0.23	100.00	1.00
CR-03	12	Glass-Related	Chalcopyrite	34.79	29.83	0.04	0.21	34.70	99.57	50.03	24.59	0.03	0.16	25.18	100.00	1.00
		Glass-Related	Pentlandite	33.02	24.14	0.30	42.09	0.14	99.68	47.12	19.75	0.23	32.81	0.10	100.00	1.12
		Glass-Related	Ni-Mss	32.66	14.97	0.18	50.20	0.59	98.60	47.29	12.43	0.14	39.71	0.43	100.00	1.11
CR-03	13	Glass-Related	Pentlandite	33.19	24.69	0.42	40.03	0.20	98.53	47.72	20.35	0.33	31.45	0.15	100.00	1.10
		Glass-Related	Pentlandite	33.47	24.14	0.49	39.15	1.20	98.45	48.11	19.89	0.39	30.74	0.87	100.00	1.08
CR-07	14	Glass-Related	Chalcopyrite	34.93	29.94	0.06	0.16	34.51	99.60	50.15	24.64	0.04	0.13	25.00	100.00	0.99
		Glass-Related	Pentlandite	33.32	26.76	0.49	39.51	0.09	100.17	47.22	21.74	0.38	30.59	0.07	100.00	1.12
CR-08	15	Included	Pentlandite	32.84	23.39	0.64	42.02	0.11	99.00	47.18	19.26	0.50	32.98	0.08	100.00	1.12
CR-09	16	Included	Pentlandite	33.36	26.90	0.55	38.65	0.24	99.70	47.44	21.93	0.42	30.03	0.17	100.00	1.11
TL-2-3	17	Included	Fe-Mss	39.11	44.73	0.37	15.58	0.39	100.18	53.09	34.81	0.27	11.56	0.27	100.00	0.88
TL-2-3	18	Included	Fe-Mss	39.74	46.23	0.32	14.31	0.00	100.60	53.53	35.70	0.24	10.53	0.00	100.00	0.87
CR-09	19	Included	Pentlandite	34.70	31.35	0.94	32.37	0.28	99.63	48.87	25.31	0.72	24.91	0.20	100.00	1.05
TL-2-3	20	Included	Fe-Mss	38.85	46.66	0.24	13.56	0.00	99.31	53.12	36.57	0.18	10.13	0.00	100.00	0.88
CR-08	21	Included	Fe-Mss	39.10	52.28	0.23	7.93	0.00	99.54	53.17	40.76	0.17	5.89	0.00	100.00	0.88
CR-02	22	Included	Fe-Mss	36.45	38.96	0.79	23.68	0.52	100.39	50.34	30.85	0.59	17.87	0.36	100.00	0.99
CR-03	23	Included	Pentlandite	33.45	32.19	0.38	33.38	0.00	99.40	47.55	26.23	0.30	25.92	0.00	100.00	1.10
CR-09	24	Included	Fe-Mss	38.77	38.19	0.44	21.35	0.03	98.78	53.41	30.16	0.33	16.07	0.02	100.00	0.87
		Included	Fe-Mss	38.70	39.46	0.39	19.52	0.08	98.15	53.57	31.32	0.29	14.76	0.06	100.00	0.87
		Included	Fe-Mss	39.56	38.40	0.47	20.86	0.10	99.40	53.98	30.04	0.35	15.55	0.07	100.00	0.85
Group 3 Samples																
TL-01	25	Interstitial	Fe-Mss	38.55	35.09	0.34	25.40	25.74	99.39	53.00	27.66	0.26	19.08	0.00	100.00	0.89
		Interstitial	Fe-Mss	38.35	35.14	0.40	25.20	25.60	99.09	52.91	27.79	0.30	19.00	0.00	100.00	0.89
TL-01	26	Interstitial	Fe-Mss	39.38	33.48	0.35	26.69	27.04	99.91	53.69	26.17	0.26	19.88	0.00	100.00	0.86

Sample ID	BMS bleb Nº	Texture	Phase	Major Element Composition (wt.%)							Calculated At.%						
				S	Fe	Co	Ni	Cu	Total		S	Fe	Co	Ni	Cu	Total	M/S
TL-06	27	Interstitial	Fe-Mss	39.74	34.94	0.44	25.03	25.47	100.15		53.93	27.18	0.33	18.56	0.00	100.00	0.85
		Interstitial	Fe-Mss	39.47	34.54	0.39	25.29	25.68	99.70		53.84	27.01	0.29	18.85	0.00	100.00	0.86
GG-13	28	Interstitial	Fe-Mss	39.03	33.80	0.24	26.60	26.84	99.67		53.41	26.52	0.18	19.89	0.00	100.00	0.87
		Interstitial	Fe-Mss	40.75	27.82	1.60	29.51	31.11	99.69		55.29	21.64	1.18	21.88	0.00	100.00	0.81
		Interstitial	Fe-Mss	39.74	33.56	0.25	26.31	26.56	99.86		54.08	26.18	0.18	19.56	0.00	100.00	0.85
GG-10	29	Interstitial	Fe-Mss	38.06	31.58	0.41	29.29	29.70	99.37		52.57	25.01	0.31	22.10	0.02	100.00	0.90
		Interstitial	Fe-Mss	37.89	32.20	0.43	27.72	28.15	98.44		52.75	25.70	0.33	21.08	0.14	100.00	0.90
TL-03	30	Interstitial	Fe-Mss	38.92	34.89	0.44	25.57	26.01	99.82		53.22	27.35	0.32	19.10	0.00	100.00	0.88
		Interstitial	Fe-Mss	38.97	34.97	0.39	25.69	26.08	100.02		53.19	27.36	0.29	19.16	0.00	100.00	0.88
		Interstitial	Fe-Mss	38.70	34.21	0.35	26.55	26.90	99.82		53.00	26.86	0.26	19.87	0.00	100.00	0.89
TL-08	31	Included	Fe-Mss	39.19	31.91	0.43	28.72	29.15	100.25		53.39	24.92	0.32	21.37	0.00	100.00	0.87
		Included	Fe-Mss	39.89	32.70	0.41	26.83	27.24	99.85		54.25	25.50	0.30	19.94	0.01	100.00	0.84
GG-05	32	Interstitial	Fe-Mss	37.67	40.32	0.41	21.24	21.65	99.86		51.80	31.79	0.30	15.96	0.14	100.00	0.93
		Interstitial	Fe-Mss	38.15	40.94	0.39	20.52	20.91	100.11		52.19	32.11	0.29	15.34	0.06	100.00	0.92
GG-05	33	Interstitial	Fe-Mss	39.02	37.67	0.43	23.07	23.50	100.20		53.12	29.40	0.32	17.16	0.00	100.00	0.88
TL-08	34	Interstitial	Fe-Mss	39.01	37.90	0.46	22.94	23.40	100.32		53.06	29.55	0.34	17.05	0.01	100.00	0.88
		Interstitial	Fe-Mss	38.69	37.13	0.48	23.65	24.13	99.95		52.88	29.10	0.36	17.66	0.00	100.00	0.89
GG-10	35	Interstitial	Fe-Mss	39.94	37.66	0.45	21.84	22.29	99.89		54.19	29.29	0.33	16.19	0.00	100.00	0.85
		Interstitial	Fe-Mss	39.81	48.36	0.32	10.37	10.69	98.86		54.26	37.79	0.24	7.72	0.00	100.00	0.84
TL-06	36	Included	Fe-Mss	38.61	51.24	0.20	9.54	9.74	99.66		52.64	40.05	0.15	7.11	0.05	100.00	0.90
		Included	Fe-Mss	39.04	49.71	0.22	10.88	11.10	99.88		53.03	38.71	0.16	8.07	0.02	100.00	0.89
		Included	Fe-Mss	35.85	39.51	0.49	23.20	23.69	100.54		49.66	31.38	0.37	17.56	1.03	100.00	1.01
GG-13	37	Interstitial	Fe-Mss	39.66	42.39	0.41	18.59	19.00	101.07		53.34	32.69	0.30	13.66	0.01	100.00	0.87
		Interstitial	Fe-Mss	39.81	41.69	0.38	18.80	19.18	101.20		53.47	32.10	0.28	13.80	0.33	100.00	0.87
		Interstitial	Fe-Mss	39.19	42.20	0.38	18.59	18.97	100.40		53.13	32.80	0.28	13.77	0.02	100.00	0.88
TL-03	38	Interstitial	Fe-Mss	38.52	43.17	0.40	18.14	18.54	100.33		52.45	33.70	0.29	13.49	0.06	100.00	0.91
		Interstitial	Fe-Mss	37.85	43.52	0.44	18.57	19.01	100.46		51.69	34.07	0.32	13.86	0.05	100.00	0.93
		Interstitial	Fe-Mss	39.16	40.05	0.40	21.25	21.65	100.86		52.96	31.05	0.29	15.70	0.00	100.00	0.89

Sample ID	BMS bleb Nº	Texture	Phase	Major Element Composition (wt.%)						Calculated At.%						
				S	Fe	Co	Ni	Cu	Total	S	Fe	Co	Ni	Cu	Total	M/S
TL-08	39	Interstitial	Fe-Mss	38.58	42.58	0.44	18.98	19.42	100.76	52.35	33.13	0.32	14.07	0.12	100.00	0.91
		Interstitial	Fe-Mss	38.37	43.43	0.43	18.42	18.85	100.69	52.14	33.83	0.32	13.68	0.03	100.00	0.92
TL-01	40	Included	Fe-Mss	38.40	43.67	0.44	17.81	18.25	100.38	52.29	34.09	0.33	13.25	0.04	100.00	0.91
		Included	Fe-Mss	38.28	45.00	0.38	16.64	17.02	100.37	52.14	35.14	0.28	12.38	0.05	100.00	0.92
TL-06	41	Included	Fe-Mss	39.04	38.71	0.40	21.39	21.79	99.56	53.37	30.34	0.30	15.98	0.00	100.00	0.87
TL-01	42	Included	Fe-Mss	35.08	35.19	0.50	29.39	29.89	100.57	48.86	28.10	0.38	22.37	0.29	100.00	1.05
TL-03	43	Included	Fe-Mss	38.64	43.49	0.41	17.84	18.25	100.45	52.52	33.89	0.30	13.25	0.05	100.00	0.90
TL-08	44	Interstitial	Fe-Mss	39.05	44.41	0.35	16.40	16.75	100.22	53.01	34.56	0.26	12.16	0.01	100.00	0.89
		Interstitial	Fe-Mss	39.47	44.03	0.35	15.88	16.23	99.76	53.04	41.17	0.23	5.56	0.00	100.00	0.89
		Interstitial	Fe-Mss	39.02	44.39	0.40	15.85	16.25	99.66	53.20	34.70	0.29	11.81	0.00	100.00	0.88
TL-01	45	Interstitial	Fe-Mss	38.97	53.25	0.28	7.21	7.49	99.74	52.94	41.47	0.21	5.35	0.02	100.00	0.89
		Interstitial	Fe-Mss	39.10	52.94	0.31	7.50	7.81	99.85	53.63	34.30	0.26	11.79	0.03	100.00	0.86
TL-01	46	Interstitial	Fe-Mss	37.34	43.59	0.39	19.14	19.53	100.66	51.08	34.19	0.29	14.31	0.13	100.00	0.96
		Interstitial	Fe-Mss	38.10	45.89	0.36	16.04	16.40	100.50	51.89	35.83	0.27	11.94	0.07	100.00	0.93
		Interstitial	Fe-Mss	38.75	51.06	0.24	10.25	10.49	100.58	52.44	39.61	0.18	7.58	0.19	100.00	0.91
GG-10	47	Included	Fe-Mss	38.27	38.36	0.43	22.96	23.39	100.02	52.40	30.11	0.32	17.17	0.00	100.00	0.91
		Included	Fe-Mss	38.47	33.04	0.57	27.87	28.44	99.96	52.73	25.96	0.43	20.87	0.00	100.00	0.90
		Included	Fe-Mss	38.99	39.46	0.47	21.49	21.96	100.41	52.97	30.73	0.34	15.95	0.00	100.00	0.89
GG-10	48	Interstitial	Fe-Mss	37.86	44.91	0.34	17.02	17.36	100.35	51.72	35.17	0.25	12.70	0.13	100.00	0.93
		Interstitial	Fe-Mss	38.35	41.82	0.38	19.90	20.28	100.76	52.13	32.59	0.28	14.78	0.21	100.00	0.92
		Interstitial	Fe-Mss	38.69	46.97	0.35	14.43	14.78	100.56	52.46	36.51	0.25	10.69	0.08	100.00	0.91
GG-13	49	Included	Fe-Mss	38.52	40.85	0.38	20.33	20.71	100.10	52.58	31.97	0.28	15.16	0.02	100.00	0.90
		Included	Fe-Mss	38.24	39.55	0.44	21.65	22.09	99.89	52.39	31.07	0.33	16.21	0.00	100.00	0.91
		Included	Fe-Mss	37.97	40.57	0.40	20.81	21.21	99.78	52.13	31.93	0.30	15.61	0.03	100.00	0.92
Group 4 Samples																
GG-14	50	Interstitial	Fe-Mss	38.83	49.33	0.31	10.81	0.18	99.45	52.99	38.60	0.23	8.06	0.12	100.00	0.89
		Interstitial	Fe-Mss	38.64	48.80	0.35	11.88	0.44	100.14	52.55	38.05	0.26	8.83	0.30	100.00	0.90
		Interstitial	Fe-Mss	38.12	46.75	0.35	13.50	0.81	99.55	52.29	36.76	0.26	10.12	0.56	100.00	0.91

Sample ID	BMS bleb Nº	Texture	Phase	Major Element Composition (wt.%)						Calculated At.%						
				S	Fe	Co	Ni	Cu	Total	S	Fe	Co	Ni	Cu	Total	M/S
GG-03	51	Included	Fe-Mss	38.69	46.55	0.33	13.11	0.50	99.18	53.02	36.57	0.24	9.82	0.35	100.00	0.89
		Included	Fe-Mss	39.14	46.36	0.38	12.21	0.49	98.57	53.74	36.49	0.28	9.16	0.34	100.00	0.86
GG-03	52	Included	Fe-Mss	40.52	38.92	0.35	16.58	2.55	98.92	55.23	30.41	0.26	12.35	1.75	100.00	0.81
		Included	Fe-Mss	39.95	41.23	0.34	14.57	2.28	98.37	54.81	32.43	0.25	10.92	1.58	100.00	0.82
GG-17	53	Included	Fe-Mss	38.88	46.11	0.38	13.36	0.50	99.24	53.20	36.17	0.28	9.99	0.35	100.00	0.88
		Included	Fe-Mss	38.44	46.36	0.33	14.08	0.27	99.48	52.64	36.39	0.25	10.53	0.19	100.00	0.90
GG-01-A	54	Included	Fe-Mss	38.83	37.12	0.35	21.85	0.29	98.44	53.65	29.40	0.26	16.49	0.20	100.00	0.86
		Included	Fe-Mss	39.52	34.52	0.33	24.01	0.23	98.61	54.34	27.21	0.25	18.04	0.16	100.00	0.84
GG-07	55	Included	Pn	33.11	32.92	0.49	31.19	1.07	98.79	47.41	27.02	0.38	24.40	0.77	100.00	1.11
		Included	Pn	33.42	33.61	0.44	30.24	1.30	99.01	47.67	27.49	0.34	23.57	0.94	100.00	1.10
		Included	Po	38.24	54.40	0.30	5.33	0.69	98.96	52.49	42.81	0.22	4.00	0.48	100.00	0.91
		Included	Po	39.14	57.20	0.21	2.21	0.18	98.95	53.36	44.71	0.16	1.65	0.12	100.00	0.87
GG-17	56	Included	Fe-Mss	39.73	40.33	0.28	17.75	0.56	98.66	54.44	31.68	0.21	13.29	0.39	100.00	0.84
		Included	Fe-Mss	39.43	37.72	0.32	20.64	0.85	98.98	54.06	29.65	0.24	15.46	0.59	100.00	0.85
		Included	Cb	35.70	39.49	0.15	1.61	22.28	99.31	50.58	32.08	0.11	1.25	15.93	100.00	0.98
		Included	Fe-Mss	40.07	39.19	0.31	18.79	0.74	99.10	54.63	30.63	0.23	14.00	0.51	100.00	0.83
GG-14	57	Interstitial	Pn	32.87	30.95	0.54	34.59	0.11	99.06	47.05	25.40	0.42	27.05	0.08	100.00	1.13
GG-01-B	59	Interstitial	Pn	34.12	32.26	0.51	30.69	1.01	98.62	48.61	26.35	0.40	23.89	0.73	100.00	1.06
		Interstitial	Pn	34.22	31.67	0.47	29.37	3.16	98.89	48.69	25.84	0.37	22.83	2.27	100.00	1.05
		Interstitial	Fe-Mss	34.93	39.10	0.53	22.66	1.14	98.37	49.48	31.75	0.41	17.54	0.81	100.00	1.02
GG-01-B	60	Included	Fe-Mss	38.40	42.77	0.43	17.75	0.40	99.76	52.56	33.56	0.32	13.27	0.28	100.00	0.90
		Included	Fe-Mss	37.69	42.79	0.39	18.01	0.26	99.14	52.05	33.88	0.29	13.59	0.18	100.00	0.92
GG-07	61	Included	Fe-Mss	38.15	42.76	0.41	17.75	0.23	99.31	52.47	33.72	0.30	13.34	0.16	100.00	0.91
GG-03	62	Interstitial	Pn	33.34	29.32	0.58	35.94	0.35	99.53	47.44	23.92	0.45	27.94	0.25	100.00	1.11
		Interstitial	Pn	33.65	29.52	0.60	36.49	0.17	100.45	47.44	23.86	0.46	28.11	0.12	100.00	1.11
GG-01-A	63	Interstitial	Pn	33.76	36.30	0.49	29.39	0.29	100.22	47.53	29.30	0.37	22.60	0.20	100.00	1.10
		Interstitial	Pn	33.02	36.29	0.49	29.30	0.29	99.39	47.01	29.62	0.38	22.79	0.21	100.00	1.13

BMS bleb Nº	Type	Trace Element Content of Sulfides (ppm)																				
		As			Se			Ru			Rh			Pd			Ag			Cd		
		Conc	1Sig	MDL*	Conc	1Sig	MDL*	Conc	1Sig	MDL*	Conc	1Sig	MDL*	Conc	1Sig	MDL*	Conc	1Sig	MDL*	Conc	1Sig	MDL*
1	3A	37.53	2.65	0.44	146.18	6.99	6.64	13.23	0.73	0.02	2.91	0.26	0.01	15.39	1.07	0.05	3.00	0.12	0.02	1.14	0.16	0.04
2	3B	2.88	0.35	0.26	193.67	7.25	3.48	10.98	0.50	0.03	3.07	0.19	0.01	42.54	4.18	0.02	13.87	0.62	0.01	0.87	0.11	0.02
3	3B	2.81	0.72	1.04	239.64	11.65	14.01	5.83	0.40	0.05	0.99	0.09	0.02	17.72	1.87	0.03	1.03	0.08	0.03	0.16	0.08	0.11
4	3A	39.39	3.07	0.62	58.59	3.76	4.63	7.66	0.78	0.02	2.97	0.42	0.01	22.88	2.39	0.03	10.93	0.42	0.01	0.88	0.21	0.02
5	3B	3.69	0.30	0.14	135.52	5.20	2.44	1.28	0.12	0.01	0.41	0.05	0.01	0.77	0.09	0.02	0.97	0.04	0.01	0.04	0.01	0.01
7	3B	96.01	8.13	0.76	234.85	16.22	10.83	81.43	4.87	0.09	14.18	1.44	0.01	117.60	8.93	0.08	10.06	0.50	0.03	1.03	0.25	0.06
8	3B	51.36	4.16	0.53	134.49	8.07	7.22	16.98	0.85	0.04	2.83	0.21	0.01	135.66	14.74	0.06	40.37	1.91	0.02	14.57	2.27	0.05
9	3B	99.84	7.94	0.60	189.39	8.02	7.89	58.92	2.50	0.05	10.45	0.70	0.01	45.63	5.17	0.04	8.95	0.45	0.03	4.65	0.69	0.06
11	3B	3.77	0.32	0.25	116.38	4.85	3.23	2.60	0.17	0.01	0.50	0.04	0.01	8.77	0.05	0.01	0.54	0.03	0.01	0.24	0.03	0.01
12	3A	8.06	1.18	0.55	93.68	9.48	8.38	9.94	0.78	0.04	2.47	0.25	0.01	12.22	1.00	0.02	4.35	0.24	0.02	0.34	0.10	0.06
10	3B	13.74	2.03	0.34	113.15	10.74	4.53	23.82	1.58	0.02	4.03	0.37	0.01	9.28	1.37	0.03	9.53	0.61	0.01	0.64	0.24	0.03
13	3B	3.31	0.31	0.26	149.53	6.55	3.72	2.27	0.16	0.01	1.52	0.11	0.01	8.42	0.51	0.01	6.79	0.30	0.01	0.12	0.02	0.02
14	3B	23.20	1.96	0.21	99.16	4.21	2.62	10.75	0.50	0.02	2.06	0.15	0.04	64.81	7.58	0.02	62.10	3.04	0.01	3.07	0.48	0.01
15	3B	18.45	1.87	0.66	163.45	8.87	8.99	5.14	0.37	0.47	1.13	0.10	0.01	20.22	2.52	0.05	10.62	0.57	0.02	0.85	0.15	0.05
6	3A	9.00	0.73	0.21	157.11	7.09	2.85	12.68	0.77	0.02	4.89	0.38	0.01	13.29	0.87	0.02	8.97	0.42	0.01	0.38	0.06	0.02
40	1A	10.23	0.84	0.11	48.46	3.76	5.54	25.49	0.56	0.05	5.12	0.49	0.01	10.21	3.98	0.02	5.36	0.62	0.02	1.49	0.42	0.04
30	1A	5.91	0.66	0.23	21.77	4.85	3.83	34.28	1.30	0.03	7.07	0.63	0.01	1.54	0.94	0.03	4.71	0.64	0.07	0.76	0.17	0.04
47	1A	8.44	0.71	0.41	37.99	2.13	5.69	84.50	3.40	0.08	2.55	0.66	0.01	0.91	0.82	0.03	3.36	0.50	0.02	2.95	0.14	0.31
49	1A	4.90	0.48	0.29	7.32	1.73	3.02	6.37	0.67	0.01	0.77	0.12	0.01	0.57	0.08	0.01	0.03	0.01	0.01	bdl	0.27	0.02
43	1A	4.08	0.42	0.26	9.49	1.72	2.78	3.56	0.40	0.02	0.66	0.11	0.01	0.56	0.08	0.02	0.03	0.01	0.01	0.03	0.01	0.02
58	1A	13.92	2.05	0.48	123.96	16.34	6.02	228.64	9.78	0.04	39.81	2.58	0.01	32.94	9.87	0.04	8.30	0.52	0.02	1.61	0.46	0.04
42	1A	4.05	0.51	0.31	80.77	4.76	3.90	214.79	9.44	0.03	36.40	2.64	0.01	1.03	0.12	0.16	1.82	0.09	0.01	0.22	0.06	0.02
24	1A	17.21	4.89	1.41	29.08	32.36	18.31	21.39	2.75	0.11	3.76	0.58	0.03	0.47	0.41	0.10	9.24	0.95	0.05	1.70	0.39	0.13
27	1B	211.56	0.87	0.22	246.50	4.60	2.81	101.08	5.14	0.02	8.05	0.55	0.01	15.03	0.86	0.01	8.59	0.37	0.01	0.60	0.06	0.02
31	1B	156.35	0.66	0.15	137.48	5.94	2.17	49.81	2.64	0.01	8.16	0.77	0.01	8.86	0.68	0.01	7.30	0.26	0.01	2.36	0.29	0.00
36	1B	89.27	0.14	0.22	80.06	3.82	3.81	4.96	0.48	0.03	0.72	0.09	0.01	4.79	0.58	0.01	0.26	0.02	0.01	bdl	0.02	0.02
37	1B	303.49	20.23	0.44	196.61	10.24	4.81	18.65	1.31	0.04	2.29	0.23	0.01	35.39	2.65	0.03	20.88	1.09	0.01	0.82	0.12	0.02
39	1B	74.18	0.18	0.18	135.64	5.05	2.97	15.73	1.15	0.01	2.35	0.22	0.01	0.81	0.09	0.01	0.05	0.01	0.01	0.08	0.01	0.01

45	1B	213.64	4.62	0.77	169.13	15.90	7.33	54.76	3.91	0.05	10.33	0.95	0.01	11.83	1.31	0.04	10.57	0.70	0.02	2.74	0.40	0.05
48	1B	85.77	0.38	0.17	100.04	4.30	2.72	4.67	0.42	0.00	0.72	0.09	0.00	1.19	0.15	0.01	0.52	0.03	0.01	0.12	0.03	0.01
56	2A	7.21	0.19	0.21	24.05	1.91	1.43	0.46	0.07	0.03	0.42	0.07	0.00	8.28	0.98	0.01	5.46	0.24	0.00	3.69	0.22	0.01
62	2A	11.12	0.10	0.12	17.78	1.63	1.50	0.34	0.05	0.01	0.50	0.07	0.00	1.86	0.20	0.01	2.50	0.10	0.00	0.47	0.08	0.01
63	2A	15.22	0.16	0.20	20.62	2.13	1.83	0.21	0.04	0.01	0.23	0.03	0.00	1.45	0.17	0.01	1.77	0.08	0.01	0.60	0.12	0.01
25	2A	32.71	2.46	0.33	367.80	13.78	4.11	1.08	0.13	0.02	1.31	0.10	0.01	2.45	0.29	0.01	10.80	0.50	0.01	1.03	0.09	0.02
28	2A	5.59	1.40	0.83	205.12	17.07	12.02	4.86	0.63	0.05	1.51	0.20	0.02	34.23	2.63	0.07	6.47	0.38	0.03	0.45	0.17	0.08
54	2A	30.94	5.67	2.39	134.01	28.89	16.94	2.46	0.73	0.12	3.16	0.44	0.02	14.43	1.89	0.09	36.84	2.13	0.05	1.93	0.58	0.13
46	2A	19.61	6.89	0.65	125.64	5.04	7.22	1.37	0.55	0.05	1.57	0.10	0.01	26.56	1.57	0.01	9.54	0.85	0.02	0.75	0.18	0.05
29	2A	18.65	3.75	0.91	221.84	16.86	7.36	2.81	0.15	0.02	3.01	0.07	0.00	15.24	0.95	0.03	5.78	0.12	0.01	1.91	0.29	0.03
38	2A	29.76	2.39	0.38	124.40	8.25	5.63	1.00	0.16	0.01	1.30	0.17	0.01	5.05	0.65	0.02	53.75	1.70	0.01	6.57	0.90	0.01
60	2B	13.76	0.31	0.37	155.65	2.83	3.56	0.32	0.07	0.02	0.11	0.02	0.00	1.96	0.24	0.01	0.53	0.04	0.07	0.06	0.02	0.02
51	2B	19.53	0.56	0.28	249.61	4.82	4.19	0.14	0.07	0.02	0.14	0.03	0.01	0.38	0.10	0.01	3.23	0.18	0.01	0.33	0.07	0.02
52	2B	14.62	1.27	0.12	321.19	2.34	1.99	0.10	0.03	0.01	0.25	0.03	0.01	0.71	0.09	0.01	4.40	0.17	0.01	2.06	0.20	0.01
55	2B	21.35	2.77	0.81	440.26	25.54	6.83	7.21	0.84	0.05	8.44	0.86	0.01	26.96	2.40	0.04	73.67	3.96	0.02	11.90	0.83	0.04
59	2B	44.61	8.09	1.54	149.37	34.45	17.15	0.25	0.39	0.12	1.03	0.31	0.02	5.36	1.44	0.09	6.70	0.82	0.06	2.00	0.60	0.11
26	2B	15.30	1.21	0.66	226.14	18.46	15.23	0.81	0.09	0.04	0.25	0.16	0.00	2.15	1.03	0.03	19.41	0.51	0.00	0.32	0.31	0.03
34	2B	35.55	0.71	0.33	242.99	11.49	5.13	6.43	0.51	0.03	1.75	0.15	0.01	61.93	3.77	0.03	9.19	0.45	0.02	0.54	0.11	0.32
41	2B	22.33	0.34	0.14	177.41	6.93	2.18	0.90	0.10	0.03	0.34	0.04	0.00	3.09	0.31	0.01	1.74	0.07	0.00	0.31	0.05	0.01
61	2B	38.67	0.38	0.14	200.41	7.30	2.37	1.04	0.10	0.01	0.38	0.04	0.00	7.35	0.71	0.01	2.82	0.10	0.01	0.37	0.05	0.01
44	2B	26.54	0.26	0.26	319.25	2.86	3.41	1.15	22.23	0.01	0.46	3.44	0.01	15.49	0.23	0.01	9.00	0.14	0.01	3.46	0.04	0.01

MDL* = Minimum Detection Limit

BMS bleb Nº	Type	Trace Element Content of Sulfides (ppm)																				
		Sb			Te			Re			Os			Ir			Pt			Au		
		Conc	1Sig	MDL*	Conc	1Sig	MDL*	Conc	1Sig	MDL*	Conc	1Sig	MDL*	Conc	1Sig	MDL*	Conc	1Sig	MDL*	Conc	1Sig	MDL*
1	3A	1.96	0.11	0.10	33.46	1.57	0.11	8.05	2.63	0.07	7.41	1.07	0.04	7.39	0.55	0.01	19.52	1.15	0.04	3.44	0.14	0.01
2	3B	0.18	0.05	0.07	25.21	1.40	0.07	bdl	-	-	7.88	0.39	0.02	5.50	0.20	0.01	4.99	0.25	0.88	0.23	0.02	0.01
3	3B	0.36	0.15	0.26	27.38	1.76	0.29	bdl	-	-	2.43	0.24	0.08	2.28	0.12	0.01	0.66	0.11	0.09	2.22	0.12	0.02
4	3A	1.19	0.08	0.09	17.35	0.84	0.09	bdl	-	-	10.65	0.92	0.03	7.21	0.55	0.01	15.92	0.59	0.03	0.59	0.05	0.01
5	3B	0.11	0.22	0.36	3.18	0.19	0.03	0.62	2.63		1.84	0.31	0.01	0.82	0.08	0.00	2.00	0.13	0.01	0.24	0.02	0.00
7	3B	4.55	0.37	0.16	42.75	9.36	0.28	1.03	1.95	0.07	11.25	2.82	0.08	34.00	2.82	0.02	112.57	7.25	0.54	3.86	0.27	0.03
8	3B	0.61	0.10	0.12	2.71	0.37	0.21	bdl	-	-	11.64	0.65	0.04	8.78	0.33	0.01	0.11	0.04	0.03	1.23	0.08	0.01
9	3B	0.35	0.08	0.13	3.86	0.38	0.19	bdl	-	-	32.60	1.54	0.05	24.91	0.82	0.01	0.11	0.03	0.01	0.86	0.06	0.01
11	3B	0.10	0.05	0.10	1.29	0.13	0.07	12.20	2.55	0.03	2.96	0.35	0.01	1.62	0.10	0.00	5.17	0.28	0.01	0.05	0.01	0.01
12	3A	0.45	0.15	0.14	13.05	1.19	0.20	bdl	-	-	8.19	1.20	0.03	6.57	0.51	0.01	12.76	0.91	0.04	1.96	0.15	0.02
10	3B	2.56	0.25	0.07	0.47	0.30	0.11	bdl	-	-	11.29	0.96	0.03	8.35	0.44	0.01	2.24	0.33	0.01	0.19	0.06	0.01
13	3B	0.07	0.04	0.07	13.24	0.66	0.07	3.32	3.72	0.01	2.14	0.28	0.01	2.34	0.15	0.01	5.47	0.31	0.02	0.18	0.02	0.01
14	3B	0.09	0.03	0.04	10.73	0.70	0.05	bdl	-	-	8.30	0.42	0.02	7.42	0.25	0.01	20.24	0.91	0.02	0.44	0.03	0.00
15	3B	0.47	0.10	0.14	8.50	0.78	0.23	bdl	-	-	2.57	0.24	0.07	2.49	0.13	0.01	3.38	0.26	0.05	0.40	0.05	0.02
6	3A	0.08	0.04	0.05	24.47	1.27	0.06	3.26	2.29	0.02	6.68	0.93	0.02	10.39	0.65	0.01	14.72	0.84	0.01	2.34	0.11	0.01
40	1A	0.79	0.14	0.15	0.65	0.06	0.15	0.06	0.00	<0.000	91.26	3.44	0.08	71.75	1.82	0.02	19.06	0.74	0.17	1.16	0.07	0.00
30	1A	1.15	0.23	0.10	2.40	0.55	0.11	0.15	0.00	<0.000	5.70	0.46	0.04	3.59	0.71	0.00	0.71	0.04	0.08	0.03	0.01	0.00
47	1A	bdl	-	-	3.86	0.32	0.12	0.62	0.00	<0.000	9.43	0.78	0.03	8.34	0.65	0.01	6.57	0.13	0.03	0.60	0.03	0.01
49	1A	0.13	0.03	0.05	0.22	0.06	0.08	bdl	-	-	6.82	0.61	0.02	4.19	0.33	0.01	0.80	0.06	0.02	0.02	0.01	0.01
43	1A	bdl	0.03	0.05	0.22	0.07	0.09	bdl	-	-	3.45	0.33	0.04	2.08	0.17	0.00	1.06	0.07	0.01	0.01	0.01	0.01
58	1A	5.17	0.60	0.11	5.45	3.42	0.15	bdl	-	-	148.48	7.00	0.04	100.63	3.40	0.01	81.26	3.86	0.02	2.66	0.22	0.02
42	1A	bdl	0.07	0.10	2.87	0.31	0.07	bdl	-	-	192.08	22.01	0.02	154.63	9.48	0.01	25.85	1.34	0.05	0.65	0.05	0.01
24	1A	2.45	0.96	0.26	7.94	2.93	0.44	bdl	-	-	7.15	1.49	0.10	6.72	0.75	0.03	11.42	1.71	0.09	0.29	0.16	0.04
27	1B	16.50	0.53	0.06	8.42	0.44	0.08	6.04	79.50	0.03	13.42	1.62	0.02	25.53	1.45	0.01	6.15	0.33	0.01	0.16	0.02	0.01
31	1B	6.62	0.25	0.03	14.07	0.78	0.05	2.53	29.91	0.01	26.89	4.10	0.01	20.60	1.61	0.00	7.52	0.50	0.01	1.14	0.06	0.00
36	1B	3.43	0.03	0.05	19.88	0.11	0.07	0.91	4.64	0.01	4.08	0.80	0.02	4.57	0.50	0.01	1.94	0.15	0.03	0.24	0.02	0.00
37	1B	2.65	0.16	0.07	57.14	3.12	0.11	0.37	2.58	0.03	12.90	2.19	0.03	13.79	1.02	0.01	12.72	0.88	0.02	0.17	0.03	0.01
39	1B	5.19	0.03	0.06	14.49	0.15	0.04	0.94	3.42	0.00	7.90	1.11	0.02	5.95	0.49	0.00	0.34	0.04	0.06	0.89	0.04	0.01

45	1B	2.21	0.32	0.12	22.50	2.50	0.02	1.70	16.55	0.06	37.79	5.82	0.04	38.42	2.68	0.02	2.83	0.49	0.04	0.85	0.15	0.02
48	1B	6.96	0.02	0.04	19.47	0.11	0.02	0.82	3.81	0.01	3.54	0.64	0.02	1.98	0.20	0.00	0.63	0.06	0.04	0.13	0.10	0.01
56	2A	0.16	0.03	0.02	3.53	0.26	0.03	bdl	-	-	0.21	0.05	0.01	0.21	0.03	0.00	7.90	0.55	0.01	0.41	0.03	0.00
62	2A	0.03	0.02	0.03	1.19	0.06	0.04	bdl	-	-	0.22	0.04	0.01	0.38	0.03	0.00	0.66	0.05	0.00	0.22	0.02	0.00
63	2A	0.03	0.03	0.03	2.41	0.08	0.05	bdl	-	-	0.14	0.03	0.01	0.24	0.03	0.00	0.72	0.06	0.01	0.24	0.02	0.00
25	2A	0.09	0.07	0.09	17.70	1.13	0.12	bdl	-	-	0.71	0.10	0.03	0.79	0.06	0.00	4.84	0.03	0.10	0.94	0.06	0.01
28	2A	0.20	0.21	0.20	50.49	3.45	0.30	bdl	-	-	3.24	0.63	0.05	3.23	0.33	0.02	18.18	1.39	0.06	4.45	0.31	0.03
54	2A	0.29	0.42	0.29	41.63	4.76	0.40	2.19	18.63	0.13	2.34	0.76	0.13	2.56	0.39	0.03	3.39	0.74	0.10	4.46	0.49	0.04
46	2A	0.51	0.11	0.11	21.32	0.48	0.12	bdl	-	-	1.71	0.17	0.04	2.82	0.25	0.01	10.87	0.84	0.04	3.60	0.08	0.00
29	2A	0.14	0.21	0.10	6.69	0.55	0.33	bdl	-	-	2.09	0.05	0.04	3.57	0.32	0.00	7.44	0.61	0.04	3.04	0.07	0.01
38	2A	0.74	0.09	0.07	13.02	0.92	0.09	0.58	2.81	0.01	0.11	0.05	0.03	0.60	0.08	0.01	1.14	0.15	0.01	4.34	0.22	0.01
60	2B	1.15	0.05	0.06	37.32	0.18	0.06	bdl	-	-	0.10	0.04	0.02	0.02	0.01	0.01	1.55	0.14	0.01	0.06	0.01	0.01
51	2B	1.72	0.15	0.06	42.00	0.28	0.01	0.04	0.32	0.02	0.05	0.04	0.02	0.02	0.01	0.01	0.07	0.05	0.02	0.09	0.03	0.01
52	2B	1.53	0.08	0.03	54.51	0.40	0.06	0.12	0.78	0.01	0.02	0.02	0.01	0.00	0.00	0.00	0.15	0.03	0.01	0.32	0.03	0.00
55	2B	2.51	0.28	0.11	76.66	5.10	0.13	2.59	17.40	0.04	4.64	0.98	0.05	2.81	0.30	0.01	9.77	0.93	0.04	3.24	0.27	0.02
59	2B	2.39	1.12	0.51	27.63	3.18	0.45	bdl	-	-	2.47	1.01	0.10	1.39	0.38	0.02	0.24	0.28	0.06	1.15	0.34	0.05
26	2B	1.65	0.35	0.06	29.91	2.25	0.15	0.92	0.00	0.00	3.11	0.14	0.03	1.23	0.16	0.00	4.44	0.23	0.05	5.25	0.61	0.00
34	2B	2.76	0.10	0.10	66.65	3.29	0.14	3.91	39.45	0.08	0.97	0.19	0.03	0.35	0.05	0.00	3.74	0.31	0.01	11.95	0.50	0.01
41	2B	3.23	0.03	0.03	37.74	0.43	0.06	0.88	3.33	0.00	0.29	0.06	0.01	0.13	0.02	0.00	0.39	0.05	0.01	0.56	0.04	0.00
61	2B	1.89	0.03	0.36	31.94	0.06	0.04	0.87	3.40	0.00	0.34	0.06	0.01	0.14	0.02	0.00	0.82	0.06	0.01	0.97	0.04	0.00
44	2B	3.06	0.05	0.08	55.20	0.29	0.06	2.16	0.08	0.00	1.26	8.16	0.02	0.86	5.64	0.01	2.63	0.93	0.02	7.23	0.03	0.01

***MDL* = Minimum Detection Limit*.**

BMS bleb Nº	Type	Pb			Bi		
		Conc	1Sig	MDL*	Conc	1Sig	MDL*
1	3A	9.19	0.57	0.01	1.22	0.10	0.01
2	3B	3.19	0.27	0.00	0.80	0.06	0.00
3	3B	0.98	0.10	0.02	0.30	0.03	0.01
4	3A	21.97	4.04	0.01	8.22	1.26	0.01
5	3B	6.56	0.55	0.36	0.21	0.02	0.00
7	3B	3.86	0.33	0.02	5.91	0.55	0.01
8	3B	71.92	6.54	0.01	26.17	2.15	0.01
9	3B	59.97	5.64	0.01	63.15	5.36	0.01
11	3B	3.75	0.13	0.01	0.20	0.01	0.00
12	3A	1.25	0.12	0.02	3.16	0.26	0.01
10	3B	32.44	3.44	0.01	9.35	0.91	0.01
13	3B	1.66	0.07	0.01	0.58	0.03	0.00
14	3B	15.91	1.55	0.00	6.06	0.53	0.00
15	3B	55.35	5.60	0.01	8.62	0.79	0.01
6	3A	8.17	0.30	0.00	0.69	0.04	0.00
40	1A	21.11	2.10	0.06	0.13	0.65	0.01
30	1A	3.62	0.77	0.01	0.43	0.38	0.01
47	1A	11.60	1.13	0.01	0.11	0.46	0.01
49	1A	2.33	0.45	0.01	0.79	0.13	0.00
43	1A	4.74	0.96	0.00	0.95	0.16	0.00
58	1A	16.90	1.54	0.01	0.56	0.17	0.01
42	1A	0.44	0.04	0.00	0.15	0.02	0.00
24	1A	82.56	9.20	0.03	0.87	0.29	0.02
27	1B	15.78	0.52	0.01	3.81	0.02	0.00
31	1B	16.06	1.05	0.00	1.58	0.14	0.00
36	1B	0.02	0.01	0.01	2.65	0.00	0.00
37	1B	26.58	0.97	0.01	13.52	0.60	0.00
39	1B	1.15	0.09	0.00	4.25	0.00	0.00
45	1B	29.84	1.24	0.01	1.21	0.12	0.01
48	1B	0.71	0.07	0.00	6.96	0.00	0.00
56	2A	25.89	4.25	0.00	0.55	0.04	0.00
62	2A	0.05	0.01	0.00	0.91	0.00	0.00
63	2A	0.28	0.05	0.00	0.18	0.00	0.00
25	2A	23.01	1.85	0.01	2.59	0.20	0.01
28	2A	4.92	0.38	0.02	1.85	0.18	0.02
54	2A	32.92	1.54	0.03	1.19	0.16	0.02
46	2A	13.14	2.81	0.01	1.26	0.78	0.01
29	2A	19.51	1.61	0.01	2.64	0.19	0.01
38	2A	29.07	2.71	0.01	2.32	0.21	0.01
60	2B	1.88	0.28	0.00	0.78	0.01	0.00
51	2B	5.31	0.40	0.01	1.13	0.02	0.00
52	2B	103.55	7.43	0.00	1.86	0.09	0.00
55	2B	429.66	15.37	0.01	17.40	0.84	0.01

BMS bleb Nº	Type	Pb			Bi		
		Conc	1Sig	MDL*	Conc	1Sig	MDL*
59	2B	15.85	2.17	0.03	0.48	0.14	0.03
26	2B	25.87	2.03	0.01	9.38	0.17	0.00
34	2B	3.72	0.17	0.01	1.21	0.07	0.01
41	2B	3.65	0.28	0.00	2.12	0.01	0.00
61	2B	7.78	0.61	0.00	3.42	0.03	0.00
44	2B	4.24	0.55	0.01	11.56	0.02	0.00

MDL* = Minimum Detection Limit

A.3. SUPPLEMENTARY INFORMATION FOR CHAPTER 4

Supplementary Methods

Electron probe microanalysis (EPMA)

The chemical composition of silicates, oxides, and apatite was determined by EPMA using a CAMECA SX-100 at the University of Michigan, Ann Arbor, MI. An acceleration voltage of 15 keV, a beam current of 10 nA and a beam size of 2 µm was used for all analyses. Peak counting times of 20 s were used for all elements, except 5 s for F and 60 s for S. Precautions were taken to prevent electron beam damage of apatite (*e.g.*, halogen migration). During the analysis, both SiO_2 and Al_2O_3 concentrations were monitored for contribution of the surrounding glass and mineral phases. Analyses indicating a contribution of the glass were discarded.

Sulphur X-ray absorption near edge structures spectroscopy (S-XANES)

In situ sulphur XANES measurements at the S K-edge were conducted at the GSECARS 13-ID-E beamline, Advanced Photon Source (APS), Argonne National Laboratory, IL. The beamline can cover an energy range of 2.4 to 28 keV and uses a high-flux beam ($\geq 4.5 \times 10^{10}$ photons/s/100mA/mm^2) that produces a high spatial resolution micro-focused 2x1 µm (µ-XANES) beam by using a Kirkpatrick-Baez (KB) focusing mirrors. The energy of the Si (111) channel-cut monochromator was calibrated to the 2481.8 (±0.2) eV white line of the spectrum for clear double-sided adhesive tape. Spectra were collected from 2450 to 2550 eV, with a step size of 0.1-0.3 eV at the S K-edge (2464 to 2484 eV) and 1 eV for the pre-and-post edge regions (0.5-3 s scan durations per energy step). Step-scan durations of 1-3 s per energy step were used to achieve higher S X-ray counts required for high-quality spectra, especially in low-S bearing apatite.

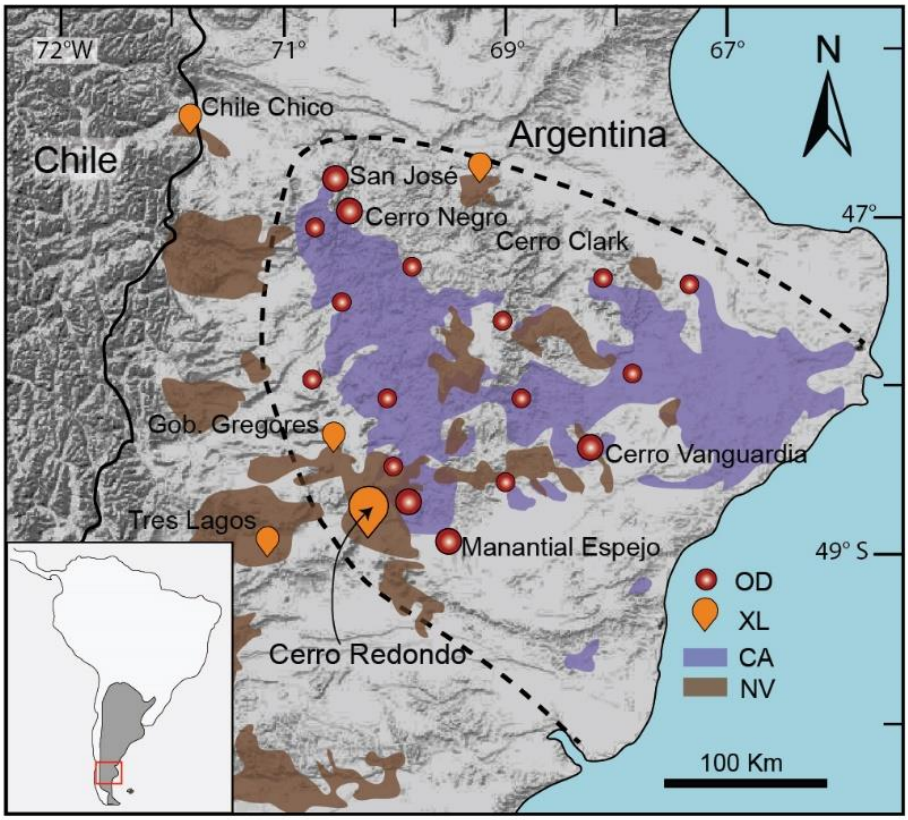

Supplementary Figure 1. Sample location. Simplified geological map of southern Patagonia, Argentina. The dashed line delimits the Deseado Massif auriferous province. CA: Chon Aike volcanic sequences; NV: Neogene Volcanism; OD: most relevant ore deposits and prospects; XL: location of different xenolith sites in the Deseado Massif. The studied peridotite xenolith was collected from the Cerro Redondo cinder cone, located at the southwestern edge of the Deseado Massif (49°7´15.41´´ S; 70°8´28.56´´ W). After Tassara *et al.* (*2017*).

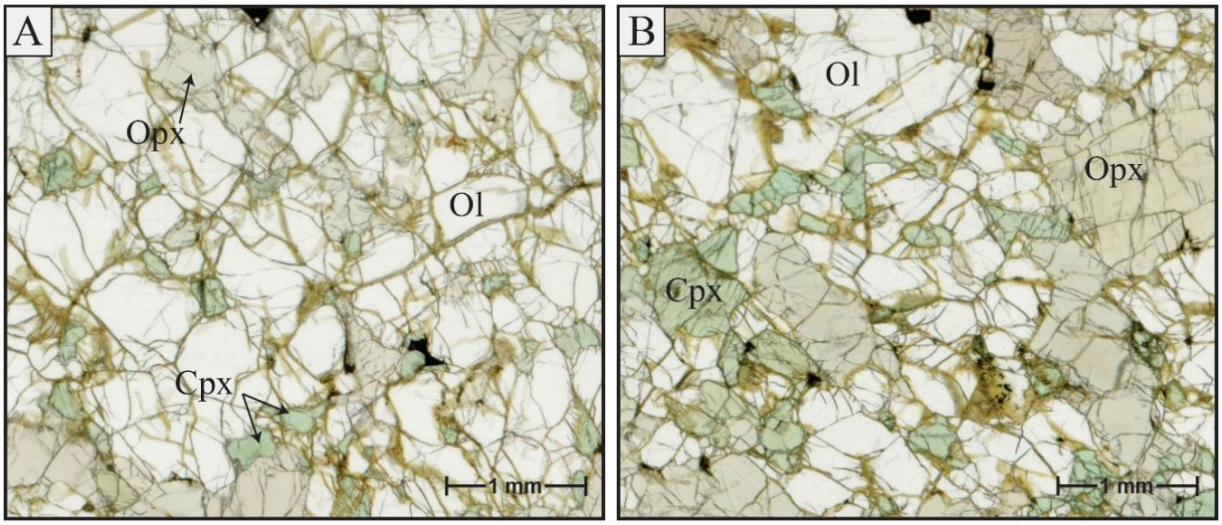

Supplementary Figure 2. Thin section scans showing the distribution of the interstitial network of glassy veinlets. Protogranular to porphyroclastic lherzolite with abundant silicate glass distributed along grain boundaries (yellowish veinlets). Ol: olivine; Opx: orthopyroxene; Cpx: clinopyroxene.

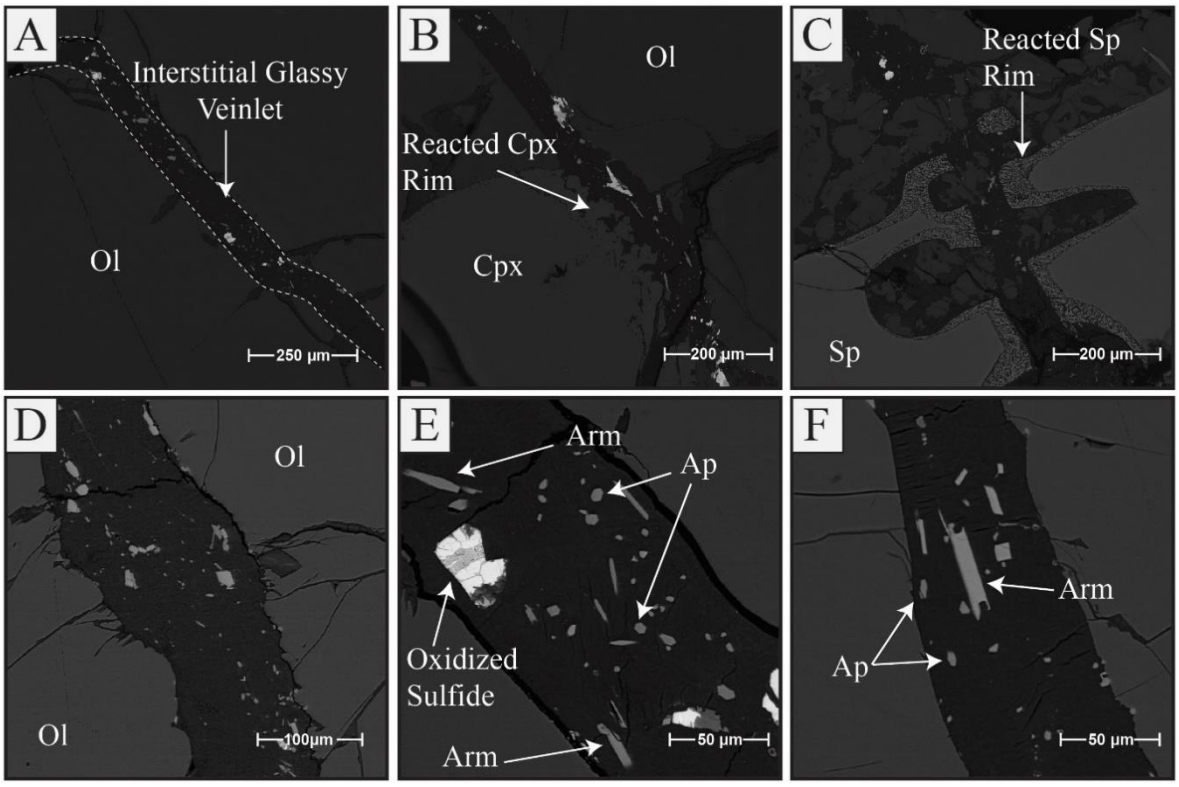

Supplementary Figure 3. Backscattered electron images of interstitial glassy veinlets in the studied lherzolite. (**A**) General view of the interstitial glassy veinlet crosscutting an olivine (Ol) grain. (**B**) Interstitial glassy veinlet and reaction rim in clinopyroxene (Cpx). (**C**) Reaction zone between the interstitial silicate glass and spinel (Sp) grains. (**D**) Detailed view of the interstitial glassy veinlet showing several crystallized phases. (**E**) Detail of the mineral assemblages present in the interstitial glassy veinlets, including oxidized Ni-Cu sulfides, armalcolite (Arm), and apatite (Ap) with euhedral forms. (**F**) Armalcolite and apatite crystals located within the interstitial glass.

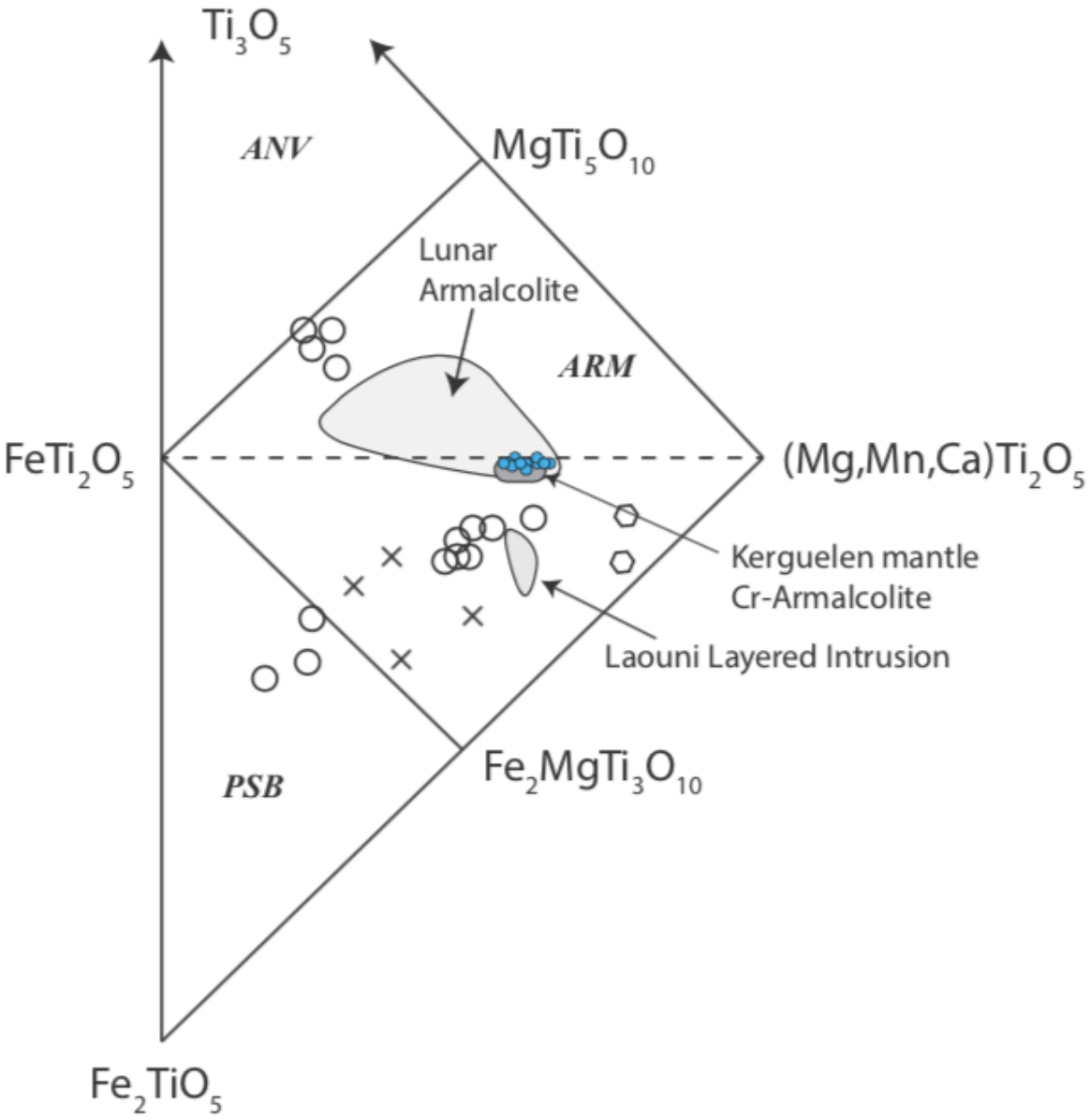

Supplementary Figure 4. Pseudobrookite group diagram showing armalcolite end members. Modified from Grégoire *et al.* (*2000*). Pseudobrookite group diagram composition after Bowles (*1988*). ANV: anosovite, ARM: armalcolite; PSB: pseudobrookite. Open Circles: armalcolite and pseudobrookite from Cancarix, Spain (Contini *et al*., *1993*). Crosses: Armalcolite from Lebombo picrites (Cawthorn *et al*., *1993*). Polygons: Kimberlitic armalcolite from Jagerfonstein (Haggerty, *1983*). Blue stars: armalcolite from this study. End member calculation and classification according to Bowles (*31*).

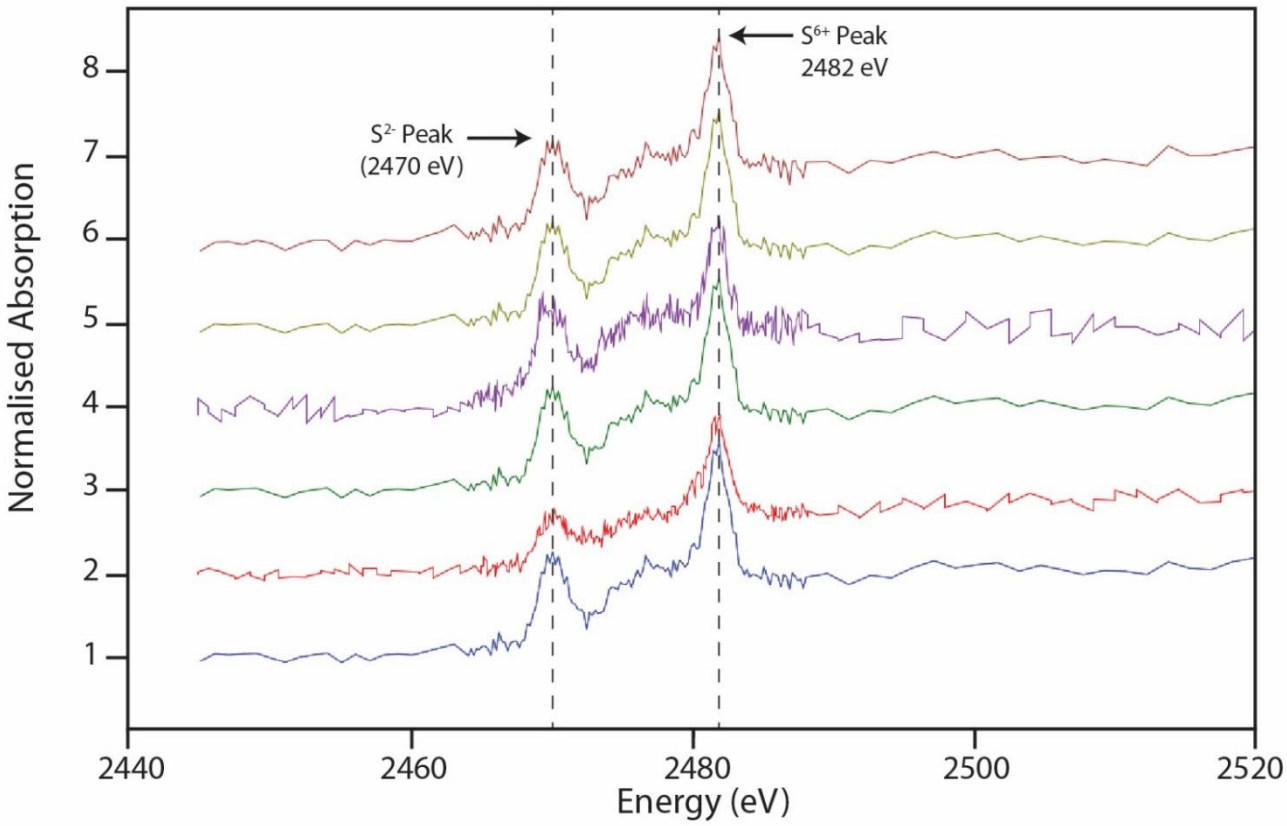

Supplementary Figure 5. Individual S µ-XANES spectra of apatite. Each representative individual S µ-XANES spectrum shows the two major peaks at the absorption energy of sulfide (2470 eV) and sulfate (2482 eV).

Weight %											
Na_2O	MgO	SiO_2	Al_2O_3	FeO	MnO	NiO	K_2O	Cr_2O_3	CaO	TiO_2	Total
Olivine											
0.03	49.27	41.31	0.05	8.91	0.16	0.42	b.d.l.	0.04	0.09	0.01	100.29
0.02	50.02	40.67	0.03	9.31	0.14	0.40	b.d.l.	b.d.l.	0.10	0.02	100.71
0.01	49.68	40.86	0.02	8.93	0.12	0.41	b.d.l.	b.d.l.	0.15	b.d.l.	100.18
0.01	50.26	40.90	0.01	8.90	0.16	0.41	b.d.l.	0.01	0.14	b.d.l.	100.80
b.d.l.	50.02	40.47	b.d.l.	9.33	0.16	0.36	b.d.l.	0.04	0.14	b.d.l.	100.52
Orthopyroxene											
0.09	33.79	54.93	3.93	5.72	0.14	0.10	b.d.l.	0.64	0.51	0.06	99.91
0.09	34.02	55.30	3.37	5.85	0.15	b.d.l.	0.01	0.53	0.60	0.06	99.98
0.08	34.20	56.62	0.71	5.86	0.19	b.d.l.	0.01	0.39	1.60	0.50	100.16
0.05	34.06	54.74	3.97	5.83	0.17	b.d.l.	0.01	0.63	0.42	0.04	99.92
0.05	34.06	54.74	3.97	5.83	0.17	0.09	b.d.l.	0.63	0.42	0.04	100.00
Spinel											
0.03	19.94	0.07	46.49	12.36	0.12	0.36	b.d.l.	18.16	0.01	0.16	97.70
b.d.l.	19.85	0.07	46.40	12.28	0.12	0.39	b.d.l.	18.49	b.d.l.	0.14	97.74
0.05	19.48	0.08	48.68	11.93	0.11	0.31	b.d.l.	17.83	0.05	0.20	98.72
b.d.l.	19.19	0.03	46.80	11.92	0.14	0.24	b.d.l.	19.43	b.d.l.	0.05	97.80
b.d.l.	19.85	0.07	46.40	12.28	0.12	0.39	b.d.l.	18.49	b.d.l.	0.14	97.74

Supplementary Table 1. Chemical composition of olivine, orthopyroxene, and spinel used for the calculation of the peridotite oxygen fugacity. Data taken from Tassara *et al.* (2014). b.d.l.: below detection limit.

Temperature (K)	Pressure (bar)	Olivine		Orthopyroxene		Log a (Fe_3O_4)	ΔFMQ*
		XFeOl	XMgOl	XFeM1	XFeM2		
1293	13600	0.09	0.91	0.08	0.08	-1.917	0.6
1293	13600	0.09	0.91	0.09	0.09	-1.950	0.8
1293	13600	0.09	0.91	0.09	0.08	-2.310	0.0
1293	13600	0.09	0.91	0.08	0.09	-2.235	0.1
1293	13600	0.09	0.91	0.08	0.09	-1.950	0.5

Supplementary Table 2. Summary of calculated parameters used for the calculation of the peridotite oxygen fugacity. * The estimated propagated error from the EPMA analysis is 0.3.

	Weight %									
	SiO_2	**TiO_2**	**Al_2O_3**	**Cr_2O_3**	**FeO**	**MnO**	**MgO**	**NiO**	**CaO**	**Total**
Arm 1	0.1	74.39	0.59	2.10	10.05	0.09	12.59	0.11	0.05	100.07
Arm 2	0.11	75.01	0.61	1.73	10.25	0.09	12.41	0.1	0.08	100.39
Arm 3	0.08	71.29	0.75	2.16	11.27	0.08	11.56	0.08	0.35	97.62
Arm 4	0.37	71.92	0.43	2.03	11.01	0.07	12.04	0.06	0.06	97.99
Arm 5	0.16	72.18	0.73	2.78	9.81	0.09	12.39	0.06	0.07	98.26
Arm 6	0.20	72.06	0.82	2.78	9.77	0.07	12.06	0.06	0.06	97.87
Arm 7	0.19	71.91	0.68	2.76	9.88	0.08	11.98	0.06	0.07	97.60
Arm 8	0.11	72.20	0.55	2.25	11.02	0.10	11.94	0.11	0.18	98.46
Arm 9	0.13	72.33	0.72	2.36	10.78	0.09	11.86	0.10	0.18	98.54
Arm 10	0.18	72.37	0.50	2.16	11.29	0.08	11.67	0.11	0.21	98.57
Arm 11	0.41	71.51	0.81	2.40	10.87	0.09	11.55	0.10	0.21	97.94
Arm 12	0.14	72.29	0.84	1.94	11.22	0.09	11.77	0.08	0.35	98.72
Arm 13	0.18	72.21	0.46	2.30	10.93	0.09	11.92	0.08	0.09	98.26
Arm 14	0.13	72.59	0.71	2.02	10.45	0.09	12.02	0.26	0.13	98.40
Arm 15	0.22	72.36	0.97	2.62	9.88	0.10	12.04	0.06	0.09	98.33
Arm 16	0.66	72.67	0.76	1.05	9.83	0.08	12.78	0.07	0.19	98.09
Std Dev	0.02	0.03	0.02	0.02	0.15	0.02	0.11	0.02	0.02	
	Atoms per formula unit (a.p.f.u.)									
	Si	**Ti**	**Al**	**Cr**	**Fe**	**Mn**	**Mg**	**Ni**	**Ca**	**Total**
Arm 1	0.003	1.943	0.024	0.058	0.292	0.003	0.652	0.003	0.002	3.002
Arm 2	0.004	1.952	0.025	0.047	0.297	0.003	0.640	0.003	0.003	2.996
Arm 3	0.003	1.924	0.032	0.061	0.338	0.002	0.618	0.002	0.013	3.016
Arm 4	0.013	1.925	0.018	0.057	0.328	0.002	0.639	0.002	0.002	3.011
Arm 5	0.006	1.934	0.030	0.078	0.292	0.003	0.658	0.002	0.003	3.006
Arm 6	0.007	1.938	0.034	0.078	0.292	0.002	0.643	0.002	0.002	2.999
Arm 7	0.007	1.941	0.029	0.078	0.296	0.002	0.641	0.002	0.003	2.999
Arm 8	0.004	1.941	0.023	0.064	0.329	0.003	0.637	0.003	0.007	3.011
Arm 9	0.005	1.940	0.030	0.066	0.322	0.003	0.631	0.003	0.007	3.007
Arm 10	0.006	1.946	0.021	0.061	0.337	0.003	0.622	0.003	0.008	3.007
Arm 11	0.015	1.930	0.034	0.068	0.326	0.003	0.618	0.003	0.008	3.004
Arm 12	0.005	1.938	0.035	0.055	0.334	0.003	0.626	0.002	0.013	3.012
Arm 13	0.006	1.944	0.019	0.065	0.327	0.003	0.636	0.002	0.003	3.007
Arm 14	0.005	1.947	0.030	0.057	0.312	0.003	0.639	0.007	0.005	3.005
Arm 15	0.008	1.936	0.041	0.074	0.294	0.003	0.639	0.002	0.003	2.999
Arm 16	0.023	1.941	0.032	0.029	0.292	0.002	0.677	0.002	0.007	3.005

Supplementary Table 3. Chemical composition of armalcolite.

		Molecular Proportion	X	$R_2O_3.TiO_2$	$MO._2TiO_2$	Ti left	$FeO._2TiO_2$	$Fe_2O_3.TiO_2$	FeO	Fe_2O_3
Arm 1	TiO_2	0.9313	0.3380	0.0196	0.6321	0.2796	0.2795	0.00005	10.0423	0.0086
	R_2O_3*	0.0196	-	0.0196	-	-	-	-		
	MO†	0.3160	-	-	-	-	-	-		
	FeO	0.1399	-	-	-	-	0.1398	-		
Arm 2	TiO_2	0.9390	0.3364	0.0174	0.6321	0.2896	0.2896	0.00000	10.4035	0.0000
	R_2O_3*	0.0174	-	0.0174	-	-	-	-		
	MO†	0.3160	-	-	-	-	-	-		
	FeO	0.1427	-	-	-	-	0.1448	-		
Arm 3	TiO_2	0.8925	0.3467	0.0216	0.5906	0.2803	0.2692	0.01113	9.6706	1.7774
	R_2O_3*	0.0216	-	0.0216	-	-	-	-		
	MO†	0.2953	-	-	-	-	-	-		
	FeO	0.1569	-	-	-	-	0.1346	-		
Arm 4	TiO_2	0.9004	0.3441	0.0176	0.6032	0.2795	0.2706	0.00898	9.7199	1.4337
	R_2O_3*	0.0176	-	0.0176	-	-	-	-		
	MO†	0.3016	-	-	-	-	-	-		
	FeO	0.1532	-	-	-	-	0.1353	-		
Arm 5	TiO_2	0.9036	0.3434	0.0254	0.6211	0.2571	0.2517	0.00535	9.0429	0.8549
	R_2O_3*	0.0254	-	0.0254	-	-	-	-		
	MO†	0.3106	-	-	-	-	-	-		
	FeO	0.1366	-	-	-	-	0.1259	-		
Arm 6	TiO_2	0.9021	0.3398	0.0263	0.6042	0.2716	0.2715	0.00009	9.7547	0.0151
	R_2O_3*	0.0263	-	0.0263	-	-	-	-		
	MO†	0.3021	-	-	-	-	-	-		
	FeO	0.1360	-	-	-	-	0.1358	-		
Arm 7	TiO_2	0.9002	0.3396	0.0248	0.6010	0.2744	0.2742	0.00021	9.8493	0.0328
	R_2O_3*	0.0248	-	0.0248	-	-	-	-		
	MO†	0.3005	-	-	-	-	-	-		
	FeO	0.1375	-	-	-	-	0.1371	-		
Arm 8	TiO_2	0.90386	0.34490	0.02024	0.60461	0.27901	0.26980	0.00921	9.6926	1.4706
	R_2O_3*	0.02024	-	0.02024	-	-	-	-		
	MO†	0.30231	-	-	-	-	-	-		
	FeO	0.15332	-	-	-	-	0.13490	-		
Arm 9	TiO_2	0.90542	0.34304	0.02254	0.60040	0.28248	0.27661	0.00586	9.9374	0.9363
	R_2O_3*	0.02254	-	0.02254	-	-	-	-		
	MO†	0.30020	-	-	-	-	-	-		
	FeO	0.15003	-	-	-	-	0.13831	-		

Supplementary Table 4. Stoichiometric calculation of armalcolite end members. Calculation of mineral compositions from EPMA following the procedures of Bowles (*1988*). *R_2O_3 = Al_2O_3 + Cr_2O_3 + V_2O_3; †MO = MgO + MnO + CaO.

		Molecular Proportion	X	$R_2O_3.TiO_2$	$MO._2TiO_2$	Ti left	$FeO._2TiO_2$	$Fe_2O_3.TiO_2$	FeO†	Fe_2O_3†
Arm 10	TiO_2	0.9060	0.3426	0.0191	0.5918	0.2950	0.2886	0.00638	10.3683	1.0188
	R_2O_3*	0.0191	-	0.0191	-	-	-	-		
	MO†	0.2959	-	-	-	-	-	-		
	FeO	0.1571	-	-	-	-	0.1443	-		
Arm 11	TiO_2	0.8953	0.3432	0.0238	0.5858	0.2857	0.2801	0.00558	10.0642	0.8912
	R_2O_3*	0.0238	-	0.0238	-	-	-	-		
	MO†	0.2929	-	-	-	-	-	-		
	FeO	0.1512	-	-	-	-	0.1401	-		
Arm 12	TiO_2	0.9049	0.3459	0.0211	0.6014	0.2825	0.2721	0.01040	9.7753	1.6610
	R_2O_3*	0.0211	-	0.0211	-	-	-	-		
	MO†	0.3007	-	-	-	-	-	-		
	FeO	0.1569	-	-	-	-	0.1361	-		
Arm 13	TiO_2	0.9040	0.3427	0.0197	0.5992	0.2852	0.2788	0.00637	10.0158	1.0166
	R_2O_3*	0.0197	-	0.0197	-	-	-	-		
	MO†	0.2996	-	-	-	-	-	-		
	FeO	0.1521	-	-	-	-	0.1394	-		
Arm 14	TiO_2	0.9087	0.3414	0.0203	0.6106	0.2779	0.2735	0.00436	9.8264	0.6961
	R_2O_3*	0.0203	-	0.0203	-	-	-	-		
	MO†	0.3053	-	-	-	-	-	-		
	FeO	0.1455	-	-	-	-	0.1368	-		
Arm 15	TiO_2	0.9059	0.3400	0.0267	0.6049	0.2743	0.2740	0.00027	9.8430	0.0437
	R_2O_3*	0.0267	-	0.0267	-	-	-	-		
	MO†	0.3024	-	-	-	-	-	-		
	FeO	0.1375	-	-	-	-	0.1370	-		
Arm 16	TiO_2	0.9097	0.3424	0.0144	0.6450	0.2503	0.2425	0.00780	8.7120	1.2455
	R_2O_3*	0.0144	-	0.0144	-	-	-	-		
	MO†	0.3225	-	-	-	-	-	-		
	FeO	0.1369	-	-	-	-	0.1213	-		

Supplementary Table 4 continued. Stoichiometric calculation of armalcolite end members. Calculation of mineral compositions from EPMA following the procedures of Bowles (*1988*). *R_2O_3 = Al_2O_3 + Cr_2O_3 + V_2O_3; †MO = MgO + MnO + CaO.

	Weight %											
	Ap2		Ap5		Ap6		Ap8		Ap9		Ap10	
	Conc	Std Dev	Conc	Std Dev	Conc	Std Dev	Conc	Std Dev	Conc	Std Dev	Conc	Std Dev
SiO_2	0.46	0.03	1.54	0.04	0.81	0.032	0.56	0.03	0.50	0.03	0.38	0.03
Al_2O_3	0.03	0.02	0.19	0.02	0.16	0.02	0.09	0.02	0.07	0.02	0.16	0.02
FeO	0.48	0.10	0.26	0.08	0.32	0.09	0.34	0.09	0.33	0.09	0.32	0.09
MgO	0.50	0.04	1.50	0.05	0.85	0.04	0.52	0.03	0.47	0.03	0.33	0.03
CaO	53.03	0.84	53.17	0.82	53.18	0.84	53.96	0.83	53.77	0.83	53.31	0.82
K_2O	0.01	0.04	b.d.l.	-	b.d.l.	-	0.02	0.04	0.02	0.04	b.d.l.	-
Na_2O	0.09	0.04	0.08	0.035	0.12	0.04	0.14	0.04	0.14	0.04	0.14	0.04
P_2O_5	41.33	0.49	40.61	0.48	40.93	0.49	41.50	0.48	41.22	0.48	41.61	0.48
Ce_2O_3	0.59	0.15	0.80	0.15	0.69	0.15	0.82	0.15	0.86	0.15	0.80	0.15
La_2O_3	b.d.l.	-	b.d.l.	-	b.d.l.	1.51	0.10	1.37	b.d.l.	-	b.d.l	-
Cl	0.18	0.03	0.18	0.03	0.13	0.08	0.16	0.03	0.12	0.03	0.11	0.03
F	3.80	0.46	3.78	0.41	3.97	0.44	3.81	0.42	3.81	0.41	3.91	0.41
SO_3	0.01	0.02	b.d.l.	-	0.01	0.02	0.02	0.02	0.00	0.02	0.04	0.02
O = F, Cl	1.64		1.63		1.70		1.64		1.63		1.67	
OH wt.%	0.00		0.00		0.00		0.00		0.00		0.00	
Total	98.87		100.48		99.48		100.39		99.68		99.73	
S (µg/g)	41.04		b.d.l.		59.56		74.08		b.d.l.		169.17	

	Atoms per formula unit (a.p.f.u.)					
Si	0.078	0.258	0.137	0.094	0.085	0.064
Al	0.006	0.037	0.032	0.018	0.014	0.032
Fe	0.068	0.036	0.045	0.048	0.047	0.045
Mg	0.127	0.374	0.215	0.130	0.119	0.083
Ca	9.673	9.539	9.653	9.722	9.760	9.662
K	0.002	0.000	0.000	0.004	0.004	0.000
Na	0.030	0.026	0.039	0.046	0.046	0.046
P	5.957	5.757	5.871	5.908	5.912	5.959
Ce	0.037	0.049	0.043	0.050	0.053	0.050
La	-	-	-	0.006	-	0.019
Cl	0.052	0.051	0.037	0.046	0.034	0.032
F	2.046	2.002	2.127	2.026	2.041	2.092
S	0.001	-	0.002	0.002	-	0.005
OH	-	-	-	-	-	-

Supplementary Table 5. Chemical composition of apatite.

	Weight %											
	Ap13		Ap14		Ap15		Ap17		Ap18		Ap21	
	Conc	Std Dev	Conc	Std Dev	Conc	Std Dev	Conc	Std Dev	Conc	Std Dev	Conc	Std Dev
SiO_2	0.36	0.03	0.30	0.02	0.47	0.03	0.72	0.03	0.32	0.02	0.37	0.03
Al_2O_3	0.04	0.02	0.03	0.02	0.03	0.02	0.09	0.02	0.05	0.02	0.17	0.02
FeO	0.33	0.09	0.37	0.09	0.39	0.09	0.4	0.09	0.54	0.09	0.32	0.09
MgO	0.43	0.03	0.4	0.03	0.45	0.03	0.68	0.04	0.43	0.03	0.36	0.03
CaO	54.2	0.84	54.13	0.83	54.41	0.84	53.68	0.83	53.69	0.83	53.9	0.85
K_2O	b.d.l.	-	0.02	0.04	b.d.l.	-	b.d.l.	-	b.d.l.	-	b.d.l.	-
Na_2O	0.06	0.03	0.10	0.03	0.06	0.03	0.09	0.03	0.03	0.03	0.07	0.04
P_2O_5	41.65	0.49	42.53	0.49	41.98	0.49	42.43	0.49	43.05	0.50	42.54	0.5
Ce_2O_3	0.68	0.14	0.54	0.14	0.67	0.14	0.71	0.14	0.35	0.13	0.58	0.15
La_2O_3	b.d.l.	-	b.d.l.	-	b.d.l.	-	b.d.l.	-	b.d.l.	-	b.d.l.	-
Cl	0.14	0.03	0.13	0.03	0.10	0.02	0.10	0.02	0.11	0.02	0.10	0.02
F	3.64	0.41	3.79	0.41	3.76	0.41	3.46	0.40	3.14	0.39	3.89	0.44
SO_3	0.01	0.02	b.d.l.	-	b.d.l.	-	0.01	0.02	0.02	0.02	b.d.l.	-
O = F, Cl	1.56		1.62		1.60		1.48		1.35		1.66	
OH wt.%	0.04		0.00		0.00		0.26		0.54		0.00	
Total	100.27		100.71		100.72		100.88		100.37		100.65	
S (µg/g)	43.04		b.d.l.		b.d.l.		44.55		62.56		b.d.l.	
	Atoms per formula unit (a.p.f.u.)											
Si	0.061		0.050		0.079		0.119		0.053		0.062	
Al	0.008		0.006		0.006		0.018		0.010		0.033	
Fe	0.046		0.052		0.055		0.055		0.075		0.045	
Mg	0.108		0.099		0.112		0.168		0.106		0.089	
Ca	9.772		9.667		9.744		9.538		9.543		9.623	
K	-		0.004		-		-		-		-	
Na	0.020		0.032		0.019		0.029		0.010		0.023	
P	5.935		6.002		5.941		5.957		6.046		6.001	
Ce	0.042		0.033		0.041		0.043		0.021		0.035	
La	-		-		-		-		-		-	
Cl	0.040		0.037		0.028		0.028		0.031		0.028	
F	1.938		1.998		1.988		1.815		1.647		2.050	
S	0.001		-		-		0.001		0.002		-	
OH	0.023		-		-		0.157		0.322		-	

Supplementary Table 5 (continued). Chemical composition of apatite.

SUPPLEMENTARY INFORMATION REFERENCES

Bowles, J.F.W. Definition and range of naturally occurring minerals with the pseudobrookite structure. *American Mineralogist* **73**, 1377-1383 (1988).

Cawthorn, R.G., Biggar, G.M. Crystallization of titaniferous chromite, magnesian ilmenite and armalcolite in tholeiitic suites in the Karoo Igneous Province. *Contributions to Mineralogy and Petrology* **114**, 221-235 (1993).

Contini, S., Venturelli, G., Toscani, L. Cr-Zr armalcolite-bearing lamproites of Cancarix, SE Spain. *Mineralogical Magazine* **57**, 203-216 (1993).

Grégoire, M., Lorand, J-P., O´Reilly, S.Y., Cottin, J.Y. Armalcolite-bearing, Ti-rich metasomatic assemblages in harzburgitic xenoliths from Kerguelen Islands: Implications for the oceanic mantle budget of high-field strength elements. *Geochimica et Cosmochimica Acta* **64**, 673-694 (2000).

Haggerty, S.E. The mineral chemistry of new titanates from the Jagersfontein kimberlite, South Africa: Implications for metasomatism in the upper mantle. *Geochimica et Cosmochimica Acta* **47**, 1833-1854 (1983).

Tassara, S., González-Jiménez, J.M., Reich, M., Schilling, M.E., Morata, D., Begg, G.C., Saunders, E., Griffin, W.L., O´Reilly, S.Y., Grégoire, M., Barra, F., Corgne, A. Plume-subduction interaction forms large auriferous provinces. *Nature Communications* **8**, 843 (2017).

A.4. SUPPLEMENTARY INFORMATION FOR CHAPTER 5

Referred to as "Appendix 1" in Chapter 5. Measured Major and volatile element composition of melt inclusions.

	Electron Microprobe Measured (Wt.%); Normalized to a water-free basis												
Inclusion #	**SiO_2**	**TiO_2**	**Al_2O_3**	**$FeO_{(tot)}$**	**MnO**	**MgO**	**CaO**	**Na_2O**	**K_2O**	**P_2O_5**	**S (ppm)**	**Cl (ppm)**	**Original Totals**
1	51.23	0.75	17.76	7.14	0.13	6.73	11.92	3.03	0.80	0.16	1293	965	97.43
2	51.87	0.78	18.19	6.71	0.19	5.89	11.84	3.10	0.88	0.12	1618	1205	97.95
3	51.78	0.78	17.16	7.66	0.11	6.62	11.67	2.84	0.81	0.10	1746	1227	96.20
4	51.54	0.74	17.14	7.72	0.19	7.03	11.48	2.79	0.79	0.13	1776	1029	96.26
5	51.20	0.76	17.08	7.78	0.19	7.35	11.55	2.78	0.74	0.12	1705	1029	96.17
6	49.21	0.75	18.02	7.06	0.11	7.64	13.08	2.62	0.69	0.11	2843	1390	96.39
7	49.37	0.60	18.11	7.36	0.16	6.83	13.14	2.89	0.71	0.12	2855	1501	95.97
8	48.30	0.76	19.29	6.73	0.16	7.11	12.88	3.25	0.83	0.11	2255	1280	98.46
9	48.20	0.82	19.31	6.65	0.16	7.13	12.99	3.13	0.86	0.15	2348	1413	98.40
10	48.32	0.78	19.23	6.65	0.16	7.19	12.99	3.15	0.86	0.11	2099	1237	98.64
11	46.99	0.81	20.36	6.49	0.14	6.94	13.51	3.15	0.81	0.16	2488	1452	98.46
12	48.11	0.67	19.85	6.15	0.09	7.01	13.66	3.04	0.80	0.16	1555	1448	98.04
13	48.93	0.76	18.60	6.61	0.13	7.54	12.92	3.01	0.78	0.11	2313	1376	98.14
14	49.35	0.70	18.46	6.39	0.07	7.52	12.95	3.00	0.78	0.14	2456	1323	97.51
15	48.38	0.85	19.67	5.29	0.08	6.95	13.81	3.26	0.90	0.15	2671	1443	99.78
16	50.33	0.75	17.83	7.39	0.13	7.75	11.27	3.08	0.90	0.18	1479	1013	97.72
17	50.22	0.74	17.84	7.36	0.12	7.78	11.36	3.17	0.87	0.17	1323	1103	97.89
18	49.95	0.72	19.09	5.46	0.10	6.93	13.04	3.05	0.82	0.13	2882	1418	96.64
19	50.11	0.82	19.80	5.86	0.06	5.37	13.32	3.14	0.79	0.17	2211	1220	98.38
20	48.07	0.82	19.55	6.11	0.09	7.55	13.09	3.06	0.84	0.16	2681	1400	97.16
21	47.50	0.89	19.52	7.27	0.12	6.86	12.97	3.28	0.85	0.17	2198	1340	98.50
22	50.10	0.74	18.63	5.98	0.10	6.66	13.53	2.76	0.71	0.14	2673	1202	96.51
23	49.84	0.75	18.48	5.84	0.12	7.00	13.65	2.71	0.69	0.14	3274	1320	96.96
24	50.11	0.75	18.22	6.51	0.08	6.47	13.74	2.70	0.64	0.11	2704	1437	96.72
25	48.82	0.77	19.29	6.63	0.07	6.93	13.13	2.86	0.76	0.13	2390	1300	97.70
26	47.91	0.78	20.15	6.42	0.11	6.86	13.25	2.93	0.81	0.16	2388	1278	95.48
27	47.74	0.81	19.75	5.94	0.13	7.08	14.00	3.03	0.78	0.12	2319	1567	95.07
28	47.82	0.81	19.75	6.11	0.14	6.98	13.78	3.05	0.77	0.13	2571	1466	96.85
29	48.40	0.84	19.79	6.13	0.09	6.63	13.37	3.14	0.84	0.17	2302	1298	98.62
30	50.05	0.78	18.00	6.78	0.13	7.09	13.18	2.52	0.87	0.11	1837	1122	97.15
31	49.94	0.79	18.94	6.06	0.13	6.44	12.96	3.16	0.89	0.05	2415	1462	97.10
32	51.35	0.72	17.80	6.31	0.05	5.55	14.16	2.56	0.66	0.13	2827	1493	93.75
33	49.90	0.74	18.24	5.85	0.14	7.36	13.15	3.09	0.82	0.10	2333	1455	96.21
34	48.99	0.69	18.47	6.53	0.15	7.55	13.24	2.79	0.71	0.14	3103	1328	97.15
35	48.85	0.72	18.96	5.87	0.08	7.41	13.60	2.89	0.77	0.11	2998	1504	98.38
36	48.49	0.69	19.65	5.86	0.11	6.89	14.32	2.62	0.65	0.14	2201	1300	97.70

37	49.32	0.76	18.57	6.28	0.10	6.94	13.58	2.81	0.71	0.19	2958	1453	96.36
38	50.33	0.74	18.22	6.84	0.17	6.36	13.29	2.70	0.67	0.09	2398	1207	96.11
39	49.63	0.71	18.03	7.43	0.10	7.76	12.30	2.65	0.71	0.12	2193	1194	95.51
40	49.08	0.69	21.80	5.76	0.06	4.71	13.53	2.72	0.77	0.14	2999	1517	97.53
41	50.84	0.80	18.48	6.20	0.03	5.55	13.52	2.76	0.84	0.13	3406	1573	94.09
42	54.73	0.78	15.22	7.44	0.13	6.13	11.25	3.00	1.08	0.13	bdl	956	97.28
43	50.47	0.73	18.35	6.46	0.13	6.92	12.40	2.72	0.74	0.20	3746	1201	94.09
44	49.12	0.73	18.02	6.35	0.15	7.75	13.38	2.90	0.78	0.13	2575	1727	93.79
45	51.18	0.64	17.47	6.49	0.09	8.32	11.79	2.71	0.54	0.14	2468	1415	94.00
46	50.87	0.80	19.31	6.09	0.08	4.96	13.74	2.49	0.66	0.16	3255	1794	95.85
47	50.88	0.67	17.05	6.76	0.18	8.31	12.19	2.46	0.67	0.13	2854	1388	95.12
48	50.58	0.65	17.30	7.18	0.14	7.34	13.19	2.35	0.52	0.09	2664	1356	93.64
49	52.46	0.73	18.00	6.70	0.13	5.67	12.51	2.30	0.66	0.10	3041	1296	94.88
50	50.04	0.70	18.15	6.86	0.21	7.08	13.21	2.49	0.49	0.06	2787	1406	95.98
51	49.86	0.70	20.17	6.50	0.10	6.30	12.86	2.23	0.41	0.19	2667	1491	96.55
52	49.29	0.76	19.65	5.55	0.06	5.43	14.87	2.65	0.70	0.17	3452	1862	95.60
53	50.26	0.75	19.44	5.91	0.08	5.52	13.54	3.09	0.71	0.16	1958	1395	96.80
54	50.33	0.88	19.84	5.86	0.10	4.45	13.92	3.07	0.77	0.21	2074	1638	95.23
55	49.63	0.75	18.40	6.90	0.08	6.76	13.07	2.83	0.81	0.10	2550	1611	94.33
56	49.77	0.75	18.67	6.63	0.11	6.70	12.62	3.17	0.94	0.10	2176	1215	94.67
57	49.13	0.77	18.33	6.72	0.14	7.44	12.82	3.12	0.82	0.10	2414	1207	96.11
58	47.79	0.78	20.40	5.53	0.16	6.20	14.14	3.38	0.74	0.19	2672	1650	98.80
59	49.02	0.80	19.79	5.90	0.08	6.18	13.71	2.91	0.76	0.10	2906	1762	97.03
60	47.68	0.86	19.27	5.80	0.09	6.94	14.35	3.44	0.81	0.19	2179	1278	95.47
61	49.62	0.81	19.34	5.84	0.12	5.63	14.28	2.69	0.73	0.23	2876	1374	96.82
62	48.20	0.82	19.62	7.34	0.12	6.75	12.89	2.78	0.68	0.14	2912	894	97.35
63	46.62	0.77	19.81	6.13	0.01	7.37	14.22	3.35	0.76	0.19	3072	1421	93.58
64	48.63	0.73	20.45	5.44	0.05	5.11	14.58	3.24	0.86	0.09	3004	2278	94.37
65	48.10	0.72	20.06	5.32	0.06	6.77	14.12	3.32	0.66	0.17	2579	1979	95.01
68	48.39	0.69	19.28	6.26	0.04	6.42	13.94	3.13	0.79	0.23	3374	1446	95.43
69	48.04	0.75	20.31	5.99	0.06	5.86	14.17	3.27	0.82	0.03	2600	1789	95.59
70	48.24	0.72	19.35	5.99	0.09	6.69	14.27	2.79	0.87	0.26	2935	1508	94.19
71	49.49	0.72	18.85	6.56	0.15	6.81	13.04	2.79	0.68	0.20	2680	1724	95.15
72	46.95	0.68	19.80	8.13	0.08	6.40	13.64	2.95	0.67	0.12	2150	1475	94.90
73	46.57	0.71	19.74	7.99	0.07	6.79	13.52	3.16	0.77	0.11	2154	1378	97.27
74	47.93	0.75	20.23	6.74	0.08	6.75	13.06	2.96	0.67	0.24	2234	1307	98.70
75	48.52	0.81	18.83	7.50	0.10	7.32	12.22	3.02	0.98	0.18	2049	1143	97.14
76	48.76	0.72	18.75	7.57	0.08	7.07	12.34	2.89	1.09	0.14	2182	1541	96.69
79	48.59	0.83	18.05	8.15	0.15	7.02	12.56	2.94	0.93	0.16	2409	1489	96.74
80	49.47	0.75	20.06	5.67	0.08	6.92	12.93	2.68	0.78	0.09	2274	1343	98.27
81	48.43	0.77	18.96	6.18	0.17	7.56	13.41	3.08	0.70	0.18	2203	1091	97.16
82	49.59	0.71	17.84	7.01	0.06	8.47	12.39	2.52	0.62	0.17	2379	1366	96.66
83	50.21	0.69	18.16	6.93	0.16	7.89	12.18	2.39	0.60	0.10	2944	1178	96.80
84	52.43	0.73	17.60	7.31	0.11	6.22	11.90	2.63	0.76	0.12	557	769	98.82

85	48.46	0.77	18.78	7.18	0.12	6.47	13.85	2.75	0.75	0.12	2905	1652	93.81
86	48.40	0.79	18.16	7.08	0.17	7.51	13.43	2.86	0.70	0.13	3157	1396	94.55
87	46.36	0.82	20.14	5.77	0.01	7.14	14.87	3.19	0.75	0.19	2977	1498	98.10
88	46.42	0.83	20.87	5.72	0.08	6.57	14.46	3.30	0.85	0.16	2818	1838	98.47
89	47.72	0.75	19.43	5.39	0.06	6.75	14.95	3.17	0.81	0.11	3371	1865	97.61
90	47.47	0.73	18.79	7.48	0.11	7.93	12.95	3.11	0.66	0.12	2610	1339	97.12
91	47.90	0.74	18.53	7.41	0.14	7.84	13.00	3.04	0.73	0.05	2411	1457	97.48
92	50.92	0.63	16.59	7.06	0.12	8.97	11.96	2.32	0.64	0.11	2660	1538	94.91
93	50.95	0.61	16.39	6.61	0.13	9.78	11.57	2.55	0.58	0.17	2712	1152	95.51
94	46.55	0.74	20.18	7.05	0.16	6.80	13.51	3.30	0.77	0.22	2793	1589	98.80
95	51.49	0.93	19.85	5.19	0.10	5.88	11.29	3.57	0.83	0.25	2478	1200	95.02
96	49.41	0.71	19.50	7.30	0.07	6.50	11.95	3.04	0.78	0.26	1748	1179	98.38
97	48.43	0.74	19.65	7.47	0.09	6.15	12.42	3.24	0.94	0.34	1899	1456	94.79
98	54.84	0.91	16.24	6.78	0.14	5.66	10.66	3.35	1.23	0.08	bdl	1015	97.58
99	54.52	0.84	17.25	6.87	0.15	5.71	10.19	3.05	1.19	0.14	bdl	795	98.18
100	54.50	0.81	16.45	6.39	0.14	6.38	10.32	3.58	1.13	0.18	bdl	1082	97.02
101	49.94	0.95	18.32	8.34	0.13	5.25	12.58	2.91	0.65	0.25	2684	1366	94.44
102	48.83	0.82	18.67	8.51	0.18	5.22	12.86	3.24	0.75	0.17	2955	1509	94.09
103	47.74	0.76	19.93	7.56	0.19	6.72	12.81	2.94	0.73	0.12	1807	1414	95.48
104	48.71	0.72	18.41	7.69	0.12	7.20	12.91	2.86	0.66	0.18	2040	1267	97.04
105	47.69	0.92	21.04	5.99	0.08	4.49	14.61	3.53	0.80	0.16	2802	1406	93.15
106	47.39	0.83	18.27	8.87	0.14	7.47	12.59	2.78	0.81	0.25	2275	1365	94.52
110	54.45	0.99	16.09	8.03	0.15	5.87	9.85	3.10	1.07	0.29	bdl	1185	97.07

Measured Composition of the olivine host to the melt inclusions.

	Olivine Host										
Inclusion #	**SiO_2**	**Al_2O_3**	**FeO**	**MnO**	**MgO**	**CaO**	**NiO**	**Cr_2O_3**	**Total**	**Fo**	**Fa**
1	41.31	0.03	8.24	0.17	50.69	0.13	0.44	0.11	101.12	91.65	8.35
2	41.33	0.21	8.25	0.17	50.06	0.14	0.43	0.06	100.67	91.54	8.46
3	41.56	0.07	8.37	0.15	49.72	0.14	0.39	0.05	100.46	91.37	8.63
4	41.41	0.02	8.17	0.15	50.12	0.13	0.41	0.06	100.48	91.62	8.38
5	41.59	0.03	8.19	0.13	50.21	0.14	0.41	0.06	100.78	91.62	8.38
6	41.57	0.04	8.41	0.12	49.95	0.13	0.40	0.05	100.67	91.37	8.63
7	41.30	0.03	8.23	0.14	49.87	0.14	0.43	0.06	100.16	91.53	8.47
8	41.66	0.04	8.50	0.11	49.44	0.16	0.37	0.05	100.33	91.20	8.80
9	41.59	0.05	8.51	0.15	50.42	0.13	0.39	0.05	101.29	91.35	8.65
10	41.52	0.06	8.84	0.17	49.71	0.15	0.39	0.04	100.86	90.93	9.07
11	41.18	0.02	8.39	0.17	49.61	0.15	0.42	0.05	100.01	91.33	8.67
12	41.10	0.17	8.12	0.14	49.50	0.13	0.38	0.06	99.61	91.57	8.43
13	41.51	0.09	8.05	0.13	49.56	0.13	0.41	0.06	99.98	91.64	8.36
14	41.44	0.11	8.15	0.13	49.82	0.13	0.38	0.07	100.21	91.59	8.41
15	41.43	0.04	8.16	0.16	49.54	0.13	0.44	0.06	99.94	91.54	8.46
16	40.74	0.04	10.04	0.20	48.13	0.17	0.25	0.07	99.64	89.52	10.48
17	40.69	0.03	9.96	0.16	48.49	0.17	0.23	0.06	99.82	89.66	10.34
18	41.71	0.07	7.98	0.12	50.54	0.14	0.44	0.06	101.05	91.87	8.13
19	40.67	0.02	8.61	0.12	49.20	0.13	0.42	0.05	99.22	91.06	8.94
20	40.37	0.03	9.44	0.18	48.56	0.17	0.28	0.05	99.11	90.17	9.83
21	41.95	0.06	8.52	0.16	50.18	0.14	0.38	0.06	101.47	91.30	8.70
22	41.52	0.04	8.09	0.14	49.66	0.15	0.44	0.06	100.07	91.63	8.37
23	41.64	0.03	8.01	0.14	49.84	0.15	0.40	0.08	100.31	91.73	8.27
24	41.49	0.03	8.01	0.10	49.90	0.15	0.45	0.07	100.21	91.74	8.26
25	40.76	1.86	7.60	0.12	49.50	0.12	0.45	0.08	100.48	92.07	7.93
26	41.11	0.11	8.12	0.11	49.80	0.12	0.46	0.07	99.91	91.62	8.38
27	39.68	0.02	8.16	0.13	52.51	0.14	0.37	0.06	101.07	91.98	8.02
28	40.85	0.03	8.28	0.13	51.73	0.16	0.39	0.04	101.64	91.76	8.24
29	41.64	0.01	8.44	0.12	49.12	0.14	0.34	0.05	99.86	91.21	8.79
30	41.24	0.03	8.38	0.11	49.49	0.13	0.41	0.05	99.90	91.32	8.68
31	41.24	0.03	8.38	0.11	49.49	0.13	0.41	0.05	99.90	91.32	8.68
32	41.51	0.04	7.63	0.14	50.01	0.13	0.47	0.07	100.03	92.12	7.88
33	41.24	0.03	7.62	0.11	49.80	0.12	0.43	0.06	99.41	92.10	7.90
34	41.16	0.03	8.41	0.12	49.00	0.14	0.38	0.05	99.31	91.21	8.79
35	41.07	0.03	8.37	0.15	48.96	0.14	0.40	0.05	99.21	91.25	8.75
36	41.65	0.01	8.36	0.13	49.10	0.15	0.39	0.04	99.87	91.28	8.72
37	41.65	0.01	8.36	0.13	49.10	0.15	0.39	0.04	99.87	91.28	8.72
38	41.70	0.02	8.37	0.14	50.43	0.13	0.42	0.06	101.27	91.49	8.51
39	39.71	2.50	8.11	0.14	48.13	0.13	0.42	0.07	99.24	91.36	8.64

40	41.65	0.03	8.54	0.12	48.35	0.14	0.40	0.08	99.31	90.99	9.01
41	41.65	0.03	8.54	0.12	48.35	0.14	0.40	0.08	99.31	90.99	9.01
42	41.58	0.02	7.81	0.11	50.19	0.12	0.43	0.07	100.33	91.98	8.02
43	42.80	0.02	7.96	0.13	50.28	0.12	0.43	0.07	101.81	91.84	8.16
44	43.74	0.45	8.60	0.14	46.58	0.58	0.36	0.02	100.48	90.61	9.39
45	41.96	0.02	8.39	0.14	48.07	0.14	0.41	0.05	99.16	91.08	8.92
46	41.65	0.03	8.54	0.12	48.35	0.14	0.40	0.08	99.31	90.99	9.01
47	41.96	0.02	8.39	0.14	48.07	0.14	0.41	0.05	99.16	91.08	8.92
48	41.96	0.02	8.39	0.14	48.07	0.14	0.41	0.05	99.16	91.08	8.92
49	41.96	0.02	8.39	0.14	48.07	0.14	0.41	0.05	99.16	91.08	8.92
50	41.96	0.02	8.39	0.14	48.07	0.14	0.41	0.05	99.16	91.08	8.92
51	41.96	0.02	8.39	0.14	48.07	0.14	0.41	0.05	99.16	91.08	8.92
52	-	-	-	-	-	-	-	-	-	**91.13**	**8.87**
53	-	-	-	-	-	-	-	-	-	**91.13**	**8.87**
54	-	-	-	-	-	-	-	-	-	**91.13**	**8.87**
55	41.57	0.01	7.71	0.11	50.49	0.13	0.47	0.08	100.56	92.11	7.89
56	41.57	0.01	7.71	0.11	50.49	0.13	0.47	0.08	100.56	92.11	7.89
57	41.57	0.01	7.71	0.11	50.49	0.13	0.47	0.08	100.56	92.11	7.89
58	41.42	0.02	9.13	0.14	49.47	0.15	0.32	0.04	100.69	90.62	9.38
59	41.33	0.02	7.76	0.13	50.28	0.13	0.32	0.09	100.06	92.03	7.97
60	41.80	0.02	7.93	0.12	50.32	0.12	0.47	0.10	100.89	91.87	8.13
61	41.89	0.03	7.93	0.12	50.28	0.13	0.47	0.11	100.95	91.88	8.12
62	41.12	0.01	9.59	0.14	48.46	0.16	0.34	0.04	99.85	90.01	9.99
63	-	-	-	-	-	-	-	-	-	**91.13**	**8.87**
64	-	-	-	-	-	-	-	-	-	**91.13**	**8.87**
65	-	-	-	-	-	-	-	-	-	**91.13**	**8.87**
68	41.58	0.02	7.81	0.11	50.19	0.12	0.43	0.07	100.33	91.98	8.02
69	41.58	0.02	7.81	0.11	50.19	0.12	0.43	0.07	100.33	91.98	8.02
70	41.55	0.03	7.86	0.12	50.09	0.14	0.44	0.08	100.31	91.91	8.09
71	41.55	0.03	7.86	0.12	50.09	0.14	0.44	0.08	100.31	91.91	8.09
72	41.92	0.02	9.54	0.15	48.18	0.13	0.27	0.05	100.25	90.01	9.99
73	41.92	0.02	9.54	0.15	48.18	0.13	0.27	0.05	100.25	90.01	9.99
74	42.17	0.01	9.46	0.15	48.50	0.13	0.27	0.04	100.73	90.14	9.86
75	40.29	0.02	8.94	0.14	49.33	0.14	0.36	0.05	99.27	90.77	9.23
76	40.29	0.02	8.94	0.14	49.33	0.14	0.36	0.05	99.27	90.77	9.23
79	40.29	0.02	8.94	0.14	49.33	0.14	0.36	0.05	99.27	90.77	9.23
80	42.07	0.02	7.94	0.11	48.81	0.13	0.46	0.08	99.62	91.63	8.37
81	42.07	0.02	7.94	0.11	48.81	0.13	0.46	0.08	99.62	91.63	8.37
82	-	-	-	-	-	-	-	-	-	**91.13**	**8.87**
83	-	-	-	-	-	-	-	-	-	**91.13**	**8.87**
84	-	-	-	-	-	-	-	-	-	**91.13**	**8.87**
85	-	-	-	-	-	-	-	-	-	**91.13**	**8.87**
86	-	-	-	-	-	-	-	-	-	**91.13**	**8.87**
87	42.39	0.04	7.97	0.12	49.98	0.13	0.45	0.08	101.16	91.79	8.21

88	42.39	0.04	7.97	0.12	49.98	0.13	0.45	0.08	101.16	91.79	8.21
89	42.71	0.03	8.03	0.11	50.73	0.12	0.45	0.07	102.26	91.84	8.16
90	41.26	0.03	9.30	0.14	49.68	0.11	0.32	0.05	100.90	90.50	9.50
91	41.08	0.01	9.29	0.13	49.67	0.12	0.34	0.06	100.71	90.50	9.50
92	41.11	0.01	7.93	0.13	50.83	0.13	0.46	0.12	100.72	91.95	8.05
93	41.26	0.02	7.96	0.12	50.61	0.13	0.46	0.13	100.70	91.89	8.11
94	-	-	-	-	-	-	-	-	-	**91.13**	**8.87**
95	42.18	0.06	7.24	0.10	49.81	0.13	0.50	0.03	100.06	92.46	7.54
96	42.57	0.06	8.92	0.13	48.82	0.14	0.35	0.05	101.05	90.70	9.30
97	42.57	0.06	8.92	0.13	48.82	0.14	0.35	0.05	101.05	90.70	9.30
98	-	-	-	-	-	-	-	-	-	**91.13**	**8.87**
99	-	-	-	-	-	-	-	-	-	**91.13**	**8.87**
100	-	-	-	-	-	-	-	-	-	**91.13**	**8.87**
101	41.84	0.01	10.76	0.16	49.49	0.16	0.25	0.09	102.76	89.13	10.87
102	41.75	0.02	10.74	0.17	49.78	0.14	0.25	0.09	102.94	89.20	10.80
103	-	-	-	-	-	-	-	-	-	**91.13**	**8.87**
104	-	-	-	-	-	-	-	-	-	**91.13**	**8.87**
105	40.44	0.04	8.44	0.14	50.62	0.15	0.39	0.06	100.28	**91.45**	**8.55**
106	40.91	0.03	10.69	0.18	48.28	0.17	0.23	0.03	100.52	**88.95**	**11.05**
110	40.91	0.03	10.69	0.18	48.28	0.17	0.23	0.03	100.52	88.95	11.05

Melt Inclusions PEC Corrected composition.

	Melt Inclusions PEC Corrected (Wt.%)												
Inclusion #	**SiO_2**	**TiO2**	**Al_2O_3**	**Fe_2O_3**	**FeO**	**$FeO_{(tot)}$**	**MnO**	**MgO**	**CaO**	**Na_2O**	**K_2O**	**P_2O_5**	**PEC (%)**
1	50.30	0.68	16.07	1.76	5.84	7.42	0.12	10.84	10.79	2.74	0.73	0.15	10.62
2	50.86	0.70	16.39	1.67	5.59	7.09	0.17	10.27	10.67	2.79	0.79	0.11	11.21
3	50.62	0.69	15.21	1.88	6.32	8.01	0.10	11.53	10.34	2.52	0.71	0.09	4.53
4	50.39	0.66	15.17	1.87	6.35	8.03	0.17	11.96	10.16	2.47	0.70	0.11	4.74
5	50.18	0.68	15.25	1.88	6.35	8.04	0.17	11.92	10.31	2.49	0.67	0.11	3.39
6	48.98	0.71	17.09	1.73	5.69	7.25	0.10	10.04	12.41	2.49	0.66	0.10	4.20
7	48.81	0.55	16.53	1.85	5.99	7.65	0.15	10.75	11.99	2.64	0.65	0.11	3.82
8	48.17	0.73	18.52	1.67	5.37	6.87	0.15	8.99	12.37	3.12	0.80	0.11	4.63
9	48.07	0.78	18.52	1.65	5.33	6.81	0.15	9.09	12.46	3.00	0.83	0.14	3.72
10	48.26	0.76	18.67	1.65	5.29	6.77	0.16	8.60	12.62	12.62	12.62	12.62	12.62
11	46.96	0.78	19.63	1.60	5.20	6.64	0.13	8.70	13.03	3.03	0.78	0.16	1.90
12	47.98	0.64	19.18	1.53	4.92	6.30	0.09	8.61	13.20	2.94	0.77	0.16	1.92
13	48.78	0.73	17.85	1.64	5.28	6.76	0.12	9.45	12.40	2.89	0.75	0.10	2.71
14	49.28	0.68	17.88	1.58	5.08	6.50	0.07	9.09	12.55	2.91	0.75	0.13	6.85
15	48.61	0.85	19.69	1.33	4.14	5.34	0.08	7.17	13.82	3.27	0.90	0.15	5.09
16	50.26	0.74	17.53	1.76	5.89	7.47	0.13	8.52	11.08	3.03	0.88	0.18	3.90
17	50.14	0.73	17.54	1.77	5.86	7.45	0.12	8.56	11.17	3.12	0.85	0.17	8.52
18	50.00	0.70	18.69	1.35	4.36	5.57	0.10	8.12	12.77	2.99	0.80	0.13	8.26
19	49.70	0.77	18.60	1.47	4.85	6.17	0.05	8.19	12.51	2.95	0.74	0.16	5.63
20	48.40	0.83	19.86	1.48	4.78	6.11	0.09	7.15	13.30	3.11	0.86	0.16	3.66
21	47.21	0.83	18.24	1.82	5.85	7.49	0.11	9.80	12.12	3.07	0.79	0.16	3.86
22	49.90	0.71	17.81	1.48	4.82	6.15	0.09	8.80	12.94	2.64	0.68	0.14	6.52
23	49.82	0.73	17.90	1.45	4.69	5.99	0.11	8.67	13.22	2.63	0.67	0.13	5.03
24	49.62	0.69	16.87	1.64	5.32	6.80	0.08	9.88	12.72	2.50	0.60	0.10	12.57
25	48.41	0.72	17.89	1.63	5.39	6.86	0.07	10.23	12.18	2.65	0.71	0.12	3.51
26	47.74	0.75	19.16	1.56	5.20	6.60	0.11	9.18	12.60	2.79	0.77	0.15	1.09
27	47.72	0.78	19.14	1.49	4.73	6.07	0.13	8.64	13.57	2.93	0.76	0.12	2.81
28	47.78	0.78	19.07	1.53	4.88	6.26	0.14	8.71	13.30	2.94	0.75	0.13	7.51
29	48.32	0.81	19.13	1.52	4.92	6.29	0.09	8.25	12.93	3.04	0.82	0.17	9.01
30	49.63	0.74	16.95	1.67	5.48	6.98	0.12	9.70	12.41	2.38	0.82	0.11	7.92
31	49.73	0.76	18.11	1.53	4.92	6.30	0.12	8.51	12.39	3.02	0.85	0.05	17.06
32	50.41	0.64	15.88	1.63	5.29	6.76	0.05	10.48	12.64	2.28	0.59	0.12	7.83
33	49.83	0.72	17.70	1.47	4.64	5.96	0.14	8.86	12.76	3.00	0.79	0.10	0.58
34	49.02	0.67	17.99	1.60	5.20	6.64	0.14	8.94	12.90	2.72	0.69	0.14	1.83
35	49.06	0.72	18.87	1.45	4.63	5.93	0.08	7.91	13.53	2.88	0.76	0.11	10.22
36	48.49	0.67	19.19	1.43	4.70	5.99	0.11	8.09	13.99	2.56	0.64	0.14	2.97
37	49.25	0.73	17.90	1.56	5.04	6.44	0.10	8.75	13.09	2.71	0.68	0.18	7.41
38	49.68	0.68	16.66	1.70	5.62	7.15	0.15	10.19	12.15	2.47	0.61	0.09	12.03
39	49.19	0.67	16.83	1.78	6.01	7.61	0.09	10.70	11.48	2.48	0.67	0.12	6.62

40	48.64	0.64	20.10	1.40	4.98	6.24	0.06	8.36	12.47	2.51	0.71	0.13	8.39
41	50.41	0.75	17.23	1.58	5.14	6.56	0.03	8.77	12.61	2.58	0.79	0.12	5.63
42													
43	50.10	0.69	17.13	1.57	5.31	6.72	0.12	10.08	11.58	2.54	0.69	0.19	10.25
44	49.33	0.73	18.01	1.59	5.01	6.44	0.15	8.01	13.37	2.90	0.78	0.13	10.41
45	51.24	0.63	17.24	1.53	5.19	6.57	0.09	9.11	11.63	2.68	0.53	0.14	8.86
46	50.22	0.73	17.62	1.53	5.23	6.61	0.08	9.04	12.54	2.27	0.61	0.15	6.81
47	50.86	0.66	16.65	1.61	5.43	6.88	0.17	9.55	11.90	2.40	0.65	0.12	1.38
48	50.13	0.61	16.18	1.75	5.84	7.41	0.13	10.27	12.34	2.20	0.48	0.08	7.03
49	51.44	0.66	16.14	1.63	5.74	7.21	0.11	10.32	11.22	2.07	0.59	0.09	2.55
50	49.71	0.66	17.11	1.66	5.60	7.09	0.20	9.74	12.46	2.34	0.46	0.06	8.42
51	49.39	0.65	18.70	1.49	5.49	6.83	0.10	9.65	11.92	2.07	0.38	0.17	5.43
52	49.18	0.72	18.74	1.41	4.57	5.84	0.06	7.80	14.18	2.53	0.67	0.16	0.64
53	49.83	0.71	18.26	1.49	4.87	6.21	0.08	8.32	12.72	2.90	0.67	0.15	5.16
54	49.61	0.80	18.05	1.53	5.01	6.39	0.09	8.57	12.67	2.79	0.70	0.19	0.19
55	49.02	0.68	16.74	1.72	5.62	7.17	0.07	10.85	11.89	2.58	0.74	0.10	9.22
56	49.22	0.69	17.21	1.66	5.37	6.86	0.10	10.25	11.63	2.92	0.86	0.09	8.93
57	48.81	0.73	17.24	1.68	5.37	6.88	0.13	10.19	12.06	2.93	0.77	0.09	7.08
58	47.95	0.77	20.24	1.40	4.38	5.64	0.16	6.81	14.02	3.35	0.74	0.19	7.24
59	48.76	0.75	18.60	1.47	4.83	6.15	0.07	9.09	12.89	2.73	0.71	0.09	5.17
60	47.70	0.84	18.86	1.52	4.53	5.90	0.09	8.05	14.05	3.37	0.80	0.19	8.24
61	49.19	0.75	17.93	1.48	4.84	6.17	0.11	9.08	13.24	2.49	0.68	0.21	8.59
62	48.03	0.78	18.70	1.75	5.98	7.55	0.12	8.95	12.28	2.65	0.65	0.13	6.16
63	46.86	0.77	19.80	1.57	4.78	6.19	0.01	7.69	14.22	3.35	0.76	0.19	3.50
64	48.57	0.70	19.57	1.41	4.41	5.68	0.05	7.33	13.96	3.10	0.82	0.08	6.11
65	48.36	0.72	20.14	1.33	4.17	5.37	0.06	6.89	14.17	3.33	0.66	0.17	7.23
68	48.19	0.65	18.12	1.61	5.06	6.51	0.04	9.34	13.10	2.95	0.74	0.22	9.68
69	47.80	0.71	19.04	1.54	4.87	6.26	0.06	8.86	13.28	3.07	0.77	0.03	3.38
70	48.14	0.69	18.50	1.52	4.81	6.18	0.08	8.86	13.65	2.66	0.83	0.25	2.65
71	49.08	0.67	17.50	1.61	5.36	6.81	0.14	10.12	12.10	2.59	0.63	0.19	3.11
72	46.60	0.63	18.29	2.01	6.63	8.44	0.08	9.71	12.60	2.72	0.62	0.11	5.05
73	46.38	0.67	18.66	1.99	6.40	8.19	0.07	9.24	12.78	2.99	0.72	0.11	12.51
74	47.88	0.73	19.63	1.61	5.45	6.90	0.08	8.20	12.67	2.87	0.65	0.24	8.60
75	48.23	0.76	17.80	1.83	6.04	7.69	0.09	9.75	11.55	2.85	0.93	0.17	4.88
76	48.40	0.68	17.55	1.85	6.12	7.78	0.08	9.93	11.55	2.70	1.02	0.13	1.57
79	48.07	0.76	16.51	2.03	6.59	8.42	0.14	10.72	11.49	2.69	0.85	0.15	2.94
80	49.41	0.73	19.49	1.33	4.60	5.80	0.08	8.36	12.56	2.60	0.75	0.08	3.21
81	48.43	0.75	18.54	1.54	4.90	6.29	0.17	8.68	13.11	3.02	0.69	0.18	5.46
82	49.54	0.69	17.38	1.66	5.62	7.11	0.06	9.75	12.07	2.46	0.61	0.16	0.92
83	50.01	0.66	17.38	1.61	5.64	7.09	0.15	9.93	11.66	2.28	0.58	0.09	5.85
84	51.11	0.65	15.63	1.77	6.11	7.70	0.10	10.95	10.57	2.34	0.67	0.11	6.52
85	48.09	0.72	17.38	1.81	5.85	7.48	0.11	9.88	12.82	2.54	0.69	0.11	8.42
86	48.33	0.76	17.41	1.77	5.65	7.24	0.16	9.51	12.88	2.74	0.67	0.13	9.34
87	46.55	0.82	19.95	1.49	4.51	5.85	0.01	7.85	14.73	3.16	0.75	0.19	11.23

88	46.54	0.81	20.38	1.46	4.54	5.85	0.07	7.88	14.13	3.22	0.83	0.15	12.25
89	47.95	0.75	19.25	1.41	4.21	5.48	0.06	7.52	14.81	3.14	0.80	0.11	6.82
90	47.49	0.71	18.34	1.84	5.93	7.59	0.11	9.14	12.64	3.04	0.64	0.12	12.73
91	47.87	0.72	18.03	1.84	5.90	7.56	0.14	9.14	12.65	2.96	0.71	0.05	12.46
92	50.66	0.60	15.81	1.67	5.67	7.17	0.11	11.15	11.40	2.21	0.61	0.10	9.36
93	51.12	0.61	16.32	1.57	5.25	6.66	0.13	10.20	11.52	2.54	0.58	0.17	8.78
94	46.47	0.70	19.17	1.77	5.65	7.24	0.16	9.19	12.83	3.13	0.74	0.21	9.83
95	51.09	0.87	18.72	1.26	4.29	5.42	0.10	8.64	10.64	3.37	0.78	0.24	5.36
96	48.86	0.66	18.03	1.75	6.02	7.59	0.07	9.81	11.05	2.81	0.72	0.24	3.85
97	47.91	0.68	18.02	1.85	6.13	7.79	0.08	9.80	11.39	2.97	0.86	0.31	7.78
98	53.36	0.81	14.57	1.74	5.63	7.20	0.12	10.01	9.57	3.01	1.11	0.08	9.03
99	52.95	0.75	15.34	1.68	5.79	7.30	0.13	10.41	9.06	2.71	1.05	0.12	10.17
100	53.59	0.76	15.39	1.61	5.18	6.63	0.13	9.11	9.65	3.35	1.06	0.17	-6.82
101	49.02	0.85	16.30	2.09	7.07	8.95	0.12	9.96	11.19	2.59	0.58	0.22	-12.73
102	48.08	0.73	16.67	2.18	7.12	9.08	0.16	9.86	11.48	2.89	0.67	0.16	-12.46
103	47.27	0.70	18.27	1.82	6.19	7.83	0.17	10.37	11.74	2.69	0.67	0.11	-9.36
104	48.21	0.66	16.97	1.89	6.23	7.93	0.11	10.60	11.91	2.64	0.61	0.17	-8.78
105	47.29	0.84	19.24	1.60	5.02	6.46	0.07	8.48	13.36	3.23	0.73	0.15	-9.83
106	47.20	0.80	17.40	2.15	7.12	9.05	0.13	9.55	11.99	2.65	0.77	0.24	-5.36
110	53.08	0.90	14.58	1.97	6.71	8.48	0.13	9.67	8.92	2.81	0.97	0.26	-10.17

Melt inclusions data with Fe XANES and fO_2 calculation.

	Electron Microprobe Measured (Wt.%); Normalized to a water-free basis												
Inclusion #	**SiO_2**	**TiO_2**	**Al_2O_3**	**$FeO_{(tot)}$**	**MnO**	**MgO**	**CaO**	**Na_2O**	**K_2O**	**P_2O_5**	**S (ppm)**	**Cl (ppm)**	**Total***
3	51.78	0.78	17.16	7.66	0.11	6.62	11.67	2.84	0.81	0.10	1746	1227	96.20
4	51.54	0.74	17.14	7.72	0.19	7.03	11.48	2.79	0.79	0.13	1776	1029	96.26
5	51.20	0.76	17.08	7.78	0.19	7.35	11.55	2.78	0.74	0.12	1705	1029	96.17
6	49.21	0.75	18.02	7.06	0.11	7.64	13.08	2.62	0.69	0.11	2843	1390	96.39
7	49.37	0.60	18.11	7.36	0.16	6.83	13.14	2.89	0.71	0.12	2855	1501	95.97
21	47.50	0.89	19.52	7.27	0.12	6.86	12.97	3.28	0.85	0.17	2198	1340	98.50
28	47.82	0.81	19.75	6.11	0.14	6.98	13.78	3.05	0.77	0.13	2571	1466	96.85
34	48.99	0.69	18.47	6.53	0.15	7.55	13.24	2.79	0.71	0.14	3103	1328	97.15
37	49.32	0.76	18.57	6.28	0.10	6.94	13.58	2.81	0.71	0.19	2958	1453	96.36
38	50.33	0.74	18.22	6.84	0.17	6.36	13.29	2.70	0.67	0.09	2398	1207	96.11

	PEC Corrected (Wt.%)										
Inclusion #	**SiO_2**	**TiO_2**	**Al_2O_3**	**$FeO_{(tot)}$**	**MnO**	**MgO**	**CaO**	**Na_2O**	**K_2O**	**P_2O_5**	**PEC (%)**
3	50.62	0.69	15.21	8.01	0.10	11.53	10.34	2.52	0.71	0.09	4.53
4	50.39	0.66	15.17	8.03	0.17	11.96	10.16	2.47	0.70	0.11	4.74
5	50.18	0.68	15.25	8.04	0.17	11.92	10.31	2.49	0.67	0.11	3.39
6	48.98	0.71	17.09	7.25	0.10	10.04	12.41	2.49	0.66	0.10	4.20
7	48.81	0.55	16.53	7.65	0.15	10.75	11.99	2.64	0.65	0.11	3.82
21	47.21	0.83	18.24	7.49	0.11	9.80	12.12	3.07	0.79	0.16	3.86
28	47.78	0.78	19.07	6.26	0.14	8.71	13.30	2.94	0.75	0.13	7.51
34	49.02	0.67	17.99	6.64	0.14	8.94	12.90	2.72	0.69	0.14	1.83
37	49.25	0.73	17.90	6.44	0.10	8.75	13.09	2.71	0.68	0.18	7.41
38	49.68	0.68	16.66	7.15	0.15	10.19	12.15	2.47	0.61	0.09	12.03

	Corrected for Fe Loss											
Inclusion #	**SiO_2**	**TiO_2**	**Al_2O_3**	**Fe_2O_3**	**FeO**	**$FeO_{(tot)}$**	**MnO**	**MgO**	**CaO**	**Na_2O**	**K_2O**	**P_2O_5**
3	50.51	0.69	15.18	3.85	4.53	8.03	0.10	11.51	10.32	2.51	0.71	0.09
4	50.30	0.66	15.14	3.51	4.86	8.05	0.17	11.94	10.14	2.47	0.70	0.11
5	50.07	0.68	15.22	3.89	4.52	8.06	0.17	11.89	10.29	2.48	0.67	0.11
6	48.58	0.70	16.95	3.03	5.14	7.89	0.10	9.96	12.31	2.47	0.65	0.10
7	48.59	0.55	16.46	3.17	5.05	7.94	0.15	10.70	11.94	2.63	0.65	0.11
21	46.95	0.83	18.14	2.92	5.25	7.90	0.11	9.75	12.05	3.05	0.79	0.16
28	46.97	0.77	18.75	2.57	5.42	7.75	0.14	8.56	13.07	2.89	0.74	0.13
34	48.33	0.66	17.73	3.39	4.71	7.80	0.14	8.81	12.72	2.68	0.68	0.14
37	48.51	0.72	17.63	2.58	5.43	7.87	0.10	8.62	12.89	2.67	0.67	0.18
38	49.22	0.67	16.51	3.05	5.12	7.94	0.15	10.10	12.04	2.45	0.60	0.09

	PEC CORRECTION						Kress and Carmichael (1991)
Inclusion #	**Fe3+/Fetot**	**Fe3+/Fetot Corrected**	**Fe3+**	**Fe**	**Fe_2O_3**	**FeO**	**ΔFMQ (1200 °C, 1 Kb)**
3	0.4986	0.4334	2.699	3.529	3.859	4.540	3.3
4	0.4540	0.3942	2.461	3.783	3.519	4.867	2.9
5	0.4971	0.4367	2.730	3.521	3.903	4.530	3.2
6	0.4030	0.3789	2.135	3.498	3.052	4.501	2.8
7	0.4168	0.3748	2.230	3.720	3.189	4.786	2.7
21	0.3813	0.3532	2.056	3.765	2.939	4.843	2.4
28	0.3915	0.3754	1.826	3.037	2.611	3.908	2.5
34	0.4823	0.4666	2.408	2.753	3.443	3.542	3.4
37	0.3822	0.3657	1.831	3.177	2.619	4.088	2.5
38	0.4295	0.3877	2.154	3.403	3.080	4.378	2.7

	Corrected for Fe Loss				Kress and Carmichael (1991)
Inclusion #	**LLDs Fe***	**FeO Lost**	**Fe_2O_3**	**FeO**	**ΔFMQ (1200 °C, 1 Kb)**
3	7.942	-	3.859	4.540	3.3
4	7.931	-	3.519	4.867	2.9
5	7.932	-	3.903	4.530	3.2
6	7.933	0.686	3.052	5.187	2.4
7	7.946	0.292	3.189	5.077	2.5
21	7.925	0.437	2.939	5.280	2.2
28	7.865	1.608	2.611	5.516	1.9
34	7.881	1.241	3.443	4.783	2.8
37	7.868	1.424	2.619	5.512	1.9
38	7.937	0.788	3.080	5.166	2.4

Referred to as "Appendix 2" in Chapter 5. Trace element composition of olivine obtained by LA-ICP-MS.

	Minor and Trace element Composition of Olivine Obtained by LA-ICP-MS											
Host to Inclusion#	**Li**	**Na**	**Al**	**K**	**Sc**	**Ti**	**V**	**Cr**	**Mn**	**Co**	**Ni**	**Zn**
40	0.60	81.00	121.00	15.00	9.30	24.00	2.40	389.00	933.00	133.80	3620.00	57.00
41	bdl	33.00	144.00	bdl	6.00	34.00	2.00	424.00	1048.00	160.00	3790.00	65.00
S6-MI2	5.00	bdl	113.40	19.00	5.90	13.00	2.40	277.00	1273.00	181.00	2890.00	57.00
43	1.40	bdl	72.00	4.00	3.40	22.00	43.00	148.00	1646.00	188.00	1360.00	131.00
62	3.50	bdl	128.00	55.00	9.80	9.00	4.40	581.00	1009.00	147.00	3810.00	78.00
44	bdl	bdl	174.00	bdl	2.70	15.00	3.90	428.00	1377.00	184.00	4370.00	103.00
45	0.30	72.00	106.70	bdl	9.40	8.50	3.20	200.00	1505.00	178.60	1740.00	91.00
55	2.20	54.00	142.50	bdl	3.80	14.90	3.70	421.00	954.00	146.60	4240.00	72.00
58	3.10	11.00	143.00	bdl	1.00	24.40	1.49	492.00	972.00	155.00	4160.00	72.00
59	5.10	81.00	130.00	14.00	5.30	34.00	2.98	408.00	1257.00	168.00	3270.00	98.00
61	2.20	73.00	122.60	10.00	8.30	18.20	2.17	479.00	930.00	156.90	3310.00	59.00
70	1.30	bdl	134.10	43.00	8.10	12.40	1.98	444.00	900.00	145.60	4350.00	65.00
68	0.90	1.00	150.80	24.00	8.30	24.00	2.95	432.00	959.00	149.50	4020.00	57.00
72	1.70	42.00	155.20	bdl	8.40	17.80	3.50	444.00	912.00	146.60	3950.00	63.00
76	bdl	7.00	117.30	11.00	8.70	20.00	3.72	290.00	1262.00	151.90	2450.00	89.00
75	2.90	16.00	113.80	bdl	6.90	27.70	3.48	411.00	1340.00	158.10	1845.00	94.00
90	3.40	56.00	100.30	9.00	6.90	29.40	3.00	246.00	1339.00	163.00	2040.00	78.00
91	4.20	91.00	130.30	58.00	11.50	14.40	4.20	338.00	1206.00	164.90	3220.00	72.00
92	2.00	bdl	116.60	bdl	6.20	13.50	3.12	356.00	1312.00	176.50	3020.00	73.00
94	3.30	60.00	157.50	11.00	5.40	20.60	3.90	515.00	929.00	147.30	4110.00	57.00
95	3.10	97.00	98.30	85.00	16.40	20.00	4.45	295.00	1065.00	157.30	2770.00	77.00
96	2.80	13.00	121.80	20.00	8.70	15.30	2.78	404.00	1280.00	180.00	4110.00	107.00
101	0.30	47.00	135.90	38.00	10.60	15.00	1.94	423.00	980.00	146.60	3690.00	94.00
102	2.30	36.00	98.60	5.00	6.40	30.00	3.50	271.00	1430.00	169.00	1990.00	59.00
S53-MI1	bdl	31.00	128.40	17.00	7.50	19.40	2.22	371.00	1011.00	143.10	3660.00	53.00
105	0.50	38.00	202.00	18.00	5.60	31.80	4.10	900.00	1043.00	151.20	3200.00	76.00
106	bdl	109.00	107.20	9.00	11.90	30.60	2.62	217.00	1366.00	158.70	2100.00	75.00
6	2.30	25.00	125.70	12.00	6.70	22.80	1.90	364.00	1080.00	146.30	3400.00	74.00
5	bdl	47.00	126.00	bdl	9.80	17.90	2.08	243.00	1220.00	161.00	2490.00	104.00
2	0.60	12.00	144.00	4.00	10.50	22.00	3.32	344.00	1004.00	143.00	3540.00	65.00
8	0.60	27.00	121.00	bdl	4.90	10.10	1.99	287.00	1068.00	148.00	3390.00	85.00
19	1.90	19.00	118.70	bdl	1.80	23.00	2.16	314.00	1075.00	157.10	3170.00	79.00
3B	3.70	26.00	82.10	14.00	5.80	33.00	2.31	170.00	1435.00	173.30	1604.00	105.00
20	3.00	43.00	128.60	16.00	3.50	17.40	2.68	321.00	992.00	141.90	3130.00	67.00
31	3.90	77.00	149.90	20.00	6.60	15.80	3.37	431.00	986.00	147.70	3890.00	68.00
34	4.90	bdl	139.00	bdl	2.50	28.90	2.50	696.00	1070.00	151.00	3940.00	70.00
30	2.10	44.00	131.50	5.00	8.20	21.90	2.35	397.00	1100.00	151.50	3370.00	61.00
29	0.50	24.00	116.60	2.00	3.20	29.10	2.03	341.00	1135.00	165.20	3560.00	59.00
27	0.30	48.00	118.00	47.00	5.70	15.10	3.10	390.00	990.00	125.00	3200.00	58.00

	Standard Deviation											
Mean	2.43	25.11	10.77	19.37	3.44	8.60	1.01	27.93	54.50	9.89	171.57	15.89
Median	2.40	23.00	9.00	18.00	3.40	8.30	0.94	20.00	52.00	9.65	170.00	15.00
Max	3.70	63.00	53.00	34.00	5.80	17.00	1.80	330.00	120.00	16.00	290.00	26.00
Min	1.20	13.00	6.60	11.00	2.20	5.10	0.58	11.00	33.00	6.80	77.00	9.80
	Limit of Detection											
Mean	5.09	71.33	7.20	10.30	6.42	12.34	1.59	8.50	3.94	2.31	2.91	17.38
Median	4.80	51.58	6.56	9.37	6.03	11.71	1.35	8.08	3.65	2.05	2.93	16.85
Max	9.84	343.63	15.13	17.81	10.07	22.04	2.48	16.65	6.86	4.50	10.05	40.15
Min	2.86	31.45	4.45	5.65	3.89	0.00	0.83	4.03	2.59	1.19	0.00	7.34

*All given values in ppm;**bdl(Below detection limit)

Referred to as "Appendix 3" in Chapter 5. Major element composition of spinel-olivine pairs and calculated fO2.

Oxides Wt.%												
MgO	**SiO2**	**Al2O3**	**FeO**	**MnO**	**NiO**	**Cr2O3**	**CaO**	**TiO2**	**Total**	**T (K)**	**FMQ**	**2σ**
12.89	0.15	14.80	21.34	0.39	0.13	47.77	0.08	0.29	97.87	1202.497	**1.40**	0.467
48.35	41.65	0.03	8.54	0.12	0.40	0.08	0.14	0.02	99.36			
12.66	0.14	13.74	21.90	0.40	0.09	48.60	0.08	0.30	97.95	1157.884	**1.72**	0.443
50.19	41.58	0.02	7.81	0.11	0.43	0.07	0.12	bdl	100.35			
12.68	0.16	14.34	22.37	0.37	0.08	47.88	0.10	0.30	98.31	1152.114	**1.75**	0.427
50.28	42.80	0.02	7.96	0.13	0.43	0.07	0.12	0.01	101.84			
12.31	0.10	13.82	24.16	0.37	0.09	45.99	0.03	0.41	97.31	1331.837	**1.25**	0.324
47.60	41.13	0.00	11.86	0.16	0.17	0.04	0.15	0.00	101.13			
13.40	0.41	14.60	18.75	0.36	0.20	48.87	0.16	0.25	97.04	1191.577	**1.16**	0.478
50.83	41.11	0.01	7.93	0.13	0.46	0.12	0.13	0.00	100.75			
13.40	0.11	13.66	18.99	0.40	0.18	50.92	0.06	0.25	98.00	1216.687	**1.20**	0.607
50.61	41.26	0.02	7.96	0.12	0.46	0.13	0.13	bdl	100.73			
13.42	0.14	14.69	20.82	0.40	0.13	49.12	0.02	0.26	99.03	1169.403	**1.65**	0.478
50.76	40.36	0.04	7.54	0.10	0.49	0.07	0.13	bdl	99.51			
14.21	0.10	13.56	18.02	0.34	0.19	50.41	0.01	0.30	97.18	1332.162	**1.15**	0.534
50.48	41.16	0.01	8.32	0.13	0.41	0.08	0.13	0.00	100.75			
13.26	0.06	15.79	22.37	0.34	0.13	45.44	0.03	0.49	97.93	1244.845	**1.57**	0.381
48.69	42.49	0.02	8.97	0.14	0.35	0.05	0.14	bdl	100.84			
13.47	0.07	15.76	22.21	0.34	0.14	45.54	0.02	0.49	98.06	1261.084	**1.59**	0.385
48.82	42.57	0.02	8.92	0.13	0.35	0.05	0.14	bdl	101.01			
14.81	0.09	14.74	18.43	0.32	0.20	48.15	0.01	0.37	97.16	1390.082	**1.36**	0.417
50.62	40.44	0.04	8.44	0.14	0.39	0.06	0.15	bdl	100.31			
14.81	0.09	15.59	18.67	0.33	0.21	47.17	0.02	0.39	97.30	1364.647	**1.39**	0.418
51.03	40.93	0.03	8.47	0.11	0.39	0.07	0.15	0.02	101.22			
10.64	0.16	12.43	21.83	0.43	0.11	51.60	0.11	0.26	97.60	1082.495	**0.73**	0.849
49.67	41.08	0.01	9.29	0.13	0.34	0.06	0.12	bdl	100.73			
11.93	0.13	15.23	20.26	0.39	0.14	49.58	0.06	0.25	98.00	1080.913	**0.85**	0.903
50.48	41.16	0.01	8.32	0.13	0.41	0.08	0.13	0.00	100.75			
11.93	0.13	15.29	20.39	0.39	0.14	49.53	0.05	0.28	98.15	1088.481	**0.81**	0.897
49.32	40.67	0.02	8.36	0.13	0.41	0.10	0.13	bdl	99.16			
14.16	0.11	13.64	16.71	0.33	0.19	52.82	0.02	0.23	98.24	1353.557	**0.41**	0.816
49.47	41.42	0.02	9.13	0.14	0.32	0.04	0.15	bdl	100.72			
14.21	0.11	13.61	16.79	0.34	0.19	52.88	0.01	0.24	98.43	1358.780	**0.44**	0.794
49.54	41.47	0.01	9.12	0.15	0.33	0.04	0.15	bdl	100.85			
14.32	0.11	13.56	16.81	0.34	0.20	52.50	0.02	0.24	98.12	1373.841	**0.55**	0.721
49.39	41.49	0.02	9.01	0.14	0.34	0.04	0.15	bdl	100.59			

Oxides Wt.%												
MgO	**SiO2**	**Al2O3**	**FeO**	**MnO**	**NiO**	**Cr2O3**	**CaO**	**TiO2**	**Total**	**T (K)**	**FMQ**	**2σ**
14.20	0.12	13.50	16.81	0.32	0.19	52.24	0.02	0.26	97.69	1360.940	**0.56**	0.744
49.30	41.47	0.02	8.91	0.13	0.34	0.04	0.16	bdl	100.39			
13.54	0.09	13.29	17.48	0.35	0.18	52.35	0.05	0.25	97.65	1235.176	**0.82**	0.810
50.32	41.80	0.02	7.93	0.12	0.47	0.10	0.12	bdl	100.92			
13.67	0.09	13.28	17.39	0.35	0.17	52.28	0.05	0.24	97.64	1248.586	**0.85**	0.775
50.28	41.89	0.03	7.93	0.12	0.47	0.11	0.13	0.02	101.00			

***Red: Data in disequilibrium; Green: Data in equilibrium; Orange: Data slightly disequilibrated*.**

Referred to as "Appendix 4" in Chapter 5. Minor and Trace Element Composition of Olivine-Hosted Melt inclusions.

Inclusion #	Li	Na	K	Sc	Ti	V	Cr	Mn	Co	Ni	Cu	Zn	Ga	Rb	Sr	Y	Zr	Nb	Sn	Sb
40	8.30	20820.00	6670.00	44.00	3900.00	297.00	195.00	848.00	30.00	44.70	127.00	72.00	20.70	11.30	580.00	13.00	52.50	0.99	0.20	1.10
42	13.40	21490.00	8500.00	37.00	4530.00	269.00	163.40	1196.00	27.10	48.50	145.80	98.60	16.70	21.80	497.00	12.76	91.00	1.29	1.06	bdl
43	13.00	24520.00	9970.00	31.00	5060.00	319.50	6890.00	1329.00	33.70	71.40	147.10	129.00	19.30	26.00	473.00	14.08	86.00	1.76	1.05	bdl
62	6.70	25700.00	6910.00	36.70	4730.00	309.00	124.00	1111.00	47.20	115.00	99.00	102.00	26.70	13.90	707.00	12.60	54.80	0.96	2.90	0.90
47	10.10	19810.00	5760.00	36.10	3980.00	278.00	214.00	978.00	28.60	86.00	115.00	74.00	21.20	11.10	559.00	12.60	45.80	1.26	0.90	1.20
55	10.70	21620.00	6710.00	35.20	4140.00	276.00	162.00	887.00	21.70	88.00	89.00	83.00	19.40	13.10	567.00	13.10	60.50	1.01	0.12	1.00
72	1.30	20600.00	6390.00	32.00	3990.00	325.00	72.00	1120.00	37.10	238.00	52.00	117.00	18.00	9.50	617.00	13.00	44.40	0.34	1.70	6.60
76	6.90	22490.00	8520.00	39.00	4060.00	280.00	112.00	1064.00	34.10	89.00	107.00	82.00	21.30	18.90	591.00	15.20	84.60	0.76	1.00	1.00
90	9.40	19600.00	5900.00	53.00	4390.00	305.00	160.00	1036.00	31.10	94.00	113.00	41.00	20.50	10.10	580.00	14.20	49.60	1.02	bdl	1.50
91	16.80	20960.00	9060.00	47.80	5440.00	302.00	106.20	1303.00	26.90	40.00	136.00	90.00	16.20	23.20	491.00	15.10	71.80	1.36	1.90	bdl
92	8.30	16490.00	4530.00	38.80	3660.00	241.00	240.00	964.00	30.50	147.00	97.00	78.00	14.60	7.60	512.00	12.20	44.90	0.82	0.20	0.50
98	10.60	24270.00	9290.00	33.20	4900.00	291.00	154.00	1123.00	26.50	90.00	146.80	83.00	20.60	23.10	500.00	14.90	69.70	1.10	1.10	0.50
102	31.00	20200.00	5820.00	42.00	4730.00	304.00	140.00	1070.00	30.00	29.00	97.00	100.00	17.00	9.80	600.00	6.40	48.00	bdl	bdl	11.00
103	7.90	22470.00	6440.00	51.50	4940.00	299.00	193.00	1107.00	27.30	39.20	116.00	76.00	17.60	14.20	622.00	15.80	58.20	0.57	0.80	bdl
103	7.80	18690.00	5640.00	21.70	3020.00	180.00	59.80	758.00	17.10	25.40	83.10	56.00	14.00	14.50	500.00	8.73	39.70	1.00	0.48	0.19
106	11.30	20060.00	5860.00	42.00	3930.00	259.00	122.00	1136.00	28.00	82.00	101.00	44.00	14.80	14.30	516.00	9.90	42.70	0.45	1.50	bdl
110	10.10	20970.00	6700.00	22.50	3210.00	198.00	53.00	780.00	15.40	48.00	83.00	55.00	18.20	16.20	488.00	8.90	45.00	0.77	2.50	bdl
6	5.80	20790.00	6110.00	50.90	4030.00	285.00	147.00	1032.00	32.40	80.00	109.00	97.00	16.70	10.80	635.00	16.20	51.70	0.64	1.50	bdl
3	10.50	22500.00	6630.00	37.30	4100.00	265.00	179.00	1219.00	31.40	77.90	106.60	120.00	20.30	14.00	579.00	14.40	54.90	1.04	0.80	0.70
1	13.00	23660.00	7450.00	42.00	3970.00	274.00	236.00	1009.00	36.70	135.00	118.00	101.00	22.60	19.90	544.00	16.90	56.40	0.93	2.50	bdl
8	2.00	24220.00	6810.00	40.10	4990.00	311.00	74.00	971.00	26.00	99.00	110.00	72.00	19.20	15.60	670.00	15.90	60.90	0.73	bdl	bdl
19	17.00	20600.00	7100.00	32.00	4590.00	270.00	166.00	1300.00	30.80	53.00	82.00	102.00	20.10	22.80	631.00	12.80	90.00	1.74	2.20	bdl
32	8.10	20480.00	5310.00	43.20	4400.00	318.00	256.00	925.00	18.50	32.80	84.10	81.00	22.50	8.90	619.00	15.50	51.30	0.49	0.91	bdl
31	12.00	18100.00	5480.00	26.00	3860.00	314.00	188.00	609.00	7.20	0.00	63.00	28.00	16.90	10.70	549.00	13.10	39.90	0.73	0.30	bdl

	Standard Deviation																			
Mean	6.06	971.67	384.58	8.41	310.83	20.69	53.43	65.58	4.77	15.87	12.92	35.44	4.03	2.68	34.58	1.97	508.57	0.46	1.50	2.81
Median	4.75	805.00	275.00	7.35	245.00	16.00	14.50	49.50	4.30	12.50	13.00	31.00	3.15	2.60	27.00	1.80	5.70	0.39	1.30	1.85
Max	19.00	2200.00	1000.00	22.00	950.00	56.00	890.00	250.00	10.00	56.00	29.00	140.00	12.00	7.30	96.00	4.50	12000.00	0.98	3.80	10.00
Min	1.70	440.00	180.00	2.20	130.00	9.50	7.60	27.00	1.50	0.00	4.10	9.60	1.50	1.10	13.00	0.75	2.50	0.21	0.40	0.67
	Limit of Detection																			
Mean	12.92	123.30	23.25	15.95		3.83	18.66	9.18	5.01	5.01	14.01	45.82	5.62	2.89	0.59	0.22	4.64	0.43	3.03	5.66
Median	9.32	89.86	17.18	12.33	22.36	2.57	14.72	6.64	3.75	3.83	11.47	30.79	3.94	2.39	0.30	0.02	0.00	0.37	2.85	3.89
Max	38.69	341.19	74.92	51.97	113.76	14.85	55.83	34.64	16.63	15.22	37.62	188.43	19.06	6.87	2.64	1.08	84.96	1.54	9.15	17.13
Min	1.68	20.17	4.49	2.15	6.22	0.85	3.62	1.34	0.81	0.00	2.52	5.17	0.90	0.70	0.00	0.00	0.00	0.00	0.64	2.05

Referred to as "Appendix 4" in Chapter 5. Minor and Trace Element Composition of Olivine-Hosted Melt inclusions (Continued).

Inclusion #	Cs	Ba	La	Ce	Pr	Nd	Sm	Eu	Gd	Tb	Dy	Ho	Er	Tm	Yb	Lu	Hf	Ta	Pb	Th	U
40	2.17	145.10	6.20	14.40	2.15	10.10	1.60	0.74	3.60	0.32	1.49	0.32	1.68	0.13	1.19	0.25	1.29	0.04	8.60	1.24	0.76
42	1.19	203.10	7.82	20.00	2.47	11.60	2.39	0.83	2.05	0.38	2.59	0.61	1.17	0.11	1.49	0.17	1.88	0.05	10.32	2.02	0.73
43	1.81	228.80	9.64	22.90	2.48	13.90	2.86	0.86	3.16	0.39	2.40	0.50	1.81	0.22	1.41	0.18	2.73	0.06	10.31	2.75	1.05
62	1.25	183.00	8.00	19.40	2.65	11.50	1.80	0.55	3.40	0.30	1.46	0.47	1.35	0.35	0.84	0.12	1.05	0.21	11.00	1.74	0.79
47	1.04	137.80	5.82	13.60	1.96	11.40	1.90	0.89	1.30	0.18	1.53	0.49	1.06	0.15	1.53	0.16	1.14	bdl	8.50	1.80	0.68
55	0.83	158.90	6.69	16.10	1.90	9.20	2.50	0.84	2.35	0.26	1.40	0.45	1.43	0.21	1.07	0.08	1.67	0.01	8.50	1.84	0.43
72	0.48	159.00	7.30	14.30	1.52	8.90	7.10	0.58	1.60	0.23	2.30	0.58	1.11	bdl		0.16	1.70	bdl	8.50	2.33	0.61
76	bdl	189.40	7.80	18.50	2.38	9.50	1.22	0.57	0.72	0.47	2.20	0.60	0.60	bdl	0.81	0.23	2.07	bdl	11.00	2.43	0.53
90	0.62	147.00	4.70	13.70	1.75	6.90	1.50	1.08	1.20	0.22	1.01	0.32	1.58	0.22	1.08	0.16	0.51	bdl	8.10	1.17	0.47
91	1.63	223.00	9.30	19.60	3.20	13.30	1.33	1.00	2.40	0.27	1.90	0.60	2.13	0.22	1.68	0.14	2.30	0.11	12.00	2.81	0.78
92	0.82	123.70	6.51	13.30	1.42	8.90	2.42	0.56	1.90	0.40	2.07	0.29	0.91	0.16	1.46	0.16	1.04	0.11	8.30	1.96	0.48
98	1.85	221.40	9.21	19.30	2.34	12.00	2.90	0.55	3.30	0.37	2.50	0.31	1.00	0.30	1.57	0.22	1.91	bdl	11.60	2.69	1.07
102	2.70	168.00	7.20	17.60	2.20	10.20	bdl	1.10	1.30	bdl	bdl	bdl	bdl	bdl		bdl	bdl	bdl	12.30	2.20	bdl
103	0.88	187.00	7.50	16.50	2.04	8.20	2.30	0.82	3.20	0.32	1.90	0.48	1.17	0.21	1.25	0.22	1.01	bdl	10.40	1.89	0.44
103	1.01	139.00	5.42	13.10	1.45	7.40	1.72	0.49	1.03	0.19	1.49	0.27	0.57	0.13	1.06	0.10	1.58	0.01	6.90	1.42	0.60
106	bdl	147.60	4.94	15.40	1.38	9.20	2.70	0.73	1.50	0.13	1.40	0.61	0.83	0.12	1.09	0.10	1.29	bdl	7.60	1.32	0.49
110	0.06	158.00	6.20	13.60	1.57	6.40	1.20	0.55	0.84	0.30	1.14	0.35	1.22	bdl	0.88	0.22	0.99	bdl	7.10	1.31	0.48
6	0.80	159.00	7.20	15.50	2.08	11.60	1.40	1.08	1.90	0.22	3.30	0.48	1.59	0.27	1.09	0.15	1.49	bdl	8.30	1.62	0.60
3	1.21	176.60	8.60	16.40	2.20	9.60	3.30	0.63	2.70	0.30	2.35	0.46	1.35	0.20	0.94	0.25	1.84	0.16	9.70	2.12	0.84
1	1.50	180.00	6.30	17.20	2.40	11.70	1.50	1.09	bdl	0.45	2.00	0.29	1.70	0.13		0.22	0.36	bdl	9.80	1.73	0.48
8	0.99	174.00	7.30	15.60	2.16	12.10	2.00	0.98	2.60	0.48	2.90	0.30	1.38	0.29	2.00	0.16	0.55	bdl	9.70	2.11	0.38
19	1.60	202.00	6.50	25.00	2.71	12.30	1.70	0.64	1.90	0.25	0.99	0.60	1.12	0.09	1.70	0.33	0.29	0.27	8.30	2.17	1.10
32	0.77	145.80	7.02	16.20	1.70	11.50	2.80	0.86	1.79	0.23	1.79	0.38	1.39	0.14	1.73	0.22	1.12	bdl	8.80	2.35	0.68
31	1.20	136.00	8.00	16.00	2.30	12.70	3.10	bdl	3.60	0.26	bdl	0.26	1.10	bdl	1.90	bdl	bdl	bdl	8.80	0.78	1.90

	Standard Deviation																				
Mean	0.82	11.70	1.26	2.18	0.55	2.98	1.30	0.42	1.35	0.19	0.84	0.22	0.63	0.13	0.80	0.14	0.67	0.10	2.24	0.55	0.32
Median	0.61	9.90	1.10	1.55	0.50	2.65	1.10	0.39	1.10	0.15	0.78	0.20	0.55	0.11	0.67	0.13	0.64	0.08	1.85	0.47	0.29
Max	2.50	27.00	3.20	10.00	1.30	7.30	4.10	1.20	3.70	0.56	1.60	0.52	1.50	0.27	2.50	0.29	1.20	0.28	6.70	1.40	1.10
Min	0.21	5.40	0.46	1.00	0.25	1.20	0.44	0.18	0.44	0.05	0.38	0.10	0.24	0.04	0.39	0.06	0.38	0.02	0.86	0.25	0.15
	Limit of Detection																				
Mean	1.76	1.03	0.07	0.13	0.11	0.11	0.56	0.17	0.68	0.05	0.30	0.09	0.10	0.03	0.23	0.05	0.39	0.04	2.77	0.01	0.04
Median	1.24	0.58	0.00	0.00	0.00	0.00	0.14	0.00	0.53	0.00	0.00	0.00	0.00	0.00	0.00	0.00	0.00	0.00	2.01	0.00	0.00
Max	7.89	3.26	0.37	0.74	0.80	1.13	4.21	0.77	4.44	0.82	1.66	0.87	0.64	0.15	2.86	0.32	3.60	0.15	11.58	0.19	0.66
Min	0.36	0.00	0.00	0.00	0.00	0.00	0.00	0.00	0.00	0.00	0.00	0.00	0.00	0.00	0.00	0.00	0.00	0.00	0.38	0.00	0.00